PSFC/RR-08-9

MECHANICAL AND ELECTROMAGNETIC TRANSVERSE LOAD EFFECTS ON SUPERCONDUCTING NIOBIUM-TIN PERFORMANCE

Luisa Chiesa

Plasma Science and Fusion Center
Massachusetts Institute of Technology
Cambridge MA 02139 USA

February 2009

This work was supported by the U.S. Department of Energy, Grant No. DE-FC02-93ER54186.

MECHANICAL AND ELECTROMAGNETIC TRANSVERSE LOAD EFFECTS ON SUPERCONDUCTING NIOBIUM-TIN PERFORMANCE

By
Luisa Chiesa
M.S., Nuclear Science and Engineering (2006)
Massachusetts Institute of Technology

Submitted to the Department of Nuclear Science and Engineering
in partial fulfillment of the requirement for the degree of

Doctor of Philosophy in Nuclear Science and Engineering
at the
MASSACHUSETTS INSTITUTE OF TECHNOLOGY
February 2009

Author ----------

Department of Nuclear Science and Engineering
December 2, 2008

Certified by ----------

Joseph V. Minervini
Senior Research Engineer, MIT Plasma Science and Fusion Center
Nuclear Science and Engineering Department
Thesis Supervisor

Certified by ----------

Jeffrey P. Freidberg
Professor of Nuclear Science and Engineering
Thesis Reader

Certified by ----------

Ronald R. Parker
Professor of Electrical Eng. and Comp. Science and Nuclear Science and Eng.
Thesis Reader

Accepted by ----------

Jacquelyn C. Yanch
Professor of Nuclear Science and Engineering
Chair, Department Committee on Graduate Students

MECHANICAL AND ELECTROMAGNETIC TRANSVERSE LOAD EFFECTS ON SUPERCONDUCTING NIOBIUM-TIN PERFORMANCE

By
Luisa Chiesa

M.S., Nuclear Science and Engineering (2006)
Massachusetts Institute of Technology

Submitted to the Department of Nuclear Science and Engineering
in partial fulfillment of the requirement for the degree of

Doctor of Philosophy in Nuclear Science and Engineering

at the

MASSACHUSETTS INSTITUTE OF TECHNOLOGY
February 2009

ABSTRACT

Cable-in-Conduit Conductor is the typical geometry for the conductor employed in superconducting magnets for fusion applications. Once energized, the magnets produce an enormous electromagnetic force and very large transverse loads are applied against the strands. This large force results in a degradation of the performance of the superconducting magnets.

In this thesis work transverse load experiments on sub-sized cables, have been designed to study the mechanical and electrical transverse load effects on superconducting cables. Two devices to apply external mechanical loads to a cable have been developed and several different size cables have been tested simulating the International Thermonuclear Experimental Reactor (ITER) Lorentz stress conditions.

The first device was designed to use a circular turn sample of a 36-strand cable. Four samples were successfully tested with this device and significant degradations of the critical current due to the external transverse loads have been measured. However, all samples showed unexpectedly large initial degradations that made an analysis of transverse load effects of the samples difficult.

The second device was developed for a hairpin configuration. Three different size cables of a single strand, a triplet and a 45-strand cable were systematically tested using this method. This hairpin sample device has successfully operated and provided very reliable experimental data.

The experimental results were difficult to explain by existing theories. A new model based on contact mechanics concepts has been developed to determine the number of contacts and the effective contact pressure among the strands in a cable. The model was used to analyze and accurately calculate the displacements of a cable under transverse

mechanical load, and it has evaluated the effective contact pressures between strands for the first time.

The new model can explain the Lorentz force and contact pressure distribution effect on the critical current degradation of the tested samples. The 3-strand data and their critical current behavior as a function of the effective contact pressure were used to predict the test behavior of a 45-strand cable. It was also used to simulate the critical current degradations of various cables including ITER full size cables. The model has predicted an initial degradation of 20% for an ITER TF cable of 1152 strands at 68 kA operational current caused by the transverse Lorentz load effect only.

Parametric studies of the model have indicated that the initial degradation could be reduced by shortening the twist pitch length of the initial stages of a full size cable or by mechanically supporting the last stage bundles of the cable.

This thesis work shows for the first time, that the transverse Lorentz load effect, which is inherent in the CICC design, contributes a significant fraction of the degradation of a large Nb_3Sn superconducting cable. The model quantifies the degradation and this information could be used in better estimating the appropriate margin requirements in magnet design.

Thesis Supervisor: Dr. Joseph V. Minervini
Title: PSFC Technology and Engineering Division Head

Thesis Reader: Prof. Jeffrey P. Freidberg
Title: Professor of Nuclear Science and Engineering

Thesis Reader: Prof. Ronald R. Parker
Title: Professor of Electrical Eng. and Computer Science and Nuclear Science and Eng.

ACKNOWLEDGEMENTS

I would like to express my deep gratitude to my supervisor Dr. Joseph Minervini, for his constant support (money money money) and for being always so positive under any circumstance. Thanks for believing I could get to the end of my studies and for pushing me to get to the end!

Thanks to Prof. Jeff Friedberg and Prof. Parker and the patience in reading this thesis. One reader was not enough; I had to make at least two professors reading this after they made me go through all those plasma physics classes (just kidding).

A very special thank to the Master, Dr. Makoto-San Takayasu. I think I would need a separate thesis entitled "Dr. Makoto Takayasu" to express my profound gratitude to one of the brightest person I have ever met in my life. Yes, sometimes during those long days taking data in the lab in Florida, I would have liked to escape while Makoto was saying "we are almost done" for the tenth time in the five hours following the first "we are almost done". Makoto you might be "almost" at your retirement age but you can work harder than anyone I know. I still hope you will run 7 miles with me one day…maybe after that you will not have the strength to say "we are almost done".

Makoto is a very patient man who always finds time to explain things and never gets tired of looking for things to improve to have a successful experiment. He got to know the best and the worst of me but he never stopped pushing me for the best.

Arigato gozaimasu Makoto!!!

Another very special thank to Dave Tracey and his smiling face any time I asked him to modify things for the second…third time. Without his technical skills and his contribution I would not be here writing acknowledgements.

Thanks to Rui Vieira for his valuable help and the work done by his group: Jeff Doody a.k.a.the "ALGOR guy", Rick Leccacorvi for the tips in Solid Edge.

A special thank to Ed Fitzgerald and the technicians: Bob, Charlie and Richie. They all work relentlessly on my parts…I don't know if this was because they really liked the job or they simply wanted me and my never ending requests of modifications to disappear as quickly as possible.

Thanks to everyone in the group especially Peter Titus and his ANSYS expertise, Darlene Marble for the constant assistance and the chocolate.

A portion of this work was performed at the National High Magnetic Field Laboratory, which is supported by NSF Cooperative Agreement No. DMR-0084173, by the State of Florida, and by the DOE. DOE supported this work with grant number DE-FC02-93ER54186. Many thanks to all the people that helped us with the experiment at the NHMFL facility. For all those cookies, oranges and apples when we were working on the experiments.

Thanks to my family, my mum and dad and my wonderful brother who together with his family (Sofia, my niece Niina and my nephew Georg) had the privilege or misfortune to share with me two years here in Boston. They liked me so much that they decided to move on the other side of the planet after that!

To my grandfather Antonio who turned 90 few days ago and who is still wondering why I am still studying.

A very special thank to Tim and Charles.

Thanks to all my special friends in Boston and their presence in my life. Thanks to Ksusha from Siberia (I can see your face Ksusha!) for reading my thesis, Antonio and Gretchen, Roberta, Paolo and Francesca, Darwin, Sejal and Jigar, Jeff, Matteo, Scott, Chudi, Jen, Matt.

Also thanks to all the special friends far away… Michela because despite being so far away she is so close and such a wonderful, truthful and sincere friend, Paolo and Jackie from the other side of the country and their long, rare but extremely relaxing phone calls full of laughs and gossip, Peter, Chris, Shlomo, Silvia, Francesca, Alessandra, Elena, Marco, Daniela, Gianni, Carrie, and whomever I forgot…

THANK YOU

INDEX

List of Figures

Chapter 1

Chapter 2

Chapter 5

Chapter 6

shape holder is rounded to be able to bring out the wires and to avoid damaging them.

Fig. I.14 (a) Bottom voltage tap wires and spacer used to maintain the desired void fraction during heat treatment. (b-c) Sample ready for heat treatment.

Fig. I.15 Preparation of the samples and installation of the samples on the heat treatment rack. Four samples can be heat treated at the same time.

Fig. I.16 Samples taken out of the oven after heat treatment. The bottom sections show a dark color due to residual organic materials formed during heat treatment. Also to notice is that only in this position the cable is supported well in the U-bend section (piece is touching bottom plate). During assembly it is necessary to maintain the sample facing up as in the heat treatment configuration to support the cable at all time.

Fig. I.17 (a) Copper leads: top section is connected to the vapor cooled leads, the bottom one is where the sample is soldered. (b) Probe set up with 10 kA vapor cooled leads and copper leads.

Fig. I.18 (a) After removing the top plate holding the pieces together the central spacer is carefully removed. The probe is sitting on the side where the surface of the U-bend section is in contact with the bottom plate. (b) Central spacer is removed. (c) Top spacer strips are removed using tweezers and small screwdriver. The bottom spacers are easily removed once the pressing plate is carefully moved from its position.

Fig. I.19 Positioning of the wedge, matching wedge pieces, extensometer and voltage tap wires in preparation of the experiment.

Fig. I.20 Working principles of the device: (a) resting position of the wedge, (b) vertical displacement of the wedge and movement outward of the matching pieces, (c) displacement measured using the extensometer.

Fig. I.21 Plates from heat treatment are use to hold the sample in position (top and bottom pictures) while the bottom plates are removed (center picture).

Fig. I.22 (a) Sample still supported by heat treatment side and top-bottom plates. Those pieces are going to be substituted with a single piece case. (b) Ready to remove side plates. (c-d) After removing the side plates the sample is hold in position momentarily by two side screws joining the sample holder and the U-bend piece. (e-f) The sample slides inside the case (remove the screws holding the sample holder and Y-bend hape). Once the sample is inserted completely into the case screws will be used to firmly position it. These screws will hold case and sample together during the experiment.

Fig. I.23 The sample is mounted inside the case and the last heat treatment support pieces are removed(top) before the sample is slid inside the grooves on the copper joints area (center and bottom pictures).

Fig. I.24 Soldering procedure. Cartridge heaters inside aluminum blocks are mounted on the sides and on the bottom of the copper joints area. Temperature controllers are used to monitor the temperature and start filling the grooves with solder.

Fig. I.25 Sample soldered. Instrumentation wires are connected to 4 wires Teflon cables that are brought outside the dewar (45 ft long).

List of Tables

Appendix II

Appendix III

Appendix IV

Appendix V

CHAPTER 1:
Introduction

Since its discovery in 1911, superconductivity has played an increasingly important role in different fields especially for magnet technology. The non-resistive characteristic of superconductor materials make them very attractive to achieve performances too demanding for conventional resistive materials. Despite superconductivity being a common characteristic of many metals, only a few of them are suitable for magnet applications requiring a balance between the difficulty and operability of the system itself and its overall cost.

There are four key magnet issues to be considered in the context of balancing cost and difficulty of assembly:

- Stability against mechanical, electromagnetic, thermal or nuclear disturbances,
- Cryogenics and efficiency of the coolant used,
- Protection of the conductor against events which would lead to a complete loss of superconductive properties (quench),
- Mechanical stability of the conductor and the supporting structure.

Although superconductivity was discovered nearly 100 years ago, practical application of this phenomenon requires a broad interdisciplinary knowledge of physics, material science and engineering (mechanical, electrical) to control the four aforementioned magnet issues.

The applications of superconductivity cover a broad spectrum of fields that includes medical, pure science (space and high energy physics), energy (power cables, magnetic storage and fusion) and transportation.

This chapter discusses the salient characteristics of superconducting materials and their applications. The chapter begins with a microscopic/macroscopic and phenomenological description of superconductivity followed by the description of the materials available (section 1.1) and the major applications of superconductivity (section 1.2). The chapter concludes with a more detailed description of fusion energy application and its challenges that provide the driving reason of the research carried out in this thesis work (section 1.3).

1.1 Background of superconductivity

A material is said to be superconductive if it shows no resistance against the passage of DC current. This property is usually obtained by sufficiently lowering the temperature below a critical temperature unique to the material. The discovery of superconductivity followed the successful liquefaction of helium in 1908 by H. Kamerlingh Onnes. In 1911 while measuring the resistivity of mercury, he discovered a state transistion at 4.2K to a resistance lower than 10-5 □ essentially discovering the superconducting state (Fig. 1.1(a)). Onnes was awarded the Nobel prize for his work in 1913. Many metals possess this property, but very few of them have all the characteristics suitable for magnet design as discussed in section 1.2.

It was not until much later (following advances in quantum physics and mechanics) that the complete microscopic theory of superconductivity was presented by Bardeen, Cooper, and Schrieffer (1957). Their theory, known as BCS theory, explained the flowing of current without resistance by introducing the key concept of Cooper pairs, pairs of electrons interacting through the exchange of phonons inside the crystal lattice.

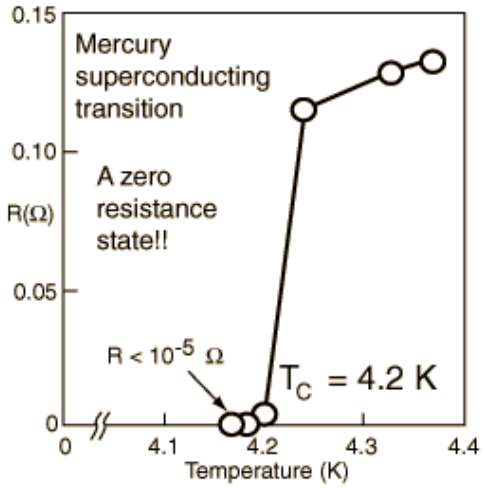

Fig. 1.1 (a) Mercury superconducting transition showed by the measured resistance as a function of temperature. For temperatures below 4.2 K mercury shows a virtually resistanceless behavior [1.1].

As discussed so far temperature is one of the requirements to obtain superconductivity. There are two other requirements in order to maintain superconductivity: magnetic field and current density.

Those three properties (current density, field and temperature) describe a surface under which the material does not show any resistance. It has also been found that axial and transverse strains affect the material performance (discussed in more details in Chapter 2). If all but one of these properties are kept fixed, once the variable property reaches its critical value the superconductive behavior will be lost. A schematic representation of the critical surface for a superconducting material is shown in Fig. 1.2 [1.2]. This plot represents the typical behavior of Nb_3Sn strands used for different applications (fusion, high energy physics (HEP) and nuclear magnetic resonance (NMR)). Each application has different requirements in term of field, temperature and current density as indicated by the colored areas in the plot.

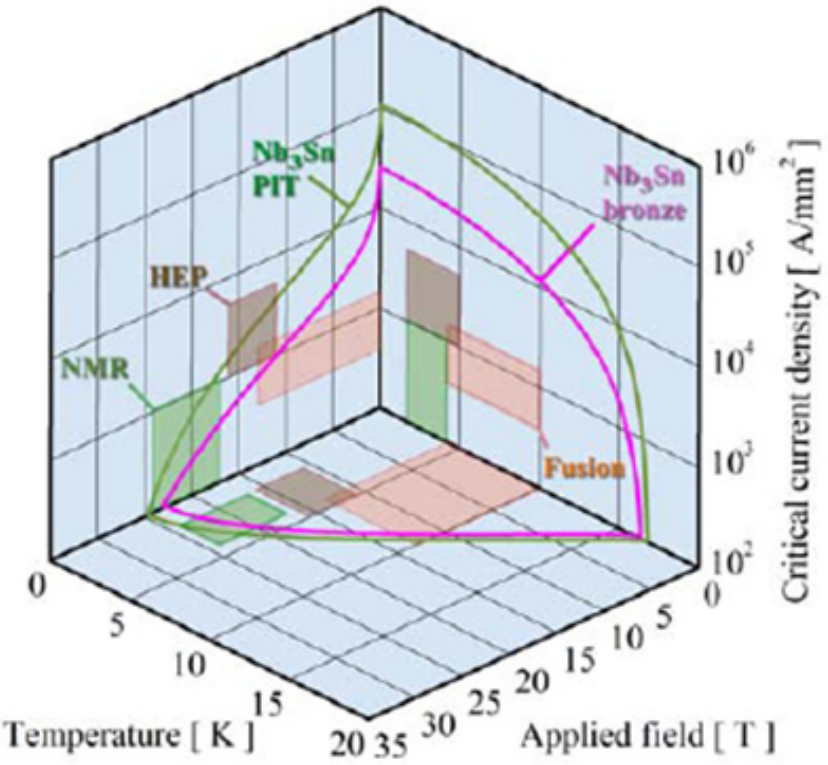

Fig. 1.2 Critical surface for Nb_3Sn strand. Current density, magnetic field and temperature define a surface above which the superconductive state is lost [1.2].

Superconductors are said to be of Type I or II depending on their magnetic characteristics. Type I superconductors show perfect diamagnetism behavior. When an external magnetic field is applied, a field equal and opposite is induced inside the superconductor) (Fig. 1.3 (a)). Type II superconductors show partial penetration when an external field is applied (Fig. 1.3 (b)). The behavior of a single superconducting strand to an external applied field is fundamental to determine its behavior inside a magnet where each strand is subjected to the field created by all the other strands.

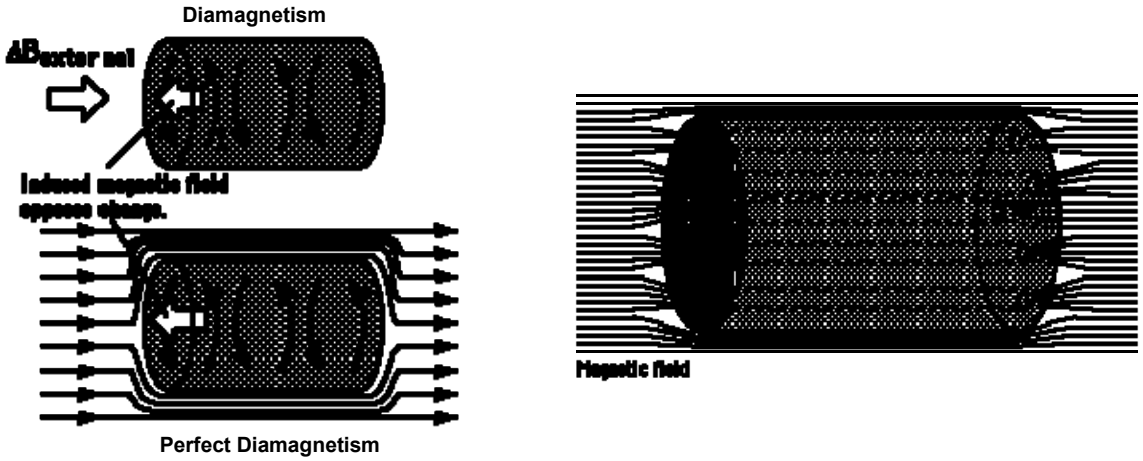

Fig. 1.3 Behavior of superconductors to external magnetic field. (a) Type I, (b) Type II [1.3].

Type I superconductors have a single critical field (B_{c1}) above which the material loses its superconductive property. They show both perfect diamagnetism and no resistance in both AC and DC conditions below the critical field. Type II superconductors are bound by both a lower and upper critical fields (B_{c1}, B_{c2}) (Fig. 1.4). Above B_{c2} the material becomes normal, below B_{c1} it shows perfect diamagnetism as for Type I while in between the two limits the material is said to be in the mixed state, allowing partial flux penetration.

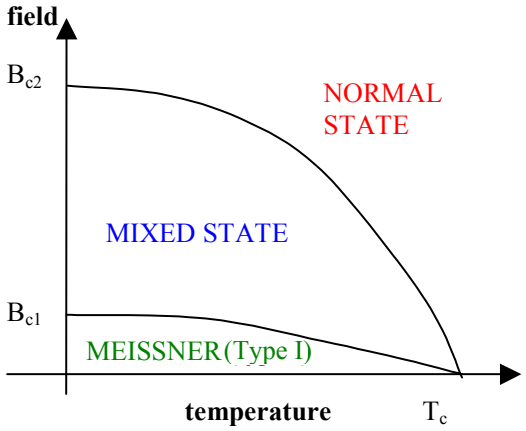

Fig. 1.4 Critical field as a function of temperature for Type I and II superconductors [1.4-1.5].

The mixed state of a Type II superconductor can be pictured as a bulk of superconducting material with normal cores (Fig. 1.5).

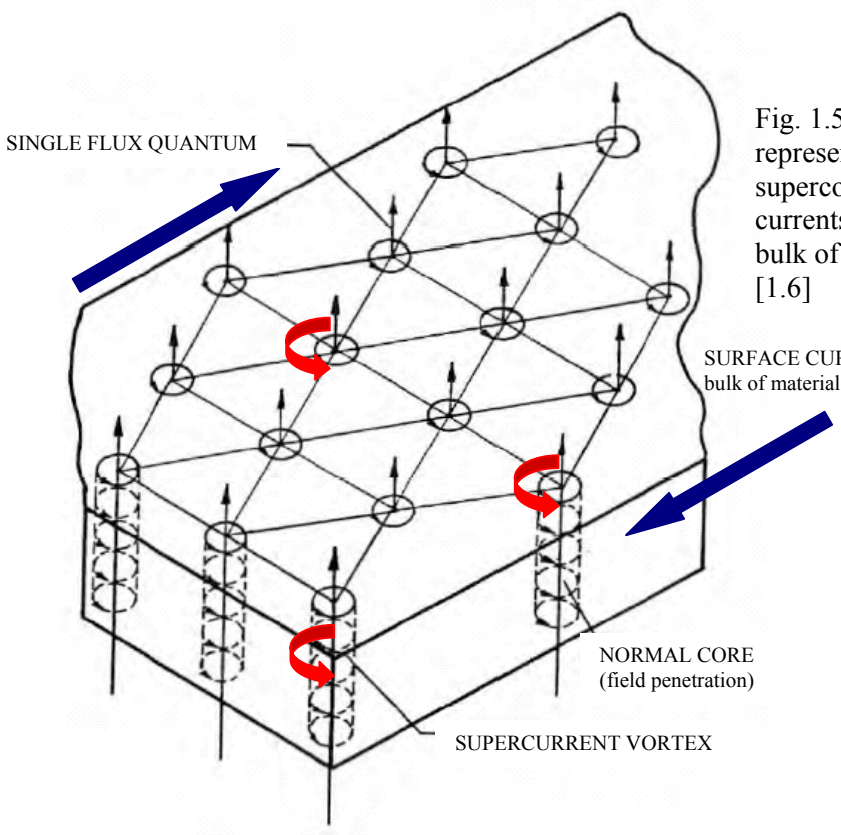

Fig. 1.5 Normal cores representation in a Type II superconductors slab. Surface currents flow to maintain the bulk of the slab diamagnetic. [1.6]

The normal cores in the mixed state represent the areas of the material where the field can penetrate. The amount of field that can penetrate is quantized and one core contains one flux quantum Φ_0 (Fig. 1.6).

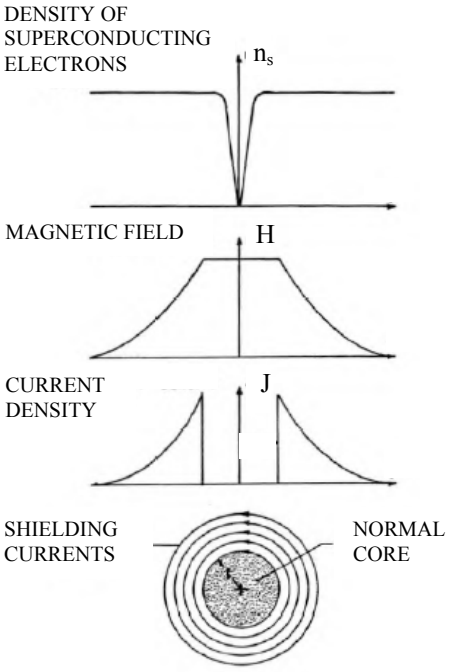

Fig. 1.6 Properties of normal cores in a Type II superconductor [1.4].

When a Type II superconductor is exposed to a magnetic field lower than B_{c1}, currents will flow on the surface opposing any external field to penetrate the material (perfect diamagnetism). When the external field exceeds B_{c1}, surface currents will still flow but normal cores will also form in the material. These normal cores tend to form at the surface and diffuse into the material. The local islands of resistive regions allow magnetic flux lines to penetrate through the mixture without destroying the overall superconductive state.

If a transport current (J_t) were applied to an ideal Type II superconductor in the presence of an external magnetic field, the resulting Lorentz force (f_L) would cause the magnetic flux lines to move and redistribute across the material:

$$f_L = J_t \times \Phi_0 \tag{1.1}$$

The movement of the flux lines induces an electric field E:

$$E = v_L \times B = v_L \times n\Phi_0 \tag{1.2}$$

where v_L is the velocity of the normal cores, , and n is the number of cores. The presence of this electric field requires a voltage to sustain the transport current. The movement of these normal zones could produce irreversible instabilities that would jeopardize the superconducting behavior of the material. This problem is obviated by carefully adjusting the heat treatment used to create grain boundary and structural defects that pin the

vortices in set positions allowing for a net transport of current through the material (Fig. 1.7). When a current is applied to the superconductor in this mixed state, the current will flow without resistance in a path around the normal cores (now pinned). As the external field increases the number of normal cores increase until it occupies the entire material at B_{c2} and the material becomes normally conducting.

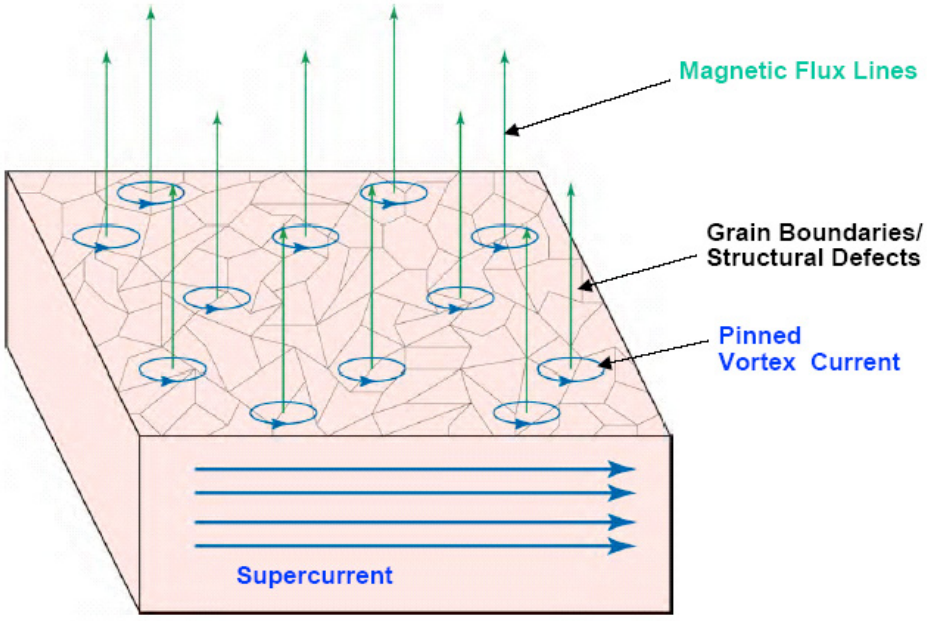

Fig. 1.7 Normal cores and pinning centers in a Type II superconductors [1.5].

The critical state is defined by the force balance between the average pinning force density (f_p) and the Lorentz force on the flux vortices:

$$J_c \Phi_0 = f_p \tag{1.3}$$

J_c is called critical current density of the superconductor. If the transport current exceeds the critical current, flux flow and dissipation occur. This quickly causes a breakdown in the superconductive state and marks the critical state level [1.7-1.8].

Most of Type I superconductors are pure metals and usually have very low critical field which make them impractical for magnet technology application. Type II superconductors are usually alloys or intermetallic compounds and have much higher critical fields (B_{c2}) that make them very attractive for magnet technology application (Table 1.1).

The critical field and temperature values are intrinsic properties of the material. On the contrary, metallurgical processing can improve the critical current density.

There are two groups of superconductors:

1. Low temperature superconductors (LTS) usually alloy or metallic compound (T_c<30 K)
2. High temperature superconductors (HTS) usually oxide compounds (T_c>30 K).

Table 1.1 Critical temperatures and fields for Type I and II superconductors [1.5].

Superconductors (Type I)		
Material	**T_c (K)**	**$\mu_0 H_{c0}$ (T)** *
Ti (metal)	0.40	0.0056
Zn	0.85	0.0054
Al	1.18	0.0105
In	3.41	0.0281
Sn	3.72	0.0305
Hg	4.15	0.0411
V	5.40	0.1403
Pb	7.19	0.0803
Superconductors (Type II)		
Material	**T_c (K)**	**$\mu_0 H_{c0}$ (T)**
Nb (metal)	9.5	0.2*
Nb-Ti (alloy)	9.8	10.5+
NbN (metalloid)	16.8	15.3+
Nb_3Sn (intermetallic compound: A15)	18.3	24.5+
Nb_3Al	18.7	31.0+
Nb_3Ge	23.2	35.0+
MgB_2 (compound)	39	~15*
$YBa_2Cu_{3-x}O_x$ (oxide: Perovskite) <YBCO>	93	150*
$Bi_2Sr_2Ca_{x-1}Cu_xO_{2x+4}$ <BSCCO2223 or 2212>	110	180*

* extrapolation at 0 K + extrapolation at 4.2 K

Several remarks can be made regarding the different materials and their applications:

- HTS conductors have much higher critical field and temperature but their application has been limited due to their recent discovery, the lower critical current density at high fields and their high cost.
- For stability and protection purposes LTS strands contain copper while BSCCO (HTS) uses silver. This makes BSCCO strands much more expensive.
- YBCO and BSCCO-2223 are available only in tape geometry
- BSCCO-2212 is competitive with other materials only at 4.2 K, limiting its high temperature applicapability (Fig. 1.8-9).
- Magnet grade conductors are presently limited to three materials: NbTi, Nb_3Sn and BSCCO-2223
- NbTi magnet technology is well established but the limited performance at high fields is driving attention to other materials
- LTS conductors are used by the High Energy Physics, Fusion Energy and NMR/MRI communities
- HTS conductors have intially found appllication in electric utility systems.

In Fig. 1.8 critical magnetic fields as a function of temperature are reported for different superconducting materials. Fig. 1.9 shows the critical current density as a function of magnetic field at fixed temperature for materials suitable for magnets.

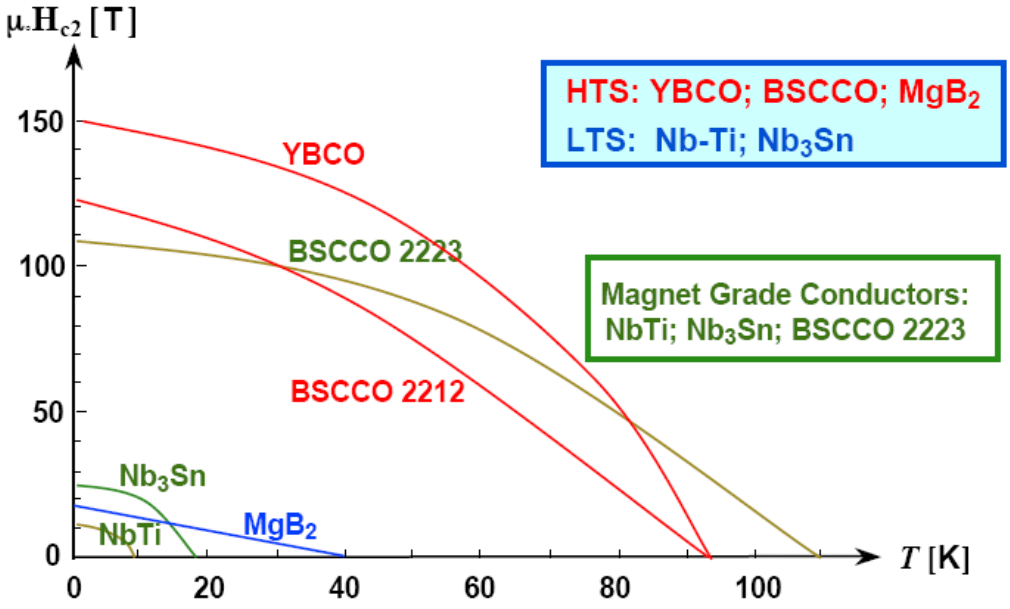

Fig. 1.8 Critical field as a function of temperature for selected LTS and HTS superconductors, the critical field at 0 K is an extrapolation from values at 4.2 K [1.5].

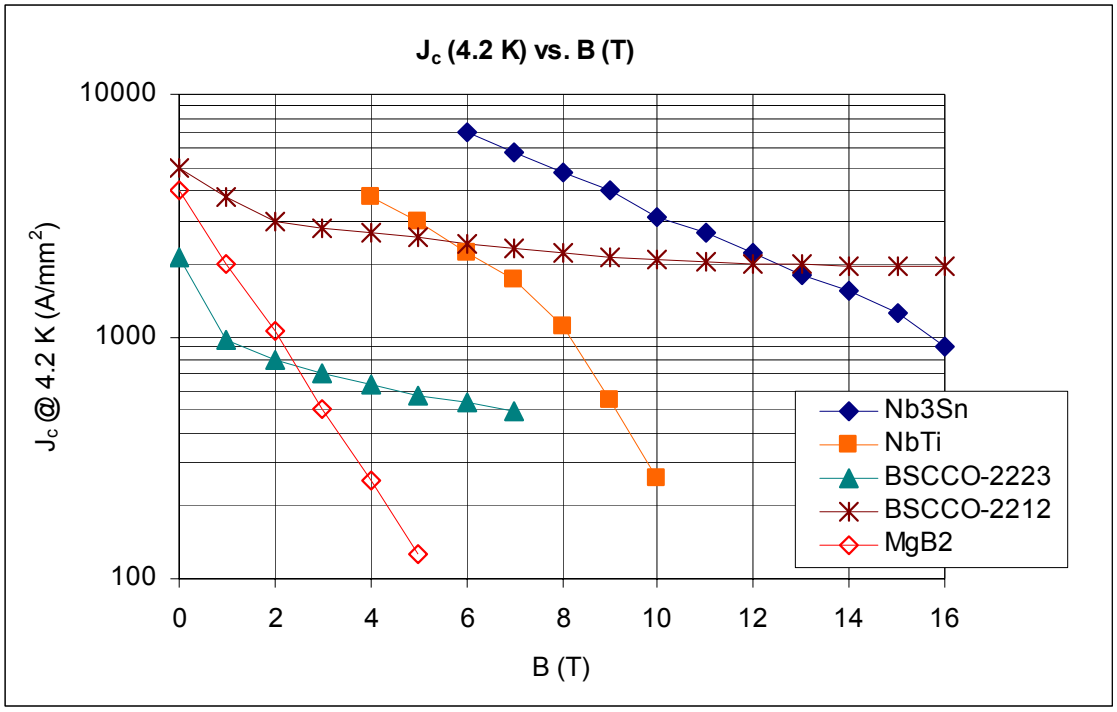

Fig. 1.9 Critical current density at 4.2 K for different superconducting material candidates for magnet design [1.9].

From Fig. 1.9 it can be seen that at 4.2 K there is no clear advantage in using HTS superconductors unless the application is for high current and high field, in which case BSCCO-2212 is the most favorable. At higher temperatures (< 77 K) HTS materials are the only ones suitable for superconducting application but at those temperature their current carrying capacity is greatly reduced from the 4.2 K values so that the overall cost-performance favors LTS materials at this time.

Wires used for superconducting applications, and in particular for magnet technology, must be capable of carrying large transport current and operate in high magnetic fields. The wires must also be produced cost effectively and in lengths appropriate for ease of magnet manufacture. Despite the promising progress of HTS materials, LTS remain the only materials that can be used for large systems and magnets. NbTi and Nb_3Sn are the most used materials. Different applications might opt for one or the other depending on the requirements of the system. NbTi is more popular and predictable for peak fields under 9 T, while Nb_3Sn is used for higher fields although there are still several challenges to be overcome.

In this thesis work the superconducting material studied was the same as the one selected for the production of the Central Solenoid US Inner Module for the ITER project.

In a typical large scale application such as this, several strands are bundled into a cable to obtain the required transport current. Typical strands have a diameter of about 1 mm and are composed of thousands of superconducting filaments, each with a diameter in the μm range. Strands are made of filaments to prevent a phenomenon known as flux jumping. Flux jumping occurs when the Lorentz forces acting on a flux bundle exceeds

the pinning force in a non-static fashion causing a cascade of events that increase the local heat deposited inside a region of the superconductor. Once this happens the flux vortices are not constrained and will start moving causing local heating that will decrease the current density and eventually could cause a quenching event.

For some large scale applications, a magnet can store megaJoules of energy so that if the magnet quenches and becomes resistive this enormous energy begins to be dissipated in the very small zone that initially turned normal. Superconducting strands are perfect conductors when they are in their superconducting state but they become very highly resistive once they lose their superonducting state. For this reason the strands are embedded in a low-resistance matrix (usually copper) to create a parallel path for the current to flow once a normal region develops. Copper also has a larger thermal and electrical conductivity than the superconducting filaments, once they lose their supersonduting state, which helps to transfer heat away faster and avoid damage in case of a quench event.

Fig. 1.10 shows a typical cross section of an Nb_3Sn wire made by IGC that was used for the US Inner Module of the ITER CSMC magnet in the 1990's. The cable is composed of 6 petals and each petal is cabled in different stages. The sub-cables of each stage are twisted together at a specific twist pitch length to minimize losses caused by a varying magnetic field (AC losses).

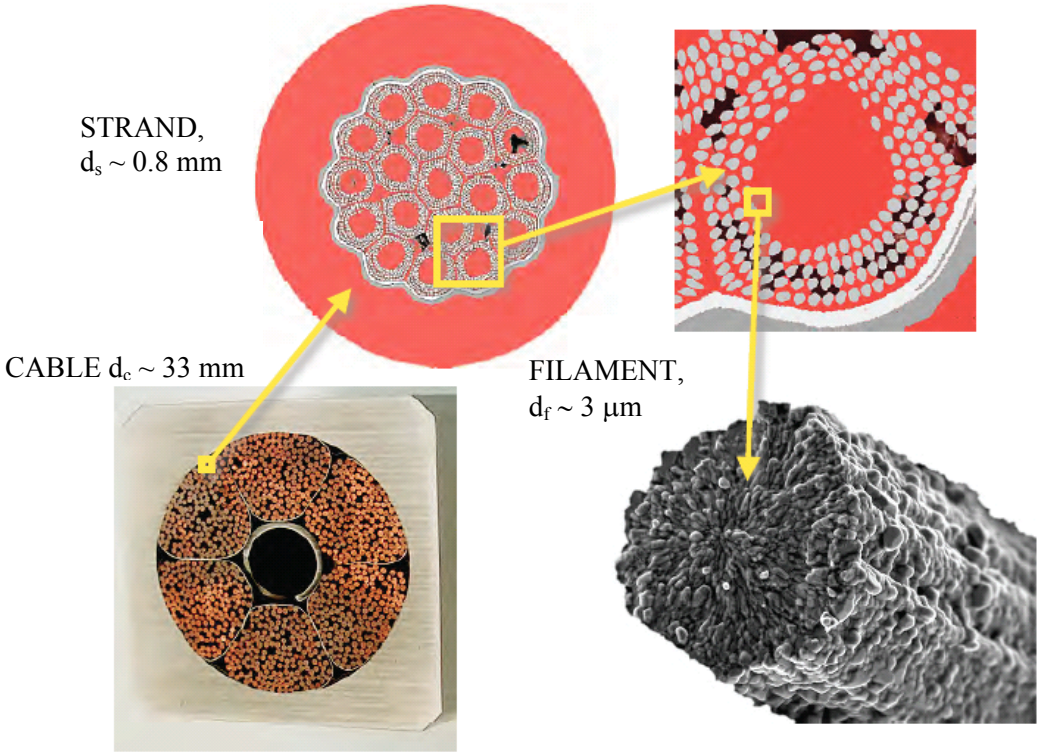

Fig. 1.10 Cross-section of the cable used for ITER CSMC US Inner Module. Starting from bottom left and proceeding clockwise: six petals CICC design with central cooling channel, IGC Nb3Sn strand used in the cable, superconducting filament bundle, and a single superconducting filament [1.5]. The filaments inside a strand are twisted to avoid flux jumping and strands are twisted using different stages to avoid AC losses.

1.2 Applications of superconductivity

Superconducting materials have their largest application in electromagnets. In fact they can achieve higher fields with less power consumption than normal conducting magnets. Though cryogenic systems are required, the overall cost for superconducting magnets is lower for many high field or large volume applications.

There are six major fields where superconductivity can be applied (Fig. 1.11):

1. Magnetic Confinement Fusion Energy

Fusion energy is a promising source of clean and abundant energy for the future. A plasma, made out of light elements (hydrogen, deuterium, tritium), is used to activate a nuclear reaction that releases high energy products that either maintain the chain reaction or are captured so that their energy can be extracted as heat and used to produce energy. The leading scheme to confine the plasma is by using a magnetic container. The typical magnetic confinement configuration is the tokamak and requires the use of very powerful electromagnets. The ITER machine is the most immediate step towards the goal of demonstrating the feasibility of fusion energy. All the magnets in this tokamak are made of superconducting materials (NbTi and Nb_3Sn). This thesis concerns one of the issues related to the superconducting cables of the machine and more details will be given in the following sections regarding the machine and the engineering challenges.

2. High Energy Physics

High field requirements turned the attention of high energy physicists to superconducting magnets. In a particle accelerator, magnets are used to accelerate, focus and analyze beams of energetic particles. The project Large Hadron Collider (LHC) in Geneva has become operational in 2008 and contains over 1500 superconducting magnets to reach the designed collision energy of 14 TeV. The Tevatron in Fermilab was, unitl the start of the LHC, the world largest accelerator so far with a collision energy of "just" 1 TeV.

3. Magnetic Resonance Imaging (MRI)

Imaging techniques using magnetic resonance greatly improved the capabilities in diagnosing and treating medical problems. Superconducing magnets are widely used since they produce a very stable DC field over a large volume with minimal power consumption compared to conventional magnets. Moreover the magnetic fields required for MRI are well within the safe margin of operation for NbTi superconductors and avoid any quenching events while providing for high magnetic field accuracy.

4. Superconducting Power Transmission Cables and Superconducting Magnetic Energy Storage (SMES)

Since the energy in superconducting magnets can be virtually stored indefinitely, they are considered good energy storage devices. SMES are now commercially available and

compatible with standard storage device for some limited applications. With the increasing power production coming from non-continuous sources (like solar, wind, waves) the presence of storage systems will be fundamental for the best integration of renewable sources in the present grid. Magnetic storage has advantages compared to other storage systems in that it does not have moving mechanical parts and can discharge energy very quickly at a very high power rate.

Additionally to improve the power-handling capabilities of existing underground circuits even further, HTS power could substitute for the standard high-voltage cables reducing greatly the foot print of the cables. A typical copper cable carries a current density of 10 A/mm2 compared with 600-1200 A/mm2 for a HTS cable. A pilot project using a 3-phase HTS cable has been successfully implemented into the existing Long Island (NY) power grid system.

Highly efficient HTS transformers would also decrease the environmental contamination caused by spills from oil-filled high voltage transformers as well as eliminate the fire hazard.

5. Magnetic Levitation

The use of superconducting magnets allows levitating trains on tracks in transportation applications. In this application the diamagnetic characteristic of the superconducting materials is used. The main advantage of magnetic levitation is that these trains will not have the standard mechanical moving parts, which reduces part wear and maintenance. This coupled with a linear synchronous motor drive system allows achievement of very high travel speeds.

6. Basic Research

Superconductivity still offers a wide spectrum of basic research applications. Among them, the most prominent is the understanding of materials at very high magnetic fields, especially for NMR application. The basic phenomenon of the interaction of phonon and electrons and their responses to different stimulation is of interest.

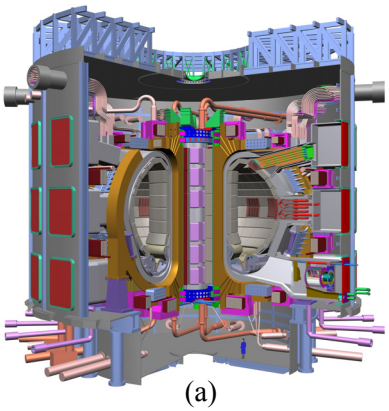

(a)

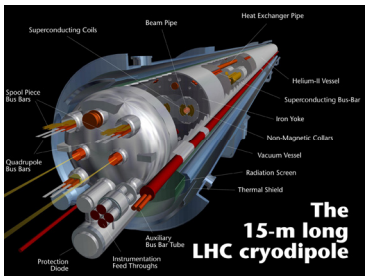

(b)

(c)

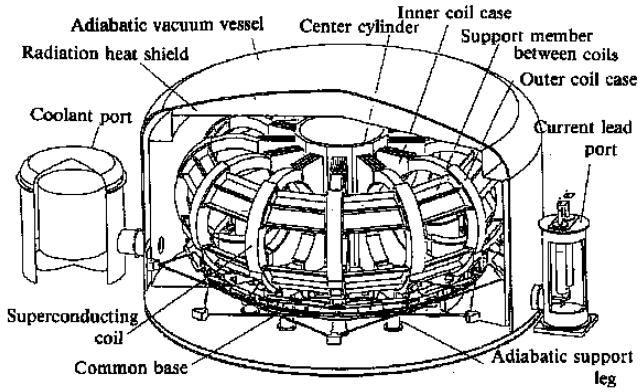

(d)

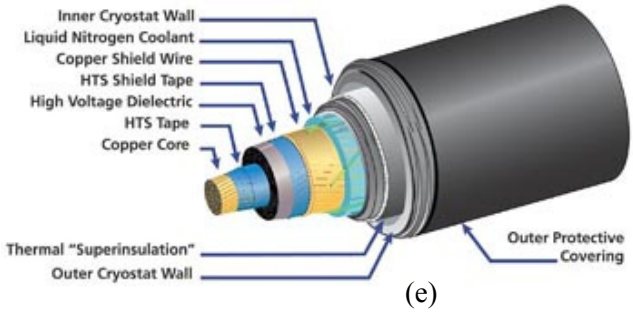

(e)

(f)

Fig. 1.11 Superconducting magnets applications: (a) fusion energy, (b) high energy physics, (c) MRI, (d) SMES, (e) power cable, (f) levitating train. [1.10].

1.3 Fusion energy, ITER magnet system and Cable-in-Conduit Conductor

The focus of this thesis work is primarily related to superconductors for fusion energy so in this section more details regarding this desirable source of energy are described together with its limitations. The principle of a fusion power plant relies on the heat captured from secondary products (typically neutrons) of a nuclear reaction. This heat is run through a heat exchanger, producing steam to drive a turbine and generate electricity. The challenging aspect of these machines is that plasma has to be created and confined at high density for enough time to be able to fuse and produce nuclear power. The leading scheme to confine the plasma uses a magnetic system that produces a large magnetic field that traps the particle in predetermined orbits.

High magnetic fields can be produced more efficiently using superconducting magnets positioned in a cryogenic system located very close to the hot plasma.

ITER is a current driven plasma experiment that could set a milestone towards the demonstration of fusion as a source of energy for the future. Fig. 1.12 shows a cutaway of the machine and a cross section of the magnet systems.

As mentioned earlier, the magnets of this machine will all be built with superconducting material since the field requirements cannot be met by resistive magnets, without using an enormous amount of power to sustain the currents. On the other hand, superconducting magnets require electric power for the cryogenic system but this is very small compared with the electric power required to drive a resistive magnet system.

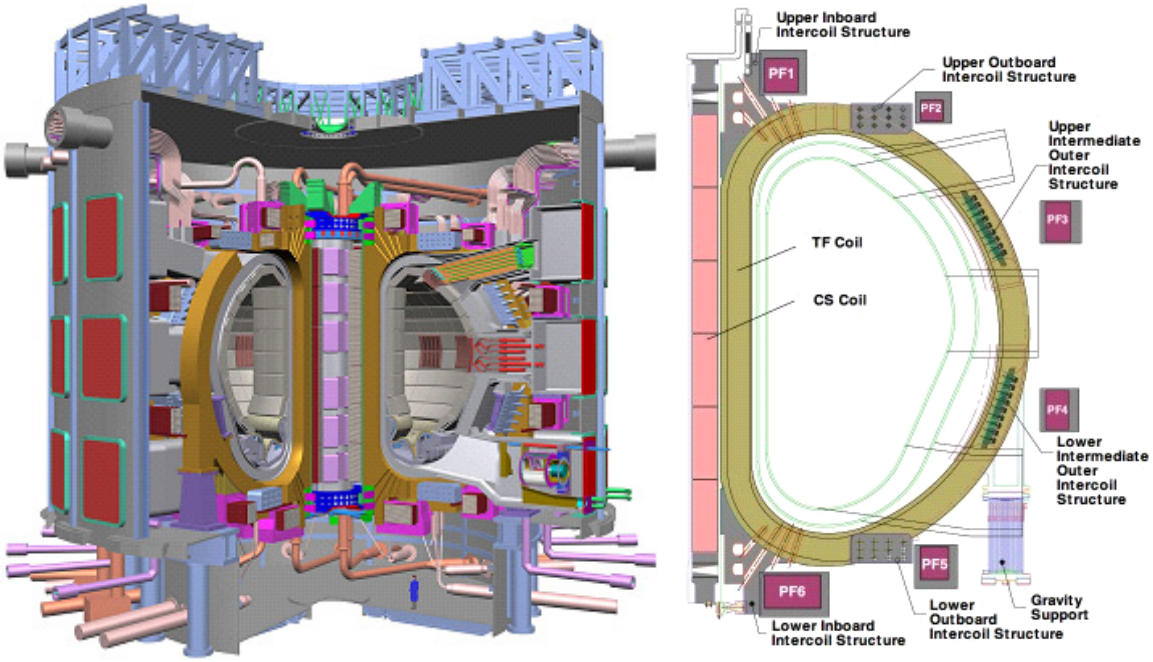

Fig. 1.12 Cut-away of ITER (left) and the magnets system of the machine (right) [1.11].

The magnet systems are composed of 18 toroidal field coils (TF), a central solenoid (CS), 6 poloidal field coils (PF) and 18 correction coils (CC). TF and CS coils are made of Nb_3Sn conductor while PF and CC coils are made of NbTi [1.11]. The central solenoid plays a key role to reach the plasma current of 15 MA of the machine. The plasma current is inductively driven by the CS coil. The CS coil is composed of 6 modules which are

independently powered. After initially charging the CS coil, a fast discharge follows and the rate of change of flux induces a voltage inside the plasma and drives the plasma current (Eq. 1.4).

$$V = -\frac{d\Phi}{dt} \tag{1.4}$$

The central solenoid is composed of 6 modules and each module is made of pancake windings. The conductor is an advanced Cable-in-Conduit (CIC) Nb_3Sn superconductor. The four components of the Cable-in-Conduit are the cable itself, the central cooling tube, the foil wraps around the cable and final stages, and the structural jacket. The CS conductors are five stages of 3x3x4x4x6 cables, where the final stage twists 6 'petals' around a central channel (Fig. 1.13 (a-b)).

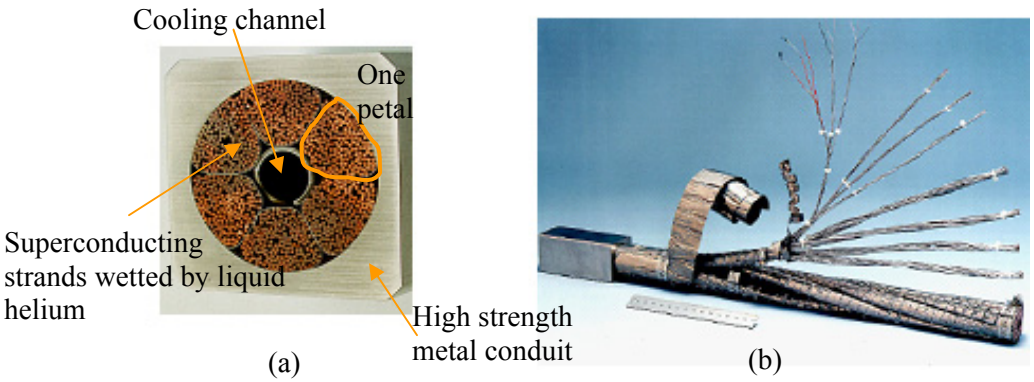

Fig. 1.13 (a) Cross section of a cable in conduit conductor and (b) different stages of the cable wrapping around a central channel [1.5].

The magnets using this type of conductor are characterized by the presence of local cooling by supercritical helium in direct contact with the conductor (helium stabilized magnets). This cable design is usually considered for large or high field magnets. In particular for magnets with large body force (RxJxB) an external jacket is used to sustain the large operational forces.

In the CICC configuration (Fig. 1.13), cabled strands of superconductor are enclosed in a conduit, which provides the mechanical strength and through which single-phase cryogen is forced to provide the necessary cooling.

The cable design incorporates the key requirements of a superconductor. The cable is composed of many strands and can carry large amounts of current. The copper content is enough to ensure transient stability and quench protection while the twisting in different stages reduces AC losses with the conduit providing the mechanical integrity.

To maintain a reasonable overall current density, the operation current has to be high since a major fraction of the cable does not carry current (the void, conduit and liquid helium channel). Additionally the conduit causes additional strain upon the cable during cooldown because of differences in thermal coefficient of expansion. This strain has to be taken in consideration during the design of the desired magnet. The CICC design is currently the standard cable design for very large magnets but it has inherent mechanical

weaknesses since each single strand is not completely supported and can experience large loads during operation that can degrade its performance.

The predictability of the performance of a Nb_3Sn cable becomes then crucial to determine the appropriate design values to reach the desired magnetic field. Any unpredicted degradation could reduce the plasma current and time of plasma burn.

1.4 Scope of the thesis work

The work in this thesis focuses on the effect of transverse forces on Cable-in-Conduit conductors for magnets used in ITER. Superconducting magnets used for fusion machine are cryostable against limited transient disturbances. The conductor used is either NbTi or Nb_3Sn in the form of CICC with a central channel for cooling purposes. During operation the Central Solenoid magnet will be energized with current and field of up to 45 kA and 12.6 T, respectively, for the high current scenario; and 40 kA and 13 T for the high field scenario. A rough estimate of the transverse load created by the Lorentz force, which accumulates through the cable cross section, is given by (Eq. 1.5):

$$\tau_{trnsv,\max}(MPa) = \frac{I(kA)\cdot B(T)}{d(mm)} \tag{1.5}$$

where I is the transport current in kA, B the magnetic field in Tesla and d the cable diameter (32.6 mm) as shown in Fig. 1.14. By substituting the design values, we obtain a maximum average transverse pressure of 17.4 MPa.

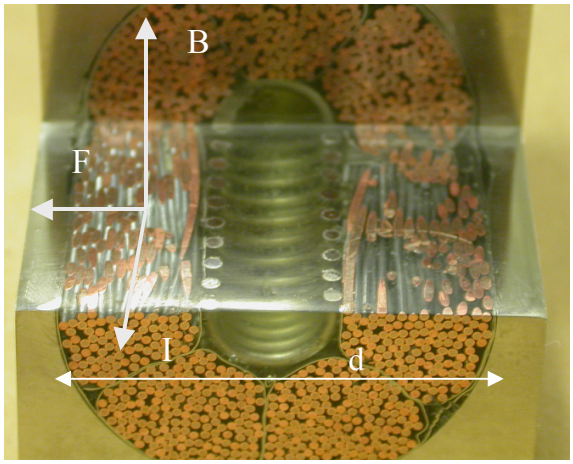

Fig. 1.14 Lorentz force due to electromagnetic interaction of current and field in a CICC cable [1.5].

When force accumulates on one side of the cable (vector F in Fig. 1.14), the strands are pushed towards the jacket surface and experience the highest accumlated pressure at this location. This pressure can be much higher (~100-150 MPa) than the averaged one so it becomes important to understand the effect of such a force on a more fundamental level. Additionally multiple effects are in play during operation including axial and

transverse strains, thermal strain, and bending and pinching inherent in the cable layout. It is rather difficult to separate theses effect from experimental measurements of full size cables. At the same time it can be limiting to study a single effect since they are closely related to each other.

Testing the effect of the electromagnetic transverse force on the real full size cable used for the magnets would be excessively expensive and difficult due to the size of the cable and the current requirements. Few full size scale experiments can be found in literature [1.9] and the general approach is to study the effect of different mechanical effects on single strand [1.10-12]. A more detailed literature review is given in Chapter 2.

A unique feature of our experimental setup is that we used subsized cables composed of different numbers of strands to try to extrapolate their behavior to a full size cable. To reproduce the same Lorentz load seen by a full size cable, currents exceeding the capability of most common power supplies available would be needed for the test. In this thesis work the load has been produced mechanically.

We used two different test rigs that are described in detail in the following chapters and we tested several different samples (36-strand cables, single strand, a triplet and 45-strand cable). The first rig uses a single turn sample (Fig. 1.15). The second rig was designed as improvement to the first one and uses hairpin samples (Fig. 1.16). Our tests were performed at the National High Magnetic Field Laboratory (NHMFL) in Tallahassee, FL using probes with 10 kA current leads and a Bitter solenoid of 20 T peak field (first test rig), and a split pair superconducting magnet of 14 T peak field (second test rig). Since the natural Lorentz force created during operation is not electromagnetically reproducible in the experimental set up (smaller number of strands), we designed the probes so that an artificial mechanical transverse stress could be applied.

The scope of this work is to apply a known transverse pressure on the cable and record any visible degradation of its superconducting properties and in particular degradation of the expected critical current.

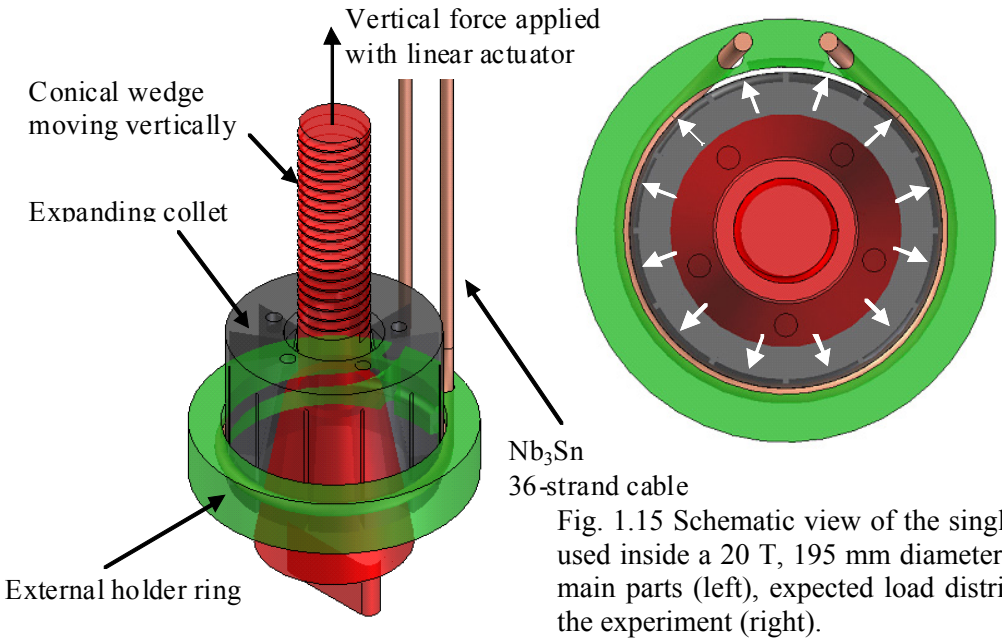

Fig. 1.15 Schematic view of the single turn test rig used inside a 20 T, 195 mm diameter bore magnet: main parts (left), expected load distribution during the experiment (right).

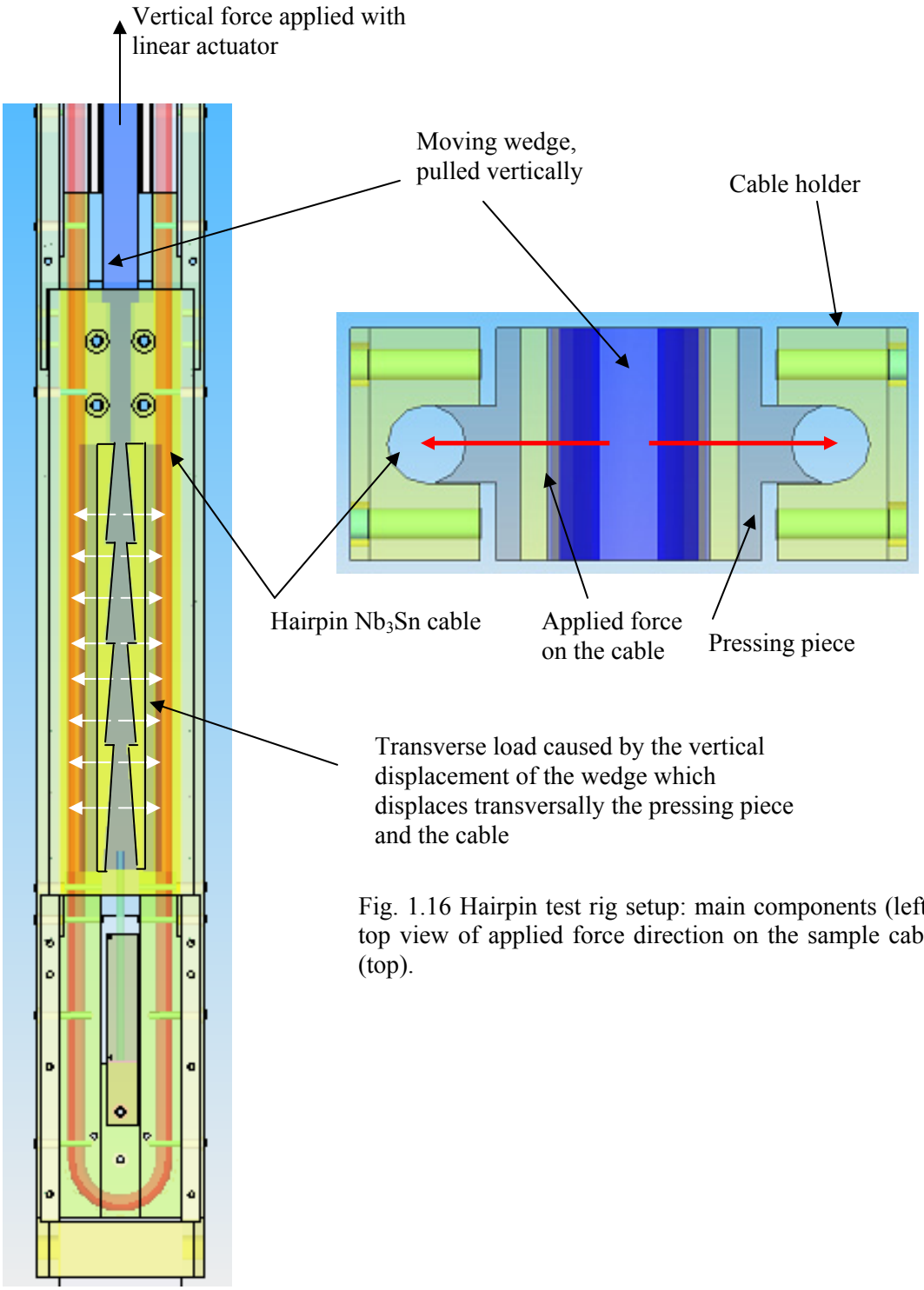

Fig. 1.16 Hairpin test rig setup: main components (left), top view of applied force direction on the sample cable (top).

CHAPTER 2:
Strain characteristics of superconducting wires and cables

As previously stated, superconductivity depends on three main parameters that describe a critical surface underneath which the material is superconducting. Later discoveries showed that superconductors are also sensitive to mechanical strains.

In a large magnet using cable in conduit conductors, there are several natural sources of strain inherent to the design and operation of magnets and it is important to know those sources of strains and quantify them as precise as possible to be able to predict the performance of a cable. Generally a single strand, carrying a certain amount of current as provided by its manufacturer, will always carry less current inside a magnet so engineering safety factors need to be applied in the design phase to take those effects in consideration. The three main strain components are: axial, transverse and bending.

The source of axial strain is the thermal mismatch between the superconducting wire and the conduit materials due to the temperature change from the heat treatment temperature to the liquid helium operation temperatures. The transverse strain is caused by the natural electromagnetic force accumulation across the cable. The bending strain is caused by the cable design and how the strands are twisted together in a configuration with a void fraction higher than 30% (the void fraction being the empty area of the cable cross section Fig. 1.10).

Quantifying those strains is extremely difficult because in a large size cable it is impossible to measure each quantity individually since all of them are acting simultaneously during operation.

Much work has been done on the subject of strain effects on superconducting strands beginning about two decades ago. The attention was mainly focused on uniaxial strain effect on the critical current of single strands (Nb_3Sn and HTS). This was followed by experimental studies of the transverse and bending strain effects on a single strand. Being an extremely complicated system, less attention has been paid in understanding the axial and transverse strain effects on a cable. In particular, the transverse strain effect is dominant for a large conductor of fusion type of magnets using CICC with a void fraction in the range ~32-37%. This is less of an issue for other types of magnets such as for high energy physics applications, because these magnets use compacted, flat, Rutherford cables and they are usually epoxy-impregnated and thus completely supported [2.1].

Ideally, one would want to have scaling laws describing the strain effects to predict the performance of a strand under certain strain condition. Unfortunately the extrapolation from a single strand to a full size cable is not straight forward and up to now only the dependence of the strand critical current as a function of uniaxial strain can be described with empirical scaling laws.

Generally a single strand is characterized by its critical current value at a certain field and temperature (generally 12T and 4.2K). This information is obtained by measuring a sample mounted and heat treated on a titanium alloy barrel. This value can be used to estimate the critical current dependence on axial strain but generally several parameters are needed to describe this dependence so that it is standard practice to perform tests to verify the predicted uniaxial dependence of the critical current. Generally the tests are done applying axial strain values between -1% and 0.5% with experimental devices described in this chapter. It is necessary to have data in this range because the initial

strain condition of a strand in cable depends on the heat treatment used for the particular cable and the conduit materials used (-0.7% for stainless steel and -0.35% for Incoloy alloy). Moreover during operation a natural hoop strain develops inside the cable and this condition generally helps improving the performance of a cable (Fig. 2.1).

The uniaxial strain dependence is the best described by empirical laws and the initial strain condition of a cable can be predicted with a small error giving confidence in being able to determine the necessary engineering factor to apply in the design of a magnet.

The bending and transverse strain effects have been receiving attention in the last few years following the poor performance of magnets that could not be explained by uniaxial strain. Quantifying the effect of those two strain sources is very challenging because the tests available are limited and the two strain sources are connected since they both depends on the cabling pattern and cable design.

Empirical laws describing those two effects do not exist so far, and more work is being put in understanding better those effects so that is possible to include their dependence on the overall performance of a cable in conduit conductor.

More work has been done on bending strain effect than transverse strain effect. This thesis work was focused on the latter one and its unique design allowed the test of single strands as well as sub-sized cables. Single strand experiments on this subject are few and experimental works on sub-sized cables are even fewer and this was the driving motivation to develop experimental devices for those measurements in this thesis work.

This chapter summarizes work done by other researchers to study these strain effects. Section 1 gives a brief introduction regarding the strain effects on superconducting strands and cables and how they are currently described by empirical scaling laws. A summary of different experiments performed by others is described starting with uniaxial strain effect on a single strand, then pinching and bending loads on single strands, tests of sub-size cables under axial strain, transverse load effects on single strand and finally tests on sub-sized cables under transverse load. This background summary is given to explain the importance of the experiments carried out with this work, since very little has been done until now on sub-cable samples. The experimental procedures used for the work of this thesis provide a unique approach and is an important addition to the work done so far by many different groups around the world.

2.1 Introduction

In this chapter a brief history of experiments dealing with the axial and transverse effects on superconductors performances is reported. Besides the dependence on current density, field and temperature, the performance of a superconducting strand or cable is affected by axial and transverse strain. The latter has a more accentuated effect and the degradation due to transverse strain is up to one order of magnitude greater than the degradation due to axial strain at the same level of strain [2.3].

The sensitivity of a Nb_3Sn superconductor to transverse loading is dependent on a large number of factors, including the copper/non-copper ratio (quantity that defines the amount of copper over the total amount of material in a strand), the ratio of distance between contact points to the strand diameter, void fraction constraints on strand deflection, pre-compression strain, heat treatment, and the exact material composition of the non-copper region. The larger degradation, for a single strand, caused by transverse

load (a factor of 10 larger than the longitudinal case) is believed to be due to the multiplier of deviatoric strain in a composite, in which the transverse compression on a composite with a stiff, unyielding component and a soft, yielding component is translated into a longitudinal tensile strain in the stiffer element. In the case of a multifilamentary superconducting strand the soft component is copper and the stiff component is the non-copper materials comprised of Nb_3Sn filaments, a diffusion barrier (usually tantalum) and a bronze matrix. The copper is the low resistance stabilizer where the current flows during a transition to the normal state. The diffusion barrier is needed to separate high purity copper during reaction heat treatment from the rest of the composite, which contains bronze, Nb and Sn. The resistance between filaments and their twist pitch (filaments are twisted together with a particular pitch to avoid flux jumping) also play a role in the way the critical current is effected by strain.

In a cable the degradation due to transverse loads is even more accentuated (~100 times larger than the longitudinal case) [2.2]. A possible explanation for this behavior is the presence of an additional bending effect on each strand inside a cable due to the twisting of the strands around each other [2.2-2.4]. A cable is typically composed of several hundreds of strands bundled together in stages. Each stage is cabled with a particular twist pitch length to minimize AC losses and strain effects on the total transport current.

A cable-in-conduit conductor (CICC) is an extremely complicated system because several components of strain come into play during each process of production and operation. Axial strain is caused by thermal strain and the natural hoop strain during operation. Transverse and bending strains are caused by the naturally occurring Lorentz load and the geometry of the cable design. An additional key factor is the cable void fraction which allows movement of individual and groups of wires in a cable during operation. Each of these strain sources needs to be accounted for, and being related to one another, the modeling of the cable system becomes a multivariable problem that is not easy to define without making assumptions. Very little mechanical modeling has been done previously on a full size cable [2.4-2.7] while an experimental approach generally has been chosen for single strand tests and sub-sized cable tests. Tests of full size cables have been done but are generally extremely expensive and time consuming so that the database of results is very limited. The uniqueness of the experimental device described in this thesis resides in the fact no other similar experiment currently exists.

Previous experiments performed by other researchers are briefly described in the following sections highlighting results and limitations.

2.2 Uni-axial strain

Much work has been done in the field of uni-axial strain effect on single strand. The large amount of test results over the years allowed extending the critical surface parameterization of Nb_3Sn, described by temperature, field and critical current, to axial strain as well. Parameterization of the critical surface is empirically described by fitting parameters that include axial strain effects and describe well a single strand behavior.

Some work was also done in studying the strain effect at the atomistic level where the electron-phonon interaction and its response to strain is the key element used to understand the behavior of superconductors [2.8-2.9].

Ekin was the pioneer of the strain dependence of superconductors [2.10]. He developed a formal relationship for strain scaling based on experimental results using an apparatus which applied simultaneously tensile strain, current and a perpendicular field to a short length of wire. The dependences on field, strain and temperature effects were empirically determined from these measurements. His approach is still used today although the proposed parameterizations differ in the type of variables used and the values of parameters given for a certain sample.

A proposed parameterization for the ITER strands (determined empirically) has been recently released [2.11] and it is summarized in the following paragraphs. The range of validity is between -1% to 0.5% uni-axial strain. This range covers the expected values of strain during operation. Several quantities need to be defined before introducing the equations describing the critical surface and these are given in Table 2.1:

Table 2.1 Definition of terminology used in the equations describing the critical surface.

	Description
$F_p = J_c(B,T,\varepsilon)\cdot B$	Pinning force density
$B^*_{c20\,max}$	Maximum critical field, at zero temperature and applied intrinsic strain
$B^*_{c20}(\varepsilon)$	Critical field, at zero temperature and applied intrinsic strain ε
$B^*_{c2}(T)$	Critical field, at temperature T and zero intrinsic strain ε
$B^*_{c2}(T,\varepsilon)$	Critical field, at temperature T and applied intrinsic strain ε
$T^*_{c0\,max}$	Maximum critical temperature, at zero field and intrinsic strain
$T^*_{c0}(\varepsilon)$	Critical temperature, at zero field and applied intrinsic strain ε
$T^*_c(B)$	Critical temperature, at field B and zero intrinsic strain
$T^*_c(B,\varepsilon)$	Critical temperature, at field B and applied intrinsic strain ε
$b = \dfrac{B}{B^*_{c2}(T,\varepsilon)}$	Reduced magnetic field
$t = \dfrac{T}{T^*_{c0}(\varepsilon)}$	Reduced temperature
$b_0 = \dfrac{B}{B^*_{c20}(\varepsilon)}$	Reduced magnetic field at zero temperature
$k(T,\varepsilon) = \dfrac{\kappa(T,\varepsilon)}{\kappa(0,0)}$	Normalized Ginzburg-Landau parameter
$\varepsilon = \varepsilon_{applied} - \varepsilon_{max}$	Intrinsic strain: longitudinal (in the direction of the strand) strain, and is referred to the applied strain $\varepsilon_{applied}$ at which the maximum critical properties are measured ε_{max}
Parameters determined by a data fitting procedure and used in the model	
C	Scaling constant
$B^*_{c20\,max}$	Upper critical field at zero temperature and strain
$T^*_{c0\,max}$	Critical temperature at zero field and strain

p	Low field exponent of the pinning force (p<1, $p \approx 0.5$)
q	High field exponent of the pinning force ($q \approx 2$)
C_{a1}	Strain fitting constant
C_{a2}	Strain fitting constant
$\varepsilon_{0,a}$	Residual strain component
ε_{max}	Tensile strain at which the maximum critical properties are reached

The underlying model for the pinning force, described in Chapter 1 can be written as

$$F_p = C \cdot \left[\frac{B^*_{c2}(T,\varepsilon)}{B^*_{c20\,max}} \right]^n \cdot \frac{1}{k(T,\varepsilon)^m} \cdot f_p(b) \tag{2.1}$$

where $m = 1$ and $n = 2$ and the normalized pinning force is

$$f_p(b) = b^p \cdot (1-b)^q \tag{2.2}$$

and the exponent p and q have values close to 0.5 and 2 respectively.

The critical field and the normalized Ginzburg-Landau dependence on temperature and strain are modeled as:

$$\begin{aligned} \frac{B^*_{c2}(T,\varepsilon)}{B^*_{c20\,max}} &= s(\varepsilon) \cdot (1-t^\nu) \\ k(T,\varepsilon) &= s(\varepsilon) \cdot \frac{1-t^\nu}{1-t^2} \end{aligned} \tag{2.3}$$

where ν is 1.52 and $s(\varepsilon)$ is the strain function that will be defined later on (see Eq. 2.9).

Combining Eqs. 2.1-2.3 we obtain

$$F_p = C \cdot s(\varepsilon) \cdot (1-t^\nu)^{n-m} \cdot (1-t^2)^m \cdot b^p \cdot (1-b)^q \tag{2.4}$$

The critical temperature at given strain is

$$\frac{T^*_{c0}}{T^*_{c0\,max}} = \left[\frac{B^*_{c20}(\varepsilon)}{B^*_{c20\,max}} \right]^{\frac{1}{w}} \tag{2.5}$$

where w is around 3 (determined experimentally).

Combining the above equations we obtain the following explicit forms for the critical field, temperature and current density

$$B_{c2}^{*}(T,\varepsilon) = B_{c20\,max}^{*} \cdot s(\varepsilon) \cdot (1 - t^{1.52}) \tag{2.6}$$

$$T_{c}^{*}(B,\varepsilon) = T_{c0\,max}^{*} \cdot [s(\varepsilon)]^{\frac{1}{3}} \cdot (1 - b_0)^{\frac{1}{1.52}} \tag{2.7}$$

$$J_c(T,B,\varepsilon) = \frac{C}{B} \cdot s(\varepsilon) \cdot (1 - t^{1.52}) \cdot (1 - t^2) \cdot b^p \cdot (1 - b)^q \tag{2.8}$$

The last equations to define are the ones related to the strain function $s(\varepsilon)$:

$$s(\varepsilon) = 1 + \frac{1}{1 - C_{a1} \cdot \varepsilon_{0,a}} \cdot \left[C_{a1} \cdot \left(\sqrt{\varepsilon_{sh}^2 + \varepsilon_{0,a}^2} - \sqrt{(\varepsilon - \varepsilon_{sh})^2 + \varepsilon_{0,a}^2} \right) - C_{a2} \cdot \varepsilon \right] \tag{2.9}$$

$$\varepsilon_{sh} = \frac{C_{a2} \cdot \varepsilon_{0,a}}{\sqrt{C_{a1}^2 - C_{a2}^2}} \tag{2.10}$$

As an example we take the parameters for an Oxford wire (Table 2.2) obtained by fitting experimental data to the proposed scaling laws [2.7]:

Table 2.2 Parameters used for Oxford wire (ITER CS wire [2.7]).

C (AT/mm^2)	77073.5
$B_{c20\,max}^{*}$ (T)	33.92
$T_{c0\,max}^{*}$ (K)	16.4
C_{a1}	53.3
C_{a2}	8.55
$\varepsilon_{0,a}$ (%)	-0.25

The results of the simulated critical current density as a function of strain and magnetic field are shown in Fig. 2.1(a-b). Results are similar as a function of temperature. In Fig. 2.1(c) experimental results are compared to the expected values estimated with the equations reported above (Eq. 2.8-2.10) [2.12].

The typical experimental setups used to make those measurements are shown in Fig. 2.2 and 2.3. In the so-called "Pacman" device (Fig. 2.2) the measurements can be taken over a relatively long length. The sample is fixed on the outside diameter of the holder and when a pure torque force is applied to the sample at the ends of the beam section, the beam diameter changes and puts the sample in either compression or tension [2.13, 2.14].

The Walters spring (Fig. 2.3) is the most common device used for strain measurements. This device can hold a sample length of 80 cm and the $TiAl_6V_4$ spring where the sample is mounted, allows linear and reversible strains up to 1.4%. The sample is fixed by either soldering or it is immobilized in a groove. The mechanism operates by applying opposite torques at each end of the spring [2.15].

Uni-axial strain measurements have been performed over the last 10 years, greatly increasing the database of experimental data that were used to improve understanding of the behavior of superconducting materials under strain. Most of the work is empirical and the data are used to determine the fitting parameters used in the equations 1-8. Several parameters are needed to describe a single strand so that more effort is now invested in

understanding the microscopic and atomistic behavior of a single strand hoping to find a universal law applicable to all strands.

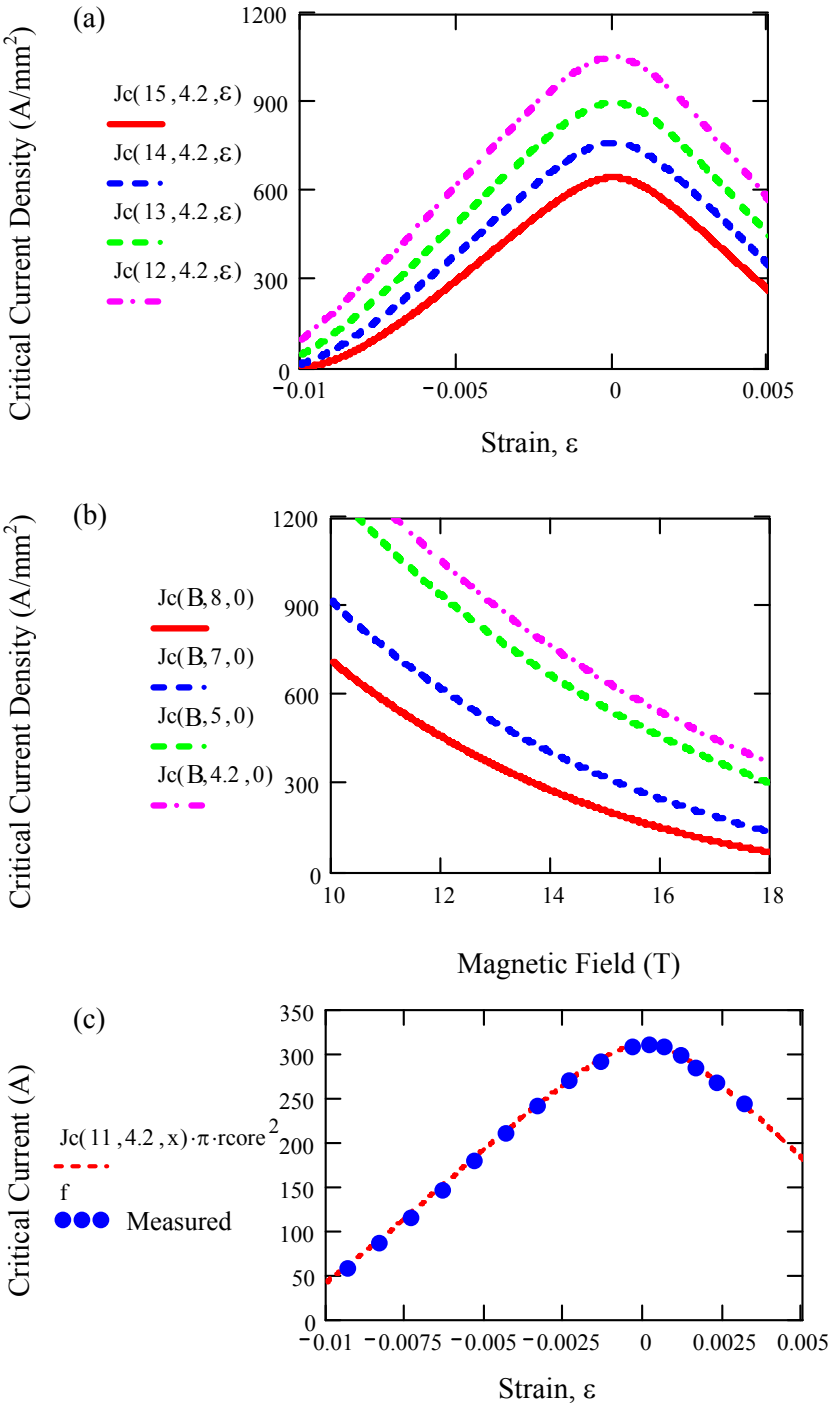

Fig. 2.1 (a) Critical current density as a function of uniaxial strain for different magnetic fields. (b) Critical current density as a function of magnetic field for different. Strains. (c) Measured and calculated critical current as a function of uniaxial strain. J_c is calculated from Eq. 2.8 using parameters given in Table 2.2 determined experimentally in Ref. [2.7].

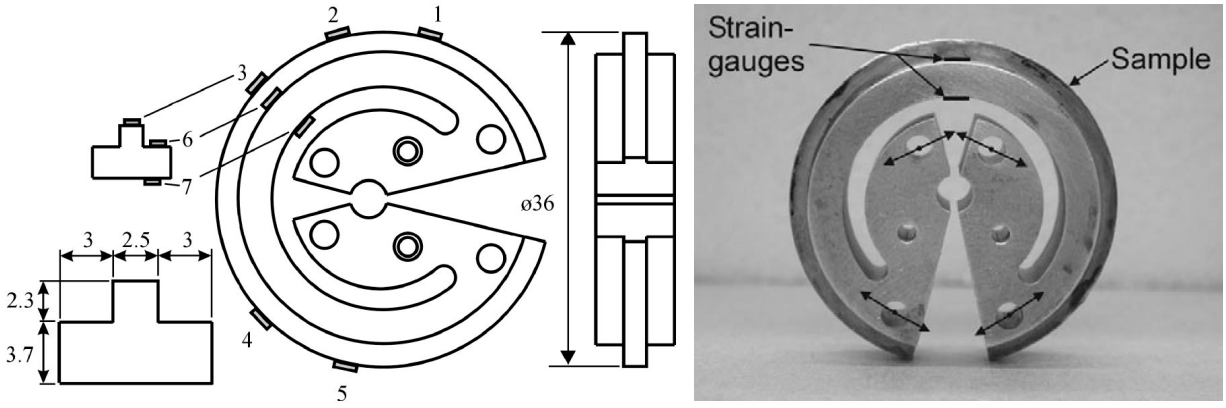

Fig. 2.2 Pacman strain device [2.13, 2.14].

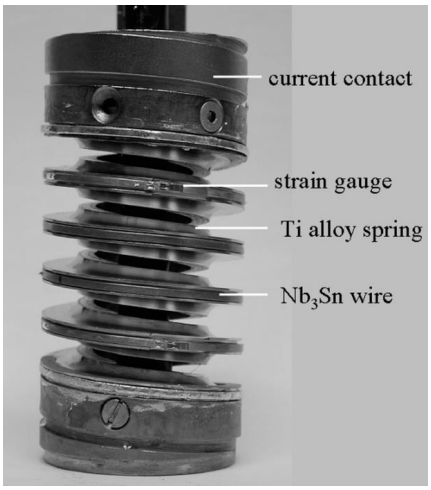

Fig. 2.3 The Walters spring (WASP) device [2.15].

In their most common applications for fusion magnets, superconducting strands are always wound in cables that are then used to build magnets. A cable can be composed of several hundreds strands. It would be useful if the strain equations describing the strain effect on a single strand could be simply scaled to predict a cable behavior. But the strands inside a cable experience several different load effects at the same time and it is not easy to isolate them. Nevertheless, a series of experiments on sub-sized cables were done in order to better understand the relationship between the effects on a single strand and the effects on a bundle of strands interacting with one another.

The availability of suitable facilities limits the type of experiments which can be done on cables of sizes which can carry currents of around 10 kA. Forces scale up with the current and having an efficient system to apply the strain required and to make measurements is not an easy task to accomplish, especially in the relatively small bore sizes available in magnets with a relevant magnetic field range.

Miller, et al. performed a series of straight line pull tests and long sample bifilar coil tests to study the effect of void fraction on initial filament strain. Void fraction is the fraction of space in the cable cross section not occupied by the strands. The cables were CICC cables composed of 27 strands. The cables were inserted into a jacket. If the jacket

is made of material with a different coefficient of expansion (COE) with respect to the cable (an example is stainless steel see Fig. 3.8), the critical current values showed a dependence on the initial void fraction of the cable (Fig. 2.4(b)). Otherwise using materials like Incoloy Alloy 908® with a coefficient of expansion closer to the one of the cable, the critical current was nearly independent of this variable [2.16]. These results were expected since, if the jacket does not match the cable COE, it is adding extra compressive strain to the cable during cool down to 4.2K. This extra strain caused by COE mismatch can greatly limit the performance of the cable. The schematic of the experimental set up is shown in Fig. 2.4.

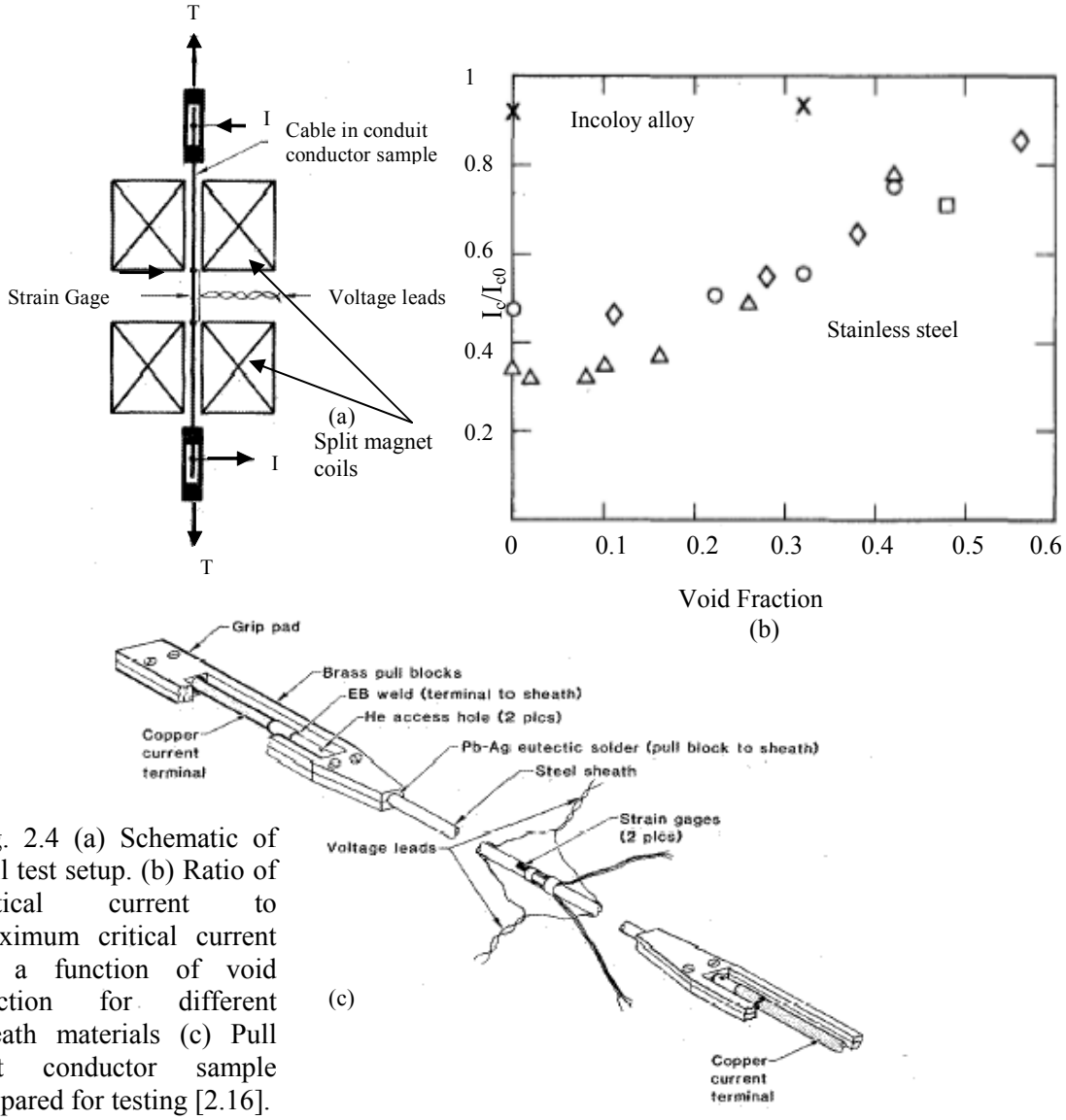

Fig. 2.4 (a) Schematic of pull test setup. (b) Ratio of critical current to maximum critical current as a function of void fraction for different sheath materials (c) Pull test conductor sample prepared for testing [2.16].

Specking has studied the effects of static and cyclic axial strains on sub-cables CICC for the Next European Torus (NET) [2.17]. His goal was to better relate single strand and sub-sized cable measurements. All samples were measured at the KernForschungsZentrum-Karlsruhe (KFK) laboratory in Germany, using the Force Field

Current (FBI) facility which allows testing of short straight samples by supplying the sample with axial force, current and field. Basic single strands measurements (Force F = 1 kN and current I = 250 A, strain measured with capacitive probe) were compared with sub-cable measurements (F < 100 kN, I < 10 kA, strain measured with resistive strain gauge extensometer). This facility has been recently refurbished with an updated power supply and current leads, and new experimental results have been presented in [2.18] after a series of tests studying the effects of twist pitch (characteristic length at which the subcables are twisted in each stage to minimize AC losses) and cable patterns and composition (with copper strands or not) for cables in stainless steel conduits. The FBI facility, various test samples, and typical results are shown in Fig. 2.5.

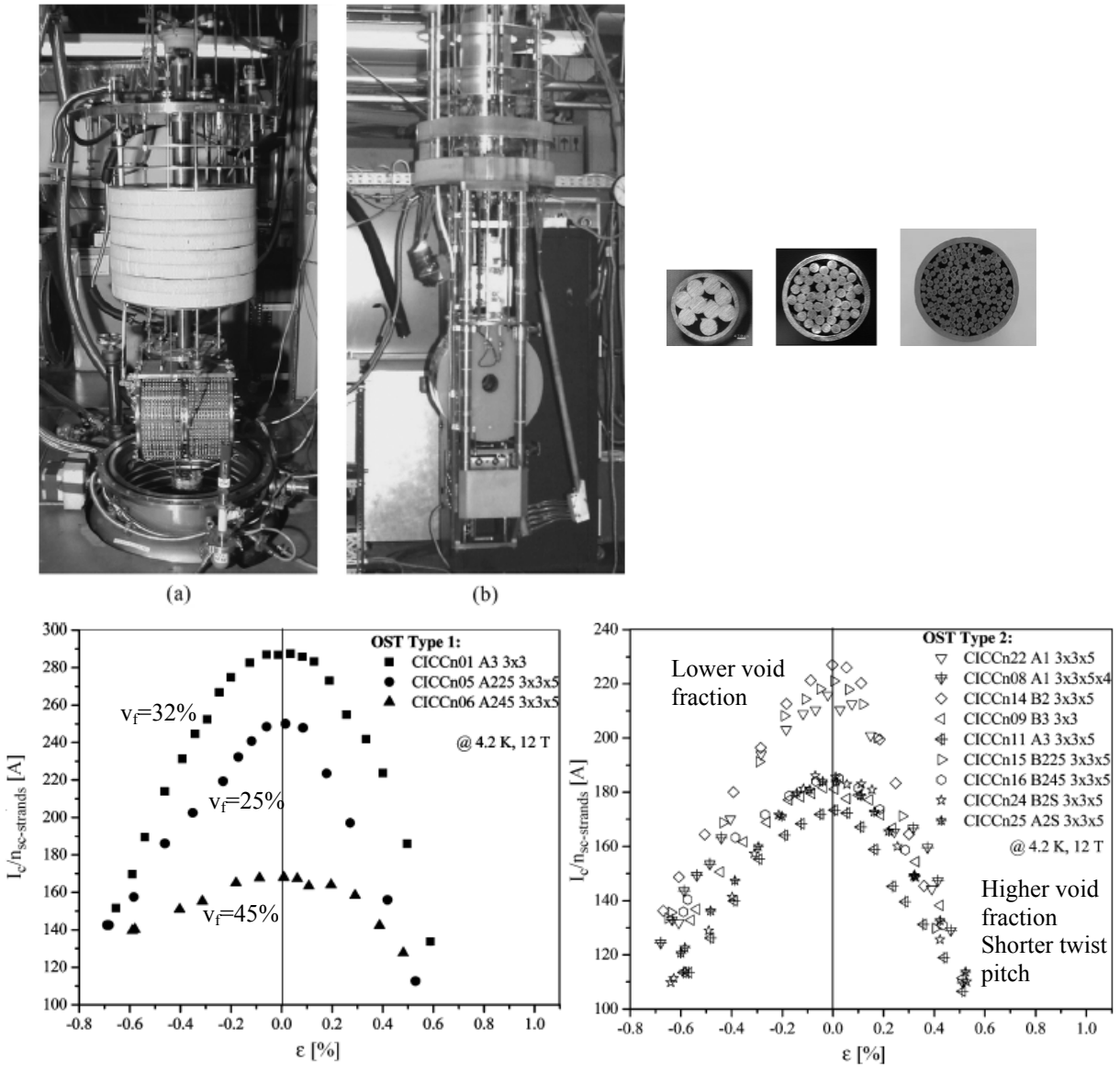

Fig. 2.5 Experimental setup and cables tested at the FBI facility. Experimental results for cables, in stainless steel jackets, with different void fraction, twist pitch and cable configurations are shown.

The measurements showed that the best performance was achieved with void fraction less than 35%. It was also observed that the shorter twist pitch worsens the performance of a cable. Additionally hybrid cables (with one copper and two superconducting strands in the first triplet) were less sensitive to applied strain than cables with all superconducting strands. Stainless steel was used as jacket material for all the samples tested.

2.3 Bending strain effect

More recent experiments deal with specific problems related to cable configurations in which a strand is under both pinching and bending effects [2.19-2.20]. A novel strain device was created after analysis of the ITER Central Solenoid Model Coil (CSMC) and Insert Coils revealed degradation higher than expected [2.21]. Test Arrangement for Strain Influence on Strands (TARSIS) was the first device used to simulate the loads experienced by a strand in a CICC cable [2.20]. The mechanism is shown in Fig. 2.6.

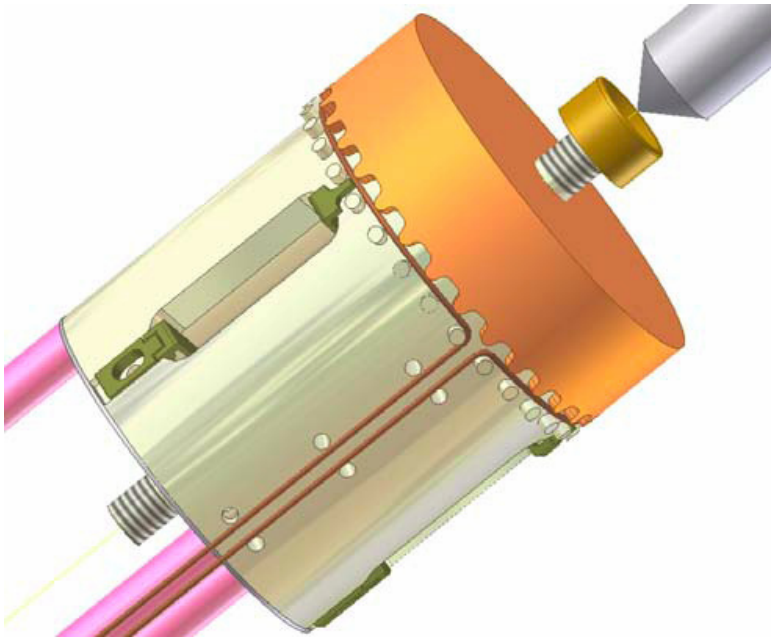

Fig. 2.6 TARSIS experimental device [2.20].

The experimental device consists of a lower drum and upper cup with a periodic circular arrangement of fingers and pins, respectively simulating the periodic bending experienced by a single strand in a cable. Operation entails closing the cap on the drum so that the fingers close press down on the wire between the pins, placing the strand in a periodic bending-tension-shearing-pinching state. Measurements showed degradation of single strand under repeated load application. The degradation is due to a plastic deformation together with a reversible degradation with loading [2.19-2.20].

Other experiments were done to isolate a single strain characteristic and to understand the fundamentals related to it. In particular experiments were done to isolate the bending strain behavior of Nb_3Sn strand. Senkowicz, Takayasu and Lee tested several strands

under different static bending conditions [2.22]. In these tests the sample was clamped in a fixture with a constant radius of curvature. The strand was heat-treated in a straight configuration and then transferred inside a groove between two curved Ti-6Al-4V clamps at room temperature (Fig. 2.7). A series of clamps were used to bend the samples to different strain levels. The strand could be tested only once at its fixed bending state, and therefore could not be loaded at multiple strain states.

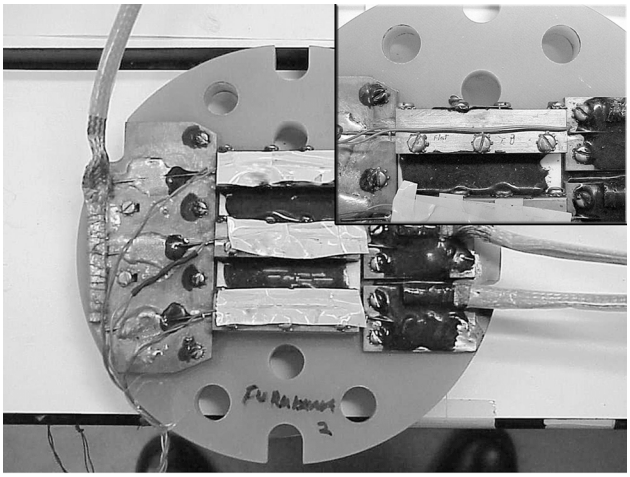

Fig. 2.7 Fixed bending strain behavior strand configuration [2.22].

A pure bending device was recently designed and successfully tested by Harris, Allegritti and Takayasu [2.23-2.24]. In this new design, a series of gears with different ratios are moved by rotating torque arms through an input shaft controlled outside the dewar. Fig. 2.9 shows a schematic of the device. The strand is mounted on a support beam and a groove is placed on the neutral axis of the beam to produce a pure bending effect on the strand. The bending strain can be increased up to 0.8% at the outside diameter of the strand (Fig. 2.8).

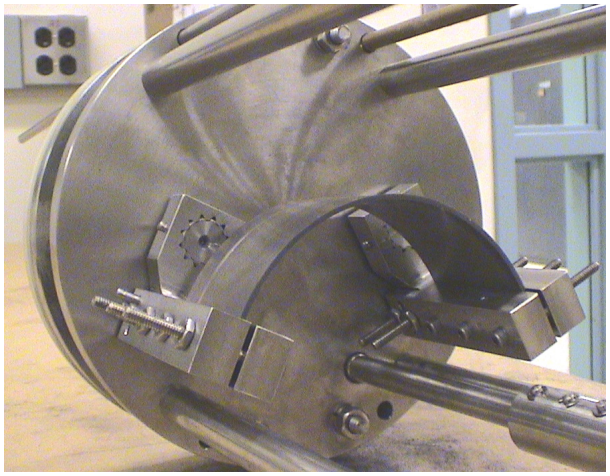

Fig. 2.8 Maximum bending applied to the support beam at room temperature during preliminary set up of the pure bending device.

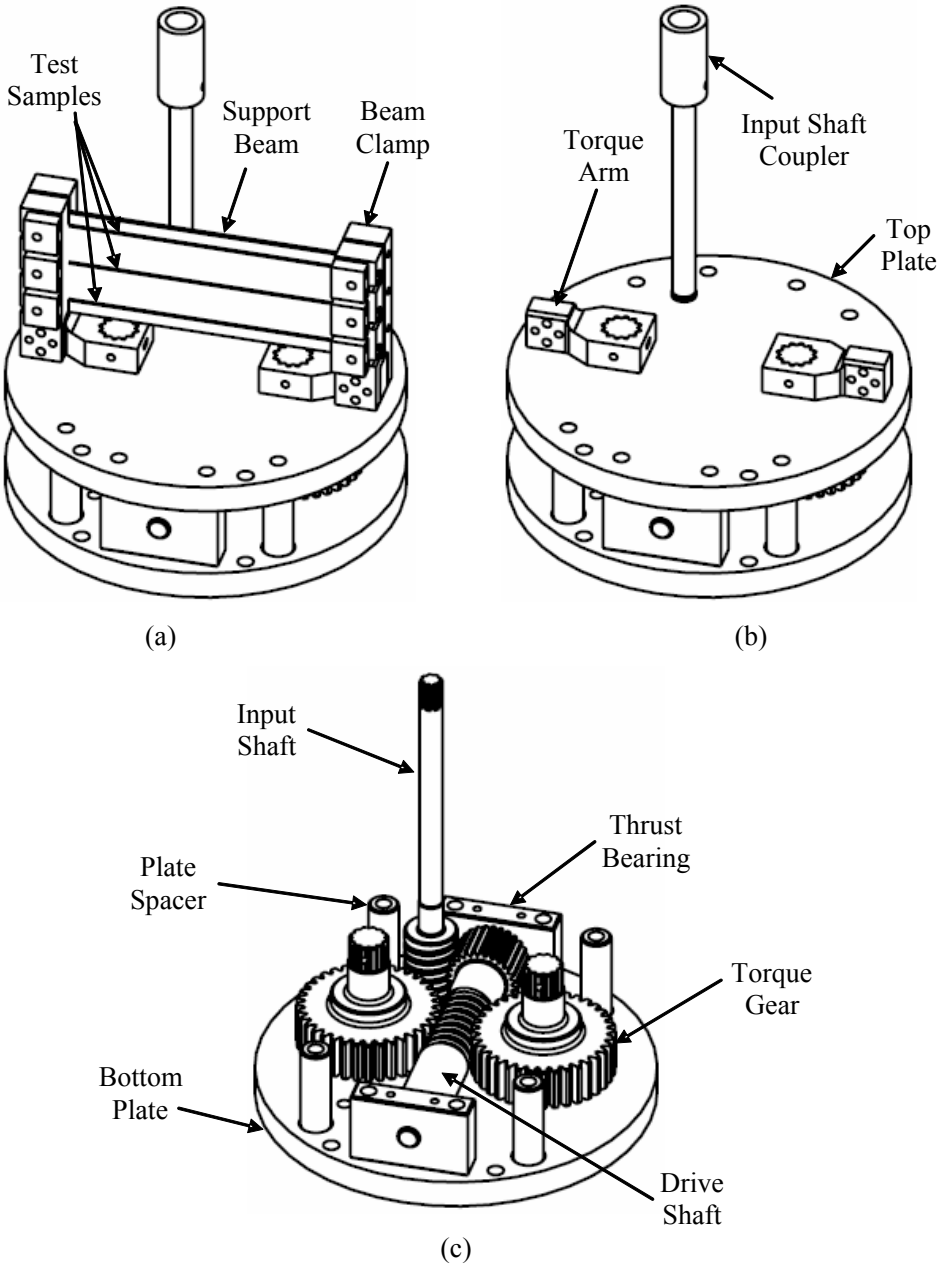

Fig. 2.9 Pure bending device components: (a) complete mechanism, (b) with strand mounting system removed, and (c) inner gear train [2.23-2.24].

Five different types of strands were tested during 2006-2007 and a summary of the results of the normalized critical current as a function of the nominal bending strain is shown in Fig. 2.10. These results showed that internal tin wires (EM-LMI, LUVATA, OST) are more sensitive to pure bending than bronze route wires (EAS, FURUKAWA). This behavior might be due to the different cross section of the wires. Internal tin strands have fewer sub-elements while bronze route strands have smaller filaments and sub-elements.

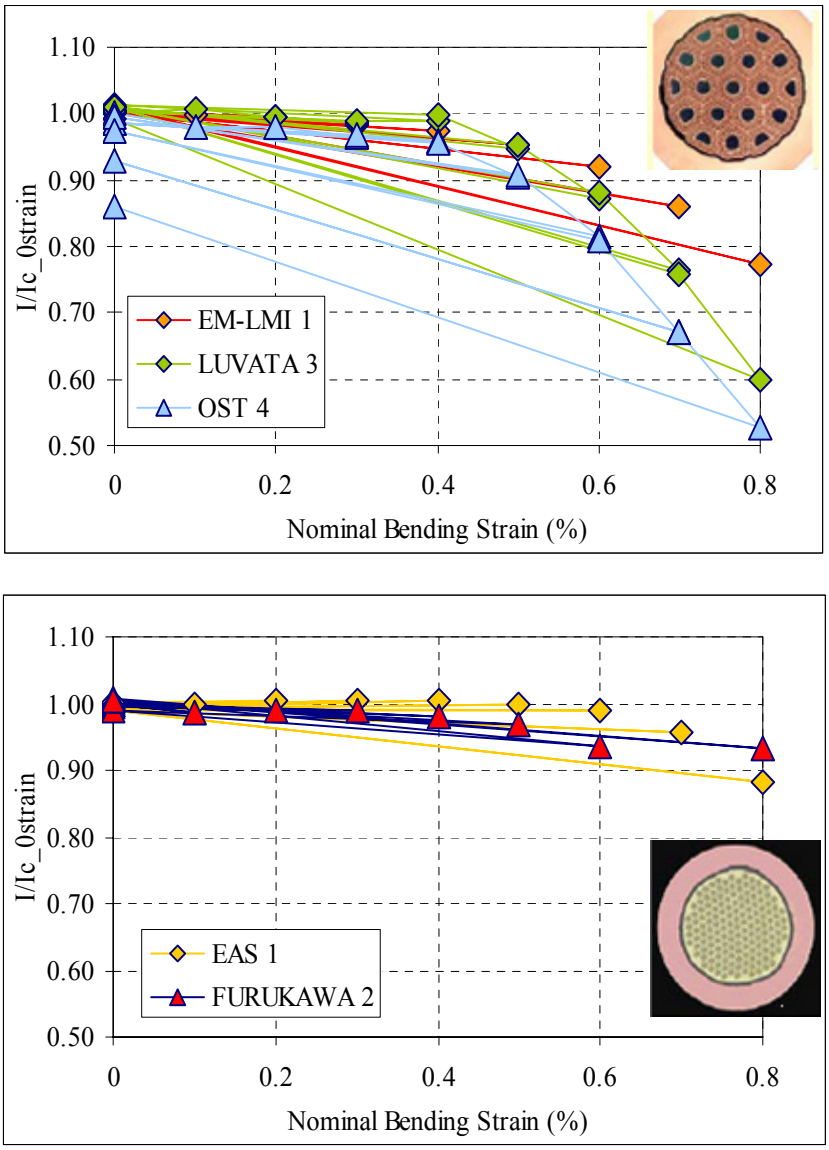

Fig. 2.10 Experimental results, normalized critical current as a function of nominal bending strain: internal tin strands (top), bronze route strands (bottom).

Bending strain can be easily added as a strain component inside the parametrical equations described earlier (Eq. 2.6-2.10). Uni-axial strain has the advantage that it can be described as a function of intrinsic strain so that it does not depend on the geometry of a strand. Bending strain, on the contrary, depends on the geometry of the strand but it can be calculated for a particular geometry from uni-axial strain equations by averaging over the uni-axial strain curve. It was recognized by Ekin [2.25] that the transport properties of a Nb_3Sn strand are not only affected by the applied bending strain but it also depends on the inter-filament electrical resistivity. The electrical resistance between filaments determines whether the distance between the periodically distributed peak strains in the filaments is short or long compared to the current transfer length. One extreme is that the current transfer between filaments is not allowed (high resistance, short filaments twist pitch) so that the minimum critical current for each filament specifies the filament critical

current. In this case the strand critical current is the sum of the minimum values for each filament which is limited by the maximum strain along filaments at any point. The other extreme (low resistance, long filaments twist pitch) allows current transfer so that the overall critical current of a strand is the sum of the filament currents at any section considering the local strain variation over the section. The critical current over the cross section of a strand can be expressed with Eq. 2.11 and 2.12.

No current transfer

$$I_c = \frac{2 \cdot \pi \cdot r^2_{core}}{\varepsilon_b^{\,2}} \cdot \int_0^{-\varepsilon_b} J_c(B,T,\varepsilon_{th}+t) \cdot t\,dt \qquad (2.11)$$

Perfect current transfer

$$I_c = \frac{2 \cdot \pi \cdot r^2_{core}}{\pi \cdot \varepsilon_b^{\,2}} \cdot \int_{-\varepsilon_b}^{\varepsilon_b} J_c(B,T,\varepsilon_{th}+t) \cdot (\varepsilon_b^{\,2} - t^2)\,dt \qquad (2.12)$$

Typically the two regimes are a boundary for the behavior of a strand experiencing bending and do not correctly describe the bending behavior (Fig. 2.11).

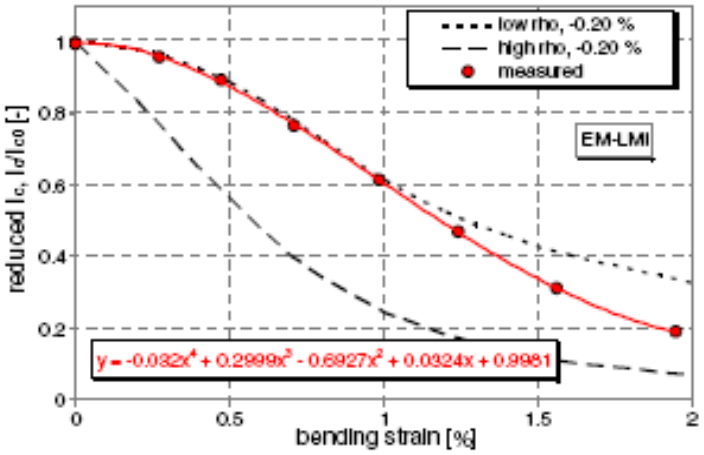

Fig. 2.11 Normalized critical current as a function of bending strain compared with the low and high resistivity regimes [2.26].

Takayasu proposed an empirical model [2.27] in which the measurements shown in Fig. 2.10 are correctly fitted by the expression in Eq. 2.11 and 2.12. In his model he considered filament breakage, neutral strand axis displacement, current transfer length and uni-axial strain release (due to the application of bending strain) as fitting parameters to be varied inside the equations proposed above (Eq. 2.11-2.12). If assumptions are made for the variation of those quantities as a function of the bending strain (Fig. 2.14(b)) the data can be properly fitted (Fig. 2.14(a)).

To include those variables we start by taking a change of variable in Eq. 2.11 and 2.12 that can be written as:

No current transfer

$$I_c = 2\pi \int_0^{R_{nc}} \left\{ \min \left| j_c(\varepsilon_y) \right|_{\varepsilon_y = \varepsilon_0 - \varepsilon_{by}}^{\varepsilon_y = \varepsilon_0 + \varepsilon_{by}} \right\} y\,dy \qquad (2.12)$$

Perfect current transfer $$I_c = 2\int_{-R_{nc}}^{R_{nc}} j_c(\varepsilon_y)\sqrt{R_{nc}^2 - y^2}\,dy \tag{2.13}$$

with $\varepsilon_y = \varepsilon_0 + \varepsilon_{by}$, ε_0 being the thermal (intrinsic) strain, $\varepsilon_{by} = \frac{y}{R_b}$, R_{nc} is radius of non-copper area, and R_b is the bending radius.

It is important to notice that in the high matrix resistivity case the worst point of the critical current does not occur always at the compression side. At a large bending rate the tension side could cause larger degradation of the critical current than the compression side since the critical current decreases at the tension side more sharply than at the compression side (Fig. 2.1).

As mentioned earlier experimental results lie in between the two limiting cases. There are several factors that could contribute to the real experimental critical current results shape.

Once bending is applied to the strand, the neutral axis of the strand could move so that:

$$\varepsilon_{by} = \frac{y + \delta}{R_b - \delta} \tag{2.14}$$

and the peak bending in tension and compression are:

$$\begin{aligned} \varepsilon_{bp}^{+} &= \frac{R_{nc} + \delta}{R_b - \delta} \\ \varepsilon_{bp}^{-} &= -\frac{R_{nc} - \delta}{R_b - \delta} \end{aligned} \tag{2.15}$$

The shift of the neutral axis can increase the fraction of a strand in tension so that the shape of the high and low matrix resistivity critical current changes. A shift between 50 and 100 μm can change the shape of the critical current curve by few percent.

A very small effect to be considered is the fact that the strand is in a pre-strain condition after cooldown but the bending cycles could remove the pre-strain decreasing the tensile strain ε_{max} and increasing the current.

More significant effects are the filament breakage fraction and the current transfer length. Filament breakages in the tension side due to bending have been found [2.28]. Filament breakages are believed to be the reason of the irreversible behavior of superconducting strand once the load is removed. If the filament breakage occurs on the surface of the tension side then the integration used in Eq. 2.12 and 2.13 is over the unbroken area. It has to be notice that filament breakage will affect much more the degradation in the case of high matrix resistivity. This is due to the fact that the effective superconducting filaments will be the only one in the center which does not overlap the broken area reducing greatly the overall behavior of the strand (Fig. 2.13(a)).

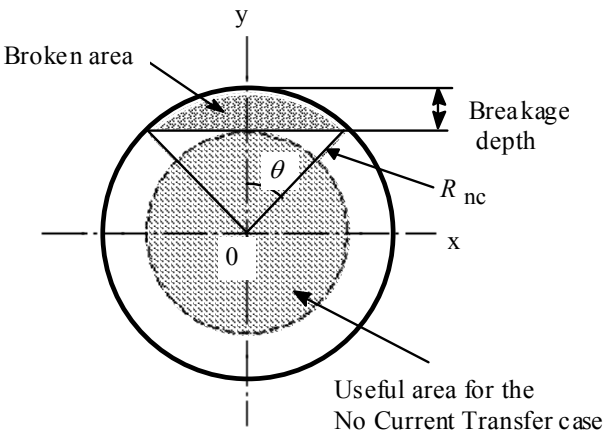

Fig. 2.12 Schematic of non-copper area having broken filament area.

The last parameter to be taken in consideration is the current transfer length. This length affects the total critical currents if compared to the twist pitch length L_p of the filaments since the critical current changes periodically along a filament. Therefore the ratio of the current transfer length and the twist pitch, L_{ct} / L_p, is an important factor for critical current behaviors. The current transfer length L_{ct} has been given as a function of the transverse resistance of matrix material between filaments and the n-vale of the resistive transition of the superconductor by [2.29-2.31 Ekin, Nijhuis],

$$L_{ct} = d\sqrt{\frac{0.106}{n}\frac{\rho_m}{\rho^*}} \tag{2.16}$$

here, n is the empirical power factor ($\rho = kJ^n$) and represents the sharpness of the resistive transition in the superconductor, ρ_m is the transverse resistance of the matrix between filaments, ρ^* is the superconductor resistivity criterion of the critical current and d is a dimensional spacing of current transfer between filaments [2.29].

Nijhuis in [2.31] used the strand diameter for the parameter d, however d could be much smaller than the strand diameter since it represents a dimension of current transfer between filaments in the superconductors (the filaments and the filaments core are smaller than the strand diameter).

It is noted that regardless of the accuracy of the current transfer length itself, the relative ratio of the current transfer length to the twist pitch (L_{ct} / L_p) is an important factor for the behavior of the of the critical current. It should be emphasized that the current transfer length dominates both the n-value of the superconductor as well as the effective transverse resistance.

To take into account the current transfer effect, the critical current of a filament at a given point z along a filament is presumed to be dominated by the minimum critical-current value between z - L_{ct} and z + L_{ct}. Now the critical current can be given using the minimum function operator defined for Eq. 2.12 in cylindrical coordinates,

$$I_c = 2\int_0^{R_{nc}} \int_{-\frac{\pi}{2}}^{\frac{\pi}{2}} \left\{ \min\left| j_c(\varepsilon_{r\phi}) \right|_{\phi=\varphi-\varphi_{ct}}^{\phi=\varphi+\varphi_{ct}} \right\} r\, d\varphi\, dr \tag{2.17}$$

where $\varepsilon_{r\phi} = \varepsilon_0 + \varepsilon_{br\phi}$, $\varepsilon_{br\phi} = \dfrac{r\sin\phi}{R_b}$, $\varphi_{ct} = \dfrac{2\pi L_{ct}\sin\theta}{L_p}$, $\theta = \tan^{-1}\dfrac{L_p}{2\pi R_{nc}}$

with

L_{ct} minimum current transfer length

L_p twist pitch length of strand

To apply the neutral-axis shift effect to the current transfer model the following equation is used for $\varepsilon_{br\phi}$; $\varepsilon_{br\phi} = \dfrac{r\sin\phi + \delta}{R_b - \delta}$.

The effects of those parameters on the two limiting cases are shown in Fig. 2.13 (a-b).

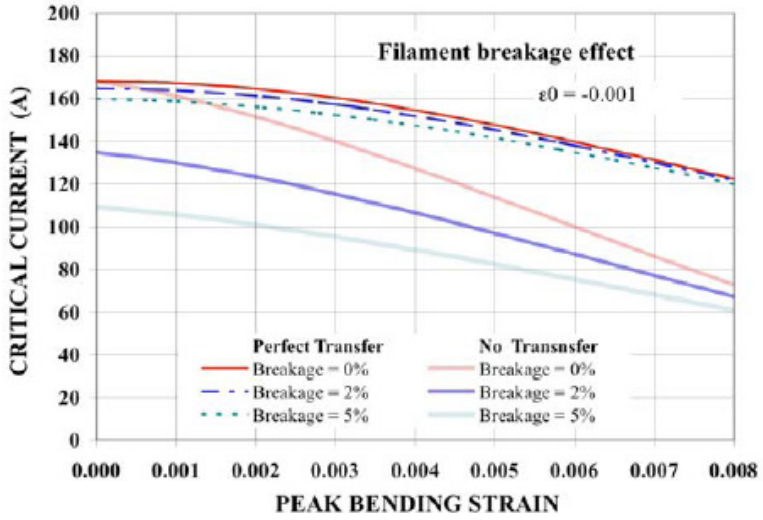

Fig. 2.13 (a) Filament breakage effect. The high resistivity case (no transfer) is more heavily affected by the filament breakage because an entire annulus of filaments is disregarded in the integration even if the breakage is local.

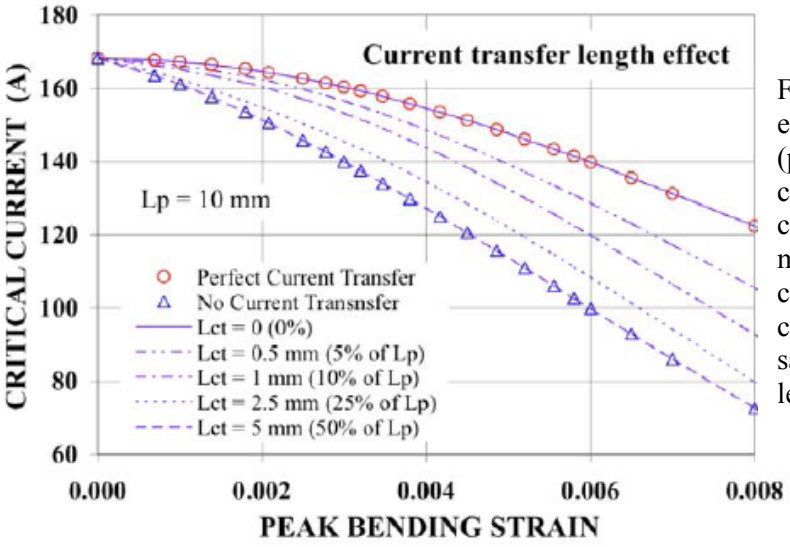

Fig. 2.13 (b) Current transfer effect. The low resitivity case (perfect current transfer) corresponds to the case of current transfer length of 0 mm, while the high resistivity case corresponds to the case of current transfer length of the same size as the twist pitch length.

As it can be seen from Fig. 2.13(a) the high resistivity case (no transfer) is more heavily affected by the filament breakage because an entire annulus of filaments is disregarded in the integration even if the breakage is local. Fig. 2.13(b) shows the effect

of the current transfer length indicating that the change in critical current as a function of bending strain is smaller if the current transfer length is shorter (perfect current transfer).

Taking all those factors into consideration the experimental results taken by Takayasu with the pure bending device were properly fitted as shown in Fig. 2.14 (a-b).

Certain assumptions on the shape of the shift, current transfer length, filament breakage fraction and uniaxial strain relaxation as a function of the bending applied need to be done in the modeling (Fig. 2.14(b)). The assumptions are believed to be fairly conservative and were used to give a best fit to the experimental data shown in Fig. 2.10.

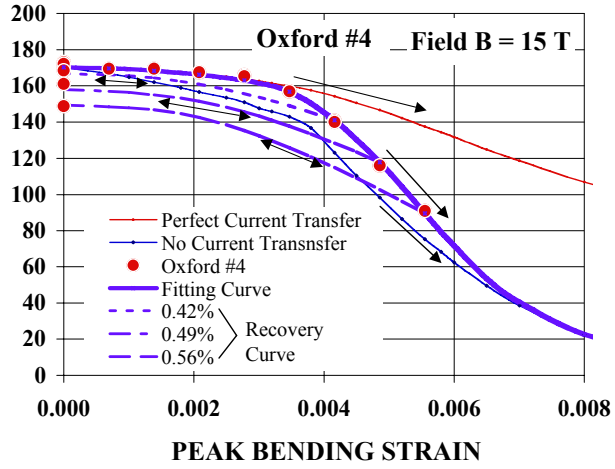

Fig. 2.14 (a) Curve fitting of the critical currents measured for Oxford wire (red solid circles). Lines are obtained from model calculations: Fine red and blue lines are for perfect current transfer and no current transfer models, respectively. Measured results fit a thick solid purple line which was obtained from the model. The dotted lines show recovery curves of the critical currents after the given bending of 0.42%, 0.49% and 0.56%. The recovered critical currents at zero bending agree well with the experimental results.

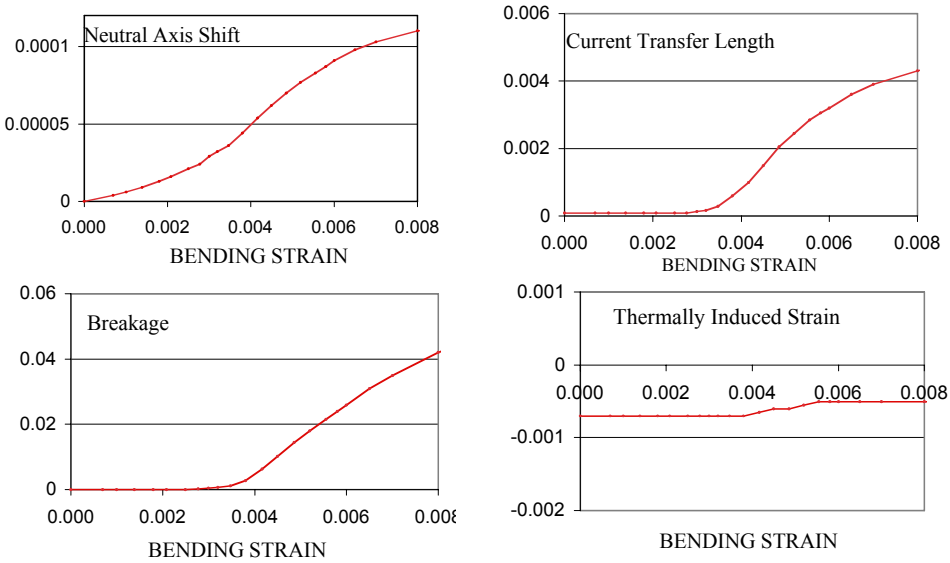

Fig. 2.14 (b) Estimated behavior of the neutral axis shift (in mm), the current transfer length (in mm), the breakage and the thermally induced strain release for Oxford wire as a function of the bending strain [2.27].

The empirical model presented by Takayasu is the first model capable of properly fitting the experimental results for bending strain data.

More experiments and theoretical work are needed to better understand the behavior of superconductors under bending strain and in particular how to relate such results to a full size cable configuration.

2.4 Transverse strain effect

Until the CSMC experimental results were obtained, the transverse strain effect on degradation was never taken into consideration in all the preceding analyses [2.21]. The observed degradation was believed to be due to the transverse strain effect from the accumulation of Lorentz load during charging. In the years since those experiments (2000-2003) only a very few experiments have been done on this subject and mostly on single strands [2.31-2.38]. Only one experiment was done on a sub-sized CICC cable. The lack of results and studies regarding the effect of transverse strain on CICC cable motivated our efforts to develop a device capable of applying transverse load on a sub-sized cable to simulate the loads in a full size cable.

J. Ekin was the first to study the effect of transverse compressive stress on the critical current and upper critical field of Nb_3Sn strand [2.32, 2.33]. In order to obtain data on the electrical effects of the transverse component of stress, he developed an apparatus to simultaneously apply mutually perpendicular components of field and current and transverse compressive stress to a single strand. The sample was compressed between two stainless steel anvil heads (Fig. 2.15). One of them was fixed while the other was designed to pivot so that it conforms to the flat surface of the first anvil head. Voltage taps were soldered to the sample within the compressed region so that the electric field was measured only over the region where stress was uniformly applied.

Two types of samples of the same bronze process were tested (one round and one flat). The same approach to estimate the stress applied was used for both the round and the flat sample so that, for the round sample, the change in contact area between the anvil and the sample were disregarded. The difference in shape between the two samples did not affect the results since the change in contact area was strongly affected by the stabilizer, a thick copper layer. This layer completely surrounded the superconductor and it served to uniformly distribute the load into the filament region. Both strands showed a strong degradation as a function of applied transverse load and the effect was much more severe than in the case of uniaxial strain. A simplified explanation for this difference given by Ekin was that, under axial strain, the axial force is apportioned among the various composite materials because they occupied parallel load-bearing paths while, in the transverse case, all the components of the composite experienced the same stress which was transferred from one material to the next in a serial load chain. For the transverse stress at 10 T, the degradation was 10% under a compressive pressure of 50 MPa. This degradation rises to nearly 30% at 100 MPa. For the axial strain, the degradation was less than 2% at up to about 200 MPa. The stress, which causes a given amount of critical current degradation at 10 T, was usually seven times less for transverse stress than for axial stress and was greater at higher fields. The critical current degradation was noted to be reversible in character (Fig. 2.15).

The authors claimed that a possible explanation for the differences in behavior under axial or transverse stress could be due to a preferred crystal growth orientation in the Nb_3Sn reaction layer. In fact the growth pattern in multifilamentary samples was radial within each filament, which would define anisotropy between axial and transverse properties. They underlined the importance of having a 3-D treatment of strain through deviatoric strain to better study the connection of axial and transverse strain, which usually exist simultaneously.

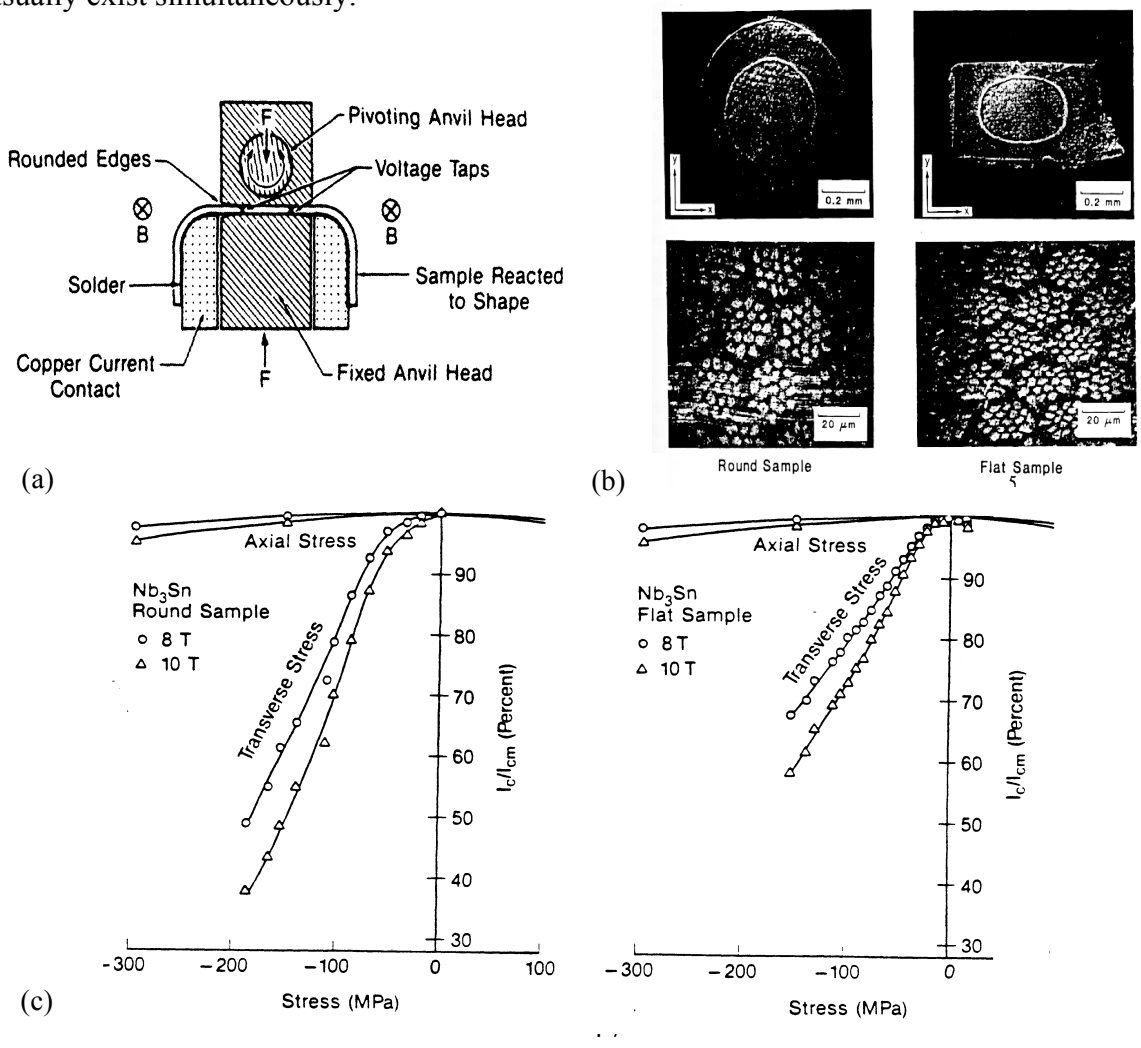

Fig.2.15 (a) Schematic view of test setup. (b) Cross section of the two samples used (round and flat). (c) Critical current degradation for transverse and axial compressive stress for round sample. (d)) Critical current degradation for transverse and axial compressive stress for flat sample [2.32, 2.33].

Specking *et al.*, made similar measurements [2.34]. The measurements were done at 13.5 T and 4.2 K on a bronze processed Nb_3Sn multifilamentary wire with an internal copper stabilizer.

In those first studies a lot of effort was applied to understand if the strand manufacturing process used to produce Nb_3Sn would play a role in the behavior under transverse load conditions. Ekin *et al* [2.35] measured the transverse stress effect on the

critical current of internal-tin and bronze-processed Nb_3Sn wires. It was observed that the bronze-processed conductor exhibited columnar grains that were radially oriented within the Nb_3Sn filaments, while the grains of the internal-tin conductor were more uniformly distributed around the axis and randomly oriented. It was expected that the radial orientation of the bronze-processed strand could enhance the transversal strain sensitivity due to this anisotropy between axial and transversal directions. It was found, however, that the transverse stress effect was not highly dependent on either grain morphology or fabrication process.

One of the concerns raised after these first tests on transverse stress effects was that in cabled conductors, stress concentrations at strand crossover points could aggravate the transverse stress effect because the stress was no longer distributed uniformly. Bray and Ekin addressed this issue by comparing uniform transverse stress results with a set of measurements done on crossover stress concentrated in contact points between the strands [2.36]. The comparison showed a critical current degradation at *equivalent load* that it is greater for the crossover situation due to the reduced area. Nonetheless they are comparable at *equivalent stress* (Fig. 2.16).

The analysis of the data were highly simplified considering the equivalent stress on the wire and not the load, showing that at equivalent stress (since crossover effect was on a much smaller area) the effect of transverse stress distributed or concentrated was the same.

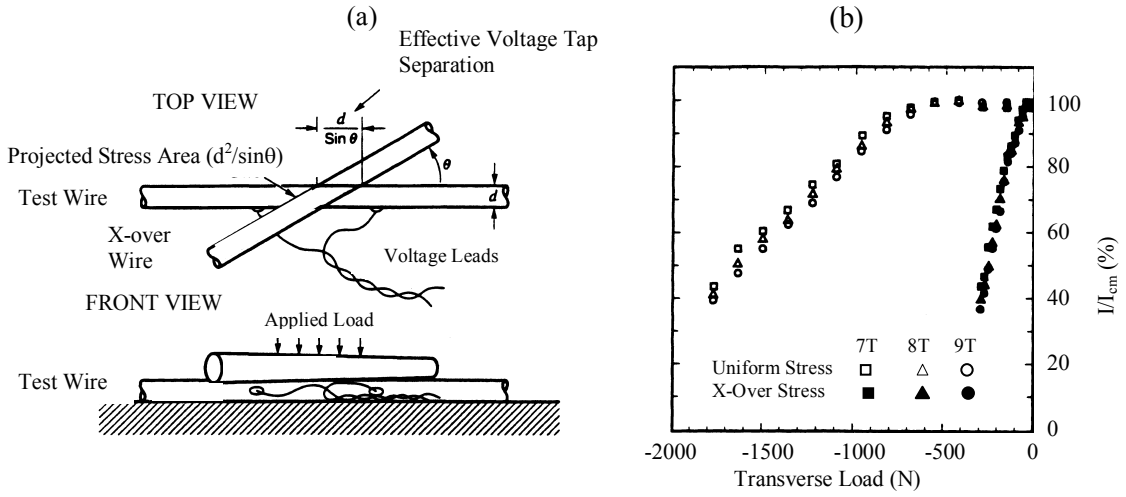

Fig. 2.16 (a) Test set up of crossover effect. (b) Critical current degradation as a function of transverse stress and magnetic field for uniform and cross over stress [2.36].

More recent work on single strands has been performed by several groups in Europe. Nijhuis et al. adapted their TARSIS setup to a X-strand configuration shown in Fig. 2.17 together with some results on a sample tested with this configuration [2.37]

Seeber at the University of Geneva is also performing mechanical tests on single strand using a configuration similar to a spring to apply the load (Fig. 2.18). The results shown are for a strand with a rectangular cross section to avoid mistake in the evaluation of the area over which the force is applied [2.38].

In general, more and more resources are being invested in understanding the mechanical behavior of superconductors. The mechanical properties and mechanical behavior of superconductors are a fundamental piece of information since electromagnets are becoming more and more powerful. The forces in those magnets are becoming the predominant focus of the design to insure the performance of the conductor. In this respect more work in determining the mechanical properties such as Young modulus for different strands are being done [2.39].

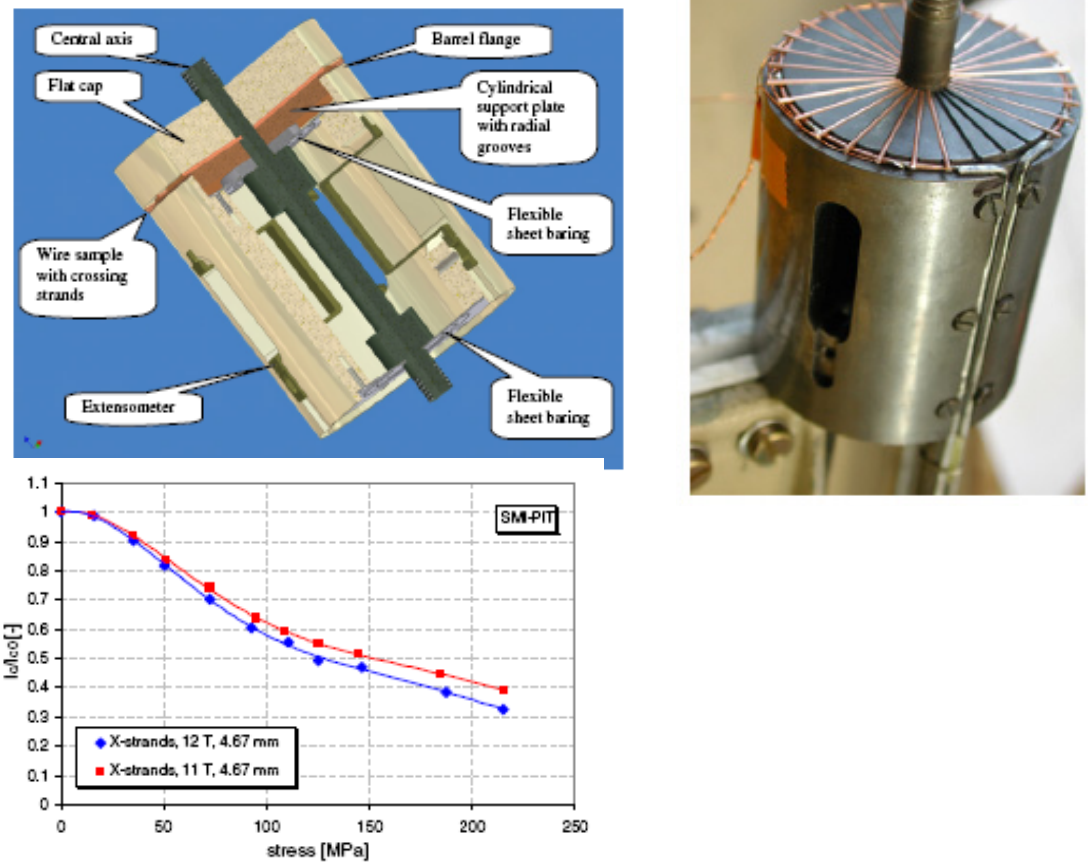

Fig. 2.17 Adapted TARSIS configuration to study crossing effects in a single strand (top). Results on a powder in tube sample (bottom) [2.37].

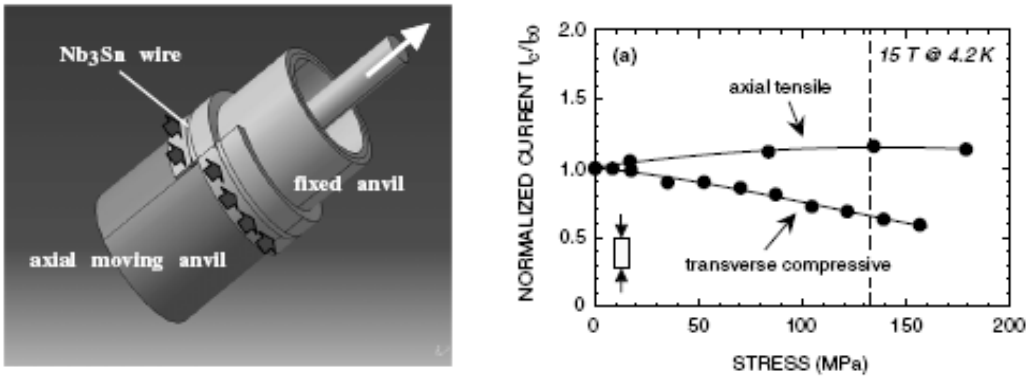

Fig. 2.18 Experimental setup used by the University of Geneva for their transverse load experiment (left). Some results of a rectangular superconducting wire for different axial and transverse loads applied (right) [2.38].

One of the limitations of the experiments considering transverse stress effects is the evaluation of the area pressed. Generally the nominal pressure values (evaluated over the diameter of the strands) are reported introducing a misleading representation of the real stresses felt by a strand since the area of contact can be much smaller than the one used to evaluate the nominal pressure. One of the unique features of the work of this thesis is that for the first time the real effective pressures caused by local contacts between strands have been analyzed as it will be presented in Chapter 5 and 6.

If some work has been done and is being done on single strands, the transverse load effect on sub-sized or full-size cables has received little attention. The main work on cables was done over 20 years ago by Summers and Miller to study the effect of transverse stress on a small cable-in-conduit conductor [2.40]. The measurements were done at 12 T and a good correlation with the single strand data was found for stress up to 50 MPa. At higher stress, the degradation for CICC is much more severe than for single wire condition (Fig. 2.19).

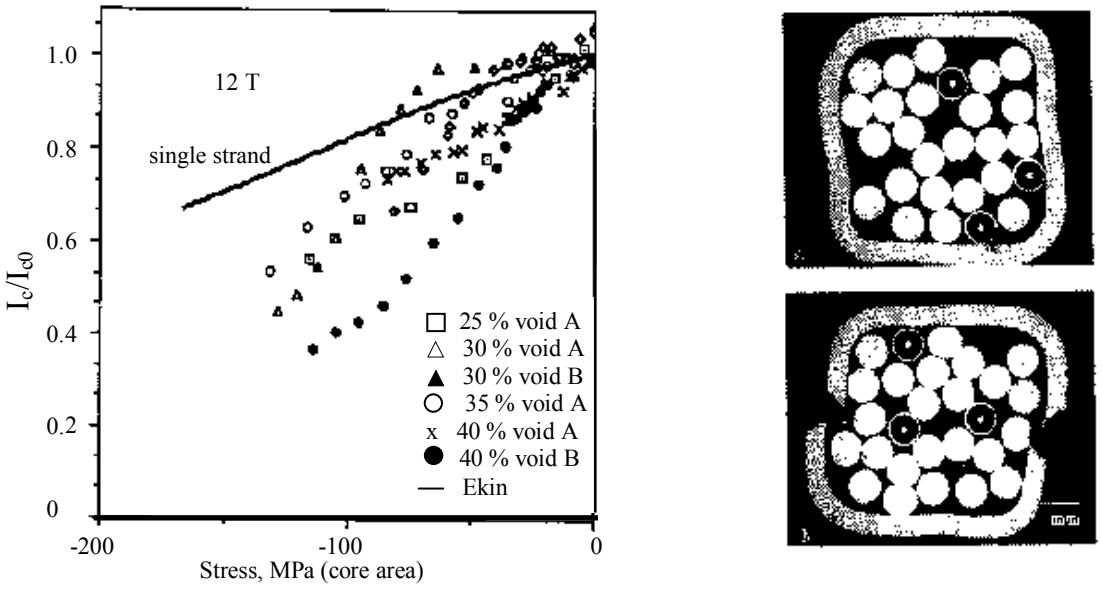

Fig. 2.19 (a) Critical current degradation as a function of transverse stress for the CICC tested. Also plotted is the single strand behavior normalized at 12 T, (b) Cross section of a 40% void fraction CICC before and after loading [2.40, 2.41].

The CICC cables were tested in a 12 T split pair solenoid superconducting magnet equipped with a transverse load cage. The cage was made of 304 SS and consists of a movable ram actuated by a pressurized diaphragm usable up to 13.5 MPa. The loading forces were transmitted through the specimen and reacted against a fixed anvil attached to a tension tube and located at the opposite end of the load cage. The anvil and ram applied the load to a 38 mm length of the CICC (Fig 20). The force applied was measured indirectly using two temperature and field calibrated strain gauges attached to the tension tube of the load cage and located 180º apart. The critical current was measured by voltage taps attached to the specimen conduit in the loaded section. The data were directly

compared with single strands measurements. The stress for this data has been expressed in terms of the projected area of the Nb_3Sn (including the surrounding bronze). For this case the stress in CICC is converted by multiplying the stress across the inside of the sheath by the factor $M = [s/(d_{core}*n)]$ where s is the inside lateral dimension of the conduit, n = (number of wires in cable)$^{0.5}$ and d_{core} is the diameter of the superconducting core.

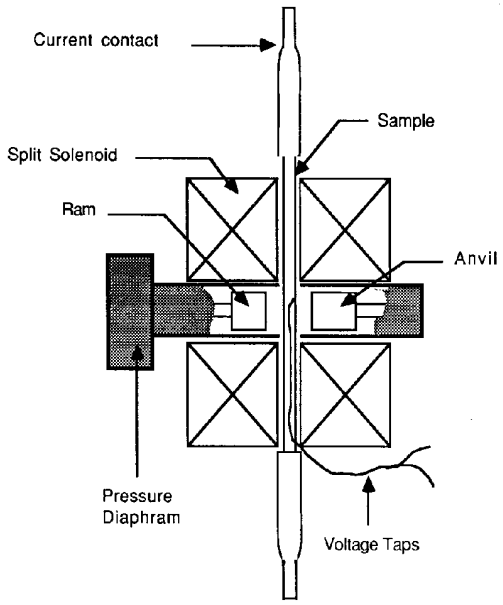

Fig. 2.20 Experimental setup: sample arrangement within the test magnet and the transverse load cage [2.40].

The degradation of the cable was larger that the one of the single wire. This was somehow expected since the load is not uniformly distributed and is enhanced by the cross over point loads between wires. In addition to this concentrated load some bending could have occurred in sections of wires immediately adjacent to the crossing points.

It might be expected that a CICC with greater compaction (less void fraction) would show a reduced sensitivity. In fact, the higher the degree of compaction, the greater the deformation at cross over points in the cable. Thus the size of contact area between wires is increased and ultimately for 0% void fraction the cable should behave as a single strand. Further studies were done to address this specific issue revealing the expected behavior. Two different void fractions were considered 0.30 and 0.40. Also in this case the jacket had a slot to remove the effect of support material and to apply the stress directly on the cable.

The data from tests (A, B in Fig. 2.19) at 30% and 40% void fractions were compared with the single strand data. While there is good agreement between the data for the two tests done on the 40 % void fraction for load below 50 MPa, there is a lot of scatter for the data at 30% void fraction. Regardless of the variation in the data, the effect of void fraction is clear. The 40% void fraction specimens receive less compaction than the 30% void specimen during processing. As a result, the crossover points between wires in the higher-void sample do not deform as much as in the low-void specimen. The load

footprint is smaller in high-void samples and causes a higher contact pressure. A higher contact pressure results in increased sensitivity to applied transverse load.

Those data were considered sufficient to conclude that there was not significant degradation caused by natural electromagnetic load up to 50 MPa which is higher that the average Lorentz load effect expected in the ITER cable (~ 20 MPa). The results were believed to be the demonstration that the electromagnetic effects were not important in full size cable and experiments on transverse load effects were abandoned.

It has to be noticed once again that those assumptions were made considering a nominal pressure approach (pressure over the diameter of the full size cable) but disregarding the effective contact pressure among strands that can be much higher and jeopardize the performance of a cable as it will be shown later in this thesis work.

It is only after the ITER CSMC test results that this effect came to attention once again since the magnet showed a degradation that was higher than the expected value from witness sample data. Those data could be explained only taking in consideration the transverse load effect of the accumulating Lorentz load across the cable cross section [2.42].

Based on the above mentioned works of the single strand tests of J. Ekin [2.32] and the small sub-sized cable experiments of Summer and J. Miller [2.40-2.41], degradations of the critical currents of ITER CSMC test results were investigated taking into account the electro magnetic transverse loads (Lorentz load) [2.42]. The general equations describing the critical field as a function of strain were modified to take in consideration the Lorentz load effect and it was shown that the test results could be properly fitted only taking in consideration this modification.

The effective upper critical field B_{c2}/B_{c2m} was approximated in a simplified form from the Nb_3Sn strand test data of Ekin [2.32] as

$$\frac{B_{c2}}{B_{c2m}} = 1 - 1.1 \cdot 10^{-4} \cdot |\sigma_t|^{1.35} \tag{2.18}$$

where σ_t is the transverse load stress of a CICC cable which is given as

$$\sigma_t = \frac{\sqrt{\pi \cdot v_f}}{2} B \cdot D \cdot J_s \cdot \frac{d}{d_c} \tag{2.19}$$

here B is the field, D is the cable diameter, J_s is the strand overall current density, d is the strand diameter, d_c is the strand core diameter, and v_f is the void fraction.

Using these equations, $B_{c20}(\varepsilon)$ in the Summers critical-current scaling equation [2.43] has been modified with

$$B_{c20}(\varepsilon, \sigma_t) = B_{c20m} \cdot (1 - 900 \cdot |\varepsilon|^{1.7}) \cdot (1 - 1.1 \cdot 10^{-4} \cdot |\lambda \cdot \sigma_t|^{1.35}) \tag{2.20}$$

here, λ is a constant parameter.

Fig. 2.21(a) shows the fitting results of the temperature dependences of the critical currents measured for the ITER CSIC Nb3Sn conductor. The temperature trends of the

analytical curves with transverse load effect fitted to the measured data better than those without the transverse load effect shown in Fig. 2.21 (b).

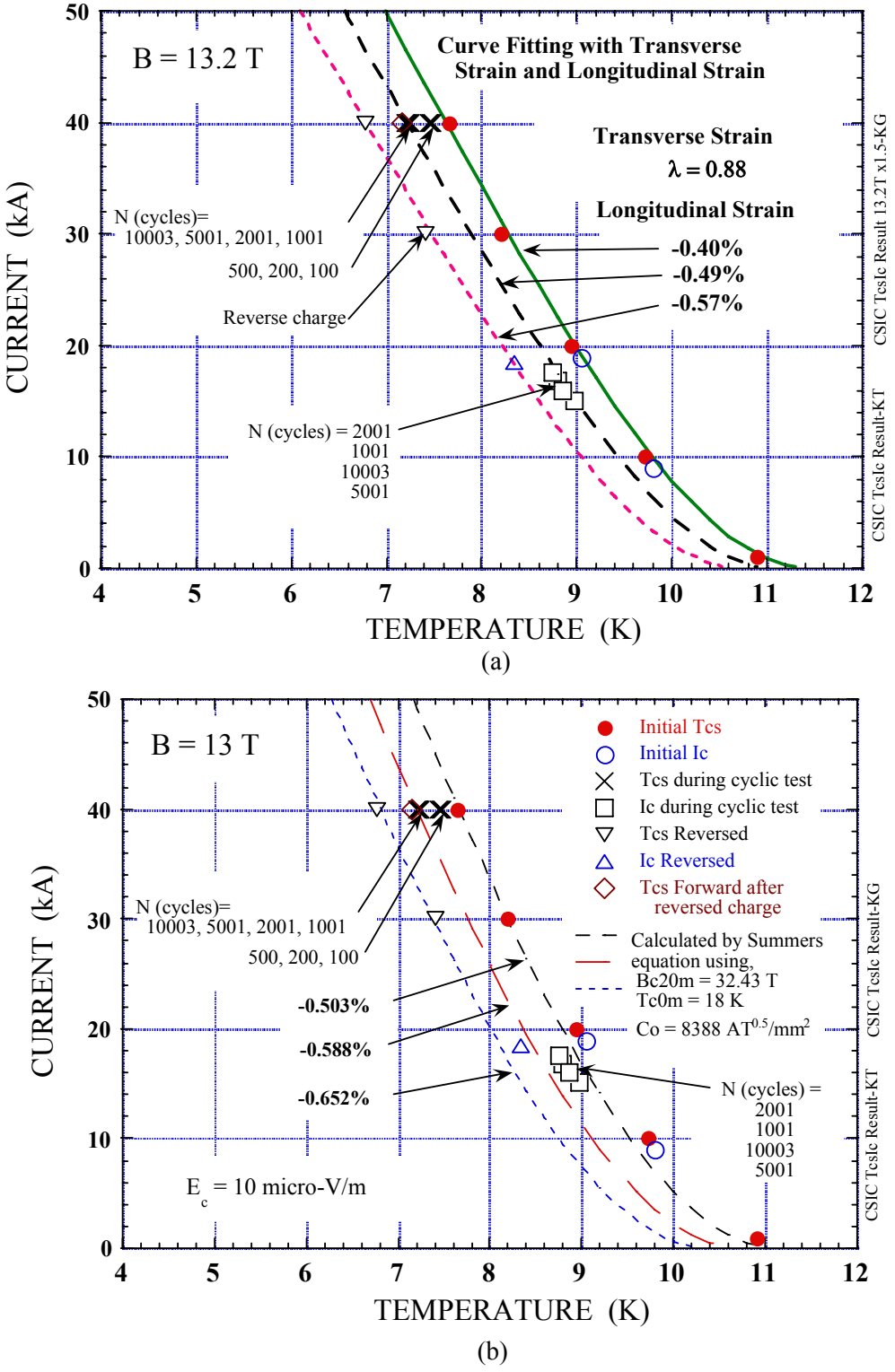

Fig. 2.21 Curve fittings of critical current temperature dependences measured for the ITER CSIC with transverse load effect (a) and without it (b).

2.5 Motivation for further investigations and challenges

In recent years, most of the experiments concentrated on axial strain effect on superconductors. Very little has been done on transverse strain effect on superconductors especially on cables, and the only experiments done on sub-sized cables were the two described at the end of the previous section [2.40, 2.41] and performed 20 years ago.

The fusion community is especially interested in this subject because CICC cables are more sensitive to this effect due to their design. Initially the transverse load effect was thought to be small enough to be disregarded and that is why experiments were abandoned. Later on, the tests of the ITER TF Model Coil and ITER CS Model coil showed measurable degradations of the cable and it is believed that these degradations are caused by the transverse strain created by the accumulation of electromagnetic force (JxB) across the cable cross section [2.21, 2.42].

The uncertainties left by the results obtained with those model coils, were the driving reasons to have further experiments studying the transverse load effect on CICC conductor. The scope of this thesis is to develop a device to take those measurements and better understand the performance of a cable during operation.

Tests on sub-sized cables are very challenging due to the high current required to test the critical current. The measurements try to emulate the magnetic Lorentz force in a cable. This force is a body force which accumulates over the cross section of the cable and creates a pressure against the strands. The range of pressures of interest is between 10 MPa and 20 MPa based on the ITER TF and CS conductor designs (nominal pressures). It is not possible to obtain this range of pressures using only the electromagnetic force. This is because to fit the existing magnet facility, a sub-sized cable is used and only loads up to about 7 MPa can be obtained electromagnetically. Thus it is necessary to simulate the pressure by applying an external load mechanically. Additionally it is of interest to study the dependence of the critical currents of cables as a function of transverse pressures higher than the nominal pressures because as it was indicated several times in this chapter, it is the effective contact pressures between strands that determine the overall behavior of a full size cable.

The design and the measurement technique of our new experiment are unique making the work of this thesis challenging but also very stimulating. In addition, these experiments are the only one performed on sub-sized cables since the work done more than 20 years ago [2.40-2.41]. Chapter 3 and Chapter 4 describe two experimental setups developed to perform several experiments on various cables including different strands types and different sizes. In Chapters 5 and 6 the experimental results are discussed and a new model is presented and correlated with the measured results. Contact mechanics is used to evaluate the real contact pressure among strands and used to estimate the effective contact pressure. It will be shown that locally the pressures experienced by the strands can go well beyond the averaged pressure of 10-20 MPa making the performance of a full size cable more vulnerable to the natural Lorentz load developed during operation.

CHAPTER 3:
Single turn experimental setup and results

3.1 Introduction

In this chapter a detailed description of the single turn experimental setup is presented. The goal of this experiment is to measure the effect of transverse load on the critical current of a 36 strands superconducting cable. The load is applied mechanically by pulling a conical wedge that expands a collet which, ultimately, applies the transverse load on the cable located between the collet and an external ring (see Fig. 3.1). A load cell was mounted outside the dewar to measure the vertical load applied to move the conical wedge upward. This force can be easily related to the actual force applied to the cable by geometrical analysis. The components of the probe used for the experiments are described in detail and the measurement technique is presented. The experimental results are presented and discussed.

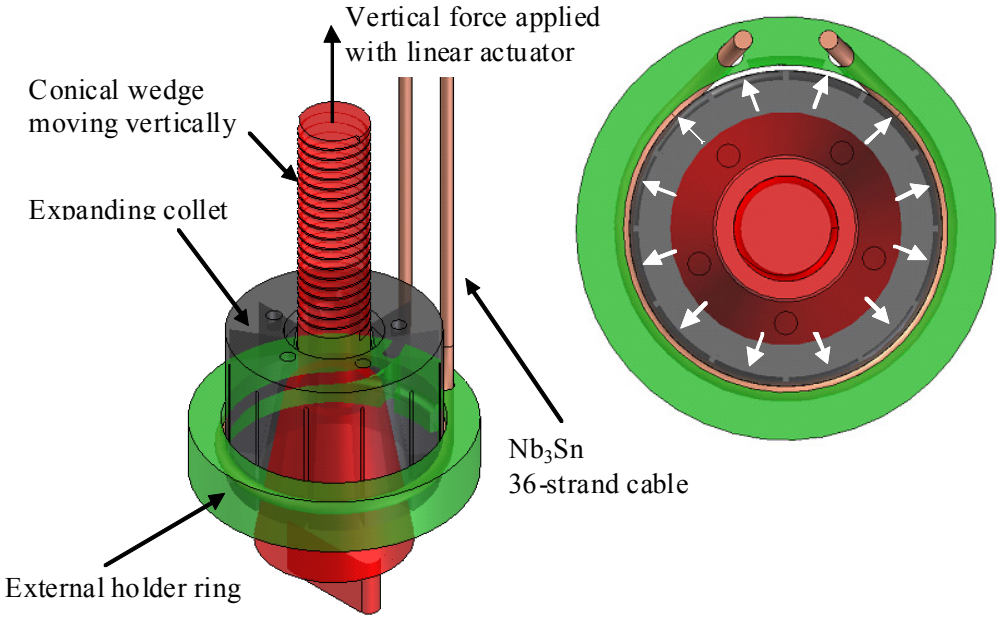

Fig. 3.1 Schematic view of the single turn test rig used inside a 20 T, 195 mm diameter bore magnet: main parts (left), expected load distribution during the experiment (right).

3.2 System requirements and probe description

Four different samples were tested with this experimental setup over four different campaigns from October 2005 to Jan 2007).

The probe used in this experiment was modified from a previous experimental work [3.1]. Minor modifications were required to increase the strength of the supporting rods of the probe itself. The rods were designed to sustain a 100 kN vertical load. The probe and its main components are shown in Fig. 3.2 with it main components.

In Fig. 3.2 the sample area and the linear actuator area are indicated. A long shaft connects the sample area to the linear actuator that is used to vertically move the conical

wedge that applies the transverse load onto the sample. The linear actuator is moved by using a motor drive. The motor allows for remote application of the displacement without being close to the current leads and for a better control of the applied displacement. A load cell is mounted between the linear actuator and the rod connected to the sample to measure the absolute vertical force applied during the experiment.

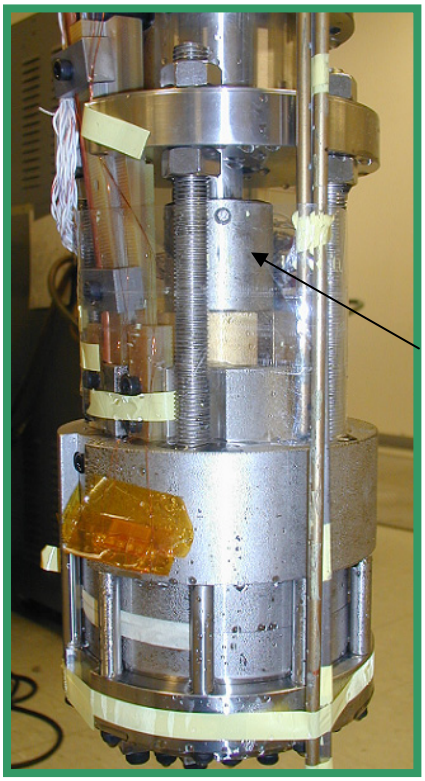

Room temperature 10 kA current lead terminations connected to the current supply. The sample is soldered to the 10 kA current leads inside the cryostat.

Connection point between conical wedge and rod, connected to linear actuator

Fig. 3.2 Probe before being inserted in the cryostat and details of the sample area and the linear actuator area.

The sample is soldered to the 10 kA current leads mounted on the probe. The current leads sit in liquid helium and helium gas. The terminations of the current leads are outside the cryostat at room temperature where they are connected to the current leads from the power supply. Fig.3.3 is a schematic representation of the circuit used during the experiment.

Once the cables were mounted on the probe, it was inserted inside a cryostat (170 mm in diameter) that is positioned inside a 20 T, 195 mm warm bore Bitter magnet (Fig. 3.4-3.5) at the NHMFL facility in Tallahassee, FL.

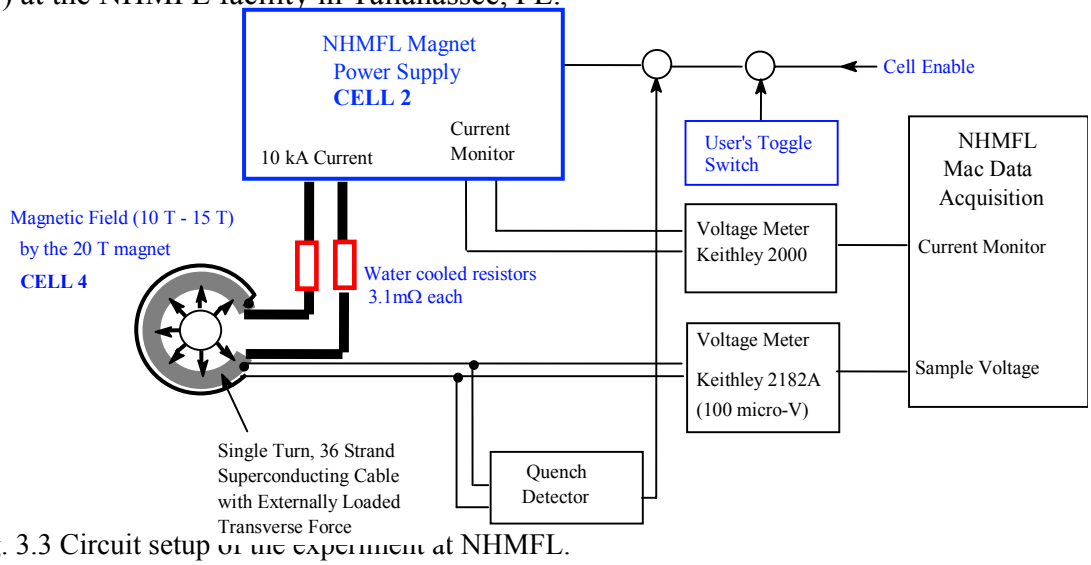

Fig. 3.3 Circuit setup of the experiment at NHMFL.

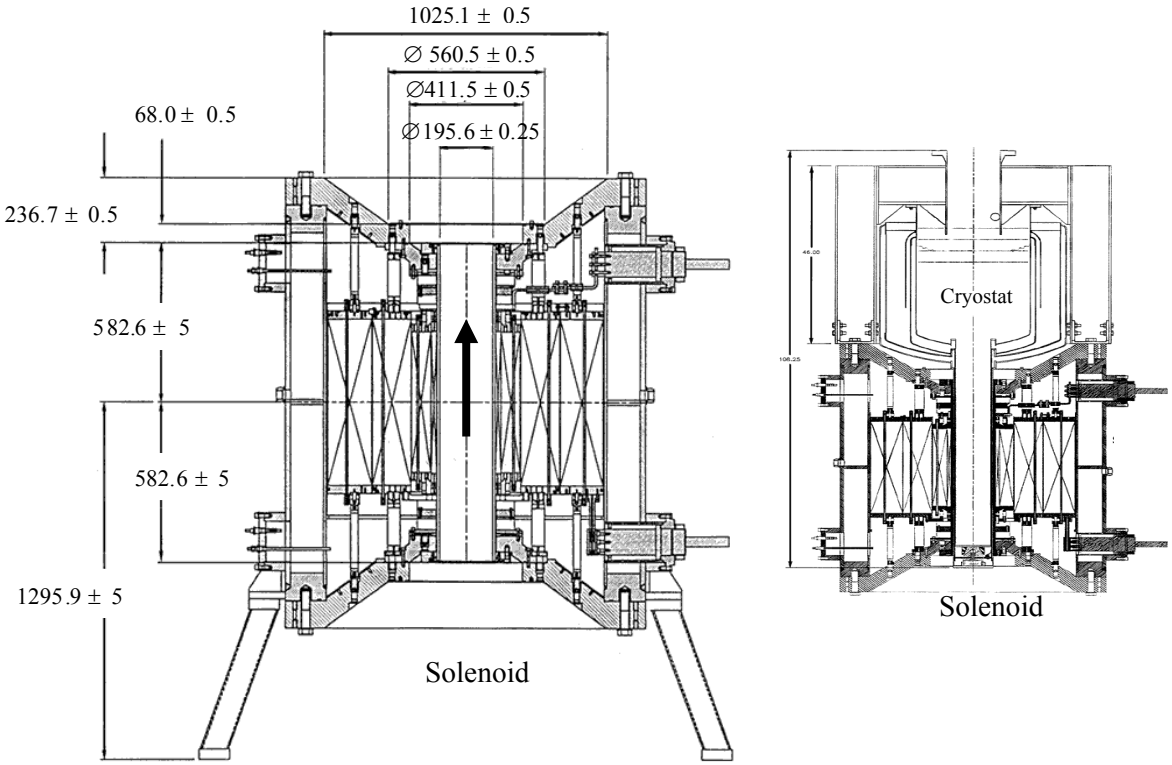

Fig. 3.4 System used for the single turn experiments: 20 T Bitter magnet (left), with the cryostat (right).

Fig. 3.5 Experiment setup. Data acquisition system and instrumentation used (top), current leads and position of water cooled resistors (bottom).

3.3 Sample area structure

The probe head where the superconducting cable is mounted is the most critical component to design and has to comply with the sample test requirements. Fig. 3.6 is a cross section of the sample area with all the different components used. The bulk of the components have the purpose of supporting the probe and avoiding damage to the fragile sample.

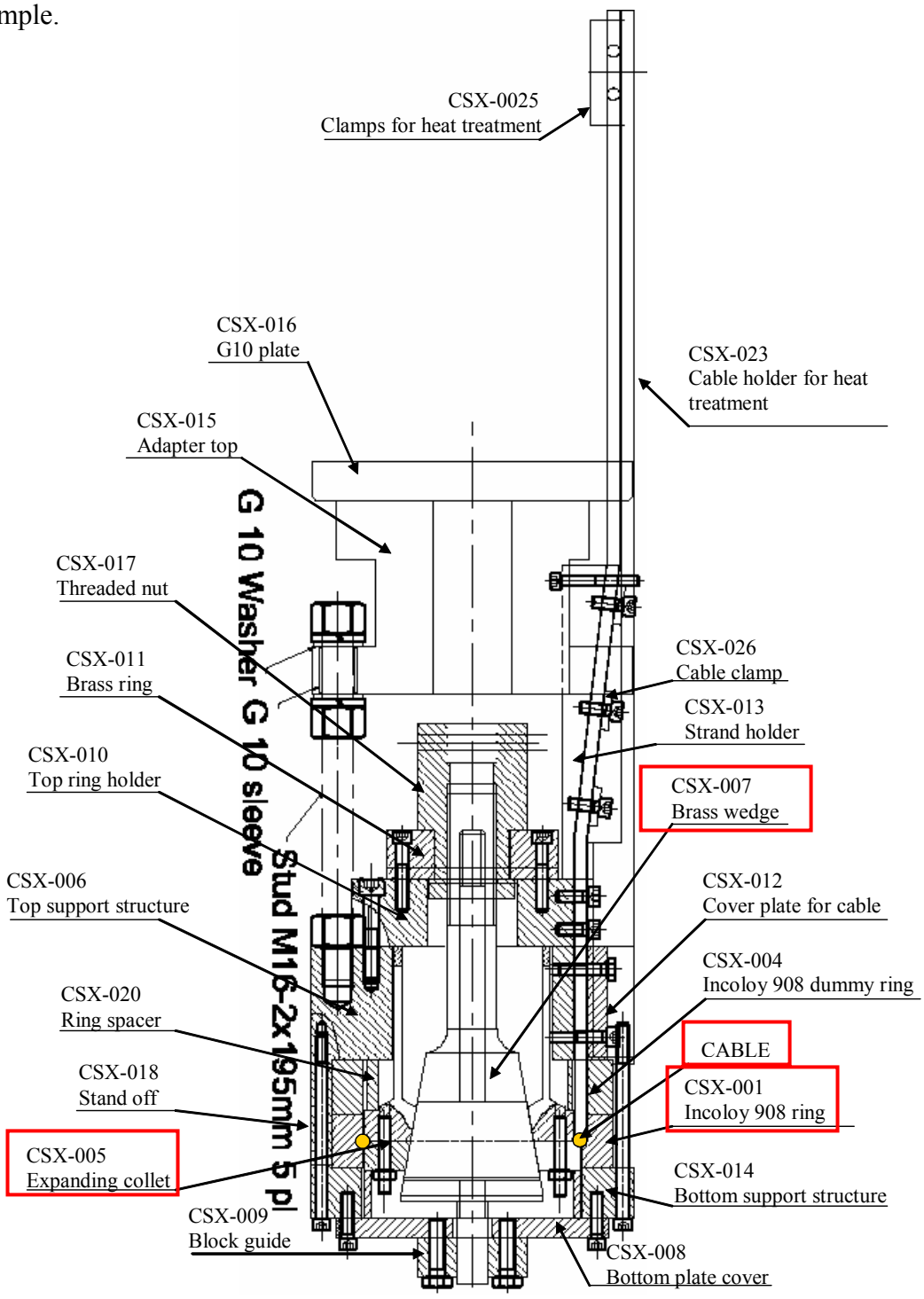

Fig. 3.6 Cross-section of the probe head structure used for the experiment.

The cable is enclosed in between a sample holder ring (referred to as outer ring CSX-001) and a stainless steel collet-type or ring (referred to as inner ring CSX-005). The inner ring can expand when the conical wedge slides vertically upward (CSX-007). Details of the components can be seen in the photographs shown in Figs. 3.7(a)-3.7(e), taken during the assembly of the first sample.

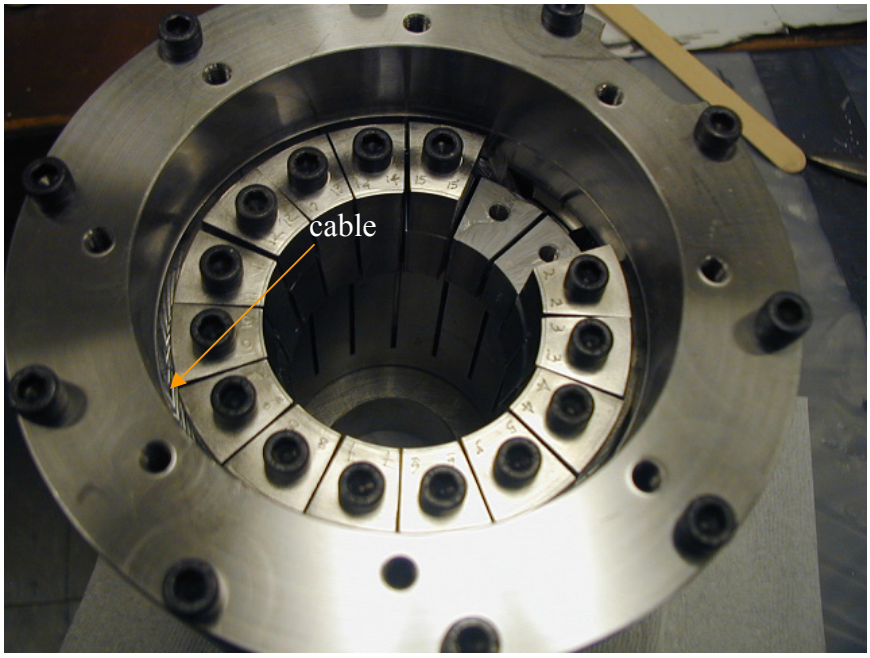

(a)

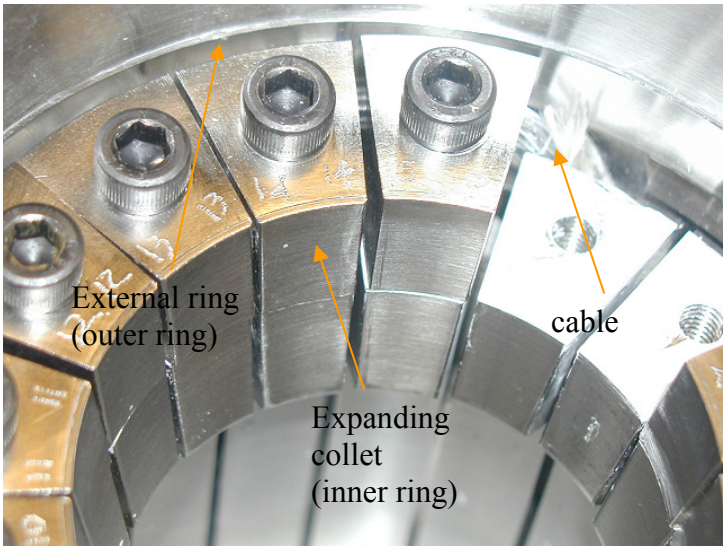

(b)

Fig. 3.7 (a) Structure seen from the bottom. The cable is between an external ring and the expanding collet. (b) Detail of the expanding collet and the enclosed cable.

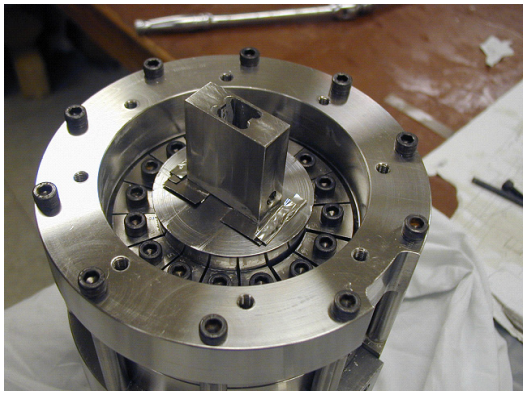

(c)

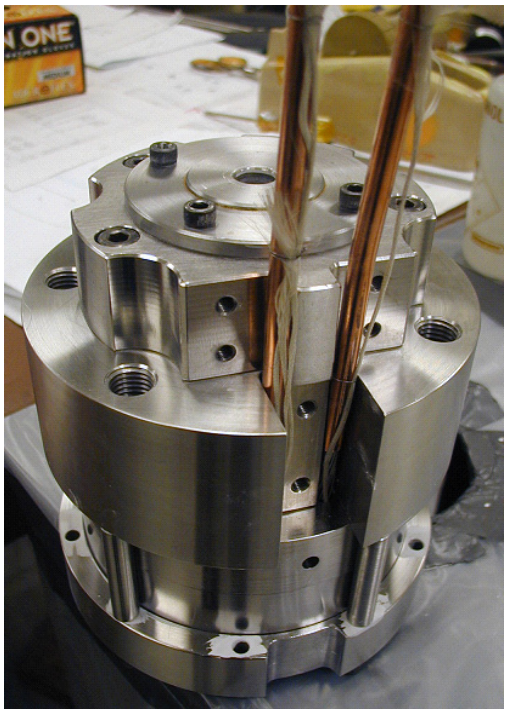

(d)

(e)

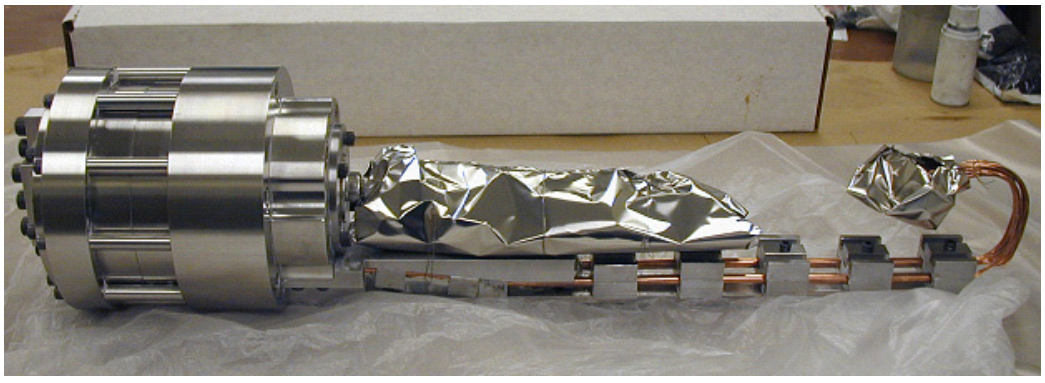

Fig. 3.7 (c) Stainless steel cone used during heat treatment to maintain the proper void fraction of the cable. (d) Cable mounted and detail about how the cable comes out of the structure. (e) Sample and structure ready before heat treatment.

The probe design was dictated by several constraints:

- Maximum inner diameter of dewar at NHMFL is 170 mm.

This constraint is met by designing the probe head with a maximum diameter of 166 mm. This constraint was not as challenging as other problems but it greatly limited the dimension of the cable which is a single turn with maximum length of 350 mm. A longer cable inside the groove would have made it easier to measure the signals from the voltage taps.

- Materials should be used for both heat treatment and test.

This requirement is dictated from the fact that Nb_3Sn material becomes very brittle after heat treatment and any handling should be avoided. In our experiments very few parts (stainless steel) needed to be removed (CSX-025, CSX-023, CSX-026) or substituted with G10 parts (CSX-013, CSX-012) and brass (CSX-007) after heat treatment. Those changes were necessary to be able to mount and solder the sample on the probe.

- Materials used should be non-magnetic.

The presence of any magnetic material could distort the uniform magnetic field seen by the sample once it is inserted in the solenoid. The first two samples tested used Incoloy Alloy 908® while the third and fourth sample were enclosed in Haynes 242.

- The materials enclosing the cable should have a similar coefficient of expansion (COE) of the cable itself.

If the materials used have a larger or smaller COE, this could create an initial strain condition on the cable and reduce its initial performance. Fig. 3.8 shows the materials available considering thermal expansion and strength requirements. From this selection the best choices to better match the thermal expansion of Nb_3Sn are titanium (and titanium alloys), Haynes 242 and Incoloy Alloy 908®. Generally a CICC is enclosed in stainless steel conduit (high strength material) but this implies accepting a ~0.5% initial axial strain on the cable that greatly reduces its performance (Nb_3Sn can carry 30-50% less current under those conditions). In our experiments we are mostly interested in studying the degradation caused by a force applied directly on the bare cable so that all our samples are enclosed by a supporting structure but the application of the force is directly on the Nb_3Sn and not on a conduit. The first two samples were mounted in an Incoloy Alloy 908® external ring. Despite being magnetic its cryogenic mechanical properties are desirable. The last two samples used Haynes 242 external ring. Haynes is not magnetic and it has strength properties similar to Incoloy.

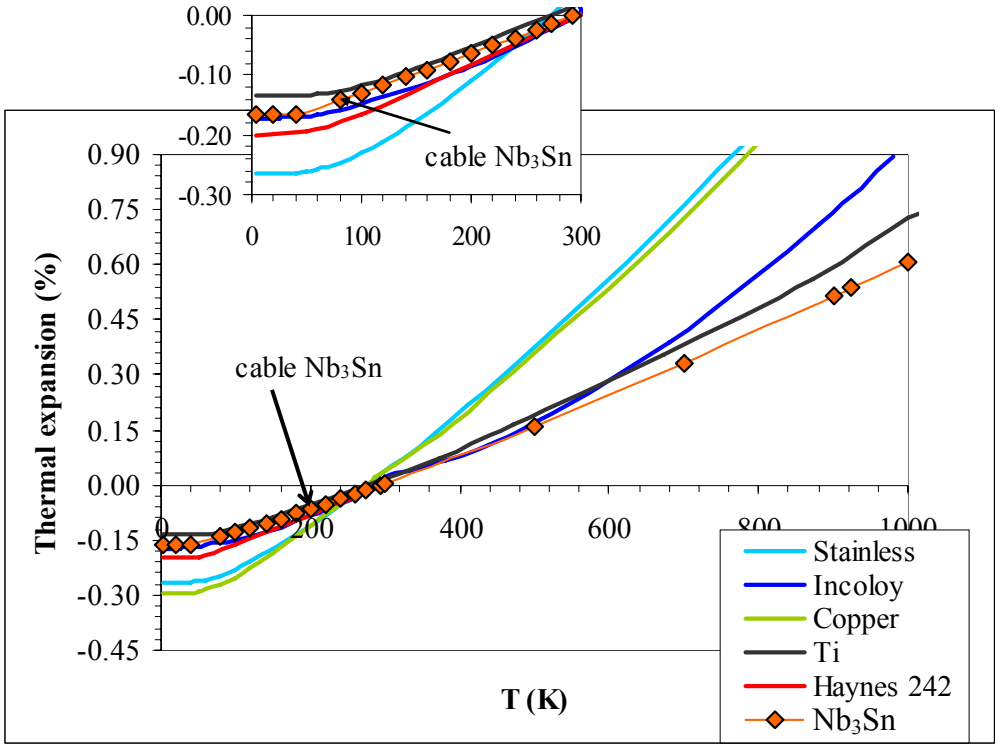

Fig. 3.8 Coefficient of thermal expansion of different materials as a function of temperature. The range of interest is between 1000 K (highest temperature reached during heat treatment) and 4.2 K (typical temperature of operation).

- The materials enclosing the cable have to be dimensionally precise to create the right void fraction before heat treatment.

CICC cables used for fusion experiments generally have void fraction between 32-37%. It was shown [3.2-3.3] that below this range the strands could be locally damaged and deformed. Above this range the strands are not supported enough when the Lorentz load act on them causing very high initial degradation.

- The expanding collet needs to be flexible enough to apply the desired load.

The material chosen for this part is stainless steel 316. The collet is slit in multiple sections (16-18) to enhance its flexibility during the experiment.

- The external ring enclosing the cable needs to be a special material so that it is possible to make measurements with strain gages but also not create too much axial strain to the test sample.

For equally applied strain, the degradation of the current due to the transverse strain is much higher than for longitudinal strain. In order to study a pure transverse effect on the cable, it is necessary to make sure that the level of transverse strain is below the level at which the longitudinal strain is important. From Fig. 3.9, it is clear that the degradation due to longitudinal strain becomes important for strain variation on the order of 10^{-3} [3.4]. If the strain level is kept at a factor of ten lower than this, the main cause of degradation

of the critical current will be the transverse strain. Otherwise, it could be very complicated to interpret the results and separate the components due to the two effects.

The longitudinal strain in this design is the hoop strain effect. The strain is measured by strain gages positioned on the external ring. Thus it is necessary to have strain values higher than 10^{-6} in order to be detected but lower than 10^{-3} to avoid longitudinal effect (Fig. 3.8). In fact, if the strain variation created by the hoop effect is low ($<3\cdot10^{-4}$) the degradation due to the axial effect will be negligible (less than 1%) and any degradation of critical current could be interpreted as transverse load effect.

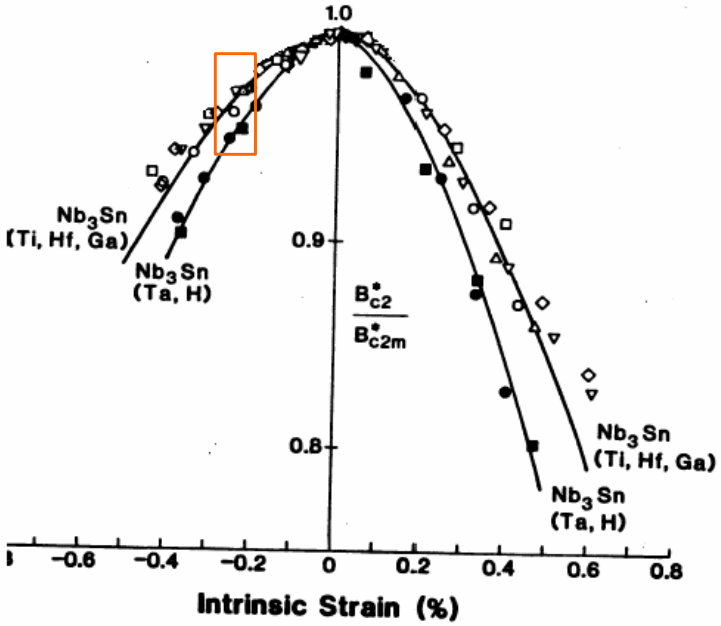

Fig. 3.9 Critical current variation as a function of uni-axial longitudinal strain applied. The orange rectangle represents the limits in which the axial contribution to the degradation has to lie in order to consider the transverse load effect as the dominant effect [3.4].

To limit the hoop tension to acceptable values, the external ring has to be thick enough and have a high Young's modulus. This is the reason why the material chosen for this part was Incoloy Alloy 908® or Haynes 242.

3.4 Sample fabrication

One of the most difficult challenges of this experimental setup has been the sample fabrication. All the samples tested showed an initial degradation so each subsequent sample has been fabricated in a more careful and detailed manner. In this section the main characteristics are discussed leaving the details to Appendix I.

The cable was wound with a cabling machine in our laboratory in 3 stages (3x3x4). The cable is equipped with voltage taps to measure the transition from superconducting to normal state during the test. The voltage taps were thin stainless steel wires covered by a fiber glass sleeve. Once the cable is mounted between the external ring and the expanding collet, it cannot be removed or touched after heat treatment. For this reason, the insulation of the voltage tap wire is made of fiber glass which is an insulating material

that can withstand the high temperatures (660 °C) reached during heat treatment. The stainless steel wire is embedded in between the stages of the cable so that it does not lie on the surface of the cable (Fig. 3.10). Once the stainless steel wires are firm in their positions the fiber glass sleeve is added to the wires. One of the two wires is wrapped around the cable and positioned in between voids left by the different sub-stages of the cable (there are 4 visible triplets). A thin stainless steel wire is wrapped at the same time, with opposite twist, to hold the wire and fiber glass in position. This wire is brought on the opposite side of the cable to eliminate any inductive voltage pickup during the experiment. Once it reaches the other side and the other wire, the two wires are twisted together again to reduce any inductive signal.

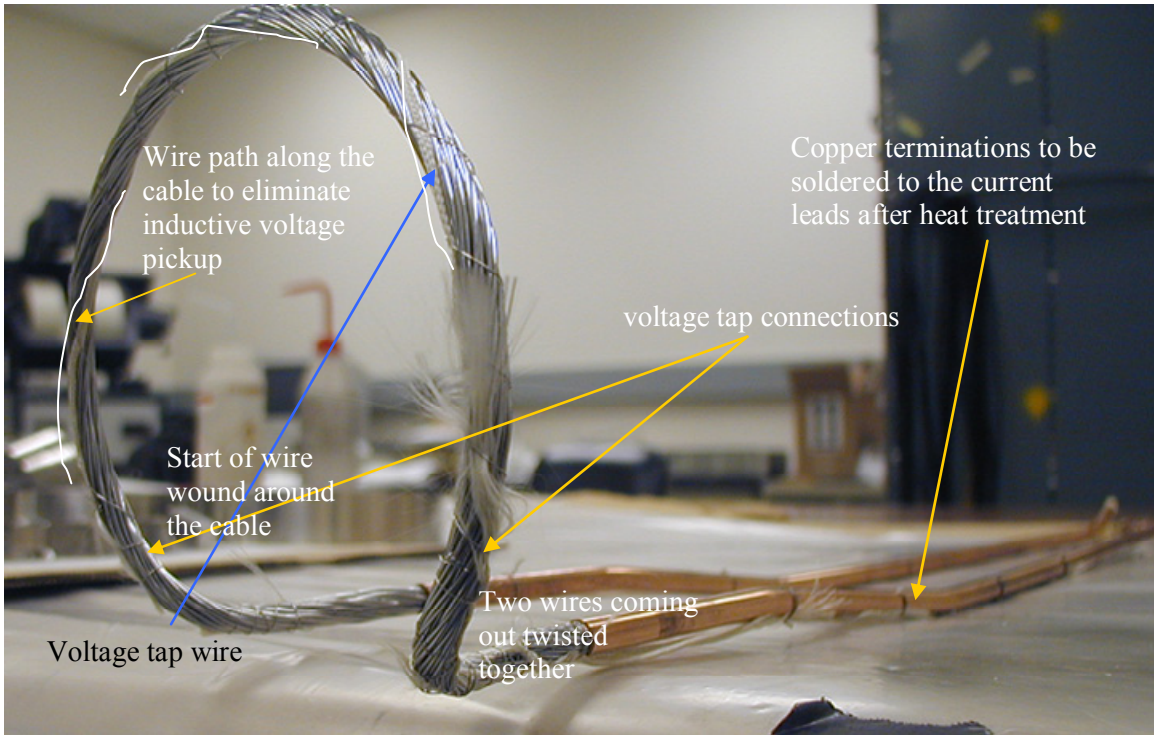

Fig. 3.10 Cable prepared for mounting. Voltage taps wires are visible (one of which is wrapped around the cable to eliminate inductive voltage pickup).

The straight section of the cable was enclosed in a copper tube swaged down to 7.5 mm diameter so that it fits the current lead slots. The copper sheath was added to protect the cable during the soldering of this section on the current leads connection after heat treatment (Fig. 3.11). Moreover, soldering was more easily done on copper.

The copper tube was swaged in steps starting from a die of 0.361 inches in diameter and diminishing with dies of 0.338, 0.325, 0.3125, and 0.294 inches.

The cable length including the termination legs inserted in the copper tube was roughly 1.6 m (test cable of 335 mm inside the groove, 135x2 mm to reach out of the structure, 465x2 mm to reach the current leads).

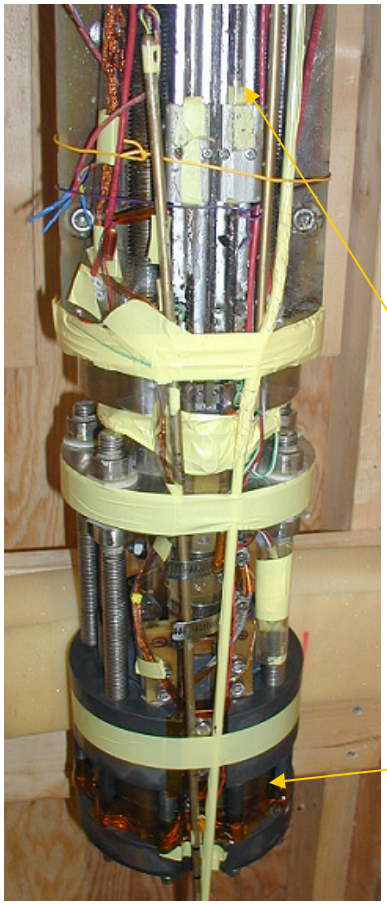

Fig. 3.11 Copper terminations soldered to the current leads connection.

The first sample was prepared applying a manual circular bend and forcing the cable inside the slot where it was supposed to sit. The void fraction of the cable (~ 35%) was reached in subsequent steps using the heat treatment stainless steel wedge. This was set during heat treatment to maintain a 1 mm distance between collet and external ring to reach the desired void fraction and have the necessary space to move the collet transversally against the sample during the test. The stainless steel collet was used to reduce the void fraction of the cable by mounting all the pieces and moving the cone upward as in the experiment and reduce the gap between the collet and the external ring. At this stage if assembly, manipulation of the cable before heat treatment should not jeopardize the superconductor performance because the superconducting filaments are not formed yet. The process was tedious and required a rather large physical strength. After the first sample test the only modification made was to improve the heat transfer characteristic of the probe since the first sample had been accidentally burned out due to a poor cooling condition. The second sample showed a much improved cooling condition but the initial degradation was still observed. With the first two samples the swaging of the copper tubes on the ends was performed once the cable was bent in its final configuration sample (single turn with 90 degree bends) so that we had to feed the two legs one at the time changing feeding direction and causing local de-twisting and relaxation of the cabled sample. With the third sample we decided to be more careful during the swaging process. It was decided to add a tube of titanium around the length of

cable that will be bent after the swaging process. So now the cable has one piece of copper, one of titanium, one of copper and some bare cable in between the three sections. The bare cable length is located at the 90 degree bends. The cable is left straight and fed inside the swaging machine in only one direction to avoid de-twisting of the cable. The copper sections are swaged one extra step compared to the titanium tubing section. The swaged straight cable was then bent into its circular form together with the titanium tube again to avoid any relaxation of the cable and to maintain the desired void fraction. Once the cable was ready in its final form the titanium tube was cut open and removed and the cable inserted inside the structure. Despite the careful operation the cable still showed some degradation (~35%). Thus in the fourth experiment we decided to follow the same operations as the third one but the titanium tube this time covered the entire length in between the two copper sections so that during the preparation of the sample in final form also the 90 degree bends could be maintained with their original void fraction and form. We also decided to remove the titanium only along the tested area (circular bend) but leave the tube where the leads are coming out (90 degree bent area) since we suspected that this was the weakest point of the sample (Fig. 3.12). Yet again the cable showed degradation. The results will be discussed in more detailed in section 3.6.

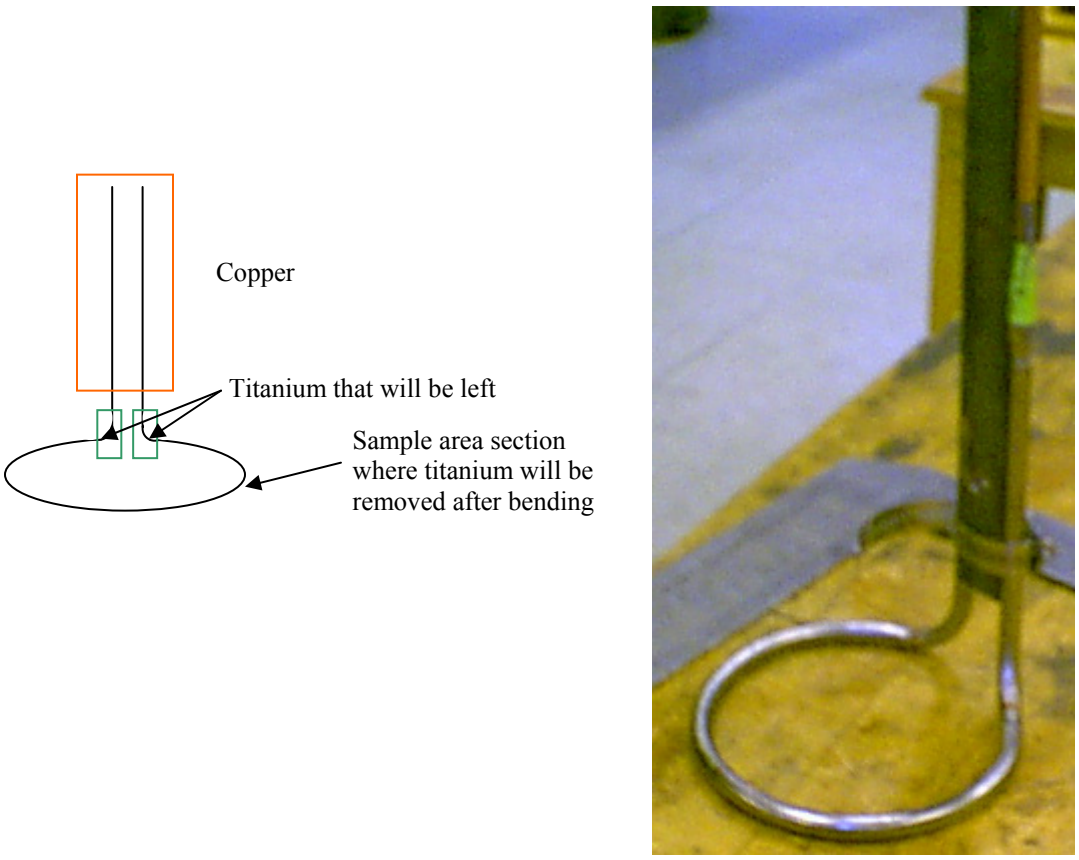

Fig. 3.12 Schematic view of the sample swaging preparation (left). Final stage before removing the titanium from the test length (right).

3.5 Instrumentation

The experimental probe has been equipped with several instrumentation tools. Three different liquid level sensors are used to determine the liquid level during the experiment. These are used to monitor and to maintain the minimum level required for safe operation (entire sample and joints to copper leads immersed in liquid helium). Located outside the cryostat there is a load cell attached to the linear actuator, which applies the vertical displacement to the conical wedge. This load cell records the vertical load applied to the experiment. Disregarding friction effect, this load is used to determine the transverse load applied to the sample by geometrical calculation as shown in Fig. 3.13 and Eq. 3.1.

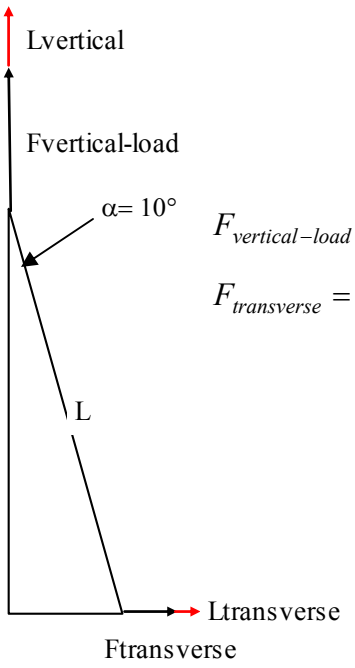

$$F_{vertical-load} \cdot L_{vertical} = F_{transverse} \cdot L_{transverse}$$

$$F_{transverse} = F_{vertical-load} \cdot \frac{L_{vertical}}{L_{transverse}} = F_{vertical-load} \cdot \frac{1}{tan(\alpha)} \qquad (3.1)$$

Fig. 3.13 Schematic view of the forces involved in the experiment and how the transverse force is estimated using geometrical arguments.

The side surface of the external ring holding the sample is equipped with strain gages that provide an additional method to estimate the pressure applied to the sample. While loading the sample, the external ring is under hoop strain that can be measured with strain gages. The collet piece expands radially when the conical wedge is pulled vertically. The collet was originally made with 16 slots but for the last experiment (January 2007) a new collet with 18 slots was used. In the first experiment (October 2005) the collet has been mounted in its original configuration with all the matching finger pieces in place (see Fig. 3.6 and Table 3.1). During this experiment was observed that the strain gages were showing a non linear behavior against the expectation of a uniform hoop tension applied on the external ring during loading. The first modification, applied to the sample tested in January 2006, was to remove two of the finger pieces (Table 3.2). The pieces removed are located where the cable is bent to be connected to the current leads. The bend is perpendicular to the plane of the single turn where the load is applied. It was believed that since the cable is missing in this section, the conical wedge could be prone to move

towards the section where it does not have to apply any load and move freely. Despite this modification (also shown in Table 3.1), the strain gages still showed a non-linear behavior (Fig. 3.14).

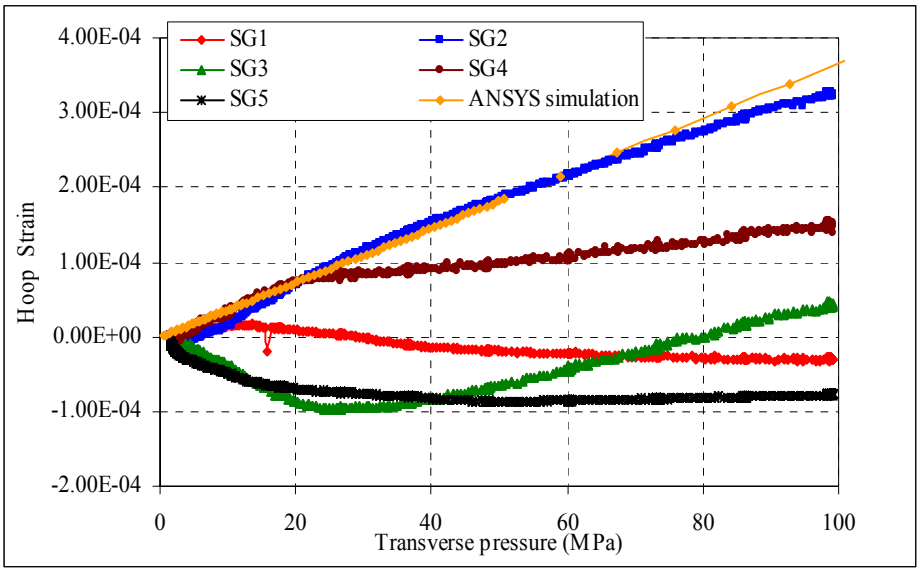

Fig. 3.14 ANSYS® simulation of expected values of hoop strain on the Incoloy Alloy 908® ring compared with measurements taken with the strain gages.

It was then decided to apply the load with a 3-points load configuration as shown in Table 3.3. This method of applying load should give a more uniform load distribution at the cost of applying load only on 3 sections of the sample and not the entire length. The analysis in Appendix II shows how this modification does not affect the sensitivity of our measurements as long as the appropriate criterion is used to estimate the critical current. With this configuration the strain gages showed a linear behavior and agreed very well with a simplified FEM simulation performed with ANSYS® (Fig. 3.15).

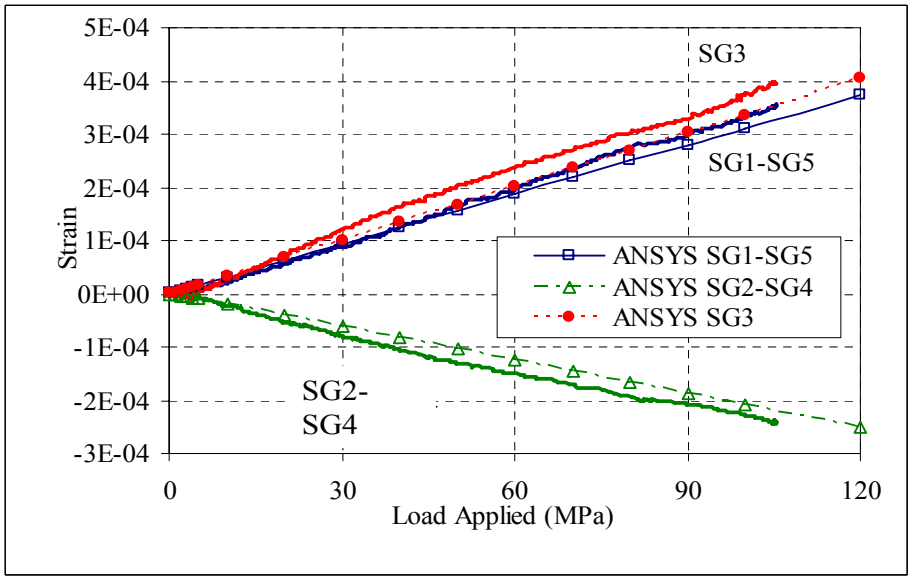

Fig. 3.15 Comparison of measured strain (solid lines) and FEM simulations (symbols) using the 3 point contact method.

The fourth sample tested on January 2007 was prepared in a very similar way to the third sample but the titanium tube used for swaging was left in position on the bends to increase the support in this area. A new collet was fabricated having 18 slots instead of 16 so that the three pressed sections were equally long (Table 3.4). The strain gages data showed a similar behavior to the previous test indicating indeed a more uniform and controlled loading process.

All the samples have at least 3 voltage taps located in different position of the sample (Table 3.1). The voltage taps are used to record the voltage across the sample that is used to estimate the critical current and n-value of the superconducting cable. The first sample showed large inductive voltages signals because not all the voltage samples were mounted appropriately. In all the other samples the voltage taps were carefully twisted and wound along the sample to reduce inductive pick up during the experiment.

Table 3.1 IGC sample loading, strain gages and voltage taps configuration.

IGC sample tested October 2005	
Strain gage configuration	Voltage taps configuration
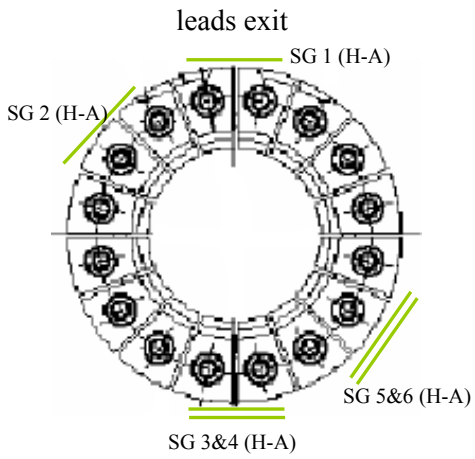	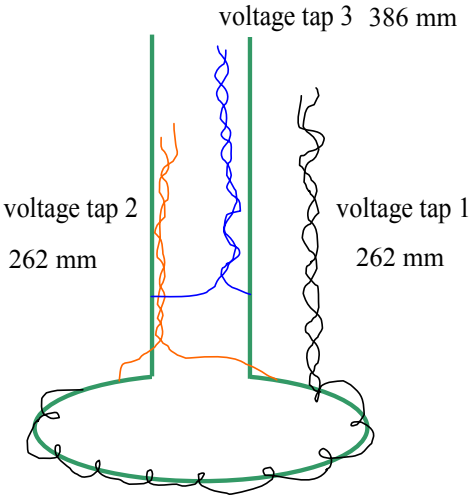

Table 3.2 Second IGC sample loading, strain gages and voltage taps configuration.

IGC sample tested January 2006	
Strain gage configuration	Voltage taps configuration
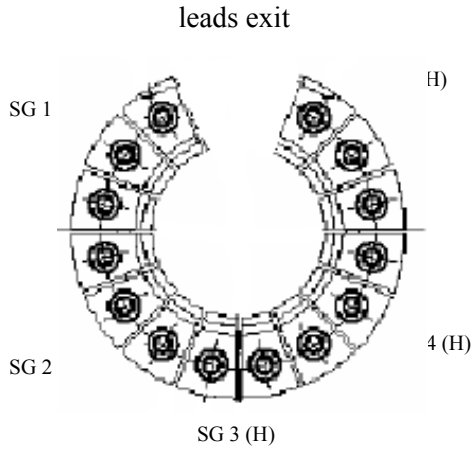	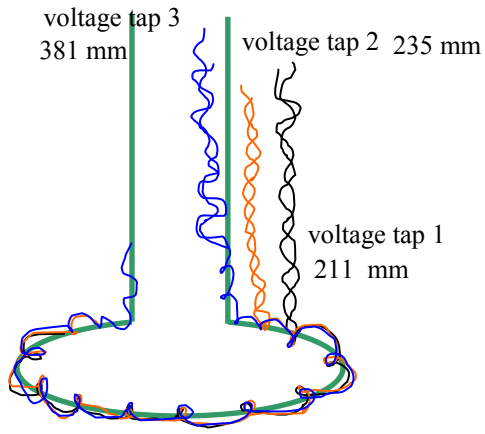

Table 3 OKAS sample loading, strain gages and voltage taps configuration.

OKAS sample tested July 2006	
Strain gage configuration	Voltage taps configuration
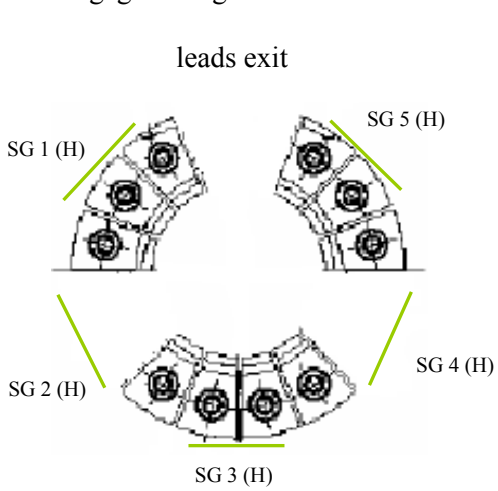	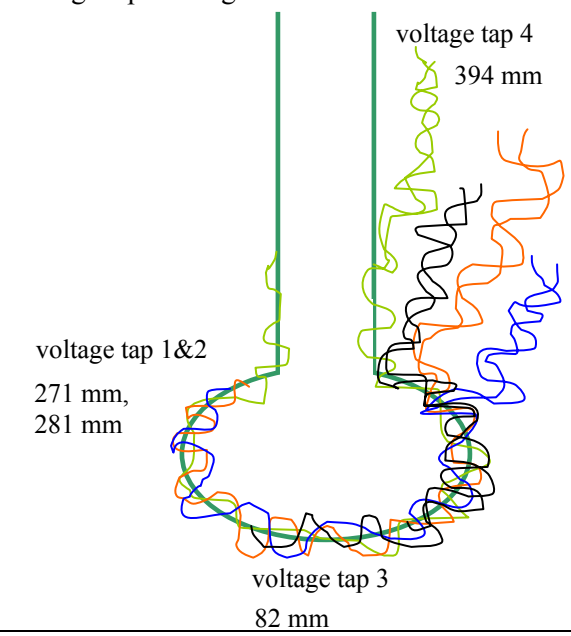

Table 3.4 OXFORD sample loading, strain gages and voltage taps configuration.

OXFORD sample tested January 2007	
Strain gage configuration	Voltage taps configuration
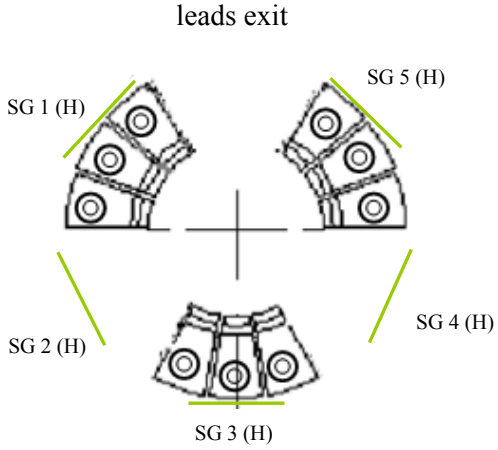	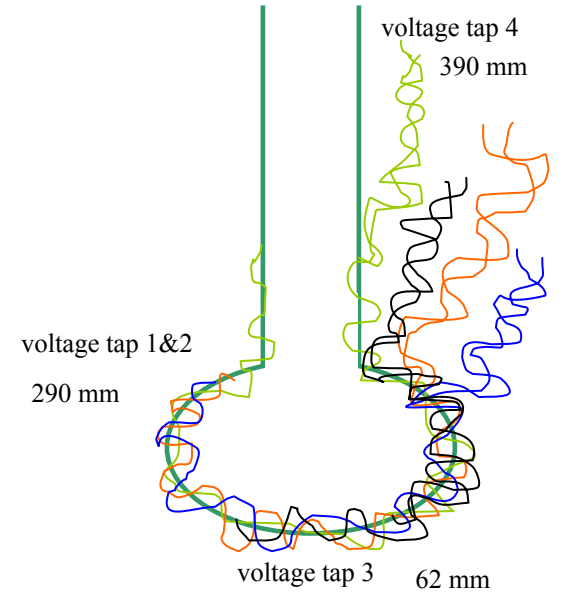

With the last three samples, an extensometer was added at the bottom of the conical wedge to have a direct measurement of the vertical displacement applied to it and to estimate with those values the displacement in the transverse direction. This information was used to estimate the Young's modulus of the cable as discussed in the following section.

3.6 Experimental results and discussion

Three different wires were used for the four samples tested. The first two samples were made with the same wire (IGC), the third sample used OKAS wire, while the last sample used Oxford wire. All the samples have the same cable pattern 3x3x4 with twist pitches of 45 mm, 85 mm and 125 mm for the three stages, respectively. The wire used for all experiments is internal tin type. An example is shown in Fig. 3.16. The main properties as given by the manufacturers are given in Table 3.5.

Table 3.5 Main properties of the wire used in the experiments.

October 2005, January 2006 samples	
Strand manufacturer	IGC
Strand Type	Internal Tin
Filament Material	Nb_3Sn
J_c (12 T, 4.2 K)	682 A/mm^2
Diameter	0.808 mm
Copper/non-copper ratio	1.5:1
Number of strands	36
Average cable diameter	6.25 mm
Cable pattern	3x3x4
July 2006 samples	
Strand manufacturer	OKAS
Strand Type	Internal Tin
Filament Material	Nb_3Sn
J_c (12 T, 4.2 K)	856 A/mm^2
Diameter	0.832 mm
Copper/non-copper ratio	1.18:1
Number of strands	36
Average cable diameter	6.25 mm
Cable pattern	3x3x4
January 2007 samples	
Strand manufacturer	Oxford
Strand Type	Internal Tin
Filament Material	Nb_3Sn
J_c (12 T, 4.2 K)	1037 A/mm^2
Diameter	0.83 mm
Copper/non-copper ratio	1.1:1
Number of strands	36
Average cable diameter	6.25 mm
Cable pattern	3x3x4

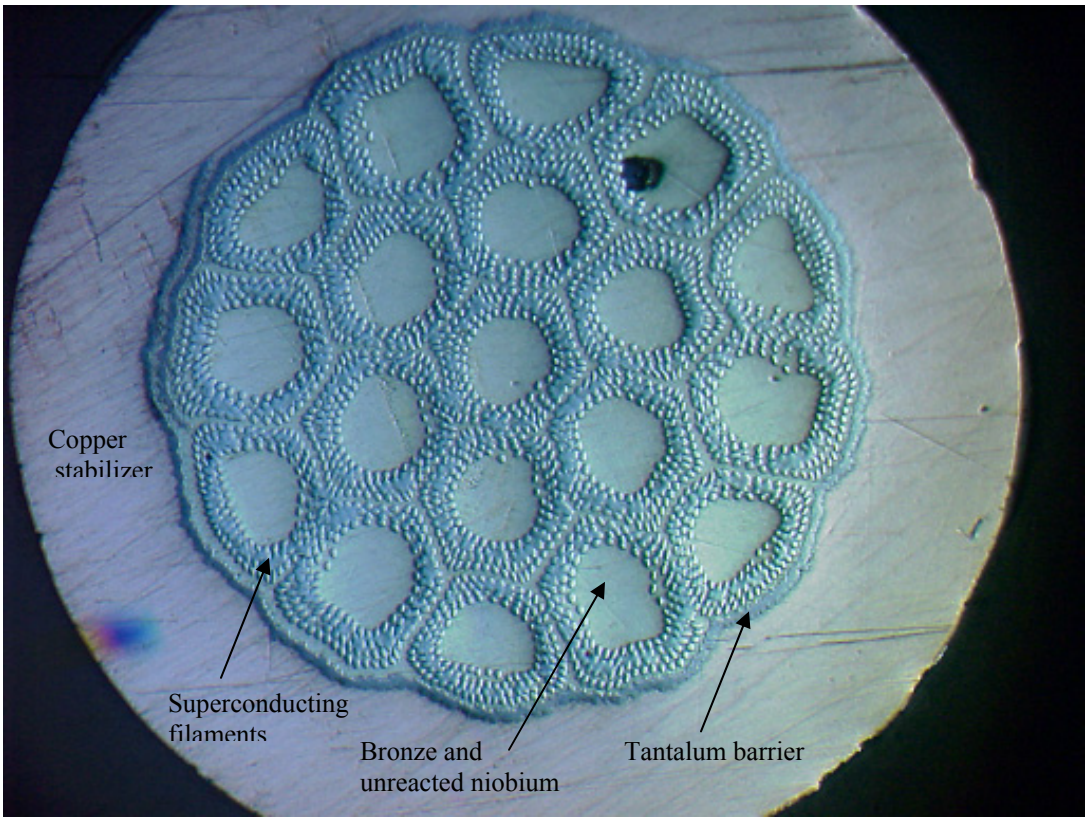

Fig. 3.16 Typical internal tin wire cross section (Oxford wire).

Typically the manufacturer provides data for the critical current at a certain field (12 T) and the n-value of the strand. The n-value represents the sharpness of the transition (described by Eq. 3.2) from superconducting to resistive state.

$$\left(\frac{E}{E_c}\right)=\left(\frac{E\cdot l_{voltagetap}}{E_c\cdot l_{voltagetap}}\right)=\left(\frac{V}{V_c}\right)=\left(\frac{I}{I_c}\right)^n \qquad (3.2)$$

where the quantities with subscript c are critical properties defined prior to the experiment, E and V being electric field and voltage across the sample (the product of electric field by the length of the voltage tap). Typical critical electric field criteria values are 10 and 100 μV/m. During an experiment the temperature is set at 4.2 K and the field is fixed at a certain level. The sample is charged up and the currents corresponding to the electric field of those values are the critical currents for a particular sample. With two values of current and voltages it is possible to evaluate the n-value. Generally the voltage is measured as a function of current and natural logarithm of both quantities is evaluated to estimate the n-value (slope of linear fit) which is then used to determine the critical current at the two established current criteria (Fig. 3.17).

It is practice to heat treat a sample on a standard barrel together with the test cable. This single strand witness sample is measured separately to determine a few points of the critical current-field curve and verify the value given by the manufacturer. This critical current curve is also used to evaluate the expected critical current for a cable (critical

current of a single strand multiplied by the number of strands). In Fig. 3.18 the critical currents of all the strands used in our experiments are shown as a function of the field. Points between 11 and 13 T are experimental values while the others are typically extrapolated values. In Fig. 3.18 there are 3 curves corresponding to the Oxford wire. The one labeled Oxford is from a strand that followed the same heat treatment as given by the manufacturer but it is not corresponding to a witness sample. The curves labeled Oxford CS and Oxford TF correspond to the witness samples of a cable using the Central Solenoid (CS) and the Toroidal Field (TF) coils strand specification. The Oxford CS wire was used for the last sample tested in January 2007. The Oxford TF wire has been used for the experiments carried out with the second test rig (Chapter 4).

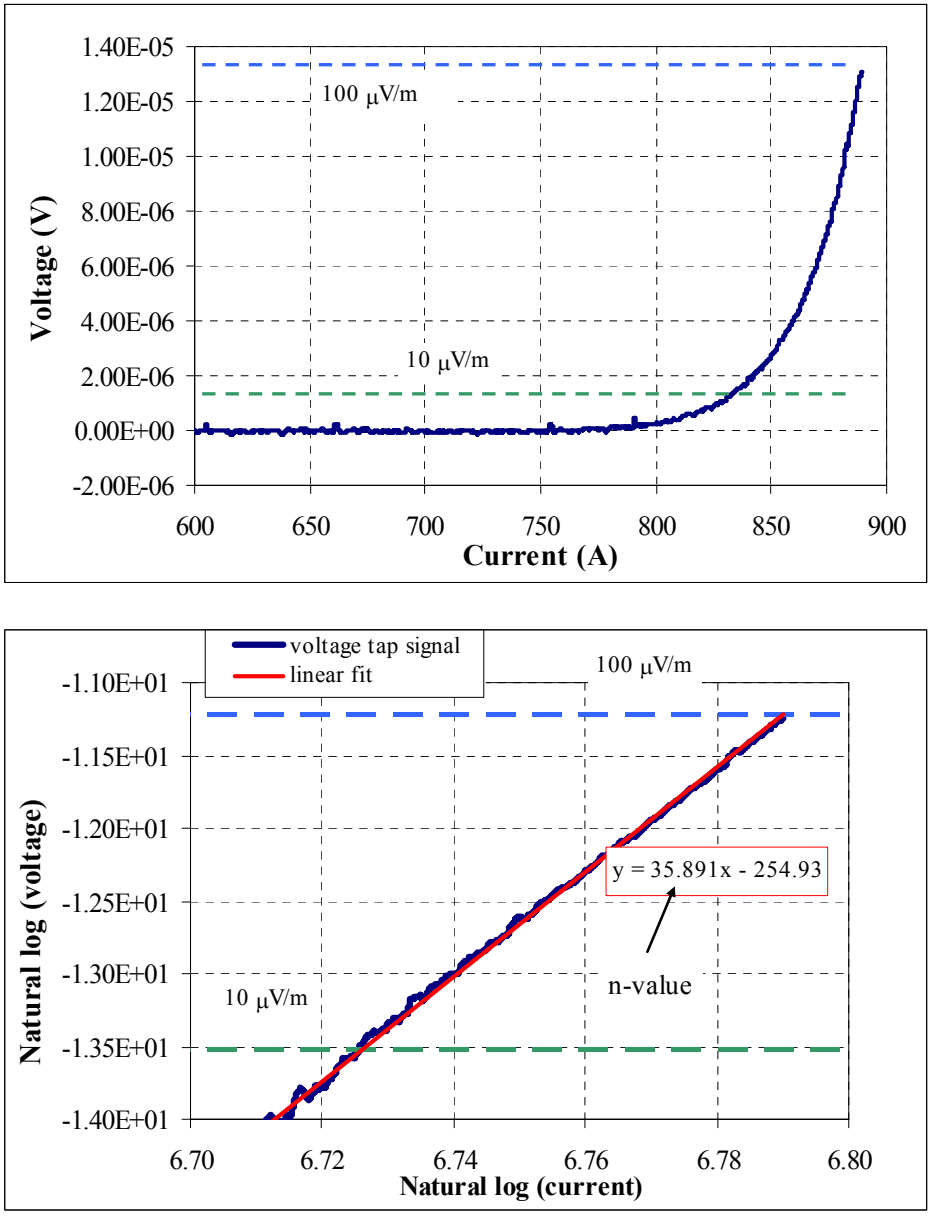

Fig. 3.17 Typical voltage trace recorded during an experiment (top), manipulation of the data to determine the n-value and the critical current values at the two established criteria.

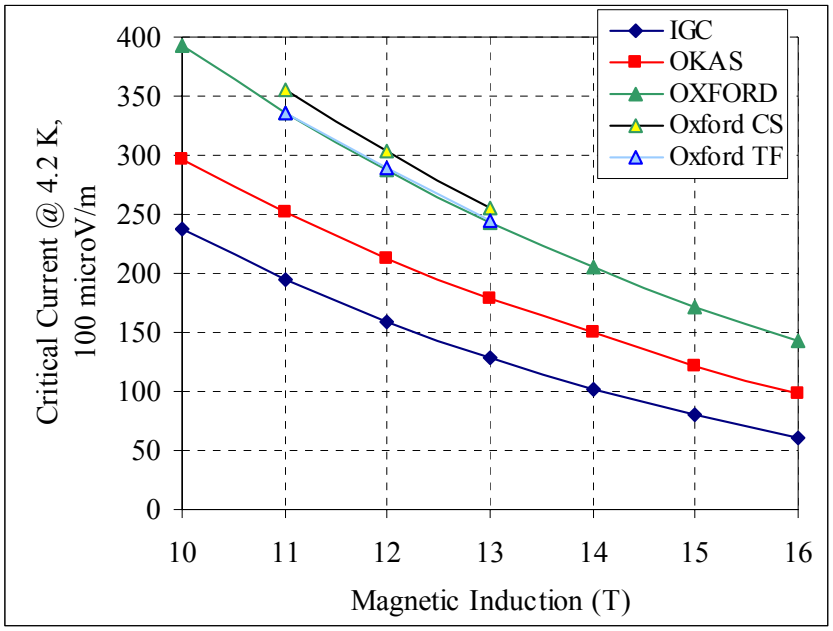

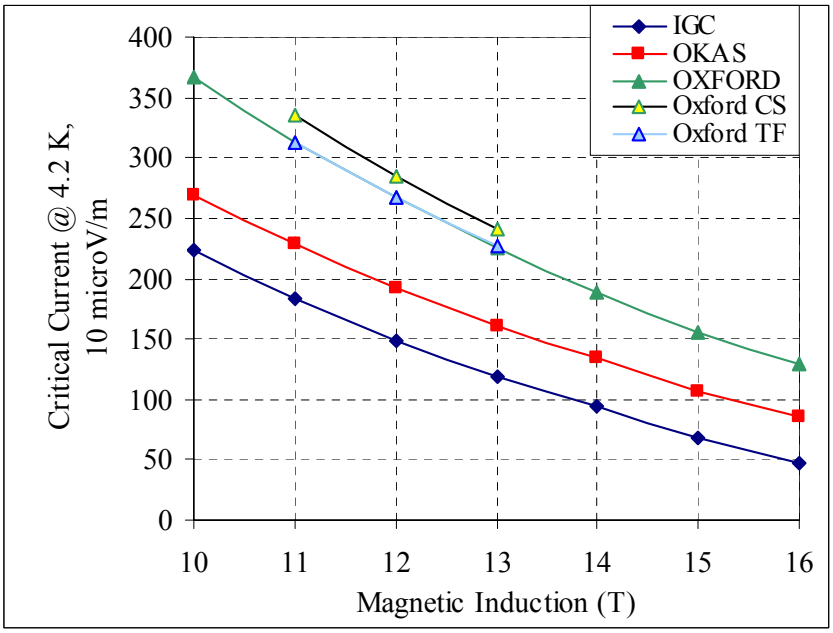

Fig. 3.18 Critical current as a function of magnetic field for single strand samples of the wires used during the experiment. The expected critical value of the cable is simply the product of the number of strands in a cable times the current of one strand.

All the samples were tested inside a dewar located in the bore of a 20 T magnet at NHMFL. Each sample test campaign was allotted a one week time frame generally split between preparation and tests. The tests include a preliminary check of the system, critical current measurements as a function of field and critical current as a function of sequential step loads at a fixed field. The preliminary check helps in debugging the system and assessing the reliability of the voltage taps on the samples. Typically only one voltage tap pair is used during the experiment but usually multiple sets are mounted in

case the chosen one stops working appropriately. While applying the load the voltage tap wires can be damaged if they were not mounted properly.

Fig. 3.19 shows the critical current as a function of the field for all the cables tested. It has to be stated that the field is the nominal field in the center of the bore. At the location of the cable there is a small radial component of the field in addition to the axial. The total effect is an increase in field of roughly 0.2 T which is not adjusted for in this plot.

Additionally for the experiments using the IGC strand the cables are inside an Incoloy Alloy 908® ring which is slightly magnetic. Thus the cable is experiencing a higher magnetic field (~ +0.3 T) than the applied background field.

Even if we had to take in consideration those two effects for the data in Fig. 3.19, it can be seen clearly that all the cables tested would show a similar large initial degradation from their expected single strand value without considering this effect.

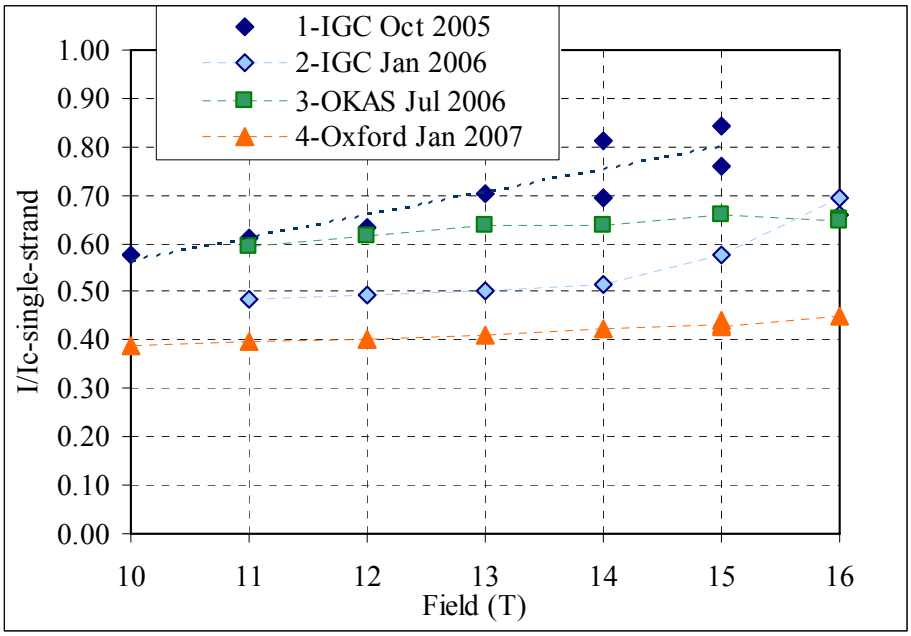

Fig. 3.19 Critical current as a function of field for the different samples tested. Those measurements are done prior applying any mechanical load. The natural Lorentz load is too small too account for any degradation (< 6 MPa). In this plot the radial component of the field and the additional field caused by the Incoloy Alloy 980® are not taken in account.

It was believed that the first two samples exhibited low performance due to the higher void fraction than the desired 35%. The third sample was carefully cabled and pre-swaged to obtain a better void fraction and it showed an encouraging improvement with respect to the second sample. Following the same procedure for the fourth sample and improving the overall support did not show any further improvement. On the contrary, it showed the worst performance.

We tried everything possible to minimize the damage during the fabrication process (before and after heat treatment), we could not determine the causes of this initial degradation. One possible explanation is that the current sharing between copper leads and sample was extremely low even if the resistance of the joints was in the nΩ range.

Despite those horrific results, the test plan was carried out and transverse load was applied to the sample in multiple steps. The first sample lacked good cooling condition

and was permanently damaged before applying any considerable load. During the second experiment it was possible to load the sample to the desired pressure but the sample was not cycled more than once. The third and fourth samples were loaded multiple times with the experience gained from the first two sample tests helping us to improve efficiency and productivity of the last two sample tests.

The results for the last three samples are shown in Fig. 3.20(a-b). It can be seen that the new ITER wires (OKAS and Oxford) are more sensitive to the applied load. Those strands have a much higher critical current density than the other two but seem to be weaker mechanically. Those samples were also loaded in different cycles as shown in Fig. 3.20(b). Once the load was removed the sample recovered but it never went back to the original starting point of the cycle. It is important to notice that the load represents the total load applied to the sample: mechanical load and natural Lorentz load. That is the reason why the starting point is not at zero load.

The load is estimated using Eq. 3.3:

$$\sigma = \frac{F_{transverse}}{Area} = F = \frac{F_{vertical-load} \cdot \frac{1}{tan(\alpha)}}{l_{pressed} \cdot D_{cable}} \tag{3.3}$$

A unique feature of this experimental setup is that the system is equipped with an extensometer that measures the vertical displacement of the conical wedge. This measurement was used to estimate the transverse displacement and calculate the dynamic Young's modulus of the cable defined by Eq. 3.4:

$$E_{transverse} = \left(\frac{D \cdot F_{transverse}}{A_{cable-x\,sec\,tion} \cdot \delta_t} \right) = \left(\frac{D \cdot F_{transverse}}{D \cdot l_{cable} \cdot \delta_t} \right) \tag{3.4}$$

Where D is the nominal cable diameter (6.25 mm), $F_{transverse}$ is the transverse load calculated from the measured vertical load (Eq. 3.1), l_{cable} is the length of the cable inside the sample holder and δ_t is the transverse displacement evaluated with the measured vertical displacement ($\delta_t = \delta_{vertical} \cdot tan(\alpha)$). The results are shown in Fig. 3.21. The very low values of Young's modulus are due to the fact that the cable has a significant void fraction. The Young's modulus reaches a saturation value at high value of force per unit length as previously shown in the literature [3.5] where similar values are observed.

The Young's modulus value is extremely dependent on the transverse displacement which is the most uncertain variable since an offset has to be applied to the vertical displacement measurements. Assuming there can be a 0.5 mm uncertainty on the vertical displacement, the error bars on those data points are of the order of unity as shown in Fig. 3.21.

This uncertainty is caused by the fact that initially the conical wedge is not touching the collet and even if were moving vertically the collet is not expanding. The value of vertical displacement for which the extensometer does not show a linear behavior indicates the conical wedge is not moving freely anymore but it is pushing against the collet.

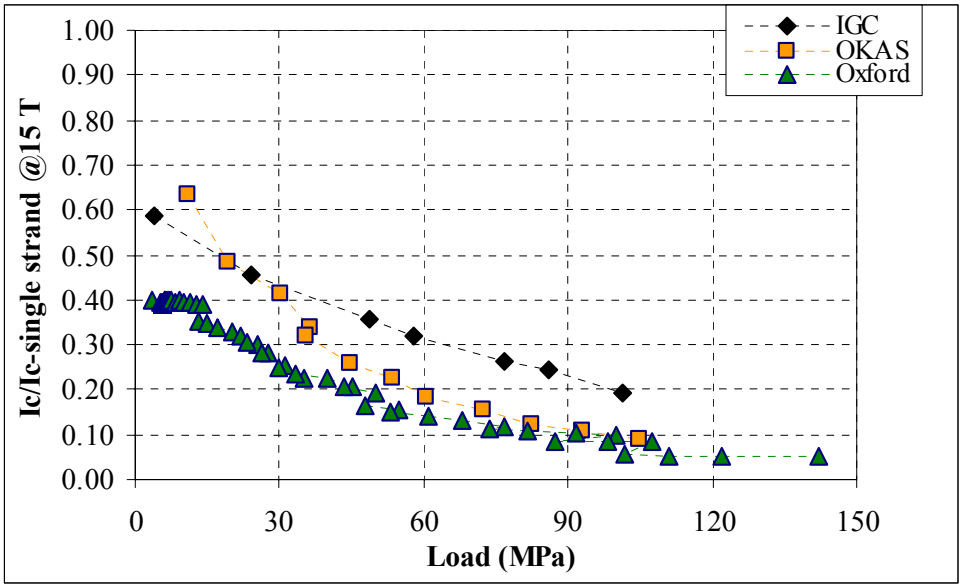

(a)

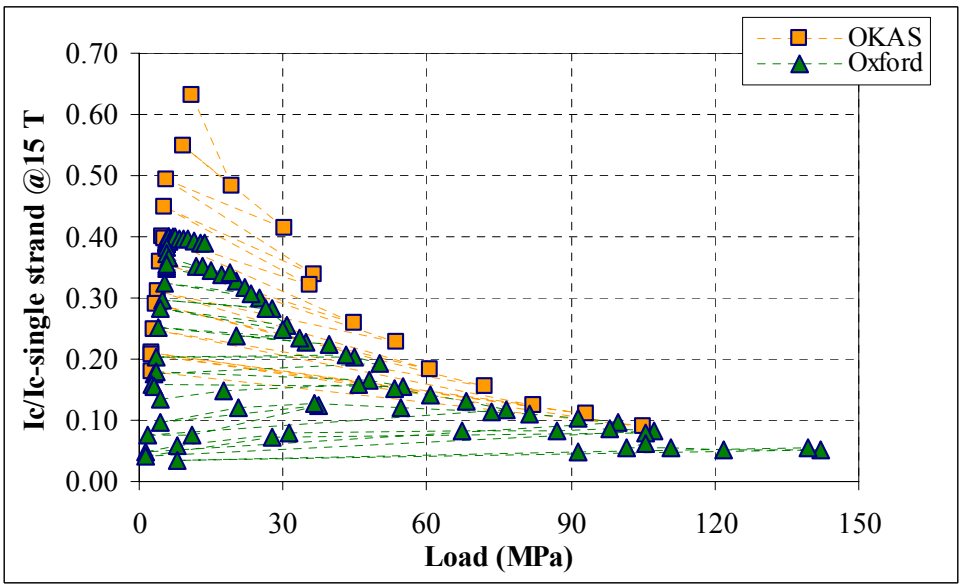

(b)

Fig. 3.20 (a) Normalized (to expected value) critical current as a function of total load applied. (b) Normalized critical current results for different cycles.

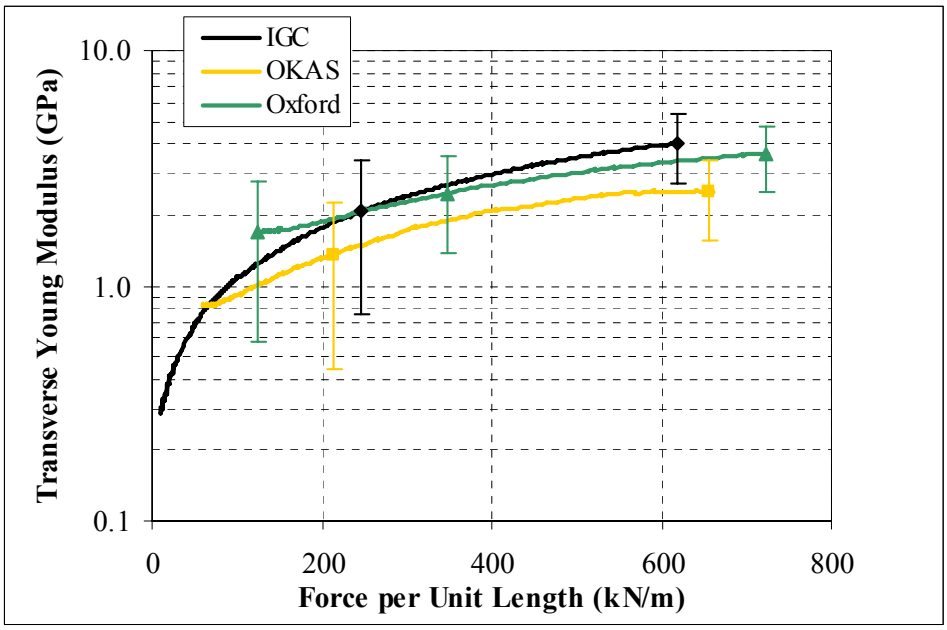

(a)

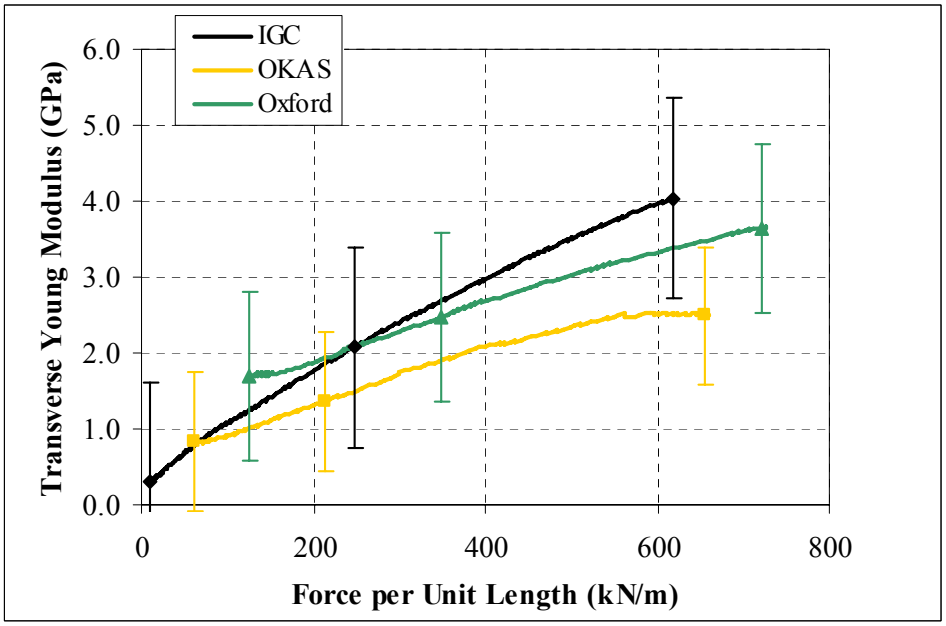

(b)

Fig. 3.21 Young's modulus measurements as a function of force per unit length: (a) in logarithm scale to show the plateau reached at high forces (to be compared with [3.5]), (b) in linear scale.

3.7 Conclusions

The four samples tested in this single turn configuration showed significant initial degradation compared to the expected values. Several different techniques to improve the fabrication process were tried with marginal success.

The testing procedure allowed us to indentify weakness of the design and it was possible to build a new test rig (see Chapter 4) in within a six months period. The rig was designed retaining the features that worked well for the single turn configuration test (strain gages, voltage taps, extensometer, linear actuator).

Despite moving to a new rig, the tests described in this Chapter were really important and interesting measurements were carried out indicating a strong dependence of the normalized critical current on the mechanical load applied.

Critical current measurements at different fields and critical current measurements at different loads and different cycles were successfully performed providing useful information and giving the confidence necessary in designing a new improved test rig.

CHAPTER 4:
Hairpin experimental setup and results

4.1 Introduction

Using the test rig described in Chapter 3, we observed significant degradation from unknown origin of the critical current before applying the external load. Therefore we decided to retain all the information learned from this experimental rig and build a new experimental setup that could perform the same type of measurements but that improved the ease of the sample fabrication and mounting. The intent was to minimize or eliminate any source of initial mechanical damage. At the same time, a magnet facility was updated and became available at the NHMFL which uses a high field superconducting split magnet. This gave us the opportunity to use a hairpin design for the test sample. The hairpin design gives more flexibility over the fabrication process. Additionally, with minor changes to the sample holder, it was possible to test different size cables including, single strand, triplet, 9-strand and 45-strand cable. In this Chapter we present a detailed description of the hairpin experimental setup as well as a summary of the experimental results.

The goal of this experiment is the same as for the previous one, that is, to measure the effect of transverse load on the critical current of a superconducting cable. The load is applied mechanically by pulling a multiple wedges piece that transversely displaces pieces that, ultimately, apply the load on the cable located inside its holder (see Fig. 1.16). The components of the probe used for these experiments are described in detail and the measurement techniques are presented in this chapter. The system to apply the load is the same linear actuator outside the cryostat that was used in the previous experiment. A load cell was mounted outside the dewar to measure the vertical load applied to move the wedge upward. This force was then translated to the actual transverse force applied to the cable by geometrical analysis as described in Section 4.5. The experimental results are presented and discussed.

4.2 System requirements and probe description

The primary magnet test facility used in this experiment is located at the NHMFL facility. The magnet system used to apply the external field is comprised of an Oxford superconducting split magnet with a 30x70 mm vertical slot where the sample can be mounted and which provides the magnetic field of 12 T uniform over a 150 mm length. Holmium pole pieces can be inserted in the center of the coils to reach 14 T magnetic field.

A picture of the magnet system is shown in Fig. 4.1 showing the slot (Fig. 4.1b) through which the sample is lowered. The magnet is located inside a cryostat. Once the sample is inserted into the cryostat and through the bore of the magnet, it has to be held in position so that it does not move while the load is applied with the linear actuator. A remotely actuated sliding pin is used to lock the bottom of the sample holder to the crysotat. Certain flexibility is required in the positioning of the sample inside the magnet. This is obtained by having a slightly oversized hole at the bottom of the probe where the pin slides in. On the top of the cryostat, outside, a bellows is mounted between two plates

and the flange of the probe rests on top of the plate. The bellows is used to adjust the vertical position to within 1 inch.

An overall schematic view of the magnet system is shown in Fig. 4.2 also showing how the probe is positioned inside the magnet. In the same figure the linear actuator is shown. The actuator is operated by an electric motor.

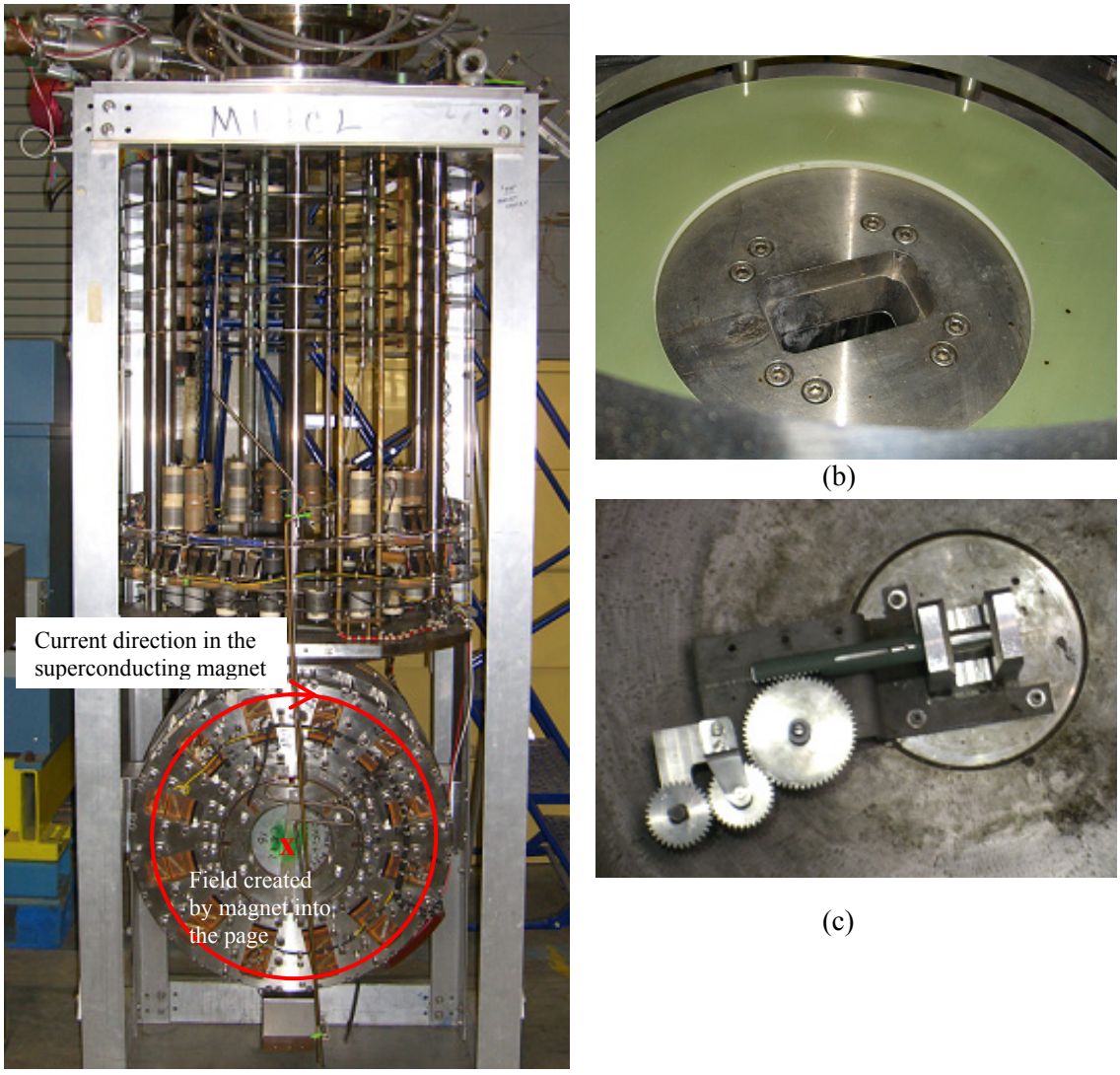

(a)

(b)

(c)

Fig. 4.1 (a) Split magnet outside the cryostat with coil current and generated magnetic field directions. (b) Slot where the probe will be lowered to be positioned in the center of the magnet. (c) Remotely actuated sliding pin used to lock the probe in position.

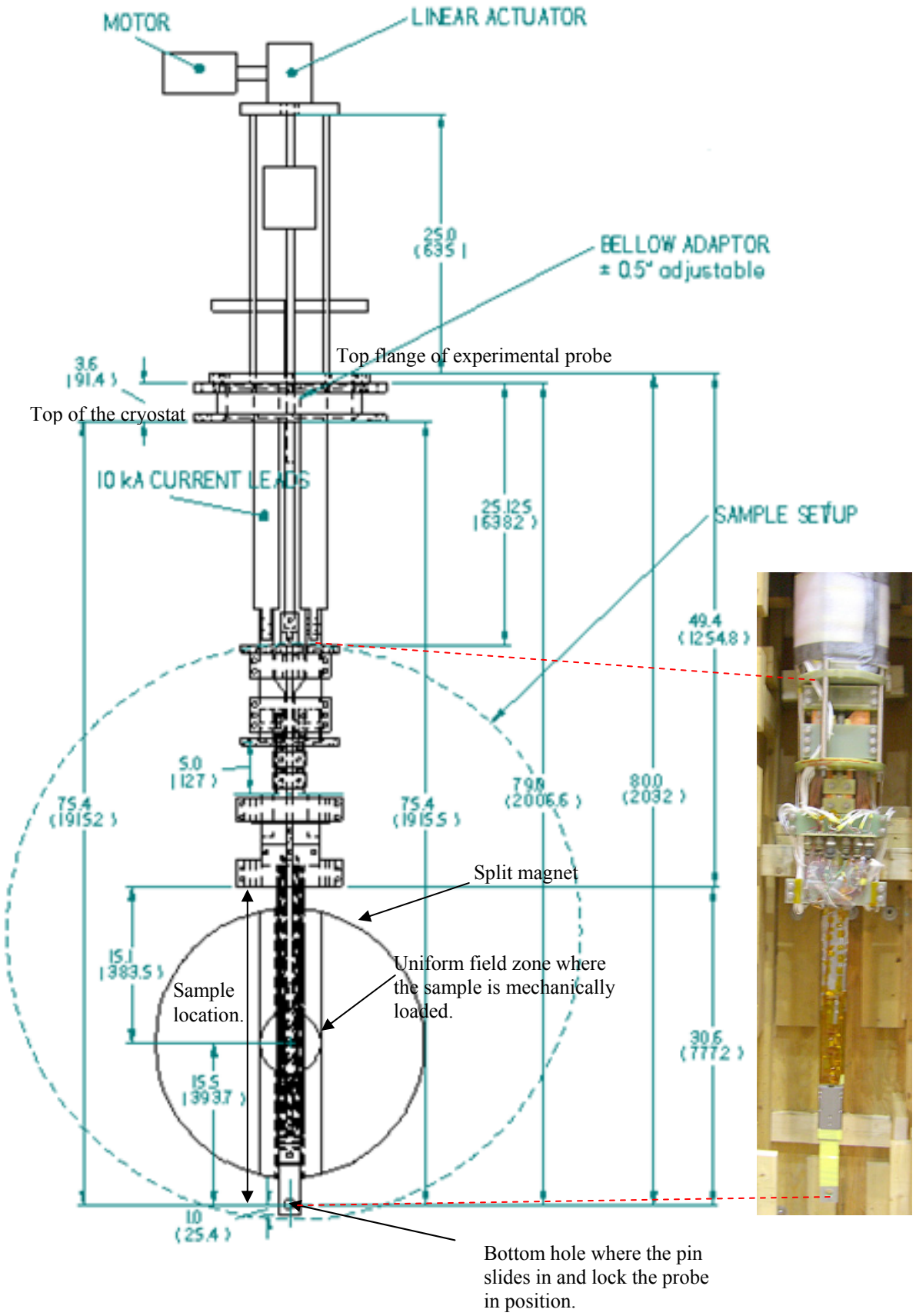

Fig. 4.2 Schematic view of the experimental setup. Positioning of the probe inside the split magnet.

Fig. 4.3 Probe inside the dewar. The picture show the top flange, the bellow used to adjust the height of the probe so that it can be easily connected to the pin sitting on the bottom of the dewar. The linear actuator and the motor used to operate it are sitting on a plate. The linear actuator is connected to the cylinder that contains the load cell and connects the actuator to the shaft connected to the wedge at the sample area.

The probe used for the experiment is the same as the one described in Chapter 3. The copper current leads which attached to the 10 kA vapor cooled leads were re-designed to improve the flexibility and to adapt the joint design to the new sample structure (Fig. 4.4).

Further details of the probe design are given in Appendix I.

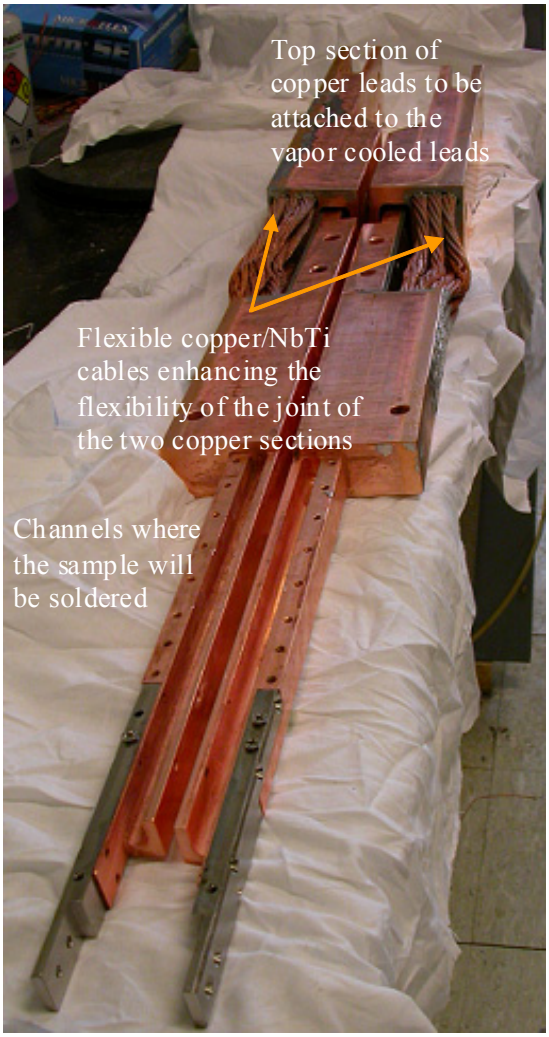

(a)

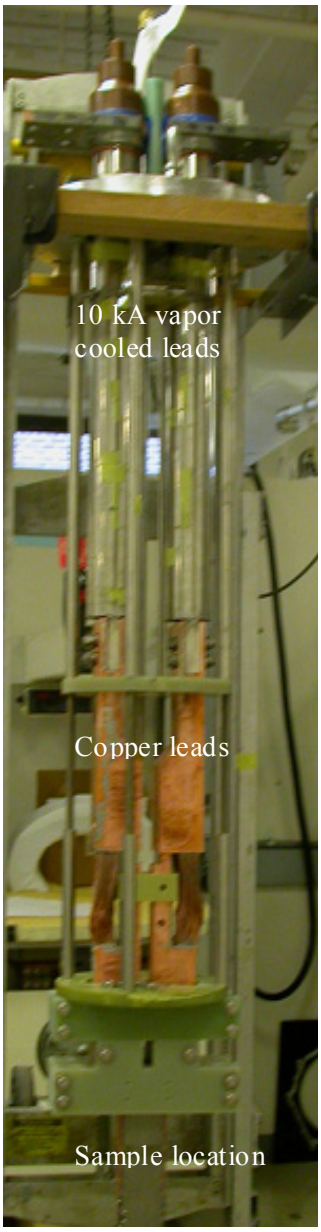

(b)

Fig. 4.4 (a) Copper leads: top section is connected to the vapor cooled leads, the bottom one is where the sample is soldered. (b) Probe set up with 10 kA vapor cooled leads and copper leads.

4.3 Sample area structure

The split magnet system creates a magnetic field perpendicular to the vertical direction and gives the flexibility to use a hairpin sample with legs that connect to the current leads without having to bend the sample out of its plane (Fig. 4.5). The field and current direction create a natural load in the same direction as the mechanically applied load applied.

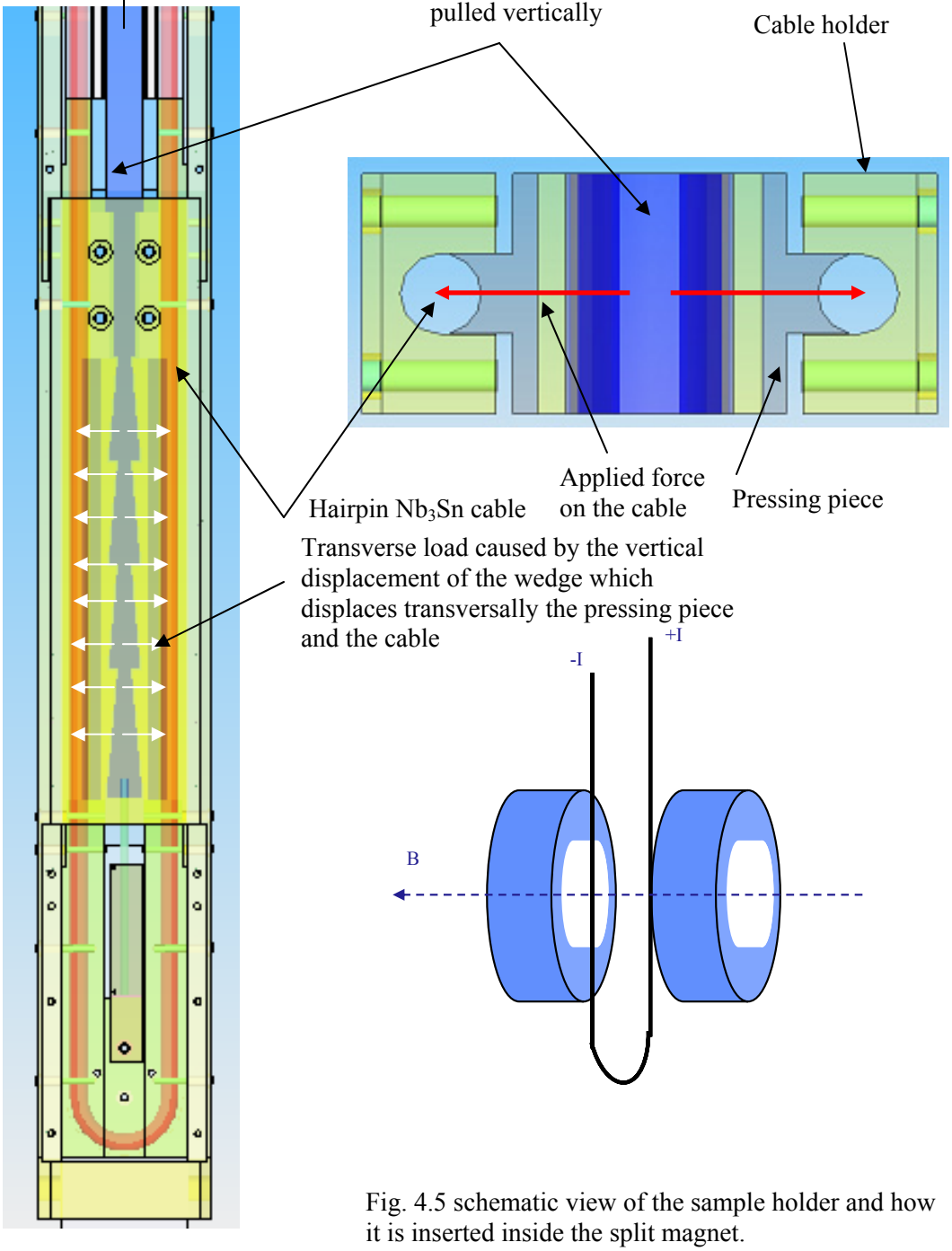

Fig. 4.5 schematic view of the sample holder and how it is inserted inside the split magnet.

The load is applied to the sample using the same technique as in the previous experimental setup. To ensure uniformity of the load applied over the length of the sample the piece moving vertically and applying the transverse load is segmented into multiple wedges. Next to this moving piece there are two matching pieces (one on each side) that are constrained vertically and can only slide horizontally. They touch two pressing pieces underneath which the sample is located, thus the sample is pressed in between the holder and the pressing piece. The matching wedges pieces are made of 316 stainless steel. This is a strong and non-magnetic material. The wedge pieces were cut using EDM technique and have very high tolerances. Any imperfection could create an undesirable localized force accumulation.

The main advantage of this design compared to the one described in Chapter 3 is that the sample is straight making it easier to handle and fabricate. The heat treatment structure is much smaller than that in the previous design (circle 115 mm in diameter compared to a block 30x70 mm). Those dimensions allowed the use of a smaller furnace and the heat treatment of multiple samples at the same time. The cooling conditions of this design are better since the helium is flowing in parallel to the cable. The entire structure was made of $TiAl_6V_4$ alloy that has an excellent strain matching with Nb_3Sn (see COE in Fig. 3.7) and it is a strong enough material to react the forces of the experiment. Another advantage is that the same structure can be used to test different size cables. The only parts that require dimensions specific to the cable size are the holder and the pressing piece reducing the overall cost for the test of multiple samples. Samples can be changed fairly easy (2 days to remove one sample and mount a new one) reducing the overall time of preparation.

The general observations made in Chapter 3 regarding void fraction and strain requirements remain valid for this experimental setup. A spacer block was used to maintain the void fraction during heat treatment together with some metal strips that maintained the correct distance between holder and pressing piece. The metal strips and the block were removed after heat treatment and the wedge pieces were mounted instead.

4.4 Sample fabrication

In this section the sample fabrication is described presenting the main characteristics of the experimental setup. More details can be found in Appendix I where the description of each step during the preparation is given.

All the samples were cabled in our laboratory. The total length of each sample is roughly 1.45 m. The two joints are each 28 cm long and they are positioned inside the channels (Fig. 4.4(a)) designed on the copper leads that need to be solder filled once the sample is mounted on the probe and properly positioned.

Four different samples were prepared and heat treated but only three of them were tested (single strand, triplet, 45-strand cable). The hairpin sample lies on a single plane and it is bent in a U-shape. It was verified on a dummy cable that the bend is not causing de-cabling of small cables (up to 9 strands) but it can cause significant de-cabling in a 45-strand cable. It was decided to pre-swage this cable inside a titanium tube and then bend it to the desired shape (Fig. 4.6). The cable outside the tube was wrapped with stainless steel sheet and pre-swaged to the desired dimension. The last die used for the 45-strand cable was 0.267” while for the 9 -strand cable it was 0.117” and swaged manually (dies

were chosen to achieve a 33% void fraction). The other two samples (single strand and triplet) did not require any pre-swaging. All the samples were inserted in their holder using glass sleeve to avoid sintering to metal part during heat treatment. The holder section where the load is applied is painted with graphite coating to avoid sintering and leave the bare cable exposed to the mechanical load. Flat plates and lateral bars are used to hold the cable holder in position (Fig. 4.7-4.8). Most of the support structure during the heat treatment is carefully removed after the heat treatment and replaced with a single piece case where the cable, its holder and pressing pieces are positioned together with the wedge pieces as shown in Fig. 4.9.

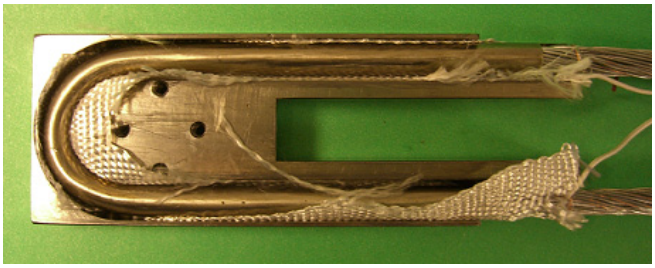

Fig. 4.6 U-shape sample in its holder. Only the 45-strand cable required a supporting titanium tube in the bending area.

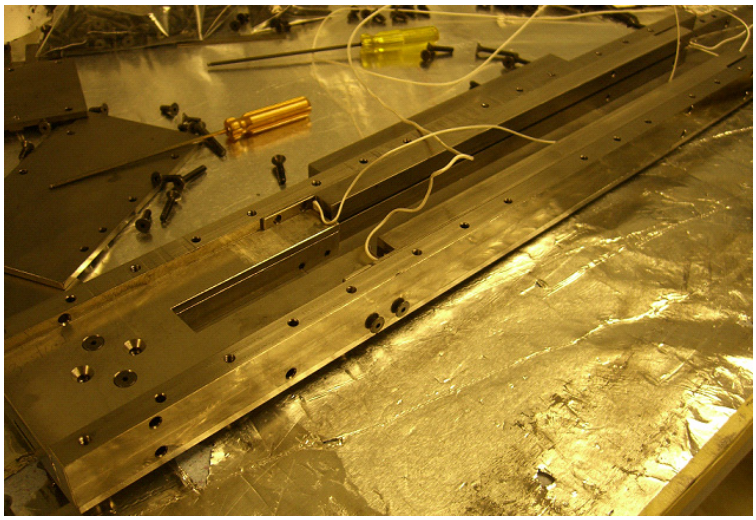

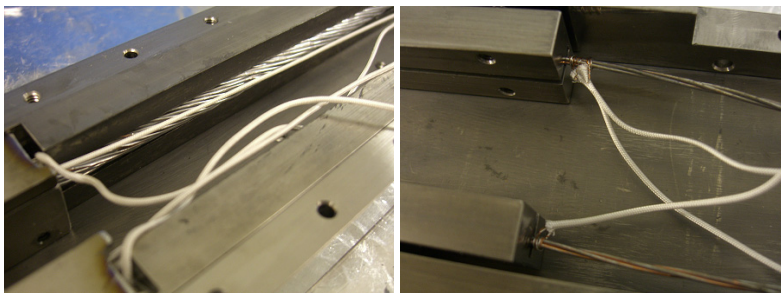

Fig. 4.7 The sample is mounted inside the U-shape holder and the two external holders (top). Bottom wires of the voltage taps (voltage taps 1, 2 and total voltage wire running along the sample to cancel inductive pickup) (bottom left). The top cover of the U-bend is recessed by grinding to be able to bring out the voltage tap wires without damaging them during the loading process. Voltage taps location at the top of the sample (bottom right).

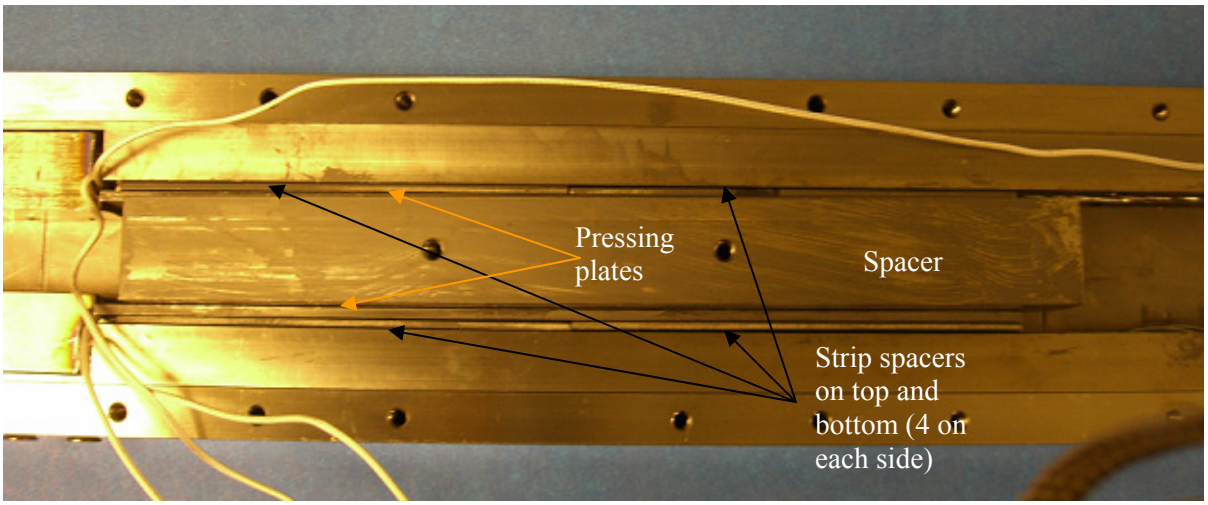

(a)

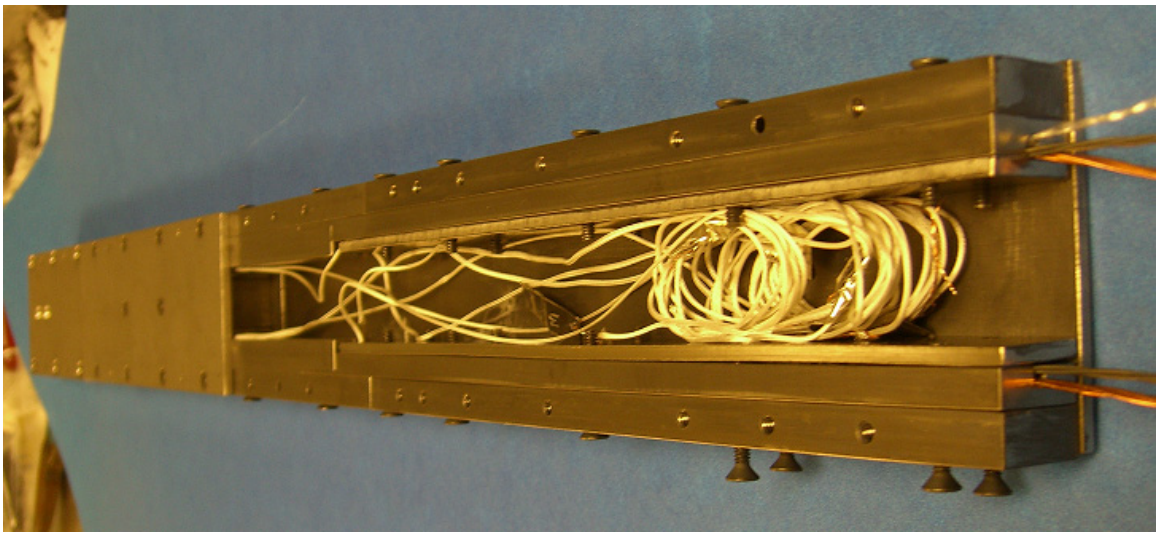

(b)

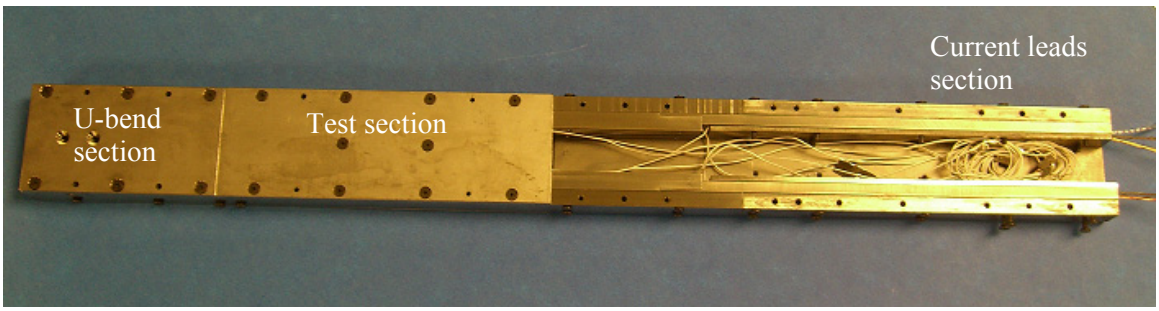

(c)

Fig. 4.8 (a) Bottom voltage tap wires and spacer used to maintain the desired void fraction during heat treatment. (b-c) Sample ready for heat treatment.

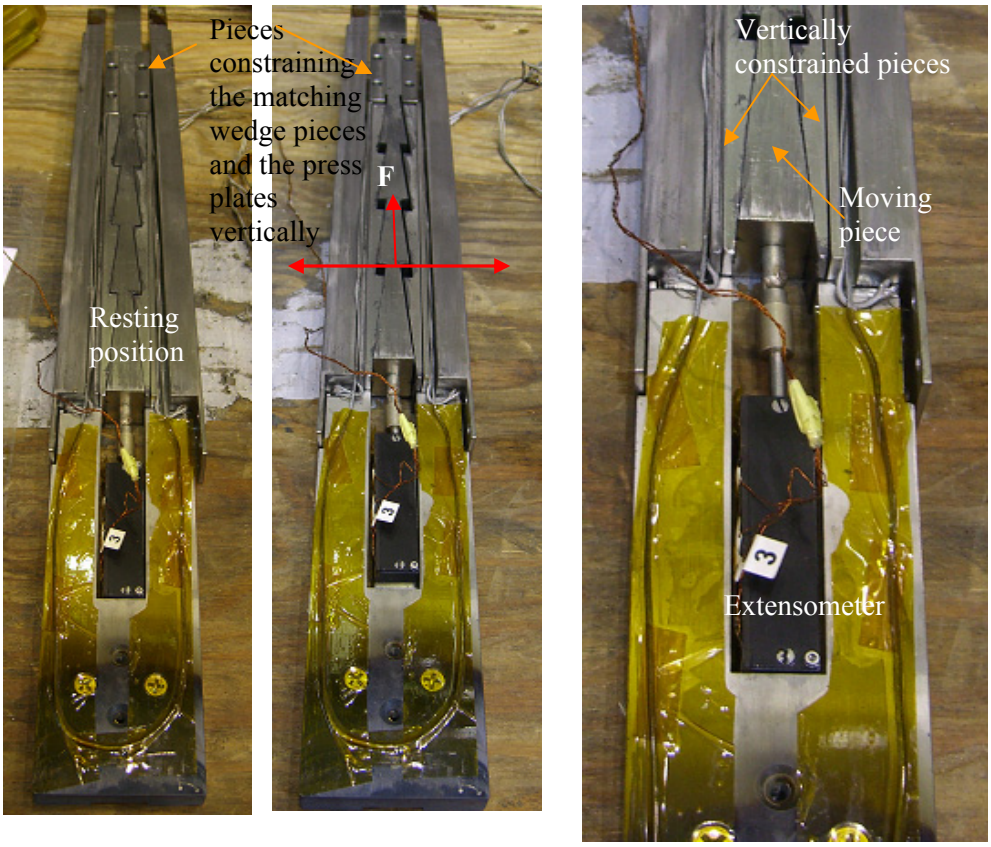

(a) (b) (c)

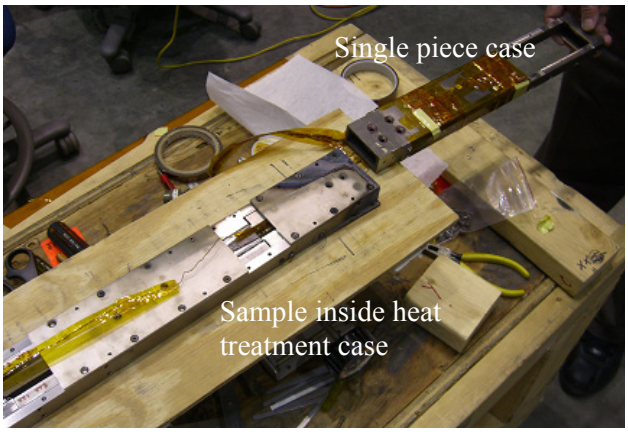

(d)

(e)

Fig. 4.9 Working principles of the device: (a) resting position of the wedge, (b) vertical displacement of the wedge and movement outward of the matching pieces, (c) displacement measured using the extensometer, (d) heat treatment case and single piece case, (e) sample inside the single piece case ready to be soldered.

4.5 Instrumentation

The experimental setup was equipped with several instrumentation tools similar to the ones described in Chapter 3. There are three different liquid level sensors to determine the liquid level during the experiment and to maintain the minimum level required for safe operation. Outside the cryostat there is a load cell attached to the linear actuator that applies the vertical displacement to the wedge piece in the cryostat. This unit records the vertical load applied to the experiment. Disregarding friction effect, this load is used to determine the transverse load applied to the sample by geometrical analysis as shown in Fig. 4.10 and by Eq. 4.1. One of the advantages of this configuration is that we used a smaller angle α (5° instead of 10°) then previously, but for the same force, we obtain half of the force in the transverse direction because the wedge is pushing two sides at the same time. These two effects balance to give a similar vertical load applied for the two configurations.

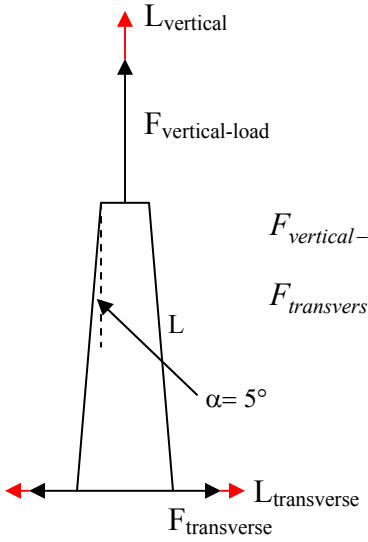

$$F_{vertical-load} \cdot L_{vertical} = 2 \cdot F_{transverse} \cdot L_{transverse}$$

$$F_{transverse} = F_{vertical-load} \cdot \frac{L_{vertical}}{2 \cdot L_{transverse}} = F_{vertical-load} \cdot \frac{1}{2 \cdot tan(\alpha)} \quad (4.1)$$

Fig. 4.10 Schematic view of the forces involved in the experiment and how the transverse force is estimated using geometrical analysis.

Strain gages were mounted on the wide side surface of the single piece case to verify the uniformity of the applied load since the wedge piece was composed of four sections. Three strain gages were mounted on the front of the case and two in the back (Fig. 4.11). A Hall sensor was mounted on the same surface to verify the direction of the split magnet field and to avoid damaging the sample in case the Lorentz load was inward (no support).

An extensometer was mounted on the wedge piece and secured on the sample so that, while the load is applied and the wedge displaced, the extensometer remains in position and measures the vertical displacement (Fig. 4.9 (a-c)). These measurements were used to evaluate the transverse Young's modulus of the tested cables as presented in the following section.

Three pairs of voltage taps were mounted along the sample with two covering each leg and one covering the entire length. The joint resistances were measured at the beginning of the experiment using one wire mounted on the joint and one taken from the

voltage tap (Fig. 4.11). The voltage taps are twisted to reduce the inductive voltage as much as possible. The voltage taps were mounted on the samples before heat treatment and insulated by glass fiber sleeves that can resist the high heat treatment temperatures.

One of the advantages of using a superconducting split magnet to create the background field is the overall reduction of noise level in the system (less than 0.5 μV).

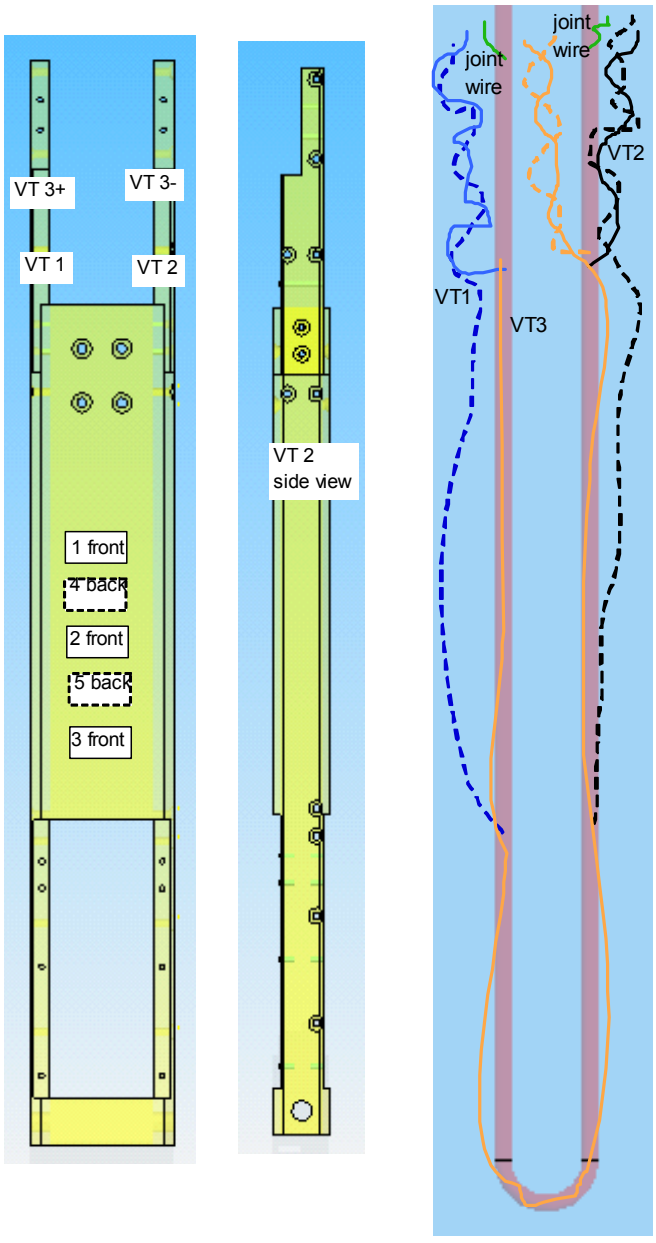

Fig. 4.11 strain gages and voltage taps location on the single piece case and on the sample. VT1 and VT2 cover the two straight legs of the sample and VT3 is the overall sample voltage.

Fig. 4.12 is a comparison between the measured strain gage values and the estimated strain gage values using ANSYS®. It can be seen that the estimated values are roughly

twice the average of the measured ones but follow the same trend. The difference could be due to the simplicity of the model that disregards any friction and interaction of the pieces of the experiments and simply considers the case geometry loaded by a transverse force. Additionally, the measurements show similar but not identical values. This could be due to some tilting of the wedge piece or some friction effect although the wedges pieces and their matching part were coated with graphite to reduce friction as much as possible. Strain gages 3 and 4 (SG3-SG4, bottom gage) read the lowest value as expected because the bottom of the wedge is the last to feel the pulling force.

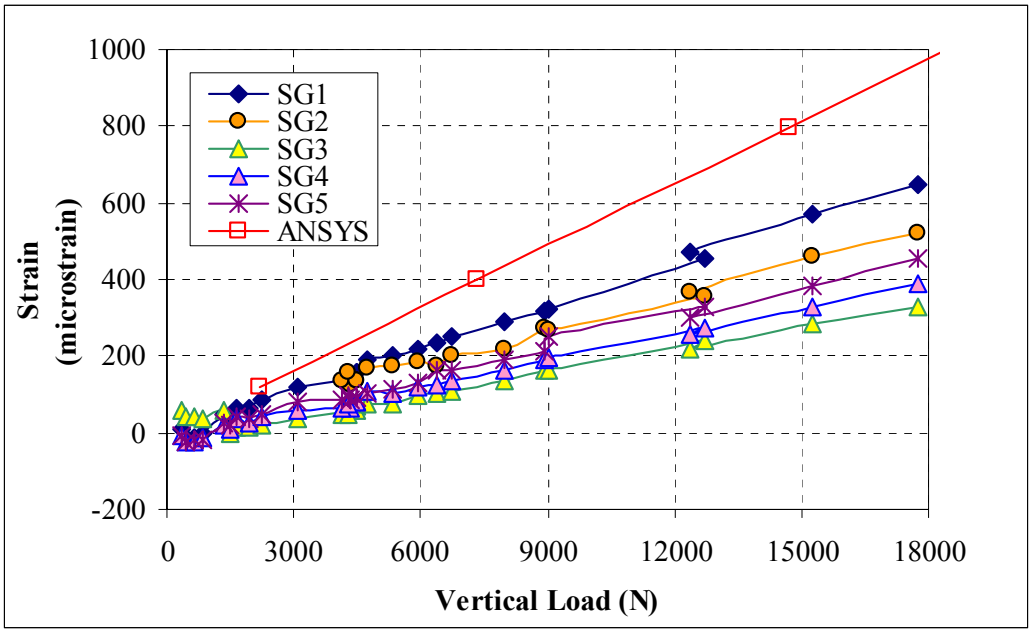

Fig. 4.12 Comparison between measured strain gage values and values computed using the ANSYS® code as a function of vertical applied load.

4.6 Experimental results and discussion

A single strand, triplet, 9-strand cable (not tested) and a 45-strand cable were prepared. The cables were made of an internal tin, Oxford wire (Fig. 4.13) and differ only by the number of strands used. The 45-strand cable is hybrid meaning that the first stage was composed of one copper strand and two superconducting strands. The 45 strands cable thus has 30 superconducting and 15 copper strands. The triplet has a twist pitch of 45 mm, the 9-strand cable has a 3x3 cabling pattern (twist pitches of 45 mm, 85 mm) while the 45-strand cable has a 3x3x5 cable pattern (twist pitches 45, 85, and 125 mm). The void fractions for the 9-strand and 45-strand cable aimed to be 33% following the general guideline of the ITER project. This void fraction is smaller that the one used for the samples in Chapter 3. The main properties of the samples are given in Table 4.1.

Table 4.1 Main properties of the sample used in the experiments.

December 2007 samples				
Strand manufacturer	Oxford			
Strand Type	Internal Tin			
Filament Material	Nb_3Sn			
J_c (12 T, 4.2 K)	1014 A/mm^2			
Diameter	0.82 mm			
Copper/non-copper ratio	1.04:1			
Number of strands	1	3	9	45
Average cable diameter (mm)	0.82	1.74	3.01	6.72
Cable pattern	1	triplet	3x3	(1Cu+2SC)x3x5

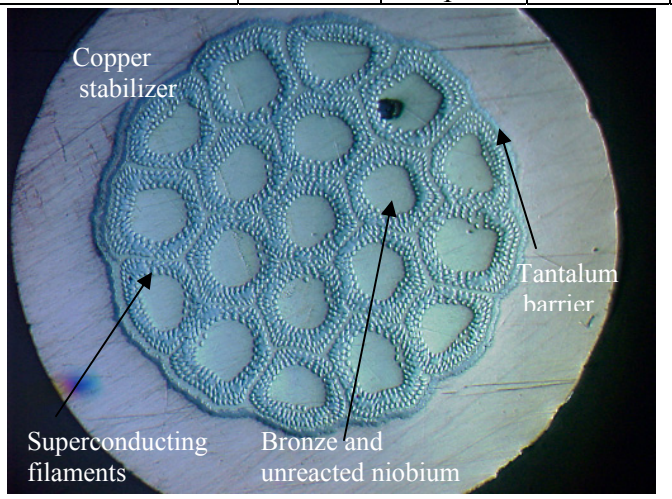

Fig. 4.13 Typical internal tin wire cross section (Oxford wire).

Typically the manufacturer provides the critical current at a certain field (12 T) and the n-value of the strand. The n-value represents the sharpness of the transition from superconducting to resistive state as described by Eq. 3.2. These manufacturer values were confirmed by witness samples reacted with the cables.
A technique similar to that described in Chapter 3, is used to evaluate critical currents and n-value (Fig. 3.16). The expected values at different fields were represented in Fig. 3.17

in Chapter 3 and they are replicated here for completeness (Fig. 4.14). The wire used in this experiment is labeled as Oxford TF. Those values are used to estimate the expected overall current in the different samples with the cable current being the product of the single strand current and the number of superconducting strands.

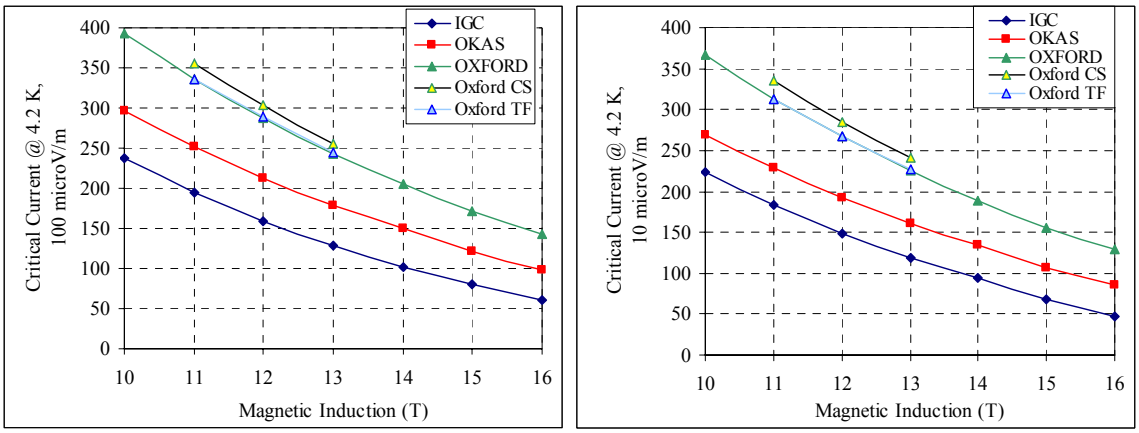

Fig. 4.14 Critical current as a function of magnetic field for single strand samples of the wires used during the experiment. The expected critical current of the cable is simply the product of the number of strands in a cable times the current of one strand.

The campaign of experiments was three weeks long and due to some facility problems of the locking mechanism at the bottom of the dewar, the 9-strand cable was not tested. It took four days for one sample test including preparation and actual test.

As already mentioned, the single piece case and the wedge pieces were the same for all the experiments. Two types of linear actuators were used for the experiments, since the single strand test required a finer sensitivity that the other two. The vertical load applied on the single strand was less than 1500 N while for the other two experiments it was 3600 N and 17700 N respectively. In addition a very fine vertical displacement had to be applied on the single strand so it was decided to use a micro-actuator (rated capacity 1000 lbs, 0.5" travel). The linear actuator for the triplet and 45-strand cable was the same (rated capacity 10 ton, 2" travel).

The first sample tested was the single strand sample. It must be noted that the external load control was not performed well for a single strand test due to the sensitivity of the mechanical measurements and controls. The testing of the triplet and the 45-strand cables followed the first experiment.

As a general comment, this experimental setup was much easier compared to our previous design, and the compact system obtained by using the hairpin sample allowed a smooth and easy interchange of the samples. A disadvantage of the system is that the background magnetic field obtained with a superconducting magnet can not be changed as quickly as with a resistive magnet so the measurements at different field were limited.

All the experiments started with critical current measurements as a function of field and the results are reported in Fig. 4.15 with the critical current evaluated at 10 μV/m criteria.

It can be seen that the single strand and triplet reached their expected values while the 45-strand cable showed an initial degradation of 23%. Initially the single strand and triplet showed a higher value than expected with the measurements showing a 40-45 A greater critical current that the nominal value. It is believed that this is caused by the fact

that a conductive Ti-6Al-4V plate was placed over the current leads for strength purposes. It turns out the plate was lying in a zero field region of the split solenoid. At zero field this material becomes superconductive so that a large fraction of the current might have been flowing inside the plate before reaching the sample itself. The data shown in Fig. 4.15 have been corrected for this effect by estimating the current leaking in the plate.

The 45-strand cable shows some degradation but it is far better than any cable tested with the previous experimental setup discussed in Chapter 3. The fabrication process has been carried out very carefully but still unexpected damages might have occurred during the process.

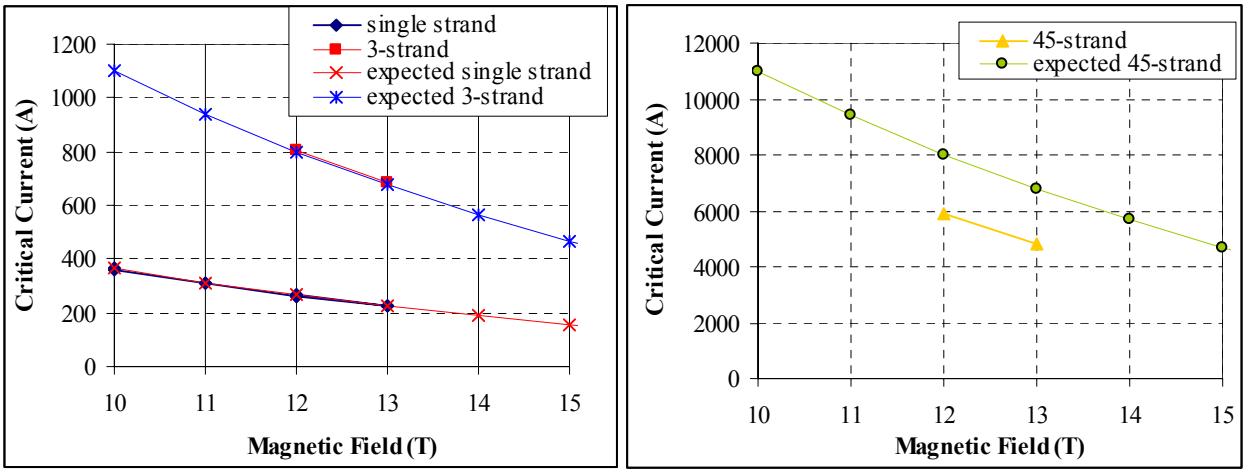

Fig. 4.15 Critical current as a function of field and comparison with the expected values.

Following the critical current measurements the mechanical loads were applied in small steps at a fixed field of 12 T. The single strand sample has been cycled only once since the time required to test the sample was longer than expected, and the micro linear actuator has been reset since it reached its maximum travel. Resetting the linear actuator was a very delicate process in which the load already applied was maintained and the linear actuator was removed and reset. After this operation the measurements were concluded with a maximum load applied of 80 MPa and a change of 40% from the initial value. Once the load was removed there was partial recovery of the critical current and its permanent degradation was roughly 20% (Fig. 4.16).

The triplet and 45-strand cable were cycled multiple times as shown in Fig. 4.16. In this figure the critical current normalized to the expected value is plotted as a function of the total load comprised of the applied mechanical load and the small Lorentz load. The mechanical pressure is estimated using the measured vertical force from which the transverse force is calculated (Eq. 4.1). The pressure is simply the ratio of this force to the cross sectional area of the loaded cable. This projection area is the product of the length pressed, $l_{pressed}$, and the diameter of the cable, D_{cable}

$$\sigma = \frac{F_{transverse}}{Area} = \frac{F_{vertical-load} \cdot \dfrac{1}{2 \cdot tan(\alpha)}}{l_{pressed} \cdot D_{cable}} \tag{4.2}$$

Several observations can be made from Fig. 4.16. First of all, the single strand and triplet do not show any initial degradation. The 45-strand cable shows a ~ 23% initial degradation from the expected values. The single strand starts showing some degradation at loads around 50 MPa while both the triplet and 45-strand cable show degradation at lower loads near 35 MPa. Another interesting observation is that the single strand data falls off more quickly than the two cables above the 75 MPa load level. This could be due to the fact that the single strand is pressed along its entire length and could be damaged over the entire length while in a cable configuration the load is more localized at the contacts among strands. It is necessary to emphasize once again that those data are plotted against the conventional pressure and the cross sectional areas used are different for each sample.

The behavior of the three samples tested is more clearly delineated if the critical currents normalized to the zero-load values are shown as a function of load (Fig. 4.17). In this figure again it can be seen again that the slope at which the single strand is degrading is more dramatic that the one of the cables.

In Figs. 4.18-4.20 the same data are plotted against the transverse force per unit length applied during the experiment. The plots show clearly the amount of force applied on each sample (the lengths on which the load was applied was similar for all the samples) and the number of cycles applied to each sample.

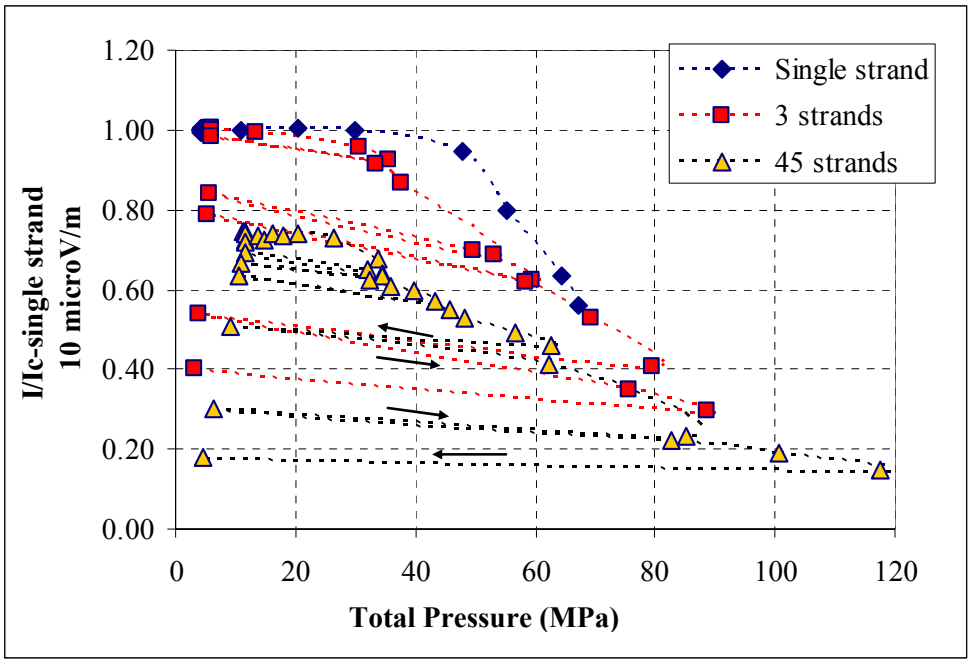

Fig. 4.16 Normalized critical current normalized to the single strand value as a function of total pressure.

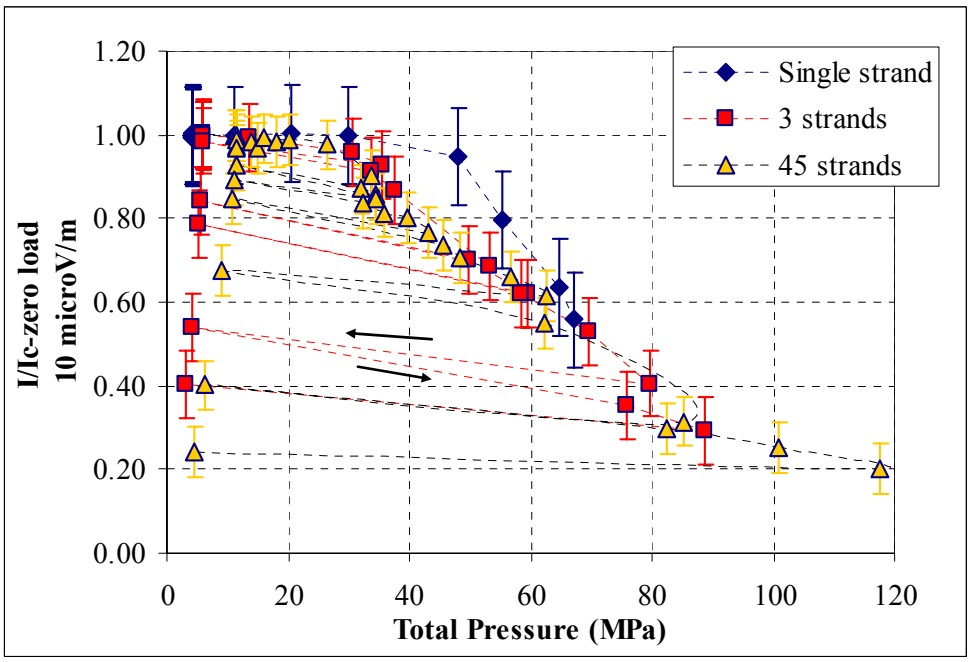

Fig. 4.17 Normalized critical current (normalized to the zero load value) as a function of total pressure.

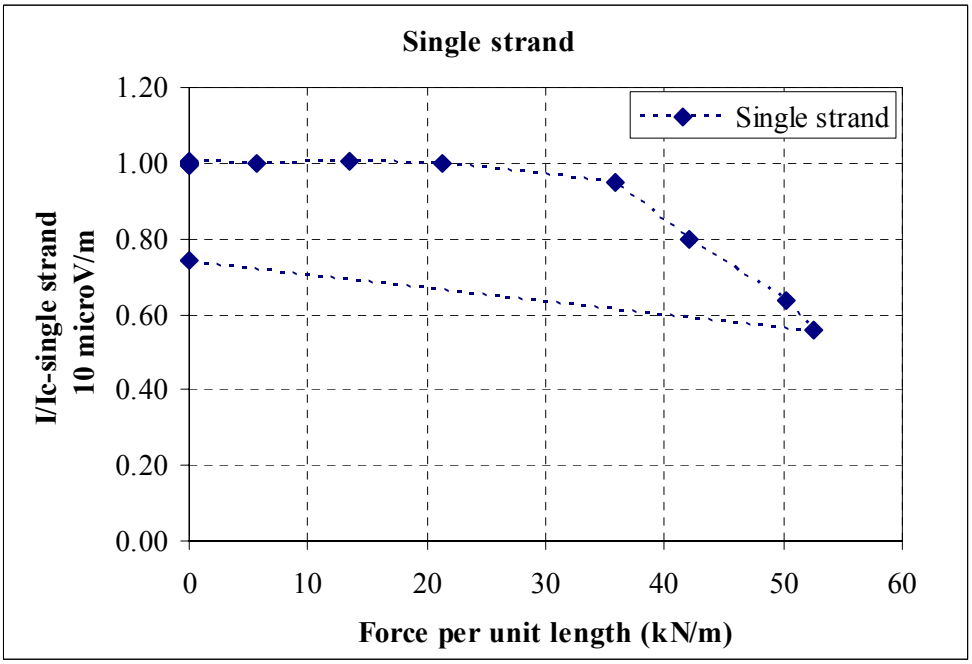

Fig. 4.18 Normalized critical current as a function of force per unit length for the single strand sample.

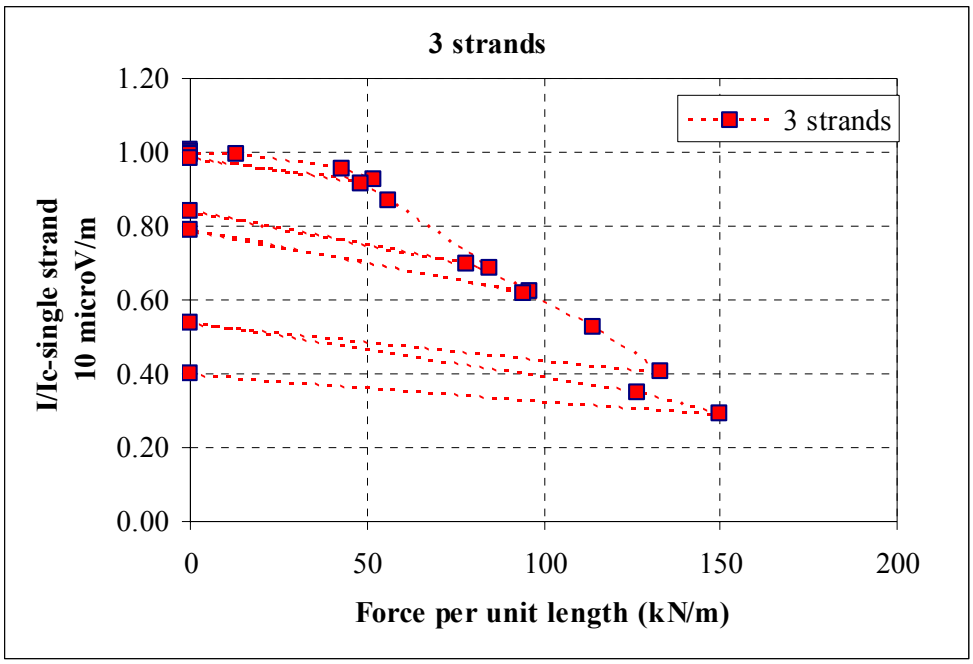

Fig. 4.19 Normalized critical current as a function of force per unit length for the 3-strand sample.

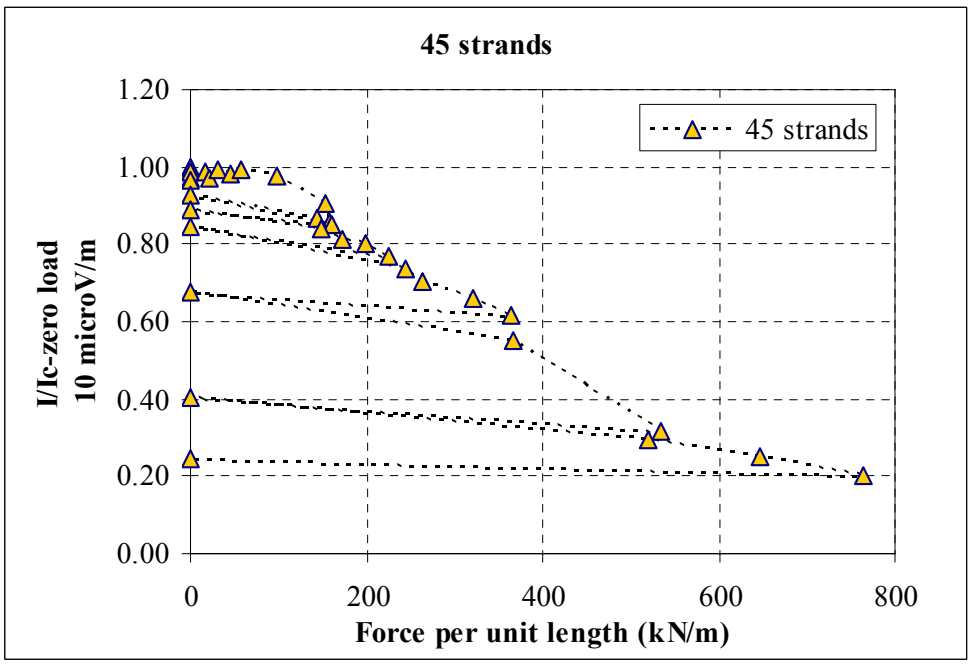

Fig. 4.20 Normalized critical current as a function of force per unit length for the 45-strand sample.

The data points after unloading the samples can be also plotted as a function of the maximum force applied to the sample before removing the load. As shown in Fig. 4.21 and 4.22 for the 3-strand and 45-strand cables, those data represent the irreversible degradation at the load applied before removing it. In other words, if we consider the 3-strand cable as an example the normalized critical current at 100 kN/m is roughly 60% of its initial value. Once the load is removed the current of the sample is not recovering completely and the normalized critical current is 80% of its initial value. Those plots indicate that above a certain load the sample is permanently degraded and only partially recovers if the load is removed.

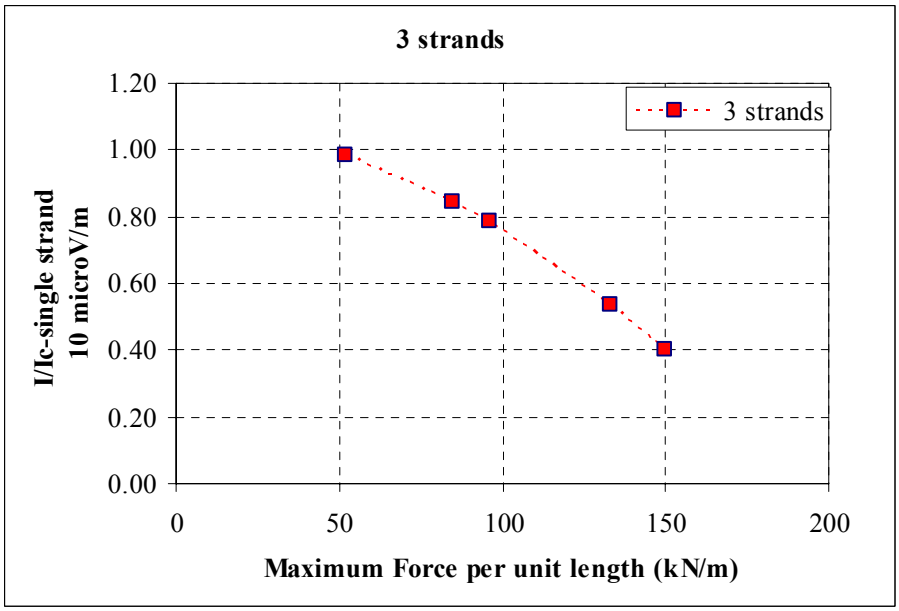

Fig. 4.21 Irreversible critical current data as a function of the maximum force per unit length applied before releasing the load (3-strand cable).

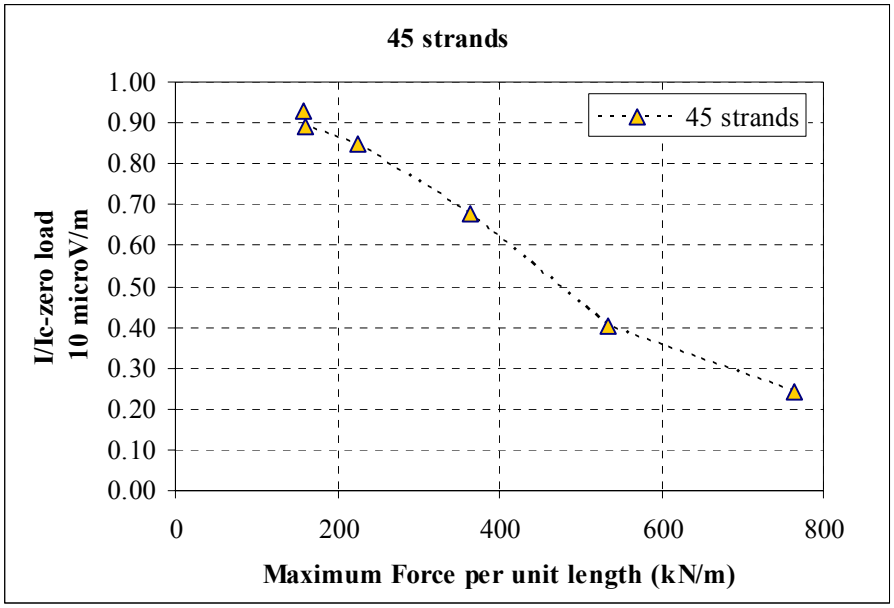

Fig. 4.22 Irreversible critical current data as a function of the maximum force per unit length applied before releasing the load (45-strand cable).

Those data are the ones that will be used for the analysis in Chapter 5 in which the force will be used to estimate the real area of contacts for each sample. In addition, in the modeling it will be required to set some parameters obtained from the measured displacements. The displacements for the three different samples are shown in Figs. 4.23-4.25.

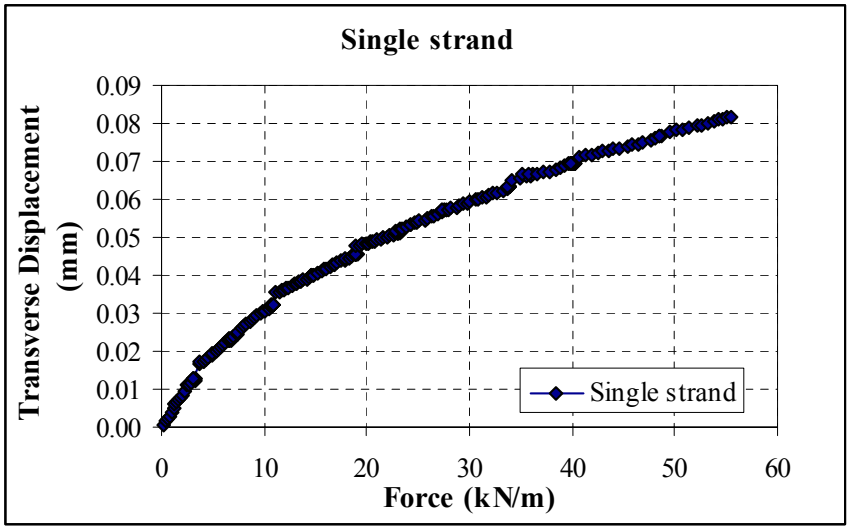

Fig. 4.23 Transverse displacement as a function of force per unit length for the single strand sample.

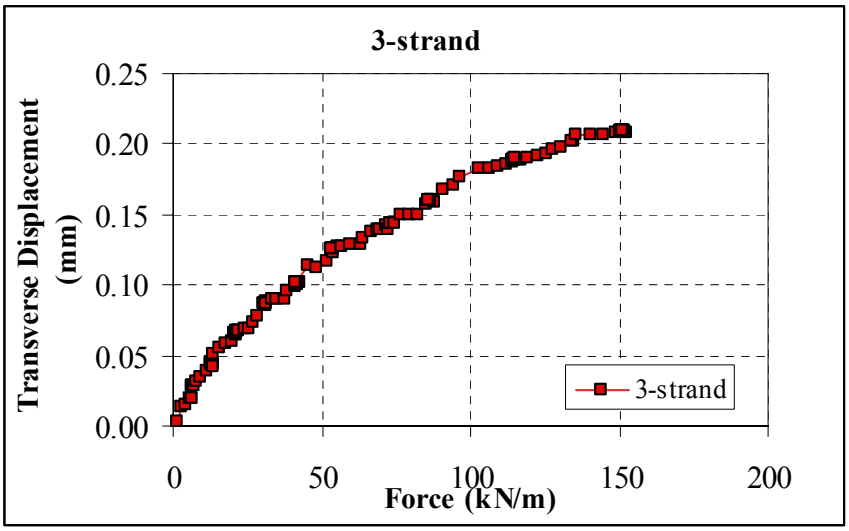

Fig. 4.24 Transverse displacement as a function of force per unit length for the 3-strand sample.

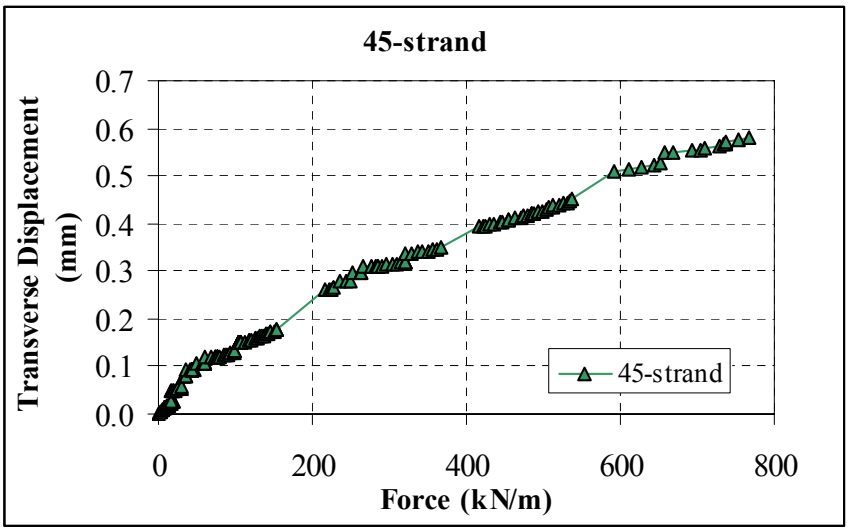

Fig. 4.25 Transverse displacement as a function of force per unit length for the 45-strand sample.

The displacement data are determined from the raw data of the vertical displacement. The force per unit length is determined from the vertical load measured with the load cell. The raw data need to be manipulated to remove the offset. In these experiments the offset is not simply driven by the instrumentation used, but it is most importantly driven by the fact that the wedge is initially hanging free in the probe so as not to apply load during cool down. The position of the wedge at which the load start affecting the sample is not very easy to determine and the initial displacement steps are very carefully applied in order to be able to determine when the wedge begins contact with the matching pieces effectively applying the load to the sample.

The extensometer data and load cell are studied for each load step until a non-linear behavior is noticed. This behavior indicates that the wedge is not free to move anymore but it is touching the matching piece and does not displace a constant amount per each step. Once the offset for the extensometer and the load are determined the data can be shown as in Figs. 4.21-4.23.

As already described in Chapter 3, the displacement measurements taken with the extensometer are used to estimate the transverse Young's Modulus of the different samples. The results are shown in Fig. 4.26-4.28 as a function of the force per unit length applied to the samples. The Young's modulus values are within previously reported values for the same quantity [4.1].

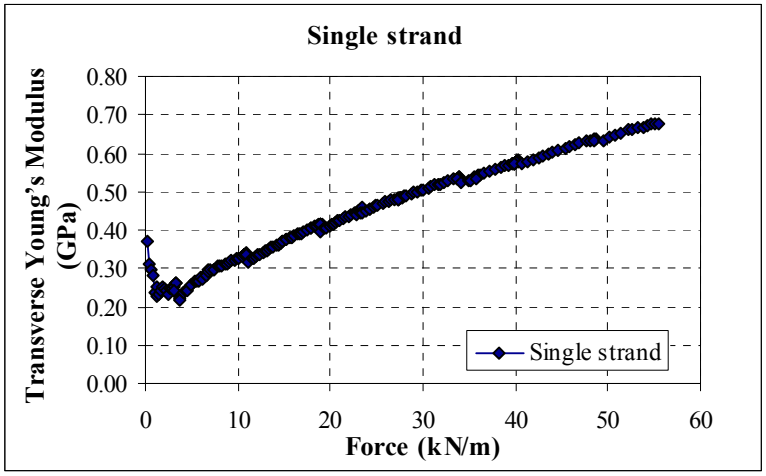

Fig. 4.26 Young's modulus measurements as a function of force per unit length for the single strand sample.

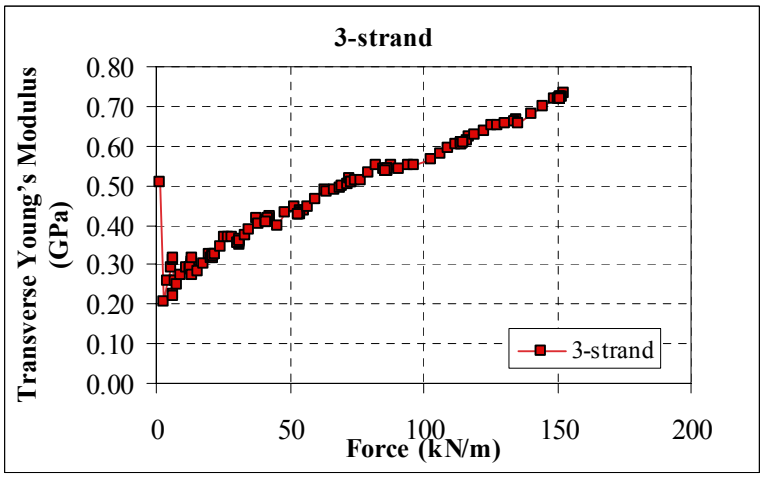

Fig. 4.27 Young's modulus measurements as a function of force per unit length for the 3-strand sample.

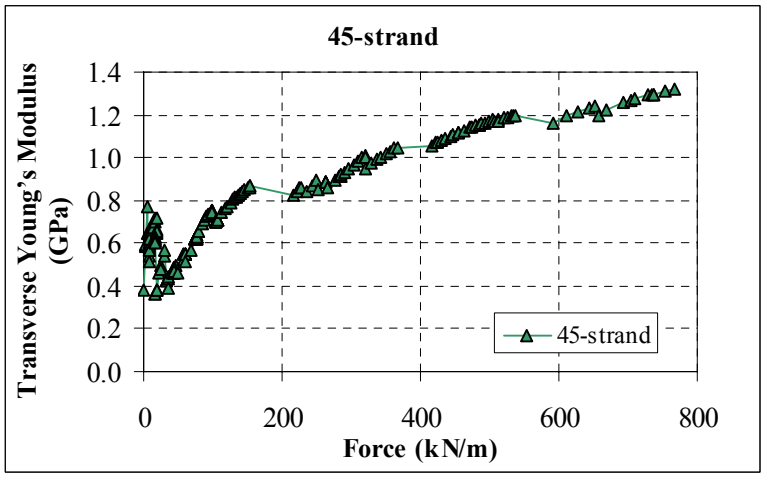

Fig. 4.28 Young's modulus measurements as a function of force per unit length for the 45-strand sample.

4.7 Conclusion on experimental results

The test rig for a hairpin sample discussed in this chapter was made possible to test at the new facility of a superconducting split magnet at NHMFL, Florida State University. The new rig is conceptually similar to the old rig presented in Chapter 3. However, the new setup has various versatilities. It allowed testing samples of different cables by changing only few parts of the probe. The samples became much more compact compared to the single turn samples. Therefore the sample fabrication is simplified, and a few samples can be heat-treated in a laboratory furnace at once. Furthermore one sample test takes less than a week including the time to change a sample.

The new test rig was designed and built in less than six months and three cables were successfully tested (single strand, 3-strand, 45-strand). It was possible to perform critical current measurements as a function of mechanical load applied.

The data were analyzed as a function of the nominal pressure i.e. force divided by the cross sectional area of the sample considered (see Figs. 4.16-4.17).

The critical current does not degrade up to a certain transverse load and then decreases sharply when the load is increased further. The results show significant transverse load degradation even for the single strand and the 3-strand cable. These degradations could not be explained by a recent bending model.

Considering those results it seems that the single strand is less sensitive to transverse load than a multi-strand cable but such a conclusion can be misleading.

It will be shown in Chapter 5 that a more meaningful analysis can be approached for the same critical current data as a function of the effective contact area and not the average cross section of the sample. If the single strand is taken as an example, the load is localized and for sure is not applied to the entire cross sectional area of the sample. This means the area over which the load is applied is much smaller resulting into a larger pressure to the superconductor.

The critical current data and displacement data will be analyzed with a newly developed model that considers the effective areas of contacts among strands under load.

CHAPTER 5:
Modeling and comparison with experimental results

5.1 Introduction

In Chapter 3 and 4 the results were presented for two different experimental setups. The data of normalized critical current were plotted as a function of the nominal pressure $p_{nominal}$ applied to the cable. This nominal pressure, Eq. 5.1, is defined, for a transverse force $F_{transverse}$, in the same way for all the cables tested as long as the appropriate dimensions are used for each of the cases:

$$p_{nominal} = \frac{F_{transverse}}{S} = \frac{F_{transverse}}{length \cdot diameter} \tag{5.1}$$

This pressure is often referred to as average pressure because it is determined from the force divided by the projected area of the sample (Fig.5.1).

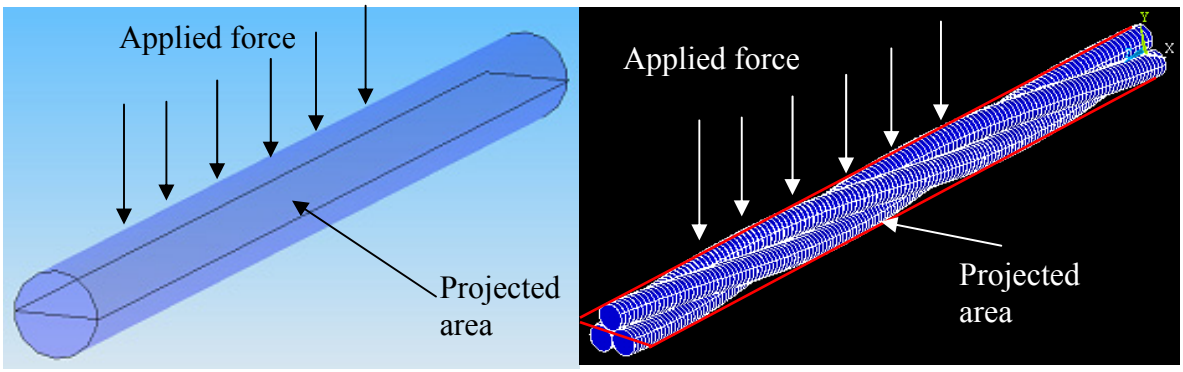

Fig. 5.1 Projected area used to estimate the average pressure on the single strand and 3-strand samples. The length of the sample is multiplied by the diameter of the sample. The diameter of the sample is the diameter of the strand for a single strand sample and for a cable it is the expected outside diameter calculated considering void fraction.

This pressure definition has been often used in the literature but, it does not take into account the actual area pressed and the local effects that might occur within the sample. In a single strand, for example, the transverse area pressed is much smaller than the projected area of the wire. In a cable composed of several strands, the real pressed area is a combination of the angle at which the strands cross over and the number of their contacts. Using the projected area of the wire or the cables is a very simplified way of estimating the pressure exerted on a sample, but it can be much smaller than the pressure caused by the local contacts in a cable and produce a distorted image of the stresses felt within the superconducting filaments of a cable during operation.

In this Chapter a technique to evaluate the real deformation of the cables under a mechanical load is presented according to the theory of contact mechanics. This approach allows calculating local effective pressures acting on strand-strand contacts in a multi-strand cable. The critical current and the displacement data measured for all the samples

(single strand, triplet and 45-strand cable) can be correlated by a newly developed model described in this Chapter. The analysis is limited to the samples tested with the hairpin design since the single turn circular samples showed a significant initial degradation that makes the interpretation of the data collected very difficult.

A brief introduction on the theory on contact mechanics used as an analysis tool is presented in Section 5.2. The single strand data is discussed in Section 5.3 while the triplet and 45-strand samples are discussed in Section 5.4 and 5.5 respectively.

5.2 Contact mechanics of circular cylinders

When two bodies come in contact it is important to study the stresses and the deformation that arise from the contact. Contact mechanics has been developed first by Hertz in 1892 [5.1] while he was studying Newton's optical interference fringes in the gap between two glass lenses and he was concerned about the elastic deformation of the surfaces due to their contact pressure. More details have been developed by Timoshenko, Goodier and Lessells [5.2-5.4] who presented derivation of elastic equations for loading of elastic half-spaces (stress, strain and displacement). The case studies most relevant to this thesis are summarized in this section [5.5] and more specific details are given in Appendix III.

When two non-conforming solids are brought into contact they touch initially in a single point or along a line and under a certain load they deform in the vicinity of the point of contact. If an appropriate coordinate system is chosen it can be shown that the separation between the two surfaces is given by (5.2):

$$h = z_1 - z_2 = Ax^2 + By^2 = \frac{1}{2R'}x^2 + \frac{1}{2R''}y^2 \tag{5.2}$$

where A and B are positive constants and R' and R'' are defined as the principal relative radii of curvature. If the x_1 and x_2 axis are inclined to each other by an angle ϕ then it can be shown that (R_e being defined as the equivalent radius):

$$(A+B) = \frac{1}{2}\left(\frac{1}{R'} + \frac{1}{R''}\right) = \frac{1}{2}\left(\frac{1}{R_1'} + \frac{1}{R_1''} + \frac{1}{R_2'} + \frac{1}{R_2''}\right) \tag{5.3}$$

$$|B-A| = \frac{1}{2}\left\{\left(\frac{1}{R_1'} - \frac{1}{R_1''}\right)^2 + \left(\frac{1}{R_2'} - \frac{1}{R_2''}\right)^2 + 2\left(\frac{1}{R_1'} - \frac{1}{R_1''}\right)\left(\frac{1}{R_2'} - \frac{1}{R_2''}\right)\cos 2\phi\right\}^{1/2} \tag{5.4}$$

$$R_e = (R'R'')^{1/2} \tag{5.5}$$

By observation, Hertz then assumed that the typical profile of the contact surface is an ellipse. He also introduced the simplification that for the purpose of estimating the local deformation, each body can be considered as an elastic half-space loaded over a small elliptical region. With this assumption the highly concentrated contact stresses are treated separately from the general distribution in the rest of the solid.

In order for this simplification to be justifiable, the contact area must satisfy two conditions:

(i) it must be small compared to the dimensions of each body so that the local stress does not influence the general behavior of the solid

(ii) it must be small compared to the relative radii of curvature of the surfaces so that the strains in the contact region are sufficiently small to lie within the linear theory of elasticity.

Additionally, the two surfaces are assumed to be frictionless. Referring to Fig. 5.2, if the significant dimension of the contact area is $2l$ and the relative radius of curvature R, the significant radii of each body R_1 and R_2 and their length and depth L, the assumptions made in the Hertz theory can be summarized as:

(i) the surfaces are continuous and non conforming: $2l << R$
(ii) the strains are small: $2l << R$
(iii) each solid can be considered as an elastic half space: $2l << R_{1,2}$, $2l << L$
(iv) the surfaces are frictionless

Fig. 5.2 Schematic view of two long cylinders in contact.

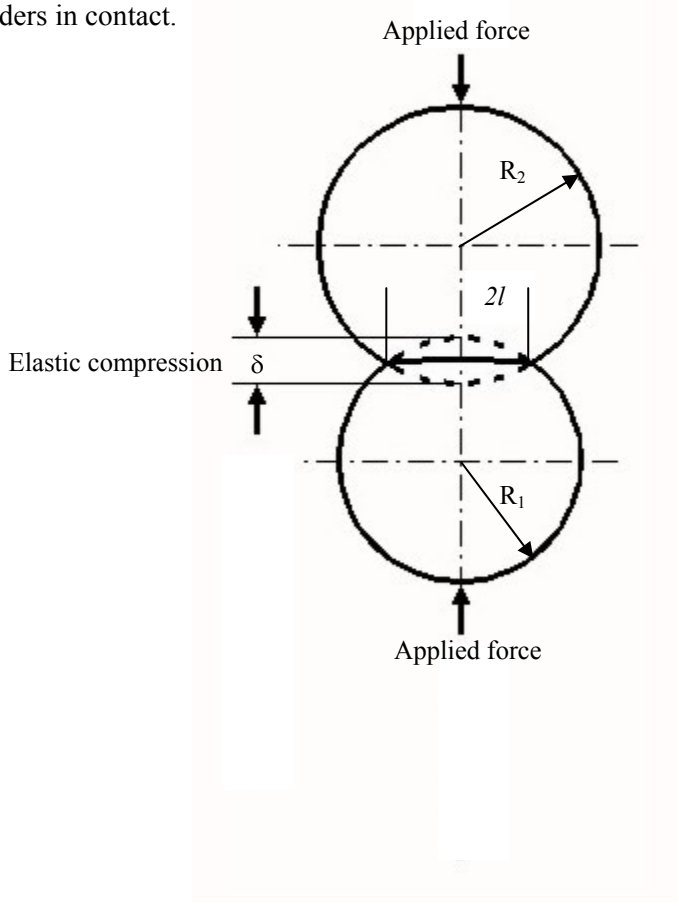

Two cases are relevant for the analysis of our data: the case of a cylinder between two plates, resembling the single strand sample on Fig. 5.3; and the case of crossing cylinders, resembling the general contacts between strands in a cable on Fig. 5.4. More details on the equations derivation can be found in Appendix III. The strategy is to use the general equations to estimate the effective contact areas in the tested cables and show that under very reasonable assumption all the samples behaved similarly with respect to the change in critical current as a function of load.

(i) Infinite cylinder (single strand)

The single strand sample (with radius *a*) tested resembles a case in which a long cylinder is pressed in between two flat plates or two solids with radius much bigger that the single strand diameter, as shown in Fig. 5.3.

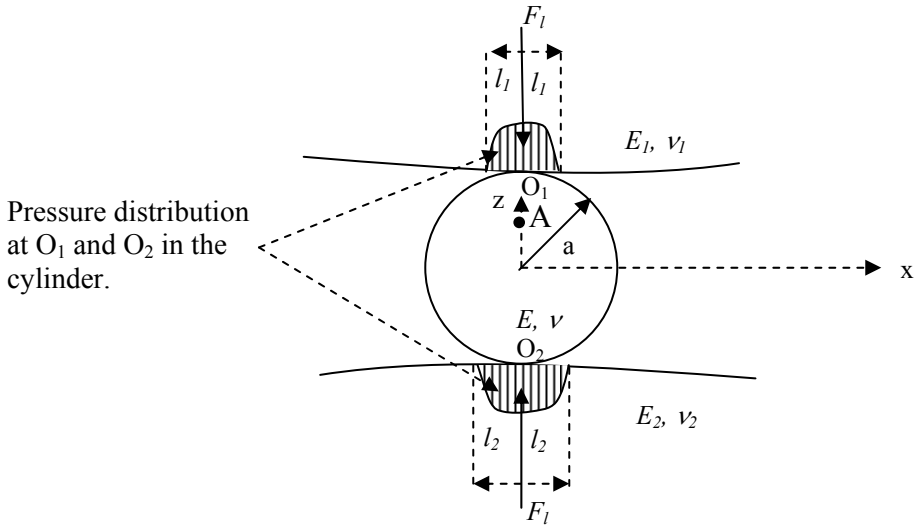

Fig. 5.3 Cylinder in contact with two solids. The contact pressure distribution developed in the cylinder is shown in the figure and is used to estimate the contact width $2l_1$, $2l_2$.

The compressive load per unit axial length F_l (N/m) gives rise to a Hertzian distribution of pressure p given by Eq. 5.6:

$$p_l = \frac{2 \cdot F_l}{\pi \cdot l_i}\left(1 - \frac{x^2}{l_i^2}\right)^{1/2} \tag{5.6}$$

where the semi-contact width l_i is given by Eq. 5.7 ($1/R_{eq,i} = 1/a+1/R_i$ given that B is zero in Eqs. 5.3-5.5):

$$l_i^2 = \frac{4 \cdot F_l \cdot R_{eq,i}}{\pi \cdot E_i^*} \qquad 1/E_i^* = (1-\nu^2)/E + (1-\nu_i^2)/E_i \tag{5.7}$$

The stress caused by the Hertzian distribution at O_1 and O_2 can be estimated using equations described in Appendix III. Using plane strain condition ($\varepsilon_y = 0$), those stress components can be used to evaluate the strain component in the z-direction. Integrating the strain component of z between $z = 0$ and $z = a$ the compression of the upper and lower half of the cylinder can be found using Eqs. 5.8 and 5.9.

The displacement (δ_1 and δ_2) of the top and bottom half of the cylinder (Eq. 5.10) is given respectively,

$$\delta_1 = \int_0^a \varepsilon_z \cdot dz = F_l \cdot \frac{(1-\nu^2)}{\pi \cdot E} \left\{ 2 \cdot ln\left(\frac{4a}{l_1}\right) - 1 \right\} \tag{5.8}$$

$$\delta_2 = \int_0^a \varepsilon_z \cdot dz = F_l \cdot \frac{(1-\nu^2)}{\pi \cdot E} \left\{ 2 \cdot ln\left(\frac{4a}{l_2}\right) - 1 \right\} \tag{5.9}$$

The total displacement δ_s is the sum of δ_1 and δ_2:

$$\delta_s = \delta_1 + \delta_2 = 2F_l \cdot \frac{(1-\nu^2)}{\pi \cdot E} \left\{ ln\left(\frac{4a}{l_1}\right) + ln\left(\frac{4a}{l_2}\right) - 1 \right\} \tag{5.10}$$

The results obtained are for the pressure distribution in Eq. 5.6. In general they depend on the profile chosen for the pressure distribution. In literature a parabolic profile is often found to describe the pressure distribution [5.9] but the total displacement is not that different from the one obtained by Eq. 5.10 (less than 8% difference).

(ii) Crossing cylinders (multi-strand cable)

The general profile of a contact between two solids will be described using the theory developed by Hertz.

It is assumed that the area of contact is elliptical in shape with semi-axis η and ξ (Fig. 5.4).

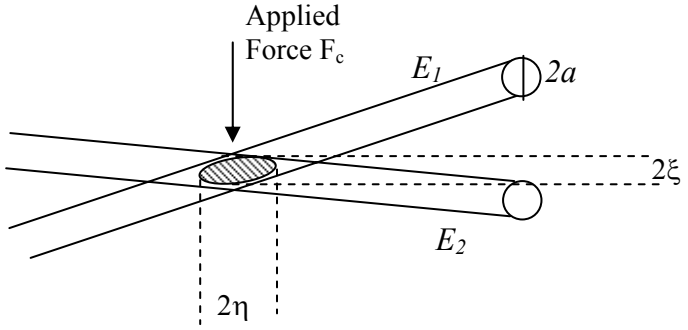

Fig. 5.4 Schematic view of the contact area between two round strands.

In Hertz's theory, using an analogy with electrostatic potential, he assumed that the pressure distribution close to the contact point can be described by Eq. 5.11:

$$p = p_0 \left\{ 1 - \left(\frac{x}{\eta} \right)^2 - \left(\frac{y}{\xi} \right)^2 \right\}^{1/2} \tag{5.11}$$

The semi-axes of the ellipse are often evaluated [5.3, 5.6-5.8] with the following equations:

$$\eta = \alpha \cdot \left(\frac{F_c \cdot K_D}{E^*} \right)^{1/3} \tag{5.12}$$

$$\xi = \beta \cdot \left(\frac{F_c \cdot K_D}{E^*} \right)^{1/3} \tag{5.13}$$

where $F_c = (2/3) \cdot p_0 \pi \cdot \eta \cdot \xi$ is the total force in Newton, α and β are tabulated values dependent on the crossing angles ϕ between the two solids (Table 5.1), $1/E^* = (1-\nu_1^2)/E_1 + (1-\nu_2^2)/E_2$, and

$$K_D = \frac{3}{2} \cdot \frac{1}{1/R_1^{'} + 1/R_2^{'} + 1/R_1^{''} + 1/R_2^{''}} = \frac{3}{A+B}$$

$$\cos\Omega = \frac{2 \cdot K_D}{3} \cdot \left\{ \left(\frac{1}{R_1^{'}} - \frac{1}{R_1^{''}} \right)^2 + \left(\frac{1}{R_2^{'}} - \frac{1}{R_2^{''}} \right)^2 + 2 \left(\frac{1}{R_1^{'}} - \frac{1}{R_1^{''}} \right) \left(\frac{1}{R_2^{'}} - \frac{1}{R_2^{''}} \right) \cos 2\phi \right\}^{1/2} = \frac{|B-A|}{A+B}$$

The cross-contact displacement δ_x in this case (deformation of both strands) can be evaluated by using Eq. 5.14:

$$\delta_x = \lambda \cdot \sqrt[3]{\frac{F_c^{\,2}}{(E^*)^2 \cdot K_D}} \tag{5.14}$$

Using Eq. 5.12 and 5.13, the contact surface can be evaluated using Eq. 5.15.

$$S_c = \pi \cdot \eta \cdot \xi \tag{5.15}$$

In the case of 3-strand and 45-strand cables, $R_1^{'} = R_2^{'} = a$; $R_1^{''} = R_2^{''} = \infty$ (a being the radius of a strand) so that:

$$K_D = \frac{3}{2} \cdot \frac{1}{1/R_1' + 1/R_2'} = \frac{3 \cdot a}{4}$$

$$\cos\Omega = \frac{2 \cdot K_D}{3} \cdot \left\{ \left(\frac{1}{a}\right)^2 + \left(\frac{1}{a}\right)^2 + 2\left(\frac{1}{a}\right)\left(\frac{1}{a}\right)\cos 2\phi \right\}^{1/2} = \left\{ \frac{(1+\cos 2\phi)}{2} \right\}^{1/2}$$

Table 5.1 Tabulated values of α and β to evaluate the semi-axis of the ellipse of contact [5.7, 5.8].

Ω	α	β	λ
0	-	0	0
1	36.890	0.131	0.047
2	22.260	0.169	0.090
3	16.500	0.196	0.130
4	13.310	0.209	0.165
6	9.790	0.255	0.227
8	7.860	0.285	0.278
10	6.612	0.319	0.320
20	3.778	0.408	0.456
30	2.731	0.493	0.542
35	2.397	0.530	0.579
40	2.136	0.567	0.614
45	1.926	0.604	0.645
50	1.754	0.641	0.672
55	1.611	0.678	0.693
60	1.486	0.717	0.710
65	1.378	0.759	0.724
70	1.284	0.802	0.737
75	1.202	0.846	0.750
80	1.128	0.893	0.764
85	1.061	0.944	0.775
90	1.000	1.000	0.777

5.3 Single strand sample

The single strand sample was located inside a narrow groove plate and pressed by the pressing plates as described in Chapter 4. The machining of the groove was very deep and narrow inside the holder, and the grooves on the pressing plates were required to be very precise but in reality the curvature of the bottom groove and the pressing plate were not well controlled. Considering the uncertainty of the contacting curvatures, the pressing mechanism was first evaluated with the following assumptions regarding the radius of the surface of contacts with the strand:

(i) extreme case of the grooves surrounding the strand to be flat ($1/R_e=1/a$)
(ii) case in which the contact is between convex surfaces ($1/R_e=1/a+1/R_i$)
(iii) case in which one of the two surfaces is concave ($1/R_e=1/a-1/R_i$)

Using Eq. 5.7 the total contact width a_1+a_2 was estimated for 3 different cases (Fig. 5.5):

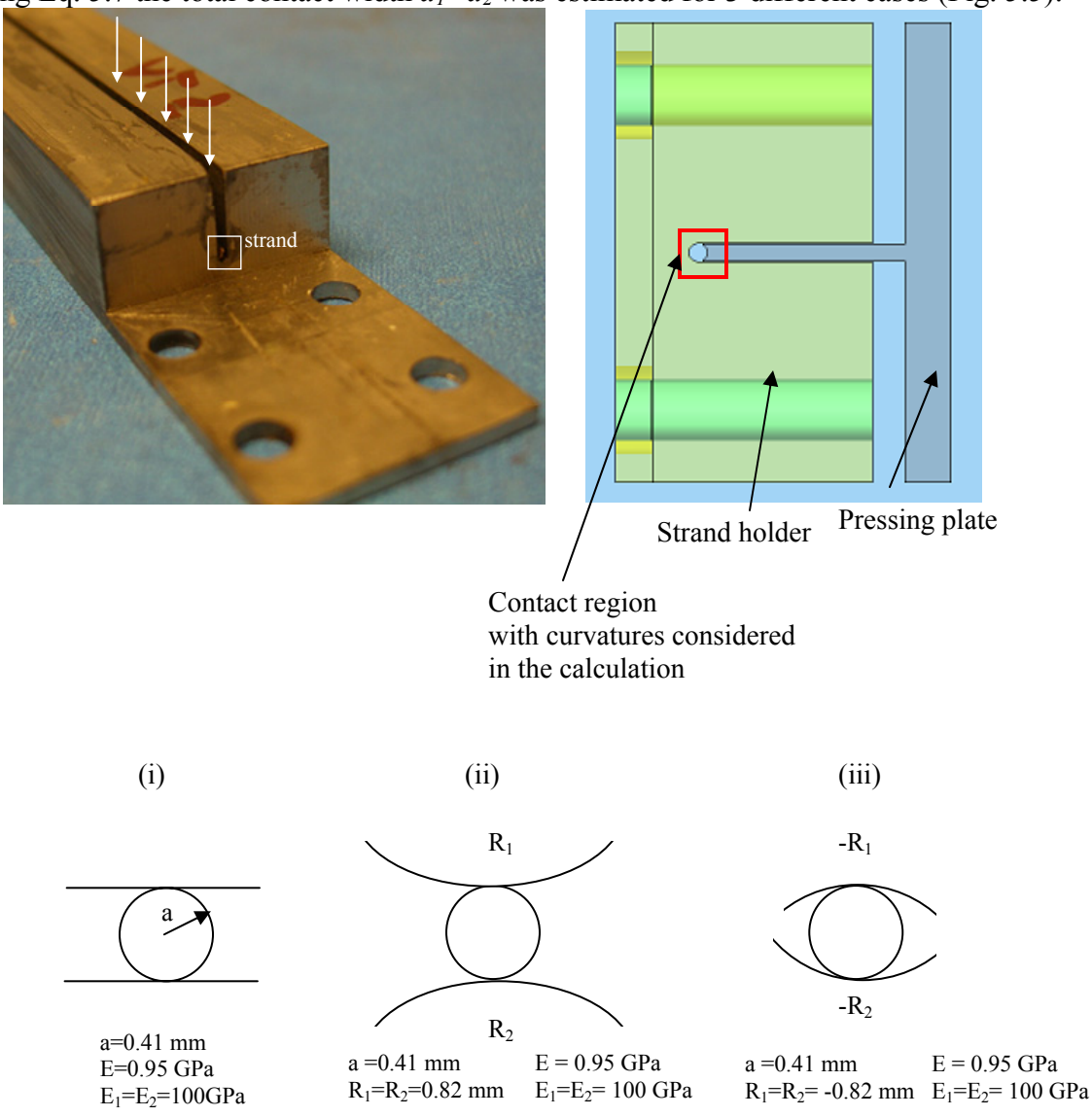

Fig. 5.5 Single strand test configuration and simplified analysis cases.

Using Eqs. 5.7 and 5.10, the transverse displacement measured in the experiments can be compared to the one evaluated numerically as show in Fig. 5.6-5.7.

Fig. 5.6 shows the contact width *2l* for the three different cases. The case with convex and concave surfaces are evaluated with radii that are double the radius *a* of the strand. The other parameters used in the analysis are:

E = 0.95 GPa Strand Young's modulus and E_1=E_2=100GPa matching pieces Young's modulus.

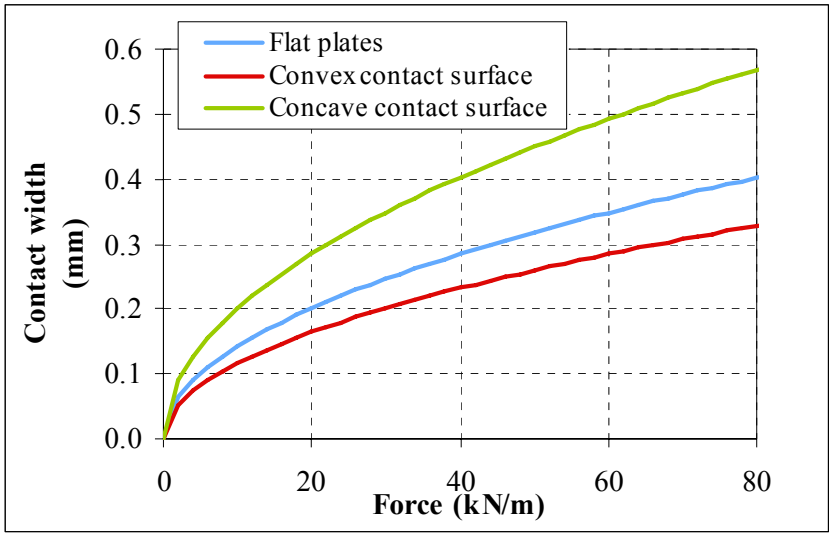

Fig. 5.6 Contact width *2l* for the three different cases considered. Flat plate $R_i = \infty$, convex surface $R_i = 2a$ and concave surface $R_i = -2a$.

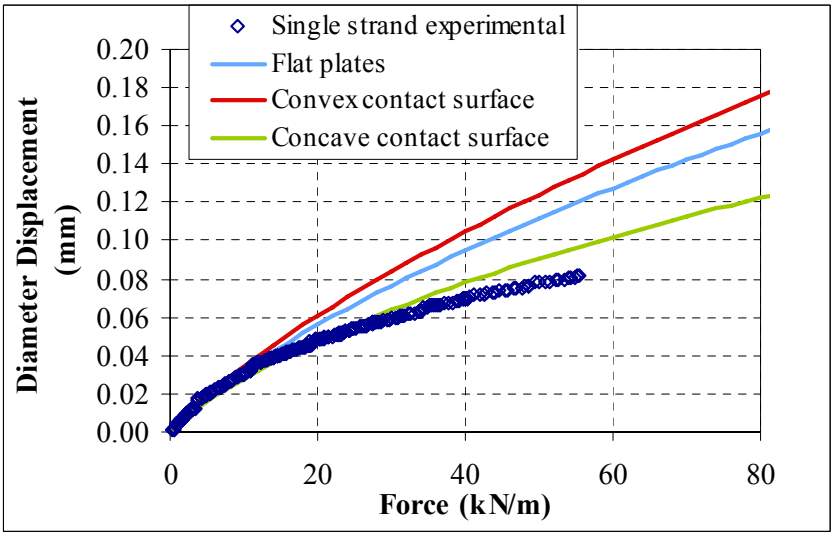

Fig. 5.7 Displacement of a single strand, 0.82 mm in diameter. Comparison between measurements and numerical evaluations. The agreement is good at low load and less good at high load as expected from having disregarded non-elastic behavior in the model.

Fig. 5.7 shows the displacement of a single strand (0.82 mm in diameter) for the three different pressing surfaces configuration calculated using Eq. 5.10. The calculated displacements are compared to the experimental results. The agreement is good at low load and less good at high load as expected from having disregarded non-elastic behavior and the limitation of l_i being much less than the radius of the strand.

In Fig. 5.7 the concave surface case shows better fitting to the experimental results and it is the more appropriate to describe the experimental setup but the precise dimensions are unknown so that there is some uncertainty on the results.

When the force per unit length F_l [N/m] is applied to a single strand, the effective contact pressure p_l [Pa] is given using Eq. 5.16:

$$p_l = \frac{F_l}{2l_i} \tag{5.16}$$

where l_i is l_1 or l_2.

Fig. 5.8 shows the experimental results of the normalized critical current plotted as a function of the contact pressure calculated with Eq. 5.16. As mentioned earlier, the pressure applied has been commonly evaluated as the ratio of the force per unit length divided by the diameter of the strand. The conventional averaged nominal pressure differs from the contact pressure evaluated using the width of the contact area described above. In Fig. 5.8 the normalized critical current is also plotted for the conventional pressure. The degradation of the single strand starts at contact pressures greater than 105 MPa in contrast with the case of nominal pressure where the degradation starts at around 40 MPa.

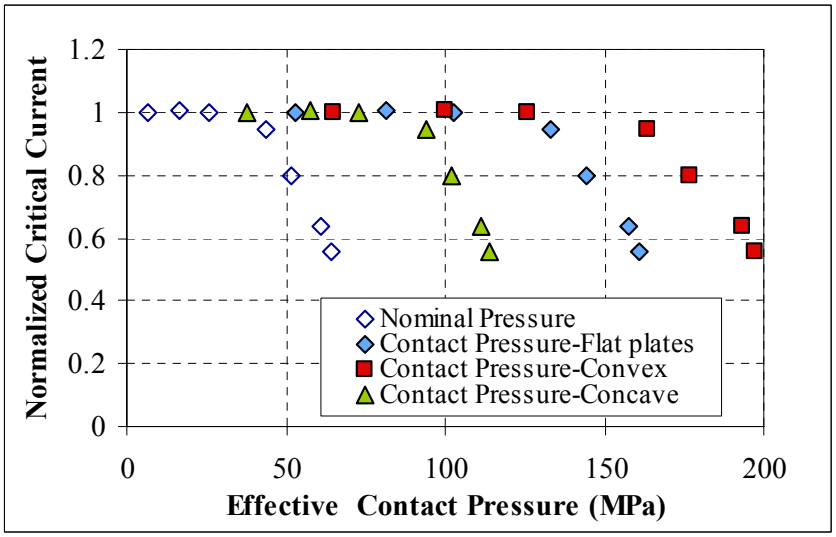

Fig. 5.8 Single strand results: nominal pressure and effective contact pressure approaches.

From Fig. 8 it can be seen that the three cases are relatively different. Considering the uncertainty on the machining of pressing pieces for the single strand the analysis results are contained between the concave case and the flat plate case. The experimental setup was not optimized for a single strand sample but for sub-cables. The flexibility of the

design allowed us to easily adjust the design to test a single strand but the overall sensitivity for this case was not ideal so that those results are not conclusive.

More systematic studies on Young's modulus and behavior of single strand samples to transverse load are necessary to better understand how the contact area is changing with the applied load.

These initial results are very promising and with future experiment the parameters for the analysis can be better redefined to obtain better agreement between experiments and simulations.

It will be possible to utilize the 3-strand cable sample results to carry on the analysis and modeling. A 3-strand cable, being the lowest stage of any full size cable seems more appropriate to use for the modeling, maintaining the attractiveness of being a simpler experiment to carry out than a multistage sub-cable or full size cable sample.

5.4 3-strand sample

The sample composed of 3 superconducting strands is treated with a similar approach to the single strand sample by using contact mechanics. But for this case a two crossing cylinders model discussed earlier, in order to estimate the local contact pressure at strand-strand contacts under a certain load. Eq. 5.12 and 5.13 are used to estimate the two semi-axes of the contact area. To evaluate those quantities it is necessary to estimate the parameters α and β that depend on the parameter $cos\Omega$ (Table 5.1). In this case considering $R_1' = R_2' = a;\ R_1'' = R_2'' = \infty$ (a being the radius of a strand):

$$K_D = \frac{3}{2} \cdot \frac{1}{1/a + 1/a} = \frac{3 \cdot a}{4}$$

$$cos\,\Omega = \left\{ \frac{1 + cos\,2\phi}{2} \right\}^{1/2} = \left\{ \frac{1 + 2 \cdot cos^2\,\phi - 1}{2} \right\}^{1/2} = cos\,\phi$$

where ϕ is the angle of crossing between two strands (in this case equal to Ω). The angle for the 3-strand cable tested can be evaluated from geometry as shown in Fig. 5.9. It had a twist pitch L_p of 45 mm, the radius of the strand, a, is 0.41 mm for the Oxford strand used in the experiment. R_0 is the distance between the cable and the strand centers. The geometrical radius of the triplet is R_0+a. The three strands will find their natural configuration with no need to reduce the void fraction at this stage.

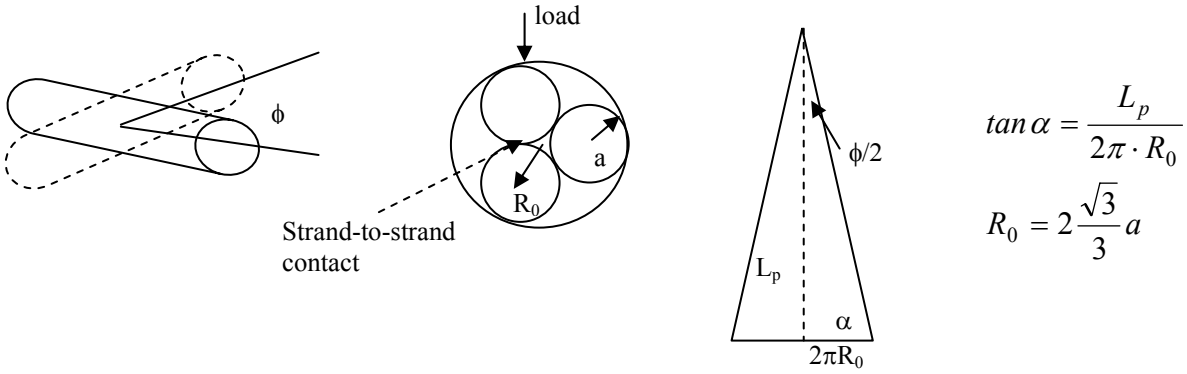

Fig. 5.9 Simplified view to estimate the angle between two strands.

Using the aforementioned parameters, it can be found that $\Omega = \phi$ is 6.549°. Interpolating the values for α and β from Table 5.1 it is easy to find that in this case α is 9.260 and β is 0.263.

Any cross section of the 3-strand cable has the same layout as in Fig. 5.9. Each strand touches any other strand at 2 points as shown in Fig. 5.10. So the total number of contacts per twist pitch is 6 (6 = 3 strands x 2 x 2 divided by 2 since one contact place is counted twice). It is also assumed that the pressure is highest where the area of contact is the lowest. The triplet tested was sitting in a groove and the reaction forces were on a much larger area than the contact forces among strands. In a larger cable the assumption of disregarding the reaction forces is also valid in first approximation because the number of

strands in contact with the surface of the conduit is small compared to the total number of strands. A more comprehensive calculation of the total number of contact points is presented in Chapter 6 where the analysis is extended to a full size cable. In this chapter the parameters and basic equations are given to analyze the behavior of the tested cables.

The number of strand-strand contact points per unit length, N_1, is written as (Eq. 5.17):

$$N_1 = \frac{6}{L_{p1}} \tag{5.17}$$

where L_{p1} is the twist pitch of the first stage.

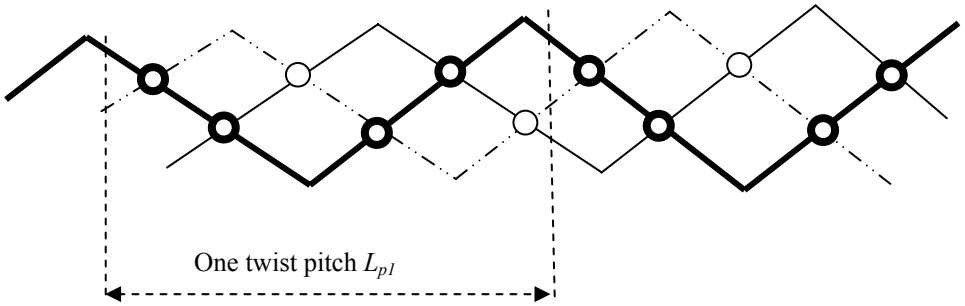

Fig. 5.10 Schematic view of strand-strand contact points of a 3-strand cable.

When the 3-strand cable has the applied force per unit length F_l [N/m], the contact force F_c and the contact effective pressure p_c of each crossed contact point between strands are given respectively by:

$$F_c = \frac{F_l}{N_1} \qquad \text{[N]} \tag{5.18}$$

$$p_c = \frac{F_c}{S_c} \qquad \text{[Pa]} \tag{5.19}$$

where the contact area S_c is obtained from $S_c = \pi \cdot \eta \cdot \xi$ using the semi-axes η, ξ of the contact area given by Eqs. 5.12-5.13.

The deformation between the centers of the strands of each contact point directly contributes to the vertical displacement due to the transverse load; therefore the displacement of the 3-strand cable is given by Eq. 5.14. Calculated displacement obtained from the equation for the 3-strand cable is shown together with the experimental results in Fig. 5.11. The calculated displacement was evaluated for different Young's modulus. If the same Young's modulus used for the single strand analysis is used, the agreement between measurements and calculation is quite poor. A value of E between 3 and 4 GPa ($1/E^* = 2(1-\nu_1^2)/E$) is used in Eq. 5.14 to give a more accurate description to the data for the 3-strand sample.

Both the experimental and calculated results agree well at low load in Fig. 5.11. It is important to notice the difference between the parameter E (Young's modulus) of the analysis describing the overall mechanical property of the material and the dynamic Young's modulus described at the end of Chapter 4. From the measured displacement data we calculated the dynamic transverse Young's modulus using Eq. 3.4 and this shows a good agreement for an assumed strand Young's modulus, E to be used in Eq. 5.14, of 3 or 4 GPa as indicated earlier (Fig. 5.12).

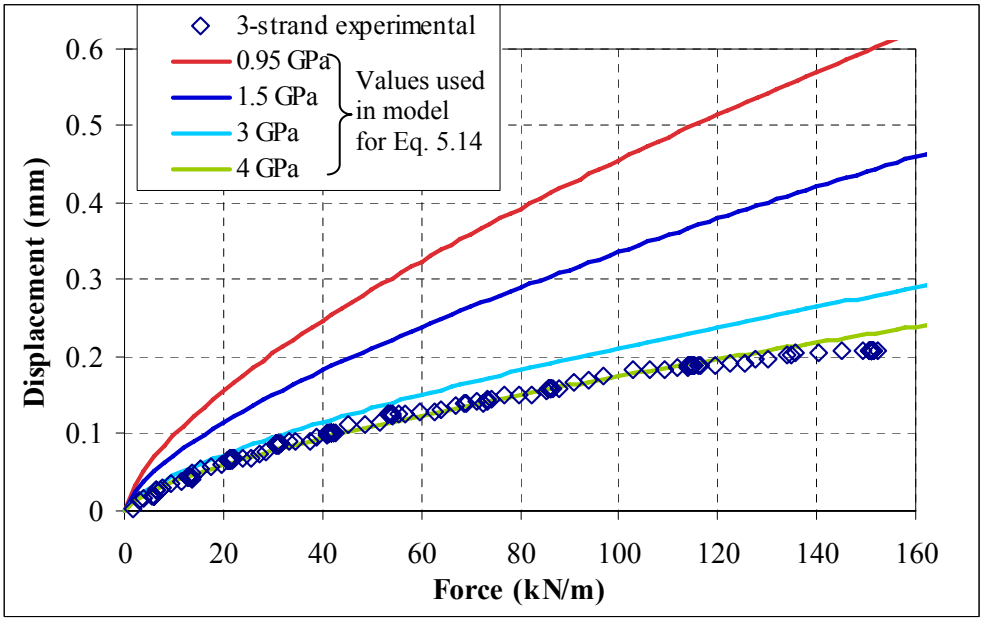

Fig. 5.11 Measured displacements as a function of force per unit length compared to the calculated ones using Eq. 5.28.

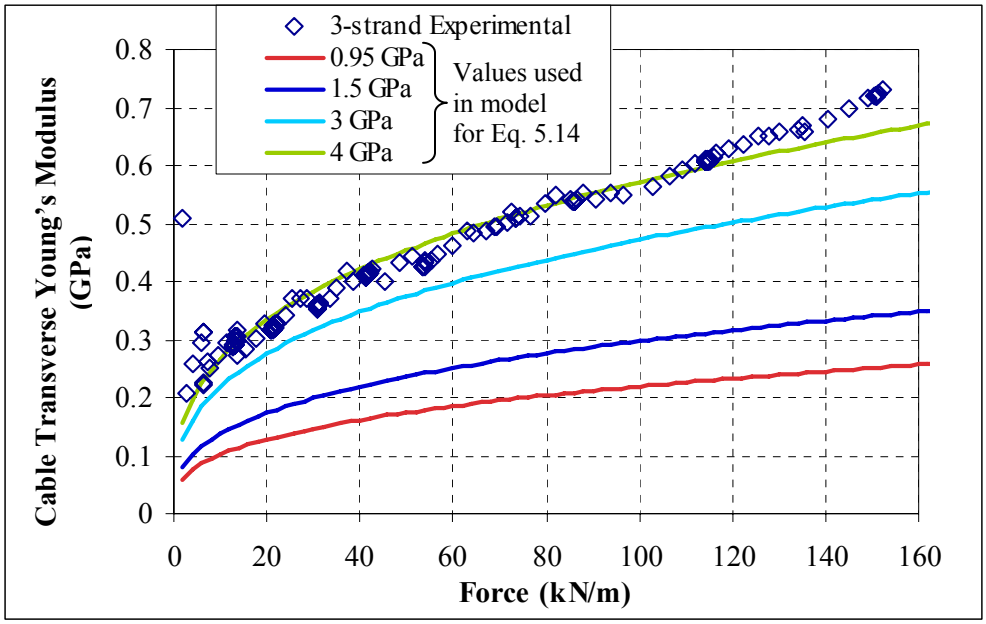

Fig. 5.12 Measured transverse Young's modulus and calculated ones for different cases.

The normalized critical current for the 3-strand cable can be plotted for the different cases considered (Fig. 5.13).

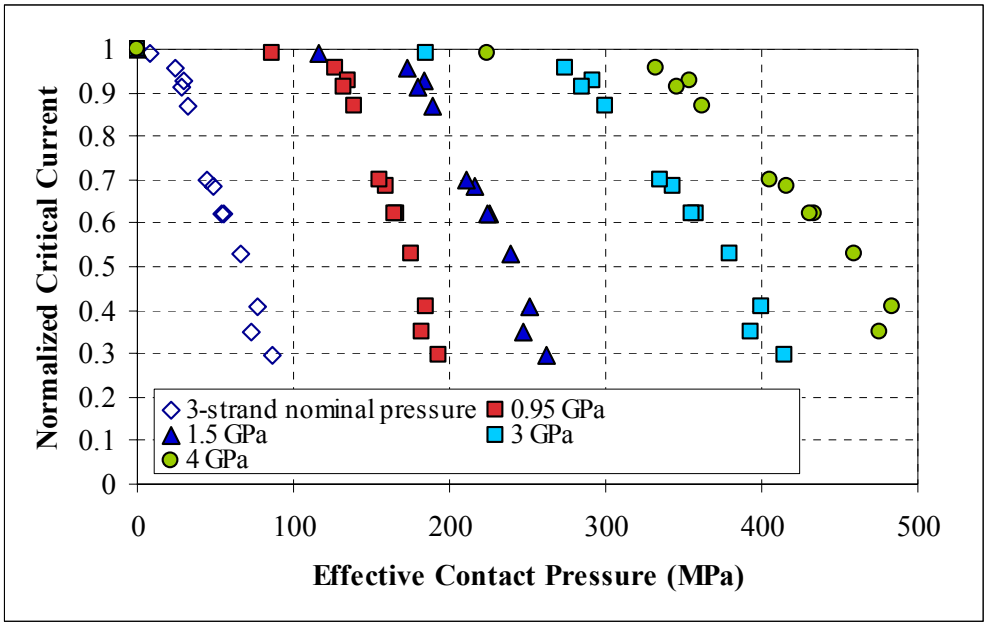

Fig. 5.13 Normalized critical currents as a function of the calculated effective contact pressure with different Young's modulus are compared with those plotted using the nominal pressure.

It can be seen that the absolute values of the contact pressures vary with the Young's modulus quite widely. The Young's modulus values itself is important to know the absolute values of the contact pressures, however the model analysis of an actual cable operation with Lorentz force presented in Chapter 6 will not lose its generality and this parameter does not play a key role in the end analysis.

5.5 45-strand cable

The 45-strand cable can be treated with a similar technique to the one used with the 3-strand cable. The main difficulty for this case is to properly estimate the number of strand-to-strand contacts in the cable and their crossing angles. Two different approaches were used to analyze a 45-strand cable. The first method uses the approximation that the cross section of the cable is square, as commonly used by others, while the second one is a more refined technique maintaining the circular cross section (Fig. 5.14).

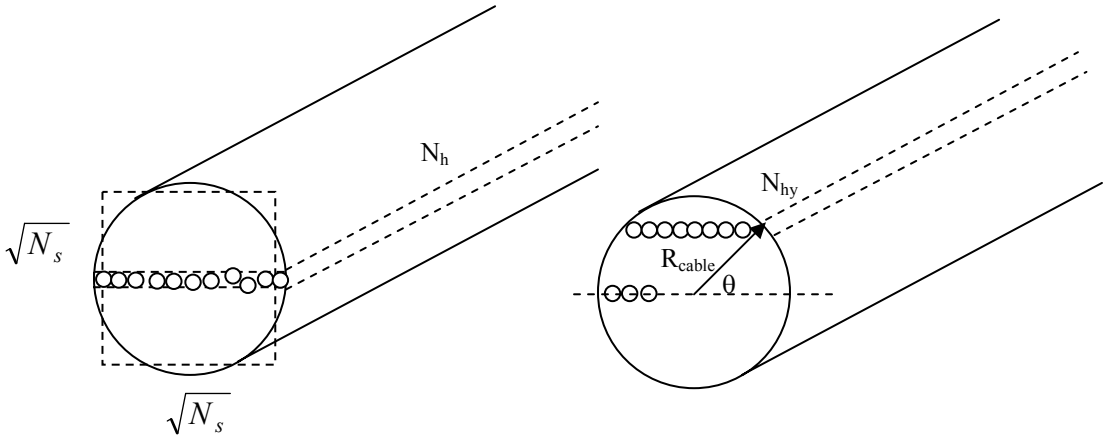

Fig. 5.14 Schematic view of the two different approaches used to analyze a 45-strand cable.

(i) Square Cross-Section Analysis

The 45-strand cable has three different stages (3x3x5) with twist pitches of 45, 85 and 125 mm, respectively.

The cross sections of the three stages are shown in Fig. 5.15. The first stage 3-strand cable has been discussed in the previous section. In the second stage of 3x3, the three 3-strand cables are twisted together in a similar way as that of the first stage. Following a similar analysis of the 3-strand cable case, each 3-strand sub-cable crosses with another 3-strand sub-cable at 2 places in one twist pitch of the second stage (85 mm), and each 3-strand sub-cable sees 2 other sub-cables. Therefore there are a total of 6 places (= 3 sub-cables x 2 x 2 divided by 2 since the same cross point is counted twice). The number of strand-to-strand contact points per unit length, N_2, of the second stage is given by:

$$N_2 = 6 \cdot \frac{n_2}{L_{p2}} \tag{5.20}$$

where n_2 is a parameter giving the number of the strand-to-strand contact points at one crossing point between the 3-strand sub-cables ($n=n_R^2$ discussed in the general analysis in Chapter 6 (ii)), and L_{p2} is the twist pitch length of the second cabling stage. The value of n_2 used is 2.43.

As presented in Chapter 6 (i), for the third stage of a 3x3x5 cable the number of strand-to-strand contact points of the third stage per unit length, N_3, is given as:

$$N_3 = 2 \cdot 5 \cdot \frac{n_3}{L_{p3}} \tag{5.21}$$

where n_3 is the number of the strand-to-strand contact points at one crossing point between the 9-strand sub-cables, and L_{p3} is the twist pitch length of the third cabling stage. The value of n_3 used is 12.15.

Now the total number of strand-to-strand contact points per unit length, $N_{T\text{-}45}$, of a 45-strand cable of 3x3x5 is given using Eqs. 5.20 and 5.21 with the contact points N_1 of the first stage as:

$$N_{T-45} = 15 \cdot N_1 + 5 \cdot N_2 + N_3 = \frac{90}{L_{p1}} + 30 \cdot \frac{n_2}{L_{p2}} + 10 \cdot \frac{n_3}{L_{p3}} \tag{5.22}$$

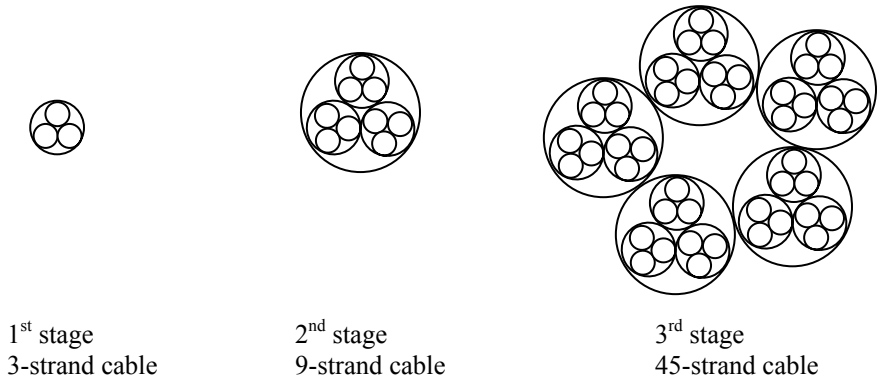

Fig. 5.15 Schematic view of the different stages composing a 45-strand cable.

Substituting the variables n_2 = 2.43, n_3 = 12.15, L_{p1} = 0.045 m, L_{p2} = 0.085 m and L_{p3} = 0.125 m the total number of contacts per unit length $N_{T\text{-}45}$ is 3829.0 m^{-1}.

If the cross section of the cable is taken to be a square instead of a circle, then the number of strand on a horizontal plane is equal to $\sqrt{N_s}$ (N_s being the number of strands, 45 for a 45-strand cable). The number of strand-to strand contact points, N_h, in one horizontal plane per unit cable length is given, under the assumption of a uniform strand distribution in the square cross-section, as follow:

$$N_h = \frac{N_{T-45}}{\sqrt{N_s}} \tag{5.23}$$

The force F_c per strand-to-strand contact is given by Eq. 5.24 (F_l being the total applied force per unit length) in the same way as Eqs. 5.18 and 5.19:

$$F_c = \frac{F_l}{N_h} \quad \text{[N]} \tag{5.24}$$

The contact pressure p_c of the strand-to-strand contact point is obtained by dividing the contact force F_c [N] by the contact area S_c [m^2]:

$$p_c = \frac{F_c}{S_c} \quad \text{[Pa]} \tag{5.25}$$

The contact area S_c is obtained from $S_c = \pi \cdot \eta \cdot \xi$ using the semi-axes η, ξ of the contact area given by Eqs. 5.12-5.13. Note that the semi-axes η, ξ depend on the angle between the cross contact strands which is a function of the twist pitch of the sub-cables. In this analysis the η, ξ for the first stage cable triplet are used for the strand-to-strand contact areas of the higher sub-cables for simplicity as will be discussed in Chapter 6.

To find the total displacement in the transverse direction for a 45-strand cable, it is necessary to evaluate the number of contacts along vertical lines. Those contacts are the ones that need to be considered to calculate the effective displacement. In the square approximation the number of vertical contact-point layers is $N_v = \sqrt{N_s}$ but the strand-to-strand contact points $\sqrt{N_s}$ are not perfectly aligned to contribute directly to the vertical displacement. A fraction of $\sqrt{N_s}$ will be the effective number of contacts for the vertical direction displacement so that the number of vertical displacement contact points is written as:

$$N_v = \rho \cdot \sqrt{N_s} \tag{5.26}$$

where ρ is the probability factor that represents the fraction of vertical contact points aligned along the same line.

As described earlier, the displacement δ_x of a pair of strand-to-strand contact points is given by Eq. 5.14 rewritten here for simplicity:

$$\delta_x = \lambda \cdot \sqrt[3]{\frac{F_c^{\,2}}{(E^*)^2 \cdot K_D}} \tag{5.14}$$

The total vertical displacement $\delta_{x\text{-}tot}$ is then given by (Eq. 5.27):

$$\delta_{x-tot} = \rho \cdot \sqrt{N_s} \cdot \lambda \cdot \sqrt[3]{\frac{F_c^{\,2}}{(E^*)^2 \cdot K_D}} \tag{5.27}$$

The calculated vertical displacement $\delta_{x\text{-}tot}$ is plotted with the experimentally measured results as a function of the load applied for different Young's modulus ($E^* = 2(1-\nu_1^2)/E$) in Fig. 5.16. In this analysis ρ is 0.3 indicating that there is a 30% chance for the strand-to-strand contacts to be aligned vertically. The results obtained show a good agreement between experimental and calculated displacements for values

similar to the 3-strand cable sample (3 and 4 GPa). As done with the 3-strand cable, the displacement measurements and calculated values can be used to evaluate the transverse Young's modulus as shown in Fig. 5.17 showing a good agreement with the 3 and 4 GPa cases.

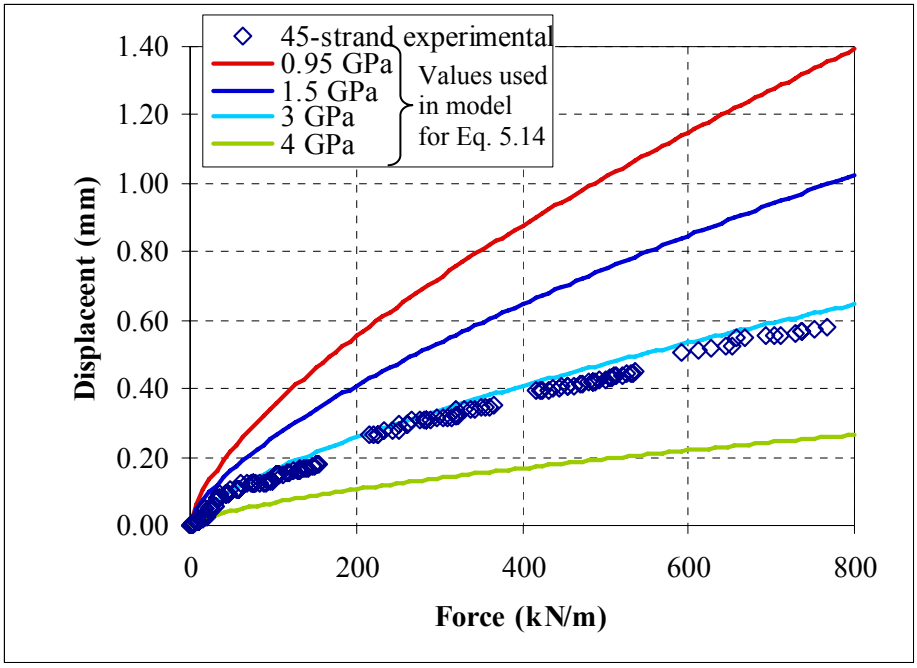

Fig. 5.16 Measured and calculated displacements for the 45-strand cable.

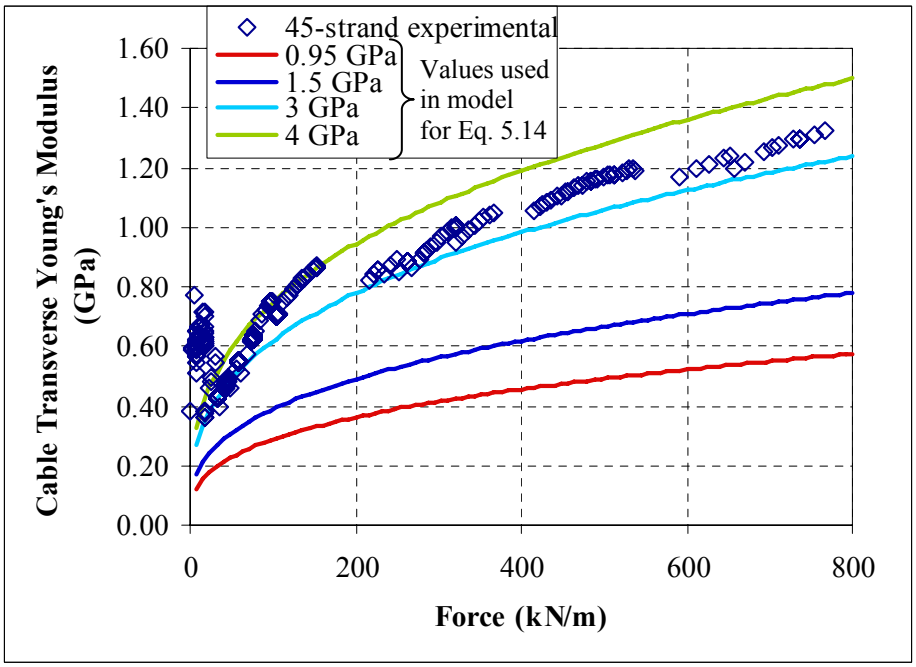

Fig. 5.17 Measured transverse Young's modulus and calculated ones for different cases.

In Fig. 5.18 the normalized critical currents of the 45-strand cable are plotted as a function of the contact pressure evaluated using Eq. 5.25 for the different cases considered.

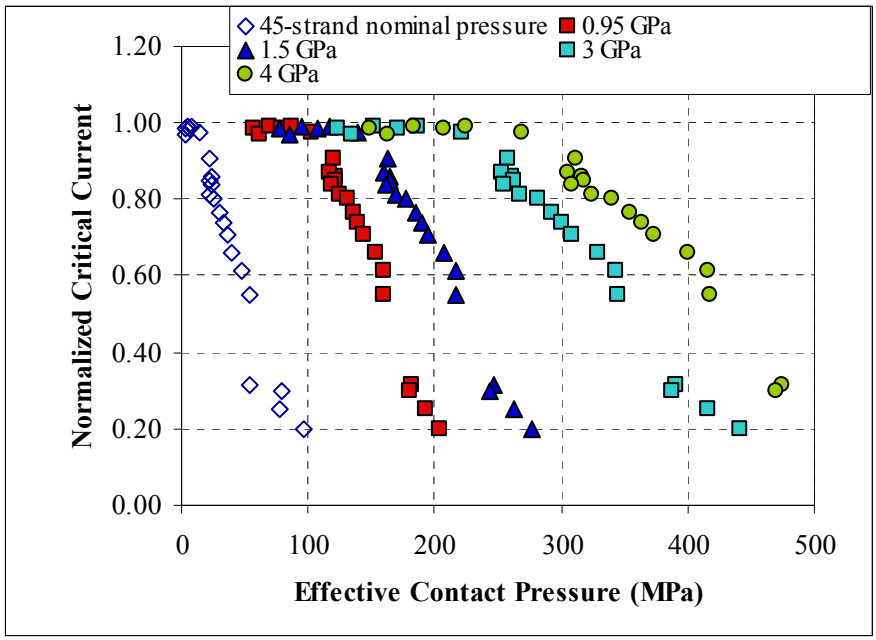

Fig. 5.18 Critical current as a function of contact pressure for the three different cables tested.

In Fig. 5.19 the normalized critical current as a function of effective pressure is plotted for the 3-strand and 45-strand samples for the case of E = 3GPa. The experimental data are fairly close in behavior indicating a similar response to the effective pressure applied.

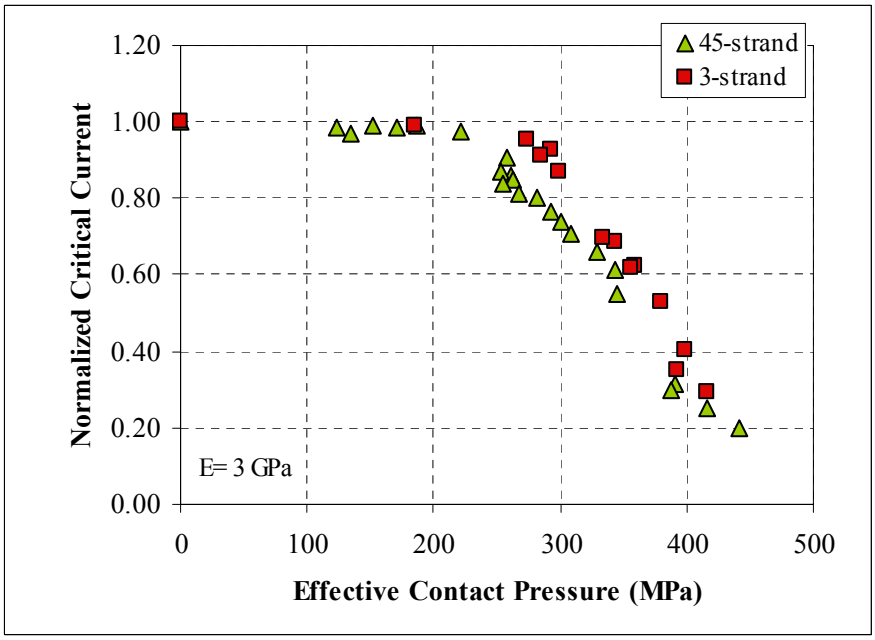

Fig. 5.19 Critical current as a function of effective pressure for the 3-strand and 45-strand cables tested.

The degradation trend of the 45-strand cable is slightly dull compared to the one of the 3-strand cable. This might be due to the fact that a square cross section was used. In a round cable the contact pressure cannot be considered uniform as done in this case. The following section describes another model (using a circular cross section) that will be used to better estimate the behavior of a 45-strand cable under load.

(ii) Circular Cross-Section Analysis

The strand-to-strand contact mechanism of a 45-strand cable using a circular cross section (actual shape) is analyzed. The analysis procedure is similar to the above method used for the square cross section analysis, except that the number of contact points now depends on the location of the horizontal plane (Fig. 5.20). That is, the number of strand-to-strand contact points in the horizontal plane is not constant as in the previous case, but it is given by a function of the vertical coordinate y. The number of strands, n_y, in a horizontal plane of a distance y from the cable center is given by:

$$n_y = \frac{4 \cdot \sqrt{(R_{cable}{}^2 - y^2)} \cdot (1 - v_f) \cos \vartheta}{\pi \cdot a} \tag{5.28}$$

where a is the strand radius, v_f the void fraction and R_{cable} the cable radius.

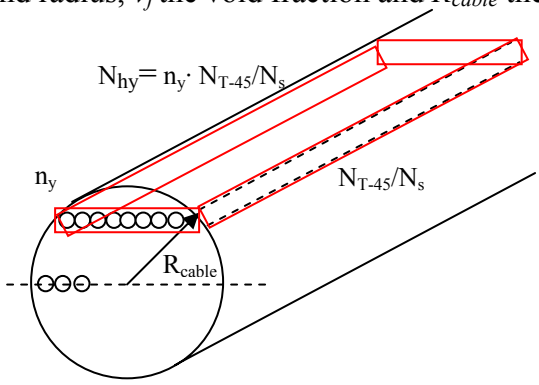

Fig. 5.20 Circular cross section schematic used to estimate the number of contact points.

The number of the strand-to-strand contact points, N_{hy}, in the horizontal plane at a certain y (per unit cable length) is given by Eq. 5.29 using the total number of points $N_{T\text{-}45}$ given by Eq. 5.22:

$$N_{hy} = \frac{N_{T-45}}{N_s} \cdot n_y = \frac{N_{T-45}}{N_s} \cdot \frac{4 \cdot \sqrt{(R_{cable}{}^2 - y^2)} \cdot (1 - v_f) \cdot \cos \vartheta}{\pi \cdot a} \tag{5.29}$$

The strand-to-strand contact force F_{cy} per contact point for a given force per unit length, F_l, is given by:

$$F_{cy} = \frac{F_l}{N_{hy}} \qquad [\mathrm{N}] \tag{5.30}$$

The contact pressure p_{cy} of the strand-to-strand contact is given by:

$$p_{cy} = \frac{F_{cy}}{S_c} \qquad [\mathrm{Pa}] \tag{5.31}$$

where contact area S_c is obtained from $S_c = \pi \cdot \eta \cdot \xi$ using the semi-axes η, ξ of the contact area given by Eqs. 5.12-5.13. Note that the semi-axes η, ξ depend on the contact force which depends on the location y, therefore also the contact area varies with the location y.

The critical current of strands in the cable depends on the contact pressure p_{cy} which is a function of y. As shown earlier, the critical current behavior of the 3-strand cable has been obtained as a function of the contact pressure (Fig. 5.13). From these results, the critical current of each strand is obtained for a given effective contact pressure. The best fit curve obtained from the experimental data is shown in Fig. 5.21 based on the 3-strand data using E=3 GPa. The experimental data points are limited, therefore it was necessary to extend the data set in the most reasonable way as seen in the figure.

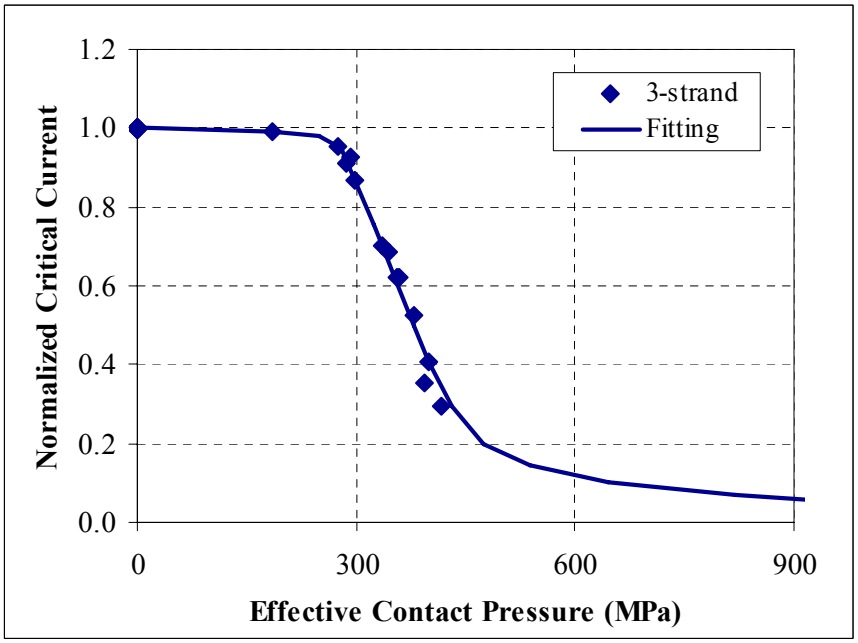

Fig. 5.21 3-strand sample data as a function of effective pressure and the extrapolation used in the analysis.

The total critical current of the round 45-strand cable is given for an untwisted cable model and a twisted cable model by an integration of Eqs. 5.32a and 5.32b, respectively:

Untwisted cable model

$$I_c = 2 \cdot (1 - v_f) \cdot \cos\vartheta \cdot \int_{-R_{cable}}^{R_{cable}} J_{cy-engineering}(p_{cy}) \cdot \sqrt{({R_{cable}}^2 - y^2)} \cdot dy \qquad (5.32a)$$

Twisted cable model

$$I_c = 2\pi \cdot (1 - v_f) \cdot \cos\vartheta \cdot \int_{-R_{cable}}^{0} J_{cy-engineering}(p_{cy}) \cdot y \cdot dy \qquad (5.32b)$$

where $J_{cy\text{-engineering}}(p_{cy})$ is the engineering critical current density as a function of the contact pressure p_{cy} evaluated from the results of the 3-strand experimental results shown in Fig. 5.21.

In the untwisted cable model the strands are parallel along the cable axis. Therefore a location of each strand is identified along the cable by a single value of y. The contact pressure of a strand is also given by the single value of y. On the other hand, in the case of a twisted cable the critical current of the strand could be evaluated with the highest contact-pressure experienced along the twisting if the current sharing of the strand with adjacent strands does not occur. The critical current of a fully twisted cable is given by Eq. 5.32b. In our present experiment the sample length between the voltage taps was 125 mm which was the same length of the last stage twist pitch; therefore the cable was not fully twisted. The twist pitch effect could be partially important since the 45-strand sample cable is in between the two cases.

The integral in Eq. 5.32 is calculated using the Gaussian method of order 40 [5.10]. The critical current equation can be written as:

Untwisted cable model

$$I_c = \int_{b_1}^{b_2} f(y) \cdot dy \cong \frac{b_2 - b_1}{2} \cdot \sum_{i=1}^{40} w_i \cdot f(y_i) \qquad [\mathrm{A}] \qquad (5.33a)$$

$$f(y_i) = 2 \cdot (1 - v_f) \cdot \cos\vartheta \cdot J_{c-engineering}(p_{cy}) \cdot \sqrt{({R_{cable}}^2 - {y_i}^2)}$$
$$= 2 \cdot \frac{(1 - v_f) \cdot \cos\vartheta}{\pi \cdot a^2 \cdot N_s} \frac{I_{c-sin\,glestrand}(p_{cy})}{I_{co-sin\,glestrand}} \cdot \sqrt{({R_{cable}}^2 - {y_i}^2)}$$

where

$b_1 = -R_{cable}$

$b_2 = R_{cable}$

Twisted cable model

$$I_c = \int_{b_1}^{b_2} f(y) \cdot dy \cong \frac{b_2 - b_1}{2} \cdot \sum_{i=1}^{40} w_i \cdot f(y_i) \qquad [\mathrm{A}] \qquad (5.33b)$$

$$f(y_i) = 2\pi \cdot (1 - v_f) \cdot \cos\vartheta \cdot J_{c-engineering}(p_{cy}) \cdot y_i$$
$$= 2 \cdot \frac{(1 - v_f) \cdot \cos\vartheta}{a^2 \cdot N_s} \frac{I_{c-sin\,glestrand}(p_{cy})}{I_{co-sin\,glestrand}} \cdot y_i$$

where

$b_1 = -R_{cable}$

$b_2 = 0$

where w_i and y_i are weights and abscissas of Gaussian integration for order 40, respectively (these numbers are given in Appendix IV). N_s is the number of strands in the cable (45), a is the strand radius (0.41 mm), v_f is the void fraction (0.33), and y_i varies between b_1 and b_2.

After finding the contact pressure using Eq. 5.31, the normalized value of $I_{c-sin\,glestrand} / I_{co-sin\,glestrand}$ at a particular applied load can be evaluated from the 3-strand data of Fig. 5.21, and then the total critical current of the cable is obtained by Eq. 5.33 using Microsoft Excel®. Calculation methods of the critical currents will be given a detailed discussion in the next Chapter.

In addition, the irreversible critical currents of the 45-strand cable were evaluated from the experimental irreversible critical current data of the 3-strand cable.

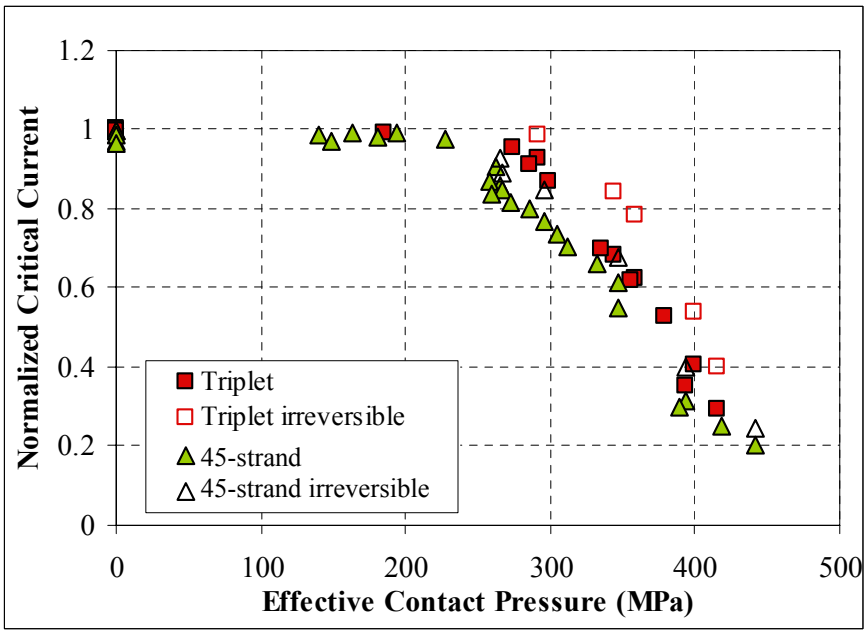

Fig. 5.22 Experimental results as a function of the effective pressure of all cycles.

The irreversible critical current is the current achieved after the load is removed at the end of a cycle. Several cycles were applied during the experiment (see Fig. 4.30). Each time the critical current would partially recover (Fig. 5.22). The recovered critical current is plotted as a function of the maximum pressure applied at each cycle in this figure. The

data points are indicated as “irreversible”. As explained earlier in Chapter 1, the superconducting magnets are cycled and any degradation caused by the cycling operations is undesirable.

In Fig. 5.23 the irreversible critical currents of the 3-strand are plotted again as a function of the peak contact pressure applied. The best fitting of the normalized irreversible critical current $I_{c-irr-strand} / I_{co-strand}$ is shown in Fig. 5.23 by a solid line. This best fitting is used for the analysis of the irreversible critical currents of the 45-strand cable and other cables in Chapter 6.

The irreversible critical current of the 45-strand cable can be calculated from Eq. 5.33 by substituting $I_{c-singlestrand} / I_{co-singlestrand}$ to $I_{c-irr-strand} / I_{co-strand}$ given in Fig. 5.23. In Fig. 5.24 and 5.25 the analytical results are plotted. It can be seen that the experimental values (both critical currents measured during a loading cycle and the irreversible critical currents) are contained between the twisted and untwisted models as expected from the fact that the sample was not fully twisted.

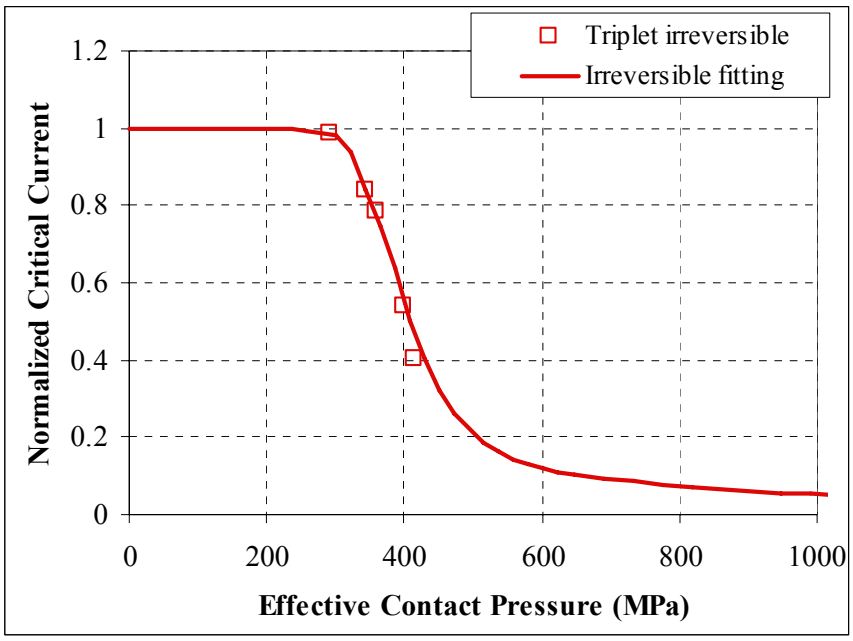

Fig. 5.23 Irreversible critical currents (3-strand measured values and fit) as a function of effective pressure.

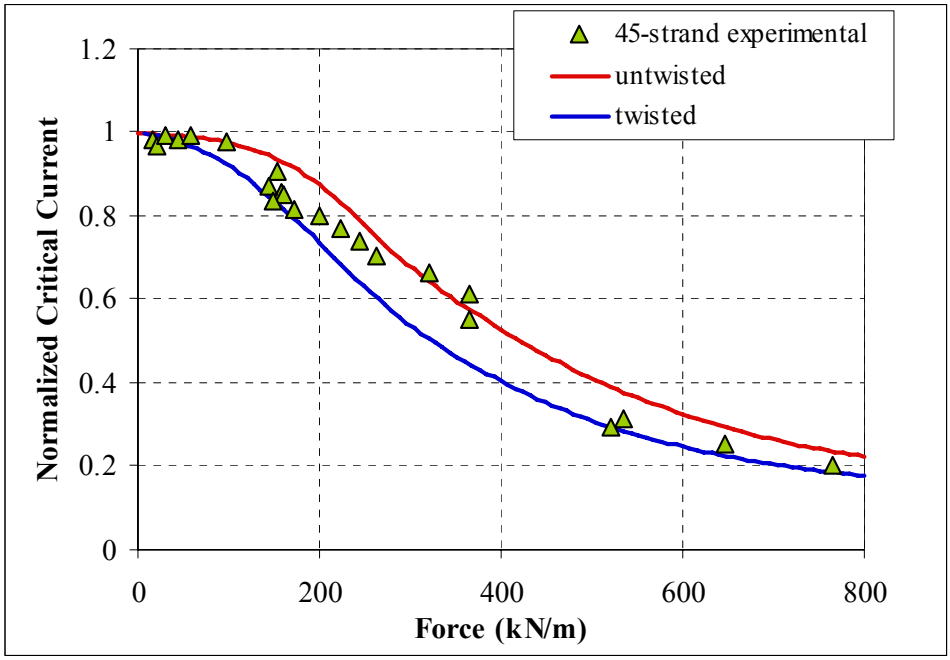

Fig. 5.24 Experimental data and analytical results as a function of effective pressure.

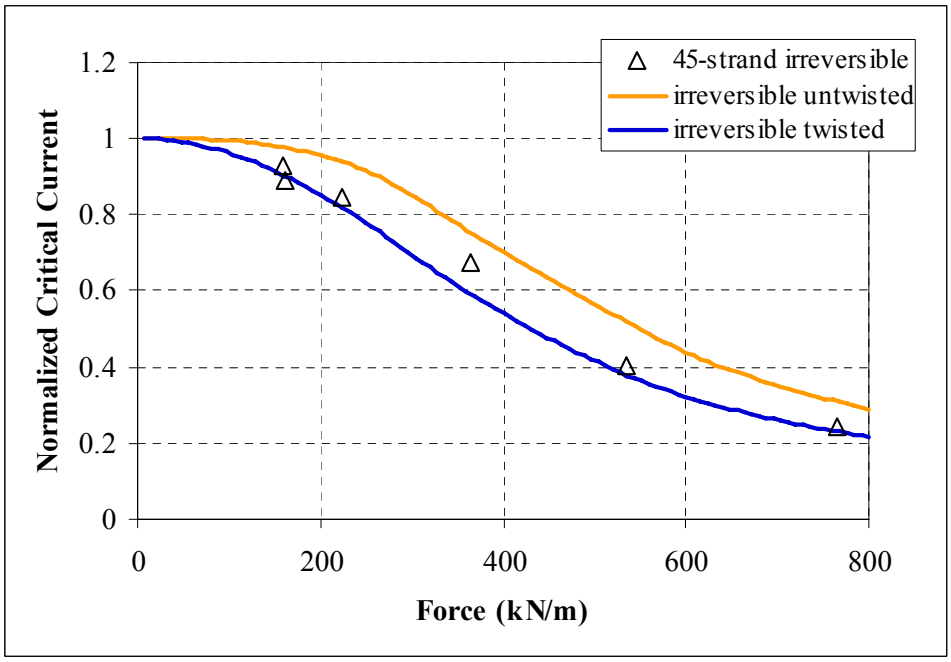

Fig. 5.25 Experimental irreversible data and analytical results as a function of effective pressure.

5.6 Summary

Degradation of the critical currents due to mechanical transverse loads has been investigated considering the contact pressure acting on strands by using contact mechanics theory.

A new theoretical model was developed to analyze the critical current of a superconducting cable taking into account the local contact pressures. Two main models were presented: a parallel strand contact and a crossing-contact between two strands in cable, the former one representing the single strand sample case and the latter the 3-strand and 45-strand samples.

The model analyzes the contact point populations in a cable which is used to find the force on each contact and its pressure.

The developed theory calculates an effective contact pressure between strands accurately. The evaluation of the transverse load effect is very different from the conventional method using the "nominal" pressure obtained from a projection area of the strand diameter (Eq. 5.1).

Experimental data of the critical currents and the displacements due to the mechanical transverse loads obtained for a single strand, 3-strand cable and 45 strand cables have been all well understood considering the local effective pressures acting between strand contacts in a cable.

An analytical model for a circular cross-section cable taking into account strand twisting has been developed and compared with the 45-strand cable test data. Irreversible critical currents of a 45-strand cable have been also analyzed. It was found that the critical current and the irreversible behaviors of a 45-strand cable agreed well with the model analysis based on that the behavior of a triplet.

In this analysis, Young's modulus of a strand for a transverse load was used as fitting parameter to analyze the experimental displacement data. For the single strand data, the Young's modulus value of $E = 0.95$ GPa was selected to obtain the best fit. On the other hand, the larger value of about $E = 4$ GPa gave better fitting for the displacement data of the 3-strand and the 45-strand samples.

It is difficult to determine the absolute values of the transverse Young's modulus of a strand from the present experiments since the experiment itself was not designed to measure Young's modulus. Those measurements would require a dedicated experiment using an absolute method to determine the displacement-force curves. In the present experiment, the Young's modulus values come as extra measurements with little effort and offer insight on the mechanical behavior of the different samples.

Considering the present experimental results and a few reported Young's modulus values of Nb_3Sn strands, for a transverse load, the extended model analysis of the Lorentz load effect for a magnet operation will be performed with the Young's modulus of 3 GPa in the next Chapter. This parameter is to be used in evaluating the semi-axes of the contact area between strands.

It can be concluded from this Chapter that the degradation of the critical current due to transverse loads of a multi-strand cable can be evaluated taking in consideration the local contact pressure between strands. The newly developed model analysis suggests that multi-strand cable degradation could be estimated from the transverse load data of a triplet cable by assuming the triplet curve as reference curve for the critical current and

the irreversible critical current as a function of effective contact pressure as we did for the 45-strand cable in this Chapter.

Chapter 6 will expand the model presented in this Chapter and it will discuss the Lorentz load effect on a 45-strand cable and a full size cable.

CHAPTER 6:
Lorentz Load Effect and Extension to a Full Size Cable

6.1 Introduction

In Chapter 5, the discussion was focused on explaining the results obtained from the experimental measurements of superconducting cables under external mechanical loads. In this Chapter the developed model of contact pressure effects is used to analyze a full size cable degradation due to the electromagnetic Lorentz force. Full size cable degradation due to the Lorentz force is discussed as well as that of a 45-strand cable.

As previously mentioned, the experiment on sub-sized cables required a system to apply a mechanical load to the samples in order to simulate the forces in a full size cable. The natural Lorentz load in a full size cable is too large to be produced in the limited space of an experimental magnet and with currents capability limited to 10 kA, so that a sub-sized cable is used to reproduce similar loads in magnitude with an external mechanical load applied.

Applying an external mechanical load is the only way to simulate the Lorentz load but there is a fundamental difference between the two approaches. The mechanical load is applied uniformly through the cross section of a cable, while the Lorentz load accumulates linearly through the cross section since the Lorentz force is produced by the self current and field distribution (Fig. 6.1).

It is shown in this Chapter that a similar approach as used in Chapter 5 can be used to predict the behavior of a cable during operation considering the natural Lorentz load created by the interaction of current and magnetic field. The model is simplified, and does not lose its generality, by disregarding the central cooling channel of a CICC.

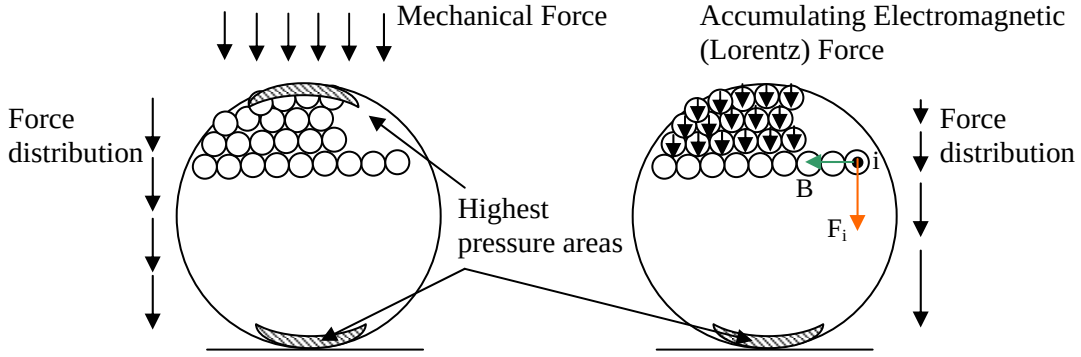

Fig. 6.1 Force configuration for a cable loaded with an external mechanical load and the accumulation of a natural Lorentz load.

6.2 Number of contact points in a multi-strand cable

(i) Crossing contact locations between sub-bundles

In Chapter 5, the modeling presented assumed the number of strand-to-strand contacts to be known and the explanation on how to find this number were deferred to this Chapter. In this section, we present first a model to count contacts in a multi-strand cable.

The number of contacts is calculated for the different stages starting from a 3-strand cable. In general a cable in conduit conductor is produced in multiple stages starting from twisting three strands together and then twisting together triplets or four bundles and so on, until the final stage is reached.

Referring to Fig. 6.2, when a transverse load is applied to a 3-strand cable it is noted that there are six places of strand-to-strand contact points that support the load in one twist pitch length as marked in the figure. At each contact, two strands overlap each other to make one strand-to-strand contact, so that the total number of strand-to-strand contacts is 6 per twist pitch, which is twice the number of strands.

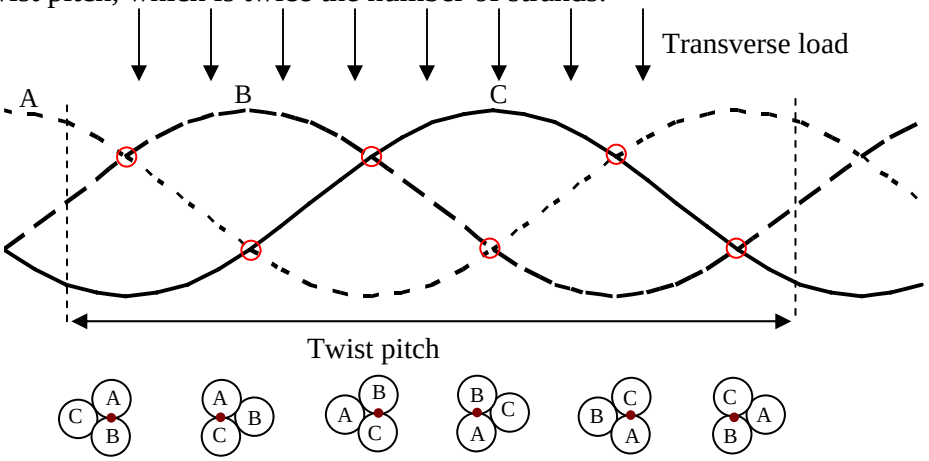

Fig. 6.2 Triplet under transverse load and contact places in one twist pitch length.

The next stage could be composed of three, four or five bundles of 3-strand cables (3x3, 3x4, 3x5) as shown in Fig. 6.3, 6.4 and 6.5, respectively. In the case of three bundles (Fig. 6.3), the number of contact places between two bundles is 6 using the same analogy of the triplet in Fig. 6.2.

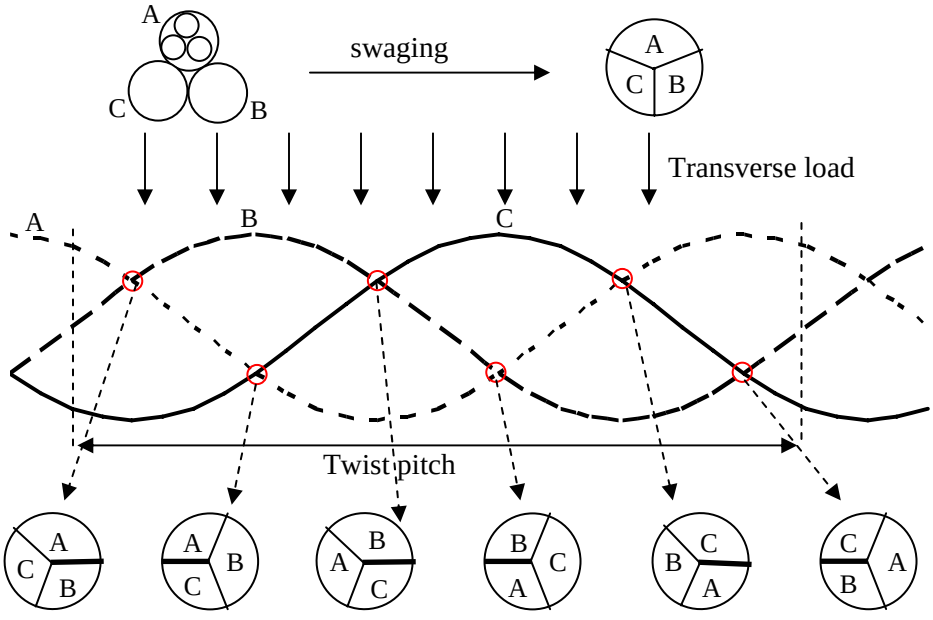

Fig. 6.3 Three-bundle cable under transverse load and contact places in one twist pitch length.

In the case of four bundles the number of effective contact places between bundles is 8 per twist pitch as shown in Fig. 6.4. Note that one cross section produces two contact places such as A-B and C–D in this case.

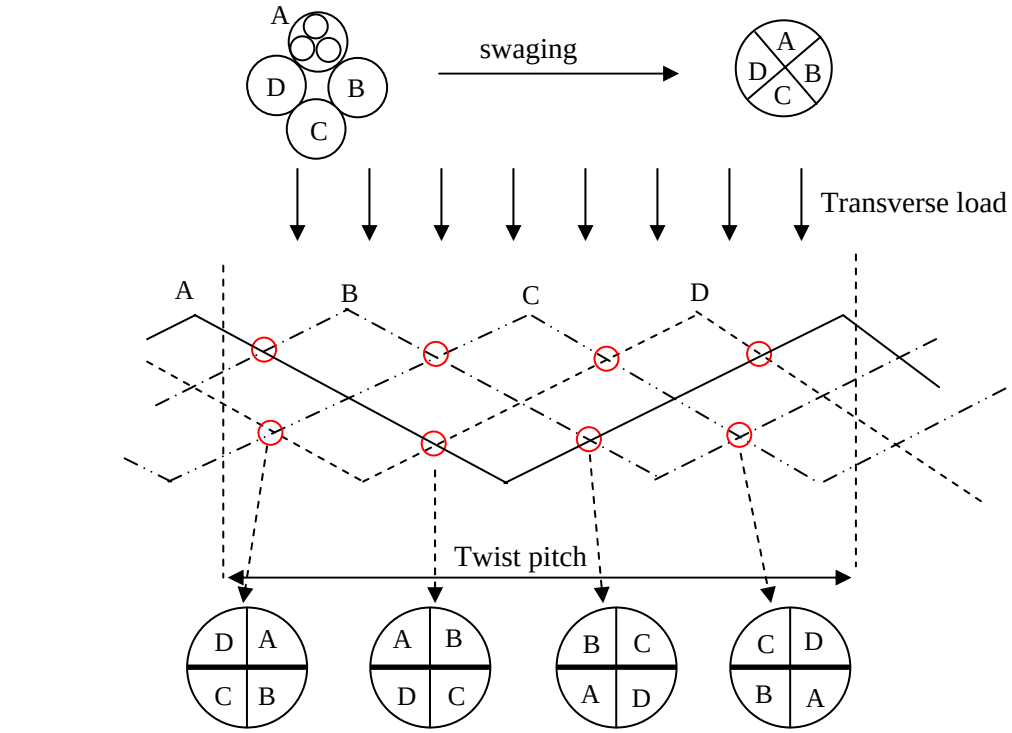

Fig. 6.4 Four-bundle cable under transverse load and contact places in one twist pitch length.

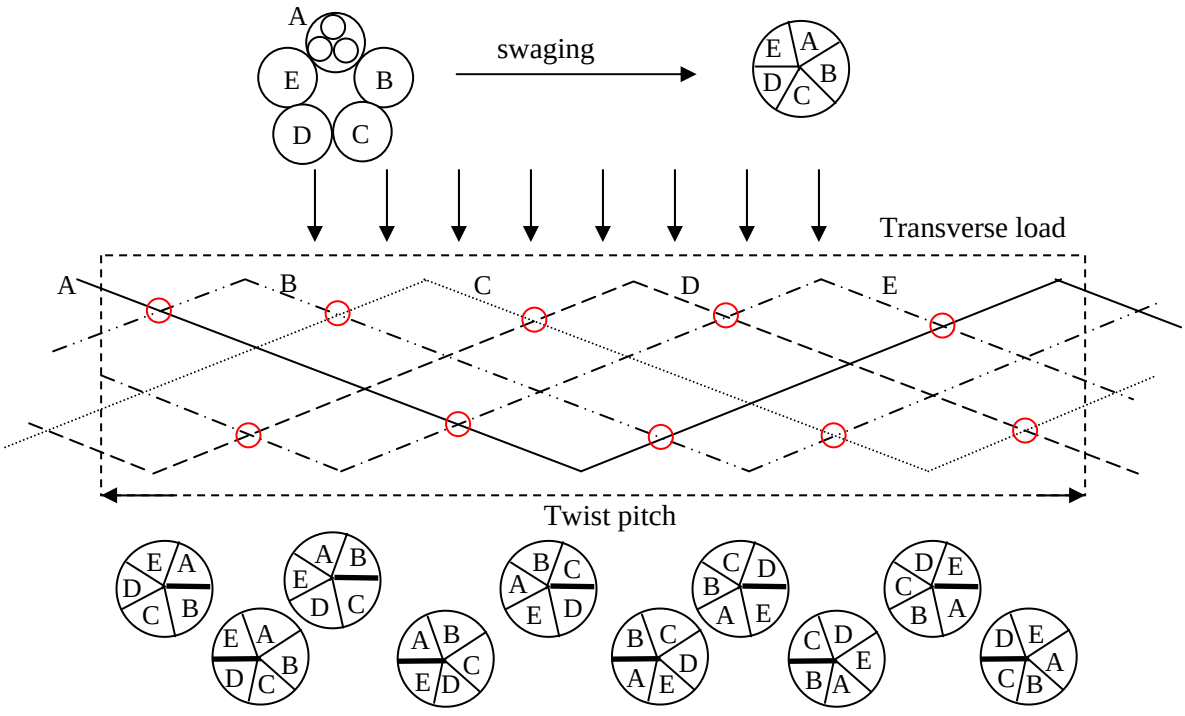

Fig. 6.5 Five-bundle cable under transverse load and contact places in one twist pitch length.

In the case of five bundles the number of bundle-to-bundle contact places is 10 as shown in Fig. 6.5. In general, the contact places between sub-bundles are given by $2 \cdot k$ where k is the number of bundles.

The approach followed with the examples just presented allows concluding that the bundle crossing contact places, $N_{cross,i}$, for the stage i, where the strand-to-strand contact points are created after cable swaging, is given per unit length by Eq. 6.1:

$$N_{cross,i} = \frac{2 \cdot k_i}{L_{p_i}} \tag{6.1}$$

where k_i is the number of bundles and L_{pi} is the twist pitch.

(ii) Number of strand-to-strand contact points

To evaluate the total number of strand-to-strand contact points it is necessary to determine the number of strands in the bundle-to-bundle contact. The strand-to-strand contacts occur between bundles as illustrated in Fig. 6.6. The width of the bundle-to-bundle contact place in a swaged cable can be taken to be equal to the radius of the cable as shown in the figure. Taking into consideration the void fraction in a cable, the radius R is derived as follows:

$$N_s \cdot \pi \cdot a^2 = \pi \cdot R^2 \cdot (1 - v_f) \cdot \cos\vartheta \tag{6.2}$$

$$R = \sqrt{\frac{N_s \cdot a^2}{(1 - v_f) \cdot \cos\vartheta}} \tag{6.3}$$

where N_s is the total number of strands, a the radius of a single strand, v_f the void fraction of the cable and θ is the average angle between strands and the cable axis. For a large cable like the ITER cable $\cos\theta$ is 0.93-0.95 and θ is 15-20°. For smaller cables $\cos\theta > 0.99$ so that it does not have to be taken in consideration in the calculations.

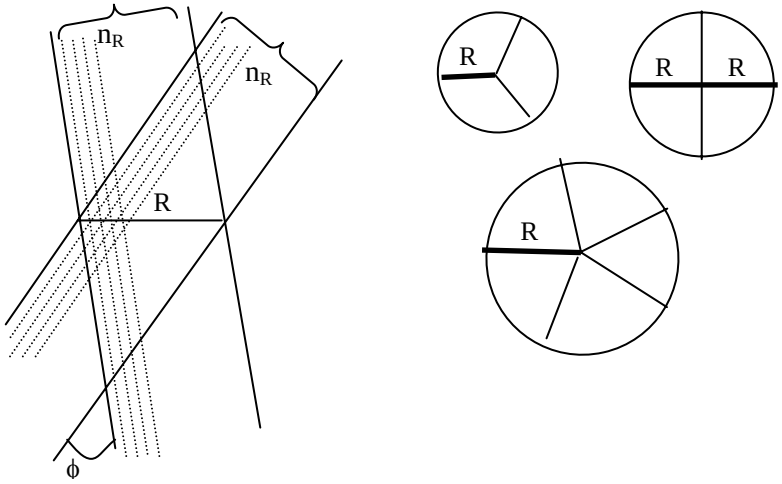

Fig. 6.6 Schematic view of the crossing between bundles in a swaged cable.

The number of strands across the radius R can be written as:

$$n_R = \frac{2 \cdot a \cdot (1 - v_f) \cos\vartheta \cdot R}{\pi \cdot a^2} = \frac{2 \cdot (1 - v_f) \cos\vartheta \cdot R}{\pi \cdot a} = \frac{2 \cdot \sqrt{(1 - v_f) \cdot \cos\vartheta \cdot N_s}}{\pi} \quad (6.4)$$

Both bundles expose the same amount of strands to the contact area as illustrated in Fig. 6.6, so that the cross contact points are given by ${n_R}^2$. For the i[th] stage cable n_R is named n_{Ri}.

Now the strand-to-strand contacts N_i of stage i of a cable with a total number of strands N_{si} of a cable composed of k_1, k_2,…k_k bundles in the first, second,…, k[th] stage is given per unit length as:

$$N_i = 2 \cdot k_i \cdot \frac{{n_{Ri}}^2}{L_{pi}} = 2 \cdot k_i \cdot \frac{4 \cdot (1 - v_f) \cdot \cos\vartheta \cdot N_{si}}{\pi^2 \cdot L_{pi}} \quad (6.5)$$

$$N_{si} = k_1 \cdot k_2 \cdot \ldots \cdot k_i \quad (6.6)$$

A five stages cable can be taken as an example, and Table 6.1 summarizes the main parameters used later in the Chapter.

Table 6.1 Parameters used to calculate the total number of contacts.

Stage i	# bundles (or strands)	Twist pitch L_{pi}	Strands N_{si}	Strand-to-strand contacts N_i
1	k_1	L_{p1}	$N_{s1} = k_1$	$N_1 = 8 \cdot k_1 \cdot \frac{(1 - v_f) \cdot \cos\vartheta \cdot N_{s1}}{\pi^2 \cdot L_{p1}}$
2	k_2	L_{p2}	$N_{s2} = k_1 \cdot k_2$	$N_2 = 8 \cdot k_2 \cdot \frac{(1 - v_f) \cdot \cos\vartheta \cdot N_{s2}}{\pi^2 \cdot L_{p2}}$
3	k_3	L_{p3}	$N_{s3} = k_1 \cdot k_2 \cdot k_3$	$N_3 = 8 \cdot k_3 \cdot \frac{(1 - v_f) \cdot \cos\vartheta \cdot N_{s3}}{\pi^2 \cdot L_{p3}}$
4	k_4	L_{p4}	$N_{s4} = k_1 \cdot k_2 \cdot k_3 \cdot k_4$	$N_4 = 8 \cdot k_4 \cdot \frac{(1 - v_f) \cdot \cos\vartheta \cdot N_{s4}}{\pi^2 \cdot L_{p4}}$
5	k_5	L_{p5}	$N_{s5} = k_1 \cdot k_2 \cdot k_3 \cdot k_4 \cdot k_5$	$N_5 = 8 \cdot k_5 \cdot \frac{(1 - v_f) \cdot \cos\vartheta \cdot N_{s5}}{\pi^2 \cdot L_{p5}}$

The total number of contacts in a multi-strand cable can be then written as:

$$N_T = k_2 \cdot k_3 \cdot k_4 \cdot k_5 \cdot N_1 + k_3 \cdot k_4 \cdot k_5 \cdot N_2 + k_4 \cdot k_5 \cdot N_3 + k_5 \cdot N_4 + N_5 \quad (6.7)$$

For an ITER cable, as described later in this Chapter, the fifth stage cabling is composed of 6 bundles. Each one of the last stage bundles is wrapped with stainless steel foil. Therefore the contacts between bundles during the fifth stage can be disregarded

(N_5 = 0). Furthermore higher stages cabling are the ones that contribute the least to the total number of contact points.

(iii) Contact force and effective contact pressure due to Lorentz force

In order to estimate the Lorentz load effect on the critical current it is necessary to find the number of strands at a plane perpendicular to the Lorentz load (Fig. 6.7) in order to evaluate the contact force and pressure.

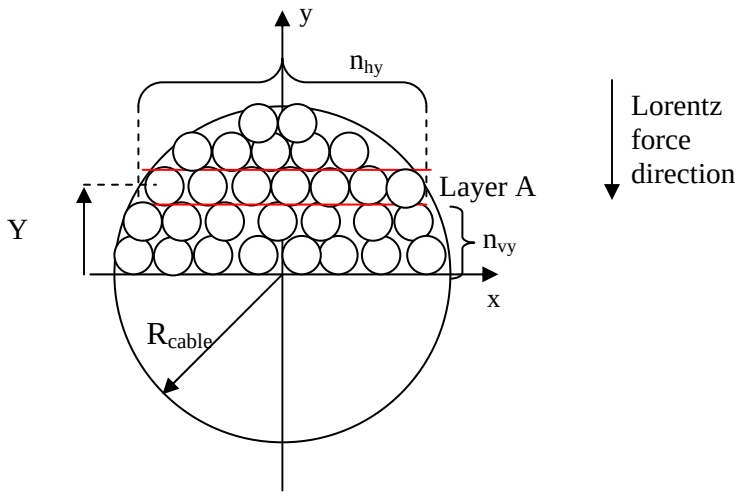

Fig. 6.7 Schematic view of a multi-strand cable indicating the number of strands n_{hy} in layer A at a certain height y.

The number of strands n_{hy} on a horizontal plane at height y when the Lorentz force is vertical, can be written as:

$$n_{hy} = \frac{2\cdot(1-v_f)\cdot\cos\vartheta\cdot\sqrt{(R_{cable}{}^2 - y^2)}\cdot 2a}{\pi\cdot a^2} = \frac{4\cdot(1-v_f)\cdot\cos\vartheta\cdot\sqrt{(R_{cable}{}^2 - y^2)}}{\pi\cdot a} \qquad (6.8)$$

$$\cos\vartheta \equiv \frac{N_s A_{strand}}{A_{cable}(1-v_f)}$$

where v_f is the void fraction, R_{cable} the cable radius, a the strand radius and θ is the average angle between strand and cable axis.

Using the expression in Eq. 6.8 the strand-to-strand contact points N_{hy} in a plane per unit length can be found as:

$$N_{hy} = \frac{N_T}{N_s} n_{hy} \qquad (6.9)$$

where N_T is the total contact points in a cable per unit length evaluated with Eq. 6.7.

The Lorentz force Δf_{LFy} per unit length caused by strands in a layer A at position y = Y (Fig. 6.7) can be written as:

$$\Delta f_{LFy} = B \cdot I_0 \cdot n_{hy} \cdot \frac{N_{sc}}{N_s} \cdot \frac{\Delta y}{2 \cdot a} = B \cdot 2 \cdot (1 - \nu_f) \cdot \cos\vartheta \cdot \sqrt{R_{cable}{}^2 - y^2} \cdot \frac{N_{sc}}{N_s} \cdot \frac{I_{c-single}(p_{cy})}{\pi \cdot a^2} \Delta y \tag{6.10}$$

where B is the magnetic field, and $I_{c\text{-}single}(p_{cy})$ is the critical current of a single strand at a certain contact pressure p_{cy}.

The total force acting on layer A, F_{LFy}, caused by the strands above the strands of layer A and the strands in layer A, is then:

$$F_{LFy} = \int_Y^{R_{cable}} \Delta f_{LFy} = \frac{2 \cdot B \cdot N_{sc}}{\pi \cdot a^2 \cdot N_s} \cdot (1 - \nu_f) \cdot \cos\vartheta \int_Y^{R_{cable}} I_{c-single}(p_{cy}) \cdot \sqrt{R_{cable}{}^2 - y^2}\, dy \tag{6.11}$$

The contact force F_{cy} experienced by a strand in contact with another strand at a particular location y is then given with the total contact point N_{hy} of Eq. 6.9:

$$F_{cy} = \frac{F_{LFy}}{N_{hy}} \tag{6.12}$$

The contact pressure can be obtained as:

$$p_{cy} = \frac{F_{cy}}{S_c} \tag{6.13}$$

here S_c is the area of a contact, as discussed in Chapter 5 evaluated using Eqs. 5.12-5.13 replicated here for the reader's convenience:

$$\eta = \alpha \cdot \left(\frac{F_{cy} \cdot K_D}{E^*} \right)^{1/3} \tag{6.14}$$

$$\xi = \beta \cdot \left(\frac{F_{cy} \cdot K_D}{E^*} \right)^{1/3} \tag{6.15}$$

$$S_c = \pi \cdot \eta \cdot \xi \tag{6.16}$$

where η and ξ are the semi-axes of the ellipse that describe the contact area, $1/E^* = (1-\nu_1^2)/E_1 + (1-\nu_2^2)/E_2$, $K_D = \frac{3}{2} \cdot \frac{1}{1/R_1^{'} + 1/R_2^{'} + 1/R_1^{''} + 1/R_2^{''}} = \frac{3 \cdot a}{4}$.

6.3 Critical current under Lorentz force load

To calculate the critical current of the cable as a function of load two cases will be considered: (i) untwisted and (ii) twisted cables. A real cable would be always twisted, but both cases will be discussed.

(i) Untwisted cable

All the strands in a horizontal plane (like layer A) have the same uniform Lorentz load, so that the currents of the strands are also the same. The total critical current of a cable can be written for an untwisted cable as:

$$I_c = \int_{-R_{cable}}^{R_{cable}} I_{c-single}(p_{cy}) \cdot n_{hy} \cdot \frac{N_{sc}}{N_s} \cdot \frac{dy}{2a} = \\ = \int_{-R_{cable}}^{R_{cable}} I_{c-single}(p_{cy}) \cdot \frac{2N_{sc}}{\pi \cdot a^2 \cdot N_s} \cdot (1-\nu_f) \cdot \cos\vartheta \cdot \sqrt{(R_{cable}{}^2 - y^2)} \frac{dy}{2a} \tag{6.17}$$

The critical current I_c is normalized by the initial value I_{c0}. The normalized critical current I_c^* is given by:

$$I_c^* = \frac{I_c}{I_{c0}} = \int_{-R_{cable}}^{R_{cable}} \frac{I_{c-single}(p_{cy})}{N_{sc} \cdot I_{c0-single}} \cdot \frac{2N_{sc}}{\pi \cdot a^2 \cdot N_s} \cdot (1-\nu_f) \cdot \cos\vartheta \cdot \sqrt{(R_{cable}{}^2 - y^2)} dy \\ = \frac{2}{\pi \cdot a^2 \cdot N_s} \int_{-R_{cable}}^{R_{cable}} \frac{I_{c-single}(p_{cy})}{I_{c0-single}} \cdot (1-\nu_f) \cdot \cos\vartheta \cdot \sqrt{(R_{cable}{}^2 - y^2)} dy \tag{6.18} \\ = \frac{2}{\pi \cdot a^2 \cdot N_s} \int_{-R_{cable}}^{R_{cable}} I_{c-single}^* \cdot (1-\nu_f) \cdot \cos\vartheta \cdot \sqrt{(R_{cable}{}^2 - y^2)} dy$$

The integral is evaluated using the Gaussian method as discusses in Chapter 5 and Appendix IV (w_i being weights of Gaussian integration for order 40):

$$I_c{}^* = \int_{-R_{cable}}^{R_{cable}} f(y) \cdot dy \cong \frac{R_{cable} - (-R_{cable})}{2} \cdot \sum_{i=1}^{40} w_i \cdot f(y_i) \tag{6.19}$$

$$f(y_i) = \frac{2}{\pi \cdot a^2 \cdot N_s} \cdot I_{c-single}^* \cdot \cos\vartheta \cdot \sqrt{(R_{cable}{}^2 - y_i{}^2)} \cdot (1-\nu_f) \tag{6.20}$$

(i) Twisted cable

In the case of a fully twisted cable each strand is assumed to spiral along the cable axis, and in a twist pitch length it will go back to its original location. This means that in a twist pitch length each strand will experience the highest Lorentz load at some point (Fig. 6.8) so that the currents of strands on the same annulus will transport the same current *I(r)* corresponding to the minimum critical current experienced in a twist pitch length. No current sharing among strands is assumed in a twist pitch length. This is true for a chrome plated wire cable.

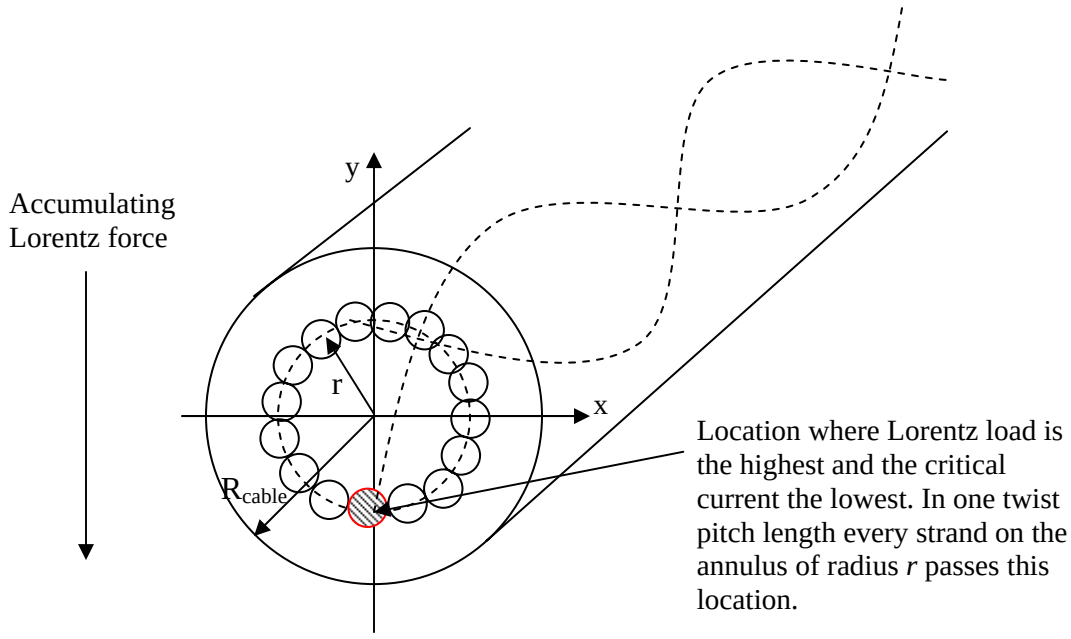

Fig. 6.8 Schematic view of a fully twisted cable.

The total critical current of a twisted cable, I_c, is written as:

$$I_c = \frac{N_{sc}}{N_s} \cdot \frac{2 \cdot (1 - \nu_f) \cdot \cos\vartheta}{a^2} \int_{-R_{cable}}^{0} y \cdot I_{c-single}(p_{cy}) \cdot dy \tag{6.21}$$

The normalized critical current I_c^* is:

$$I_c^* = \frac{I_c}{I_{c0}} = \frac{2 \cdot \pi \cdot (1 - \nu_f) \cdot \cos\vartheta}{N_s \cdot \pi \cdot a^2} \int_{-R_{cable}}^{0} I_{c-single}(p_{cy}) \cdot y dy \tag{6.22}$$

The integral of Eq. 6.22 is again calculated using Gaussian integration but this time the integral is evaluated between $-R_{cable}$ and 0 since the factor $2\pi y$ in the equation takes into account both halves of the cross section.

$$I_c^* = \int_{-R_{cable}}^{0} f(y) \cdot dy \cong \frac{0 - (-R_{cable})}{2} \cdot \sum_{i=1}^{40} w_i \cdot f(y_i) \tag{6.23}$$

$$f(y_i) = \frac{2 \cdot (1 - \nu_f) \cdot \cos\vartheta}{N_s} \cdot \frac{I_{c-single}(p_{cy})}{a^2} \cdot y_i \tag{6.24}$$

6.4 Numerical calculation method of critical current

The integration of the critical currents given in Eq. 6.19 and 6.23 are calculated using Microsoft Excel®. To calculate the contact pressure p_{cy} the strand currents are required.

Therefore an iteration process is used to perform critical current calculations. It is necessary to start off with an assumed current $I_{c\text{-}single}=I_0$ to properly operate the iteration process.

The critical current for an untwisted cable is calculated with the following steps:

(a) Give an initial strand current $I_{c\text{-}single}=I_0$ for the first segment of Gaussian integration $i=1$ (Fig. 6.9)

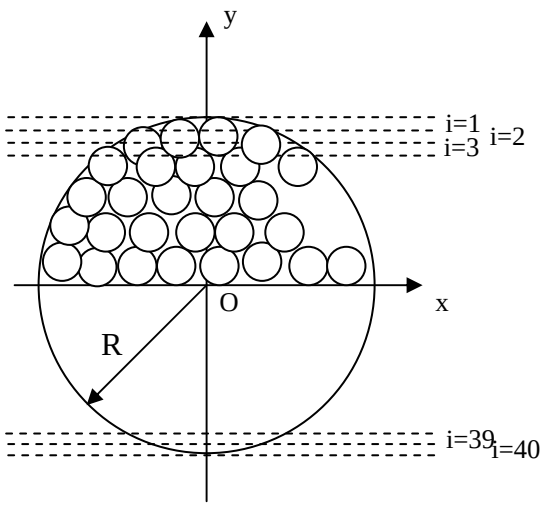

Fig. 6.9 Schematic view of the intervals *i* used to evaluate an integral with the Gaussian method.

(b) Calculate the Lorentz force $f_{LFy}(i=1)$ for segment $i=1$ ($I_{i=1}=I_0$)

$$f_{LFy} = B \cdot I_0 \cdot n_{hy} \cdot \frac{N_{sc}}{N_s} \cdot \frac{y_0 - y_2}{2 \cdot a}, \qquad y_0=R_{cable} \tag{6.25}$$

(c) For $i=2$ the accumulating Lorentz force $F_{LFy}(i=2)$, at the location y corresponding to $i=2$, is:

$$\begin{aligned} F_{LFy} &= f_{LFy}(i=1) + f_{LFy}(i=2) \\ f_{LFy}(i=2) &= B \cdot I_{c-single}(p_{cy}) \cdot n_{hy} \cdot \frac{N_{sc}}{N_s} \cdot \frac{y_1 - y_3}{2 \cdot a} \end{aligned} \tag{6.26}$$

The accumulating force at a location y corresponding to a certain interval i and using Eq. 6.13 for p_{cy} is then:

$$\begin{aligned} F_{LFy} &= f_{LFy}(i=1) + f_{LFy}(i=2) + ... + f_{LFy}(i=i-1) + f_{LFy}(i) \\ f_{LFy}(i) &= B \cdot I_{c-single}(p_{cy}) \cdot n_{hy} \cdot \frac{N_{sc}}{N_s} \cdot \frac{y_{i-1} - y_{i+1}}{2 \cdot a}, \; y_{41} = -R_{cable} \end{aligned} \tag{6.27}$$

(d) Obtain $I_{i=3}$, $I_{i=4}$…$I_{i=40}$ using the measured critical current as a function of the transverse load for a 3-strand as shown in Fig. 5.21 and 5.22 (once the load is known the normalized critical current can be found) and use it to recalculate steps (a)-(c) until the iteration converges.

(e) Obtain total current $I_c = I_{i=1} + I_{i=2} +…+ I_{i=40}$

Table 6.2 summarizes the calculation steps for an untwisted cable.

Table 6.2 Steps used in the iterative process to calculate the normalized critical current of an untwisted cable.

Step Number	*Lorentz Load*	*Contact Force*	*Contact Surface*	*Contact Pressure*	*Normalized Critical Current*
i=1 I_0	f_{LFy-1}	F_{c1}	S_{c1}	P_{c1}	$c_1=I_{c1}/I_{co}$
i=2 $I_0 \cdot c_2$	$f_{LFy-1}+f_{LFy-2}$	F_{c2}	S_{c2}	P_{c2}	$c_2=I_{c2}/I_{co}$
i=3 $I_0 \cdot c_3$	$f_{LFy-1}+f_{LFy-2}+f_{LFy-3}$	F_{c3}	S_{c3}	P_{c3}	$c_3=I_{c3}/I_{co}$
⋮	⋮		⋮	⋮	⋮
i=39 $I_0 \cdot c_{39}$	$f_{LFy-1} + f_{LFy-2} +… + f_{LFy-39}$	F_{c39}	S_{c39}	P_{c39}	$c_{39}=I_{c39}/I_{co}$
i=40 $I_0 \cdot c_{40}$	$f_{LFy-1}+f_{LFy-2}+… +f_{LFy-39}+f_{LFy-40}$	F_{c40}	S_{c40}	P_{c40}	$c_{40}=I_{c40}/I_{co}$

For a twisted cable, the critical current is obtained with two iteration processes. One is the same as the one used for an untwisted cable to calculate a self-consistent current with its Lorentz force effect. The other iteration process is to make a requirement of the strand currents as following: $I_{i=1} = I_{i=40}$, $I_{i=2} = I_{i=39}$, $I_{i=3} = I_{i=38}$, …., $I_i = I_{41-i.}$

Table 6.3 summarizes the calculation steps for a twisted cable.

Table 6.3 Steps used in the iterative process to calculate the normalized critical current of a twisted cable.

Step Number	*Lorentz Load*	*Contact Force*	*Contact Surface*	*Contact Pressure*	*Normalized Critical Current*
i=1 $I_0 \cdot c_{40}$	f_{LFy-1}	F_{c1}	S_{c1}	P_{c1}	$c_1=I_{c40}/I_{co}$
i=2 $I_0 \cdot c_{39}$	$f_{LFy-1}+f_{LFy-2}$	F_{c2}	S_{c2}	P_{c2}	$c_2=I_{c39}/I_{co}$
i=3 $I_0 \cdot c_{38}$	$f_{LFy-1}+f_{LFy-2}+f_{LFy-3}$	F_{c3}	S_{c3}	P_{c3}	$c_3=I_{c38}/I_{co}$
⋮	⋮		⋮	⋮	⋮
i=39 $I_0 \cdot c_{39}$	$f_{LFy-1} + f_{LFy-2} +… + f_{LFy-39}$	F_{c39}	S_{c39}	P_{c39}	$c_{39}=I_{c39}/I_{co}$

6.5 Lorentz load effect on a 45-strand cable

The 45-strand cable tested in the experiment was a hybrid cable in which one of the 3 strands of the first stage triplet had a pure copper wire, the other two being superconductor. The cabling pattern is (2 superconductors +1 copper wire)x3x5 so that the total number of strand N_s = 45 ($k_1 \cdot k_2 \cdot k_3 = 3 \cdot 3 \cdot 5$), and the total number of superconducting strands is N_{sc} =30.

In this case $cos\theta$ is 0.991 and could be disregarded since it has only a 1% effect on the results.

Table 6.4 summarizes the assumed parameters and the calculation of the total number of contacts per unit length (N_T) using Eqs. 6.1-6.7.

Table 6.4 Parameters assumed to estimate the total number of contact points in a 45-strand cable.

Given Parameters			
k_1	3	Field (T)	12
k_2	3	Strand Radius *a* (mm)	0.41
k_3	5	E (GPa)	3
L_{p1} (mm)	45	Poisson's ratio	0.3
L_{p2} (mm)	85	N_s (N_{sc})	45 (30)
L_{p3} (mm)	125	v_f	0.33

Calculated Parameters	
$n_{R1}^2 = \frac{4 \cdot (1 - v_f) \cdot \cos\vartheta \cdot k_1}{\pi^2}$	1*
$n_{R2}^2 = \frac{4 \cdot (1 - v_f) \cdot \cos\vartheta \cdot k_1 \cdot k_2}{\pi^2}$	2.43
$n_{R3}^2 = \frac{4 \cdot (1 - v_f) \cdot \cos\vartheta \cdot k_1 \cdot k_2 \cdot k_3}{\pi^2}$	12.15
$N_1 = 2 \cdot k_1 \cdot \frac{n_{R_1}^2}{L_{p1}}$	133.3
$N_2 = 2 \cdot k_2 \cdot \frac{n_{R_1}^2}{L_{p2}}$	171.5
$N_3 = 2 \cdot k_3 \cdot \frac{n_{R_3}^2}{L_{p3}}$	971.7
$N_T = k_2 \cdot k_3 \cdot N_1 + k_3 \cdot N_2 + N_3$	3829

* The calculated value for n_{R1}^2 is less than 1 but in a real cable this value should be 1.

Using the information in Table 6.4 it is possible to estimate the contact force and pressures using Eqs. 6.10-6.16. The effective contact pressures are then used to estimate the normalized critical current in Eq. 6.18 and Eq. 6.22 for the case of untwisted and twisted cable respectively using the 3-strand cable data of Figs. 5.21 and 5.22 for the loading and irreversible cases respectively.

In general cables are fully twisted so that the most important results will come from this condition.

Several results can be obtained with the modeling discussed in the previous sections. It is interesting to plot the current distribution and the contact pressure distribution in the cable. Fig. 6.10 shows the strand current distribution of both untwisted and twisted cables for the non-degraded strand current of 280 A. It can be seen that the current distribution is very similar for the twisted and untwisted case, but the twisted case shows a symmetric distribution with respect to the center plane ($y=0$) of the cable because the currents are determined by the lowest currents at the highest pressure points (bottom half of the cable $0<y<-R_{cable}$). In the untwisted case the strands at the top of the cable ($y = +R_{cable}$) are the ones carrying the highest current since the accumulating Lorentz force is the smallest.

Similarly the contact pressure distributions for the two cases are very similar, and the pressure is very low at the top of the cable since the strand currents are small. The pressure increases gradually across the cable (the larger number of contacts is in the middle) before peaking at $y = -R_{cable}$.

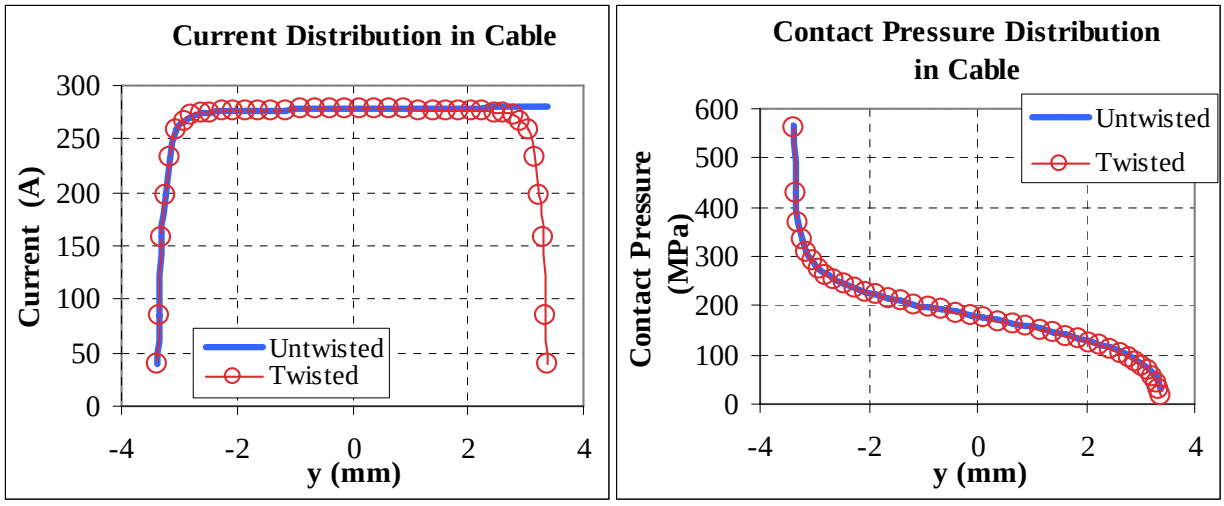

Fig. 6.10 Current distribution and contact pressure distribution in a 45-strand cable as a function of the position across the cable.

Fig. 6.11 shows the cable currents as a function of the nominal current ($I_{single\text{-}strand}$xNumber of strands) which is expected without degradation.

One can see the degradation of the cable currents and the irreversible currents due to the Lorentz loads. Fig. 6.12 shows the degradation rates calculated from the data in Fig. 6.11. It can be clearly seen that the Lorentz load created an inherent degradation which is mostly accentuated when the cable is twisted. For example, in the 45-strand cable test presented in Chapter 4, the cable contained 30 superconducting strands each one capable of carrying a current as high as 280 A. The expected maximum current was 8400 A but in reality the Lorentz force effect degrades the cable which is then expected not to carry more than 7800 A (twisted case).

In Chapter 4, we stated that a 23% initial degradation of the tested 45-strand cable was observed. The present analysis indicates that for the 45-strand cable sample an initial degradation of at most 7.5% should have been expected caused by Lorentz load.

As we mentioned earlier our sample was too short to be considered as a fully twisted sample, so that the expected degradation could range between 1.5% (untwisted case) and

7.5% (twisted case). It is worth to notice that our model predicts degradation caused only by the transverse load due to Lorentz force. Thermal contraction could be responsible of the remaining 15% of the initial degradation. Bending effect due to Lorentz force could also be a cause of some degradation.

Those results indicate that the ideally expected current from single strand data can never be reached since the Lorentz load effect cannot be avoided. The degradation though is not very large for a 45-strand cable.

However this effect is much more important in a large size cable, like an ITER cable, as it will be shown in the next section.

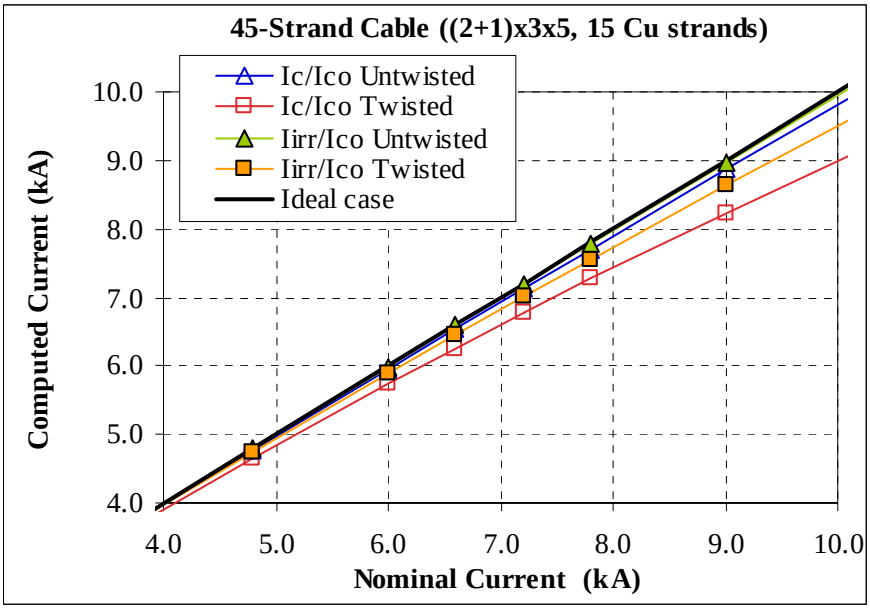

Fig. 6.11 Normalized critical current as a function of nominal current.

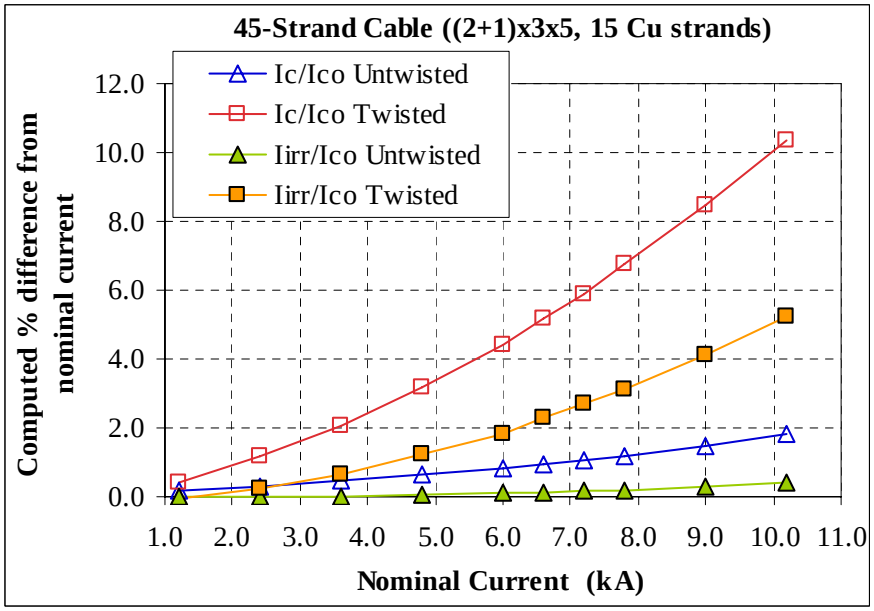

Fig. 6.12 Percent difference between the nominal current case and the expected values considering the natural Lorentz load effect.

6.6 Lorentz load effect for a full size cable

A full size cable of five stages (k_1xk_2xk_3xk_4xk_5) has a total number of strands $N_s = k_1 \cdot k_2 \cdot k_3 \cdot k_4 \cdot k_5$ with the total number of superconducting strands being $N_{sc} = 2 \cdot k_2 \cdot k_3 \cdot k_4 \cdot k_5$ (typically the first stage has 2 superconducting strands and 1 copper strand).

Table 6.5 summarizes the assumed parameters. The calculation of the total number of contacts per unit length (N_T) is obtained using Eqs. 6.1-6.7. This model cable has the original cable pattern proposed for the TF coil in ITER (3x4x4x4x6) with all strands being superconductive.

As expected the number of strand-to-strand contacts in this case is much larger than in the case of the 45-strand cable, and the Lorentz force accumulation is also greatly increased considering the total number of strands (1152).

Table 6.5 Parameters assumed to estimate the total number of contact points in a full size cable.

Given Parameters			
k_1	3	Field (T)	12
k_2	4	Strand Radius *a* (mm)	0.41
k_3	4	E (GPa)	3
k_4	4	Poisson's ratio	0.3
k_5	6	N_s (N_{sc})	1152 (1152)
L_{p1} (mm)	65	v_f	0.33
L_{p2} (mm)	90	$cos\theta$	0.95
L_{p3} (mm)	150		
L_{p4} (mm)	270		
L_{p5} (mm)	430		

Calculated Parameters	
n_{R1}^2	1*
n_{R2}^2	3.10
n_{R3}^2	12.38
n_{R4}^2	49.53
n_{R5}^2	0.00
N_1	92.3
N_2	275.2
N_3	660.4
N_4	1467.5
N_5	0.0
$N_T = k_2 \cdot k_3 \cdot k_4 \cdot k_5 \cdot N_1 + k_3 \cdot k_4 \cdot k_5 \cdot N_2 + k_4 \cdot k_5 \cdot N_3 + k_5 \cdot N_4 + N_5$	86,516

* The calculated value for n_{R1}^2 is less than 1 but in a real cable this value should be 1.

Similar figures to those shown for the 45-strand cable can be obtained for this case using the normalized critical current as a function of load of the 3-strand cable.

Fig. 6.13 shows the computed current and pressure distributions for a non-degraded strand carrying 120 A. In this case the difference in the current distribution in the twisted and untwisted case is much larger than in the case of the 45-strand cable (Fig. 6.10) indicating a larger effect of the accumulated Lorentz load on the current distribution. The larger Lorentz load accumulation, caused by the large number of strands, creates a larger contact pressure between strands, causing a significant degradation on their critical currents.

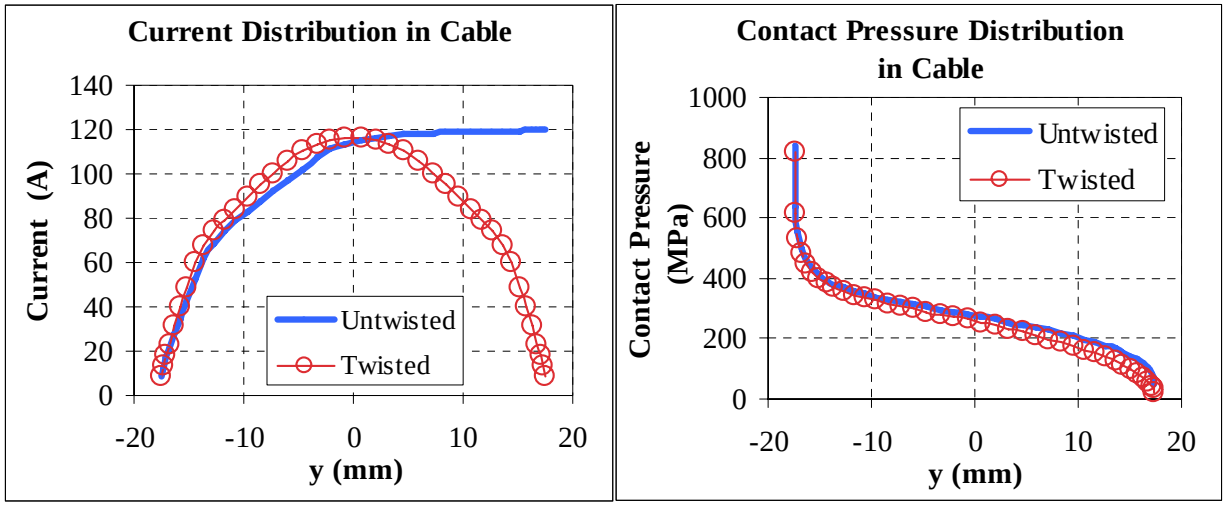

Fig. 6.13 Computed current distribution and contact pressure distribution in a full size cable as a function of the position across the cable.

In Fig. 6.14 the calculated currents are plotted as a function of the expected nominal current without degradation from single strand data. If a fully twisted case is considered the expected initial degradation caused by Lorentz load can be as high as 20% for a current similar to the one expected in the TF coil (68 kA), as shown in Fig. 6.15. The irreversible degradation can be more than 10% at 68 kA.

The model presented only considers degradation caused by transverse load due to the natural Lorentz load (contact pressure between strands). Axial and bending strains caused by thermal contraction and Lorentz load are additional sources of degradation as described in the work done by Mitchell, Zhai and Nijhuis [6.1-6.3]. The overall degradation could then be higher than 20%.

The initial degradation of a full size cable is very important information to know considering that the superconducting magnets are the most expensive component of a tokamak machine. Typically the magnets are designed in a very conservative way and the operation current in each strand is much smaller than its real carrying capability. For example in this cable 1152 strands are used and only 60 A is applied to each strand even if the strands could carry a much higher current.

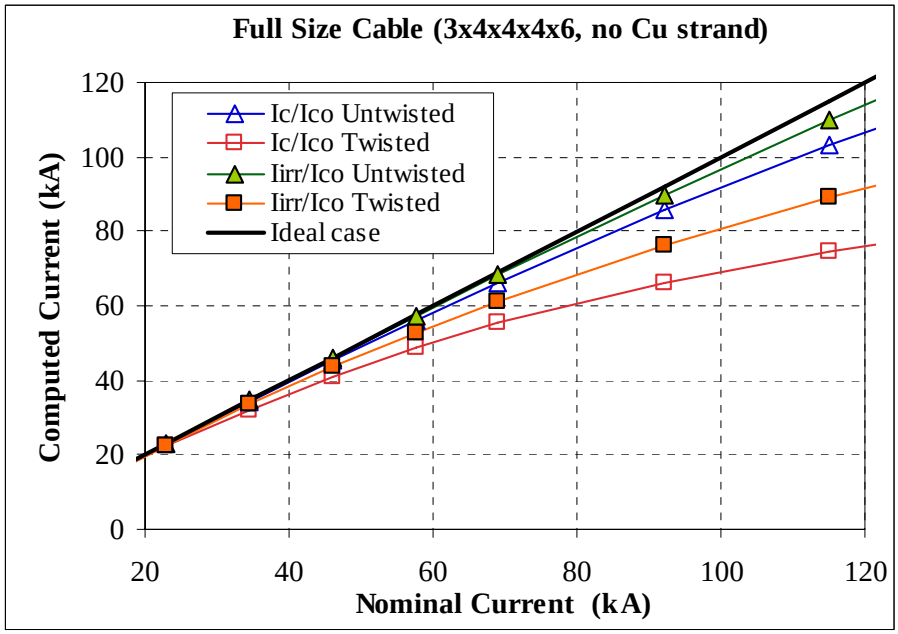

Fig. 6.14 Normalized critical current as a function of the nominal current.

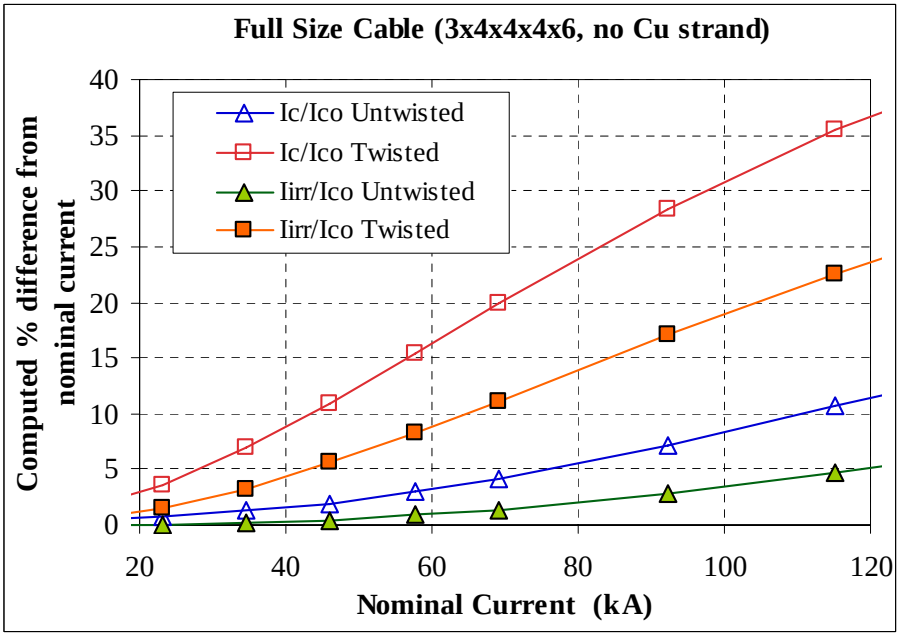

Fig. 6.15 Percent differences between the nominal current and the expected values considering the natural Lorentz load effect.

Parametric studies have been carried out to determine what would be the best configuration for a cable in conduit conductor. The goal is to minimize the inherent Lorentz load effect on the critical current.

Figs. 6.16 and 6.17 show results for five cables in which the same amount of total current is carried by different numbers of strands. Only the twisted cable case is considered since it is the most relevant to a cable design. From these figures it can be clearly seen that the smaller the number of strands the higher is the degradation caused by

the Lorentz load accumulation. This is intuitively obvious considering that if a cable is composed by a smaller number of strands; each one of them has to carry a higher current so that the Lorentz load effect is higher. For example, for a 1152-strand cable carrying a nominal current of 68kA, each strand has to carry a current of 60 A while each strand of a 288-strand cable (used for illustration purposes) should carry at least 236 A if the same wire dimensions are maintained. Therefore the transverse loads are larger and the local contact pressure increases. By increasing the number of strands, the transverse loads can be distributed across the cable and among strands. The smaller cable (288 strands) is expected to have an initial degradation as high as 40% which is 20% more compared to the standard design with 1152 strands.

It is then preferred to have a larger cable with less current for each strand to smear out the Lorentz load effect over a larger number of strands.

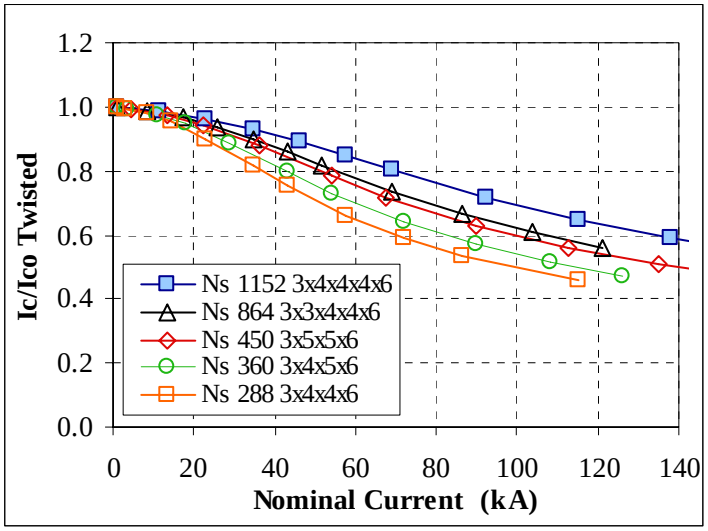

Fig. 6.16 Normalized critical current as function of nominal current for cables with different number of strands.

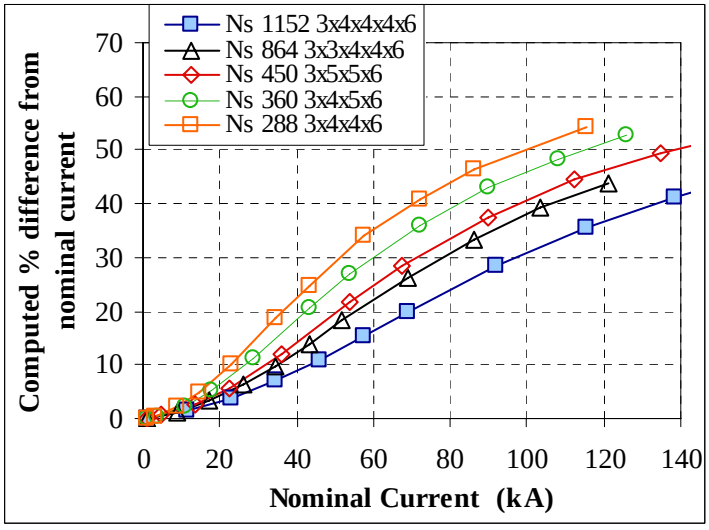

Fig. 6.17 Percent differences between the nominal current and the expected values considering the natural Lorentz load effect for cables with different numbers of strands.

Additionally it can be observed from Fig. 6.17 that the cabling pattern is affecting the degradation. For example, a cable with 864 strands with cable pattern 3x3x4x4x6 has a degradation that is more similar to a cable with 450 strands with cabling pattern 3x5x5x6 than a cable with 1152 strands and a 3x4x4x4x6 pattern. This behavior is driven by the choice of using a second stage composed of 3 bundles reducing the number of contacts. This effect is more clearly represented in Fig. 6.18 where a cable composed of 486 strands and a cabling patter 3x3x3x3x6 shows a larger degradation than a cable composed of 450 strands and a cabling pattern 3x5x5x6 (the degradation is 10% larger).

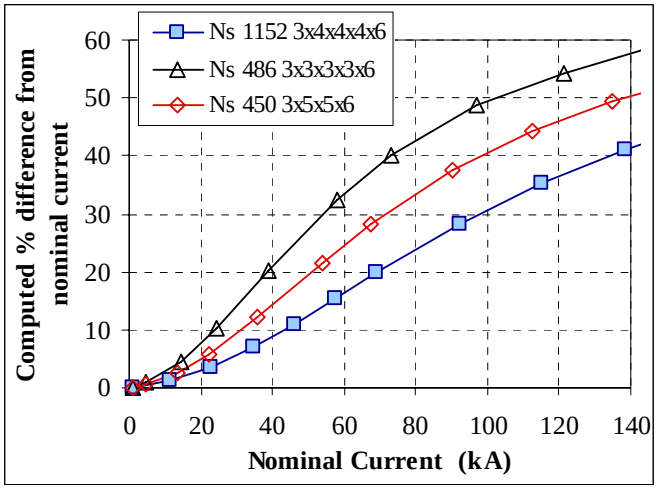

Fig. 6.18 Percent differences between the nominal current and the expected values considering the different cabling patterns used for the cables.

An advantageous configuration for a full size cable would be one in which the 6 petals of the last stage are completely independently supported (each one is mechanically supported and does not affect the other petals) so that the load accumulation is limited to an area which is six times smaller than the original size cable. This configuration, despite increasing the fabrication challenges, would allow reducing the current and the total Lorentz load in each petal. The degradation in this configuration would be 6% at 11.3 kA instead of the 20% at 68 kA for the standard design (Fig. 6.19).

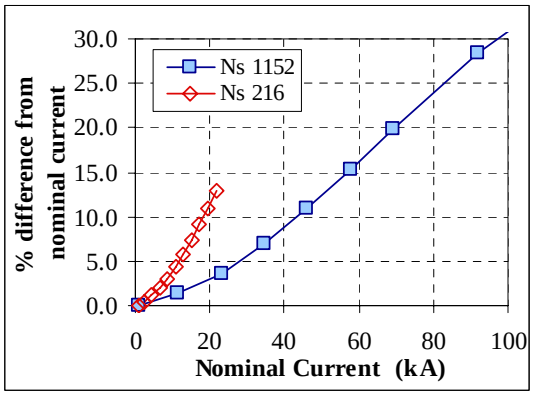

Fig. 6.19 Percent differences between the nominal current and the expected values considering the natural Lorentz load effect for a full size cable and one with isolated petals inside a full size cable.

Another critical parameter of a cable is the cabling pattern and, in particular, the twist pitches selected for each stage composing the cable. The model presented here estimates the number of contacts in a cable, and concludes that the larger the contact-points number is, the better the performance of the cable. In fact a larger number of contacts lead to a smaller pressure felt by each strand which translates into a smaller degradation.

Results for different twist pitch configurations are plotted in Fig. 6.20. The figure reports the nominal case for a TF ITER cable labeled 1x1x1x1x1, indicating that the twist pitches are the nominal ones used for this cable (given in Table 6.5). The other curves have twist pitches that are a fraction of the original twist pitch. For example the label 0.75x1x1x1x1 indicates a cable with a first stage twist pitch that is 25% smaller than the original case and so on.

The figure shows that having shorter twist pitches help the performance of a large cable. For example, a decrease of 25% of the twist pitch of the first stage reduces the initial degradation at 68 kA nominal current from 20% to 16.5%.

These results are in contrast with the ones obtained by Nijhuis and others using their bending model [6.1]. Their work indicates that a longer twist pitch in the first stage helps reducing the bending degradation effect. In their work the transverse load effect is considered to be small but the pressure is evaluated using an averaged value on the diameter of the strand.

As explained in Chapter 5, this averaging approach can be misleading because locally the pressures can be much higher that this nominal value. We believe that their results are very valuable and that indeed the choice of a longer twist pitch could reduce the bending effect. We also believe that the cable design should be a compromise between the bending effect and other sources of degradation present in a cable in conduit conductor namely the transverse Lorentz load contact pressure effect considered in this work.

For example, if the first pitch length is increased by 25% and the twist pitch lengths for the 2nd, 3rd and 4th stages are reduced by 25%, the benefit of reducing the bending effect could be retained but also the Lorentz load initial degradation could be reduce from 20% to 16.9% by increasing the number of contact points (Fig. 6.21).

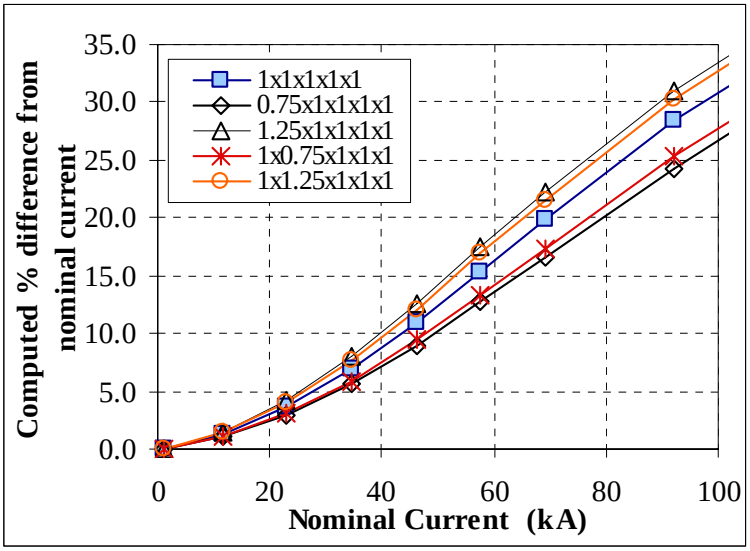

Fig. 6.20 Percent differences between the nominal current and the expected values considering the natural Lorentz load effect for a full size cable with different twist pitch configurations.

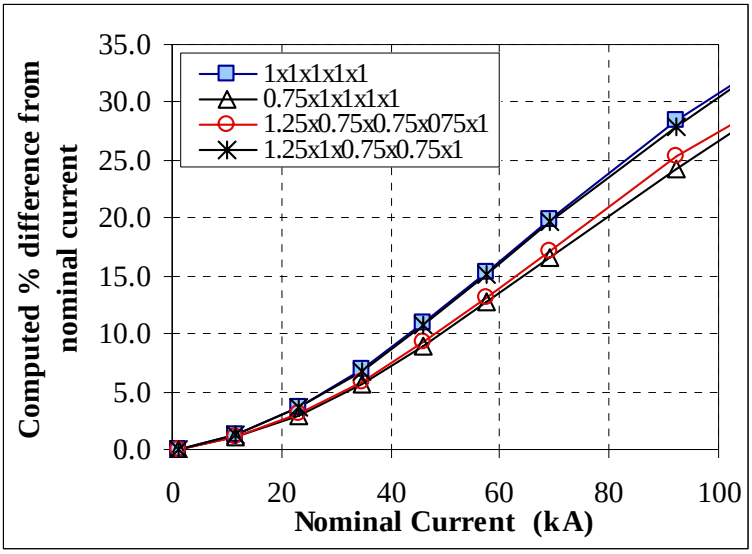

Fig. 6.21 Percent differences between the nominal current and the expected values considering the natural Lorentz load effect for a full size cable with different twist pitch configurations indicating the benefit of shorter twist pitches in the higher stages of the cable configuration.

It is important to stress the fact that the presented model only predicts the degradation caused by transverse contact pressure caused by Lorentz load. Axial and bending strains caused by thermal contraction and by Lorentz load could be additional sources of degradation and can affect the performance of superconducting strands and of a full size cable, as discussed in Chapter 2. Those effects are complementary and not mutually exclusive so all should be considered in the overall performance of a cable. The work of this thesis was limited to the contact pressure effect due to transverse Lorentz load.

For example we can consider the test results of the ITER Central Solenoid Model Coil (CSMC) and the CS Insert which were tested in 1999-2000. The coils were designed with a large safety margin and they reached successfully their operational values but the conductor showed a significant degradation which was unexpected.

The tests in large magnets usually measure the current sharing temperature at a certain current. For example the CS insert was charged up to 40 kA at 12 T and the current sharing temperature measured was 7.6 K. The cable was composed of 1152 strands so that the current for each strand was 34.7 A. The critical current per strand at 7.6 K, 12 T is 70.2 A as estimated with equations discussed in Chapter 2 (Eqs. 2.3-2.10) [6.4]. This indicates that the degradation of the strands in the insert was 51%.

By using the model presented in this chapter with the parameters summarized in Table 6.6, the results of the simulation of the ITER CS Insert are shown in Fig. 6.22. From this figure it can be clearly seen that the expected degradation from the transverse Lorentz load contact pressure effect is 12% which partially explains the estimated experimental degradation of 51%. Axial and bending strains caused by thermal contraction and by Lorentz load could be additional sources of degradation so that overall degradation could be significantly higher than 12%.

Table 6.6 Parameters assumed to estimate the total number of contact points in the CSMC Insert.

Given Parameters			
k_1	3	Field (T)	12
k_2	4	Strand Radius *a* (mm)	0.41
k_3	4	E (GPa)	3
k_4	4	Poisson's ratio	0.3
k_5	6	N_s (N_{sc})	1152 (1152)
L_{p1} (mm)	65	v_f	0.36
L_{p2} (mm)	90	$cos\theta$	0.95
L_{p3} (mm)	150		
L_{p4} (mm)	270		
L_{p5} (mm)	430		

Calculated Parameters	
n_{R1}^2	1*
n_{R2}^2	2.96
n_{R3}^2	11.83
n_{R4}^2	47.31
n_{R5}^2	0.00
N_1	92.3
N_2	262.8
N_3	630.8
N_4	1401.8
N_5	0.0
$N_T = k_2 \cdot k_3 \cdot k_4 \cdot k_5 \cdot N_1 + k_3 \cdot k_4 \cdot k_5 \cdot N_2 + k_4 \cdot k_5 \cdot N_3 + k_5 \cdot N_4 + N_5$	84,229.4

* The calculated value for n_{R1}^2 is less than 1 but in a real cable this value should be 1.

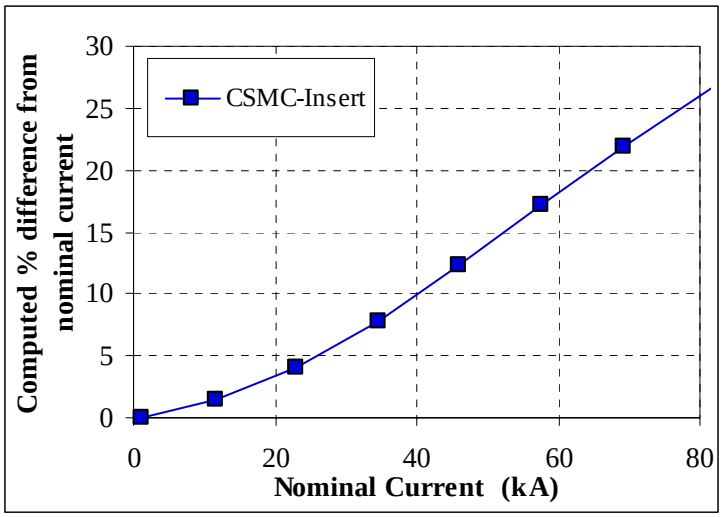

Fig. 6.22 Percent differences between the nominal current and the expected values considering the natural Lorentz load effect for the CSMC Insert cable.

6.7 Summary

Further discussions of the newly developed cross-contact model have been continued in this Chapter. In this model, the critical current degradation occurs due to transverse stresses at the cross contacts between strands. The contact mechanisms between strands and the contact-point population in a cable have been discussed and analyzed. The model has been extended to the transverse load effect on the critical current due to electro-magnetic loads of Lorentz force in a general cable. Simulations of the critical current degradation for a 45-strand cable and an ITER full size cable have been performed.

Lorentz load effects on a 45-strand sub-sized cable similar to the cable used in the experiment have indicated that the critical current degradation of the cable could be as high as 7.5% at the measured critical current of 6.5 kA (the expected current from witness sample was 8.4 kA). It means that one third of the initial degradation 23% observed during the experiment can be explained by the Lorentz force effect. Other major origin of the initial degradation could be the thermal strain effect.

A full size cable simulation using an ITER TF conductor design has revealed degradation as high as 20% due to Lorentz force load itself at the operation current of 68 kA. These simulations have been performed based on the experimental data obtained with the 3-strand cable presented in Chapter 5.

Parametric studies considering different number of strands and different twist pitches have been also presented. Those studies indicated that to obtain the desired current it is better to use a large number of strands with a small current than using a small number of strands with a large current. Additionally, a cable with shorter twist pitches has a smaller degradation caused by the Lorentz load effect. Since other work show a benefit in having longer twist pitches to reduce the bending degradation, a compromised design has been also discussed. It was shown that the number of contacts is greatly reduced if the second stage is composed by 3-bundles increasing the overall degradation of a cable with this cabling pattern.

As mentioned in Chapter 5, the newly developed contact pressure model can predict the critical current degradation of a CICC cable from transverse load data on a 3-strand cable, which is the smallest stage of a multi-stage cable. This means that a relatively simple test could be carried out on a small 3-strand sample and the experimental information could be used to predict degradations of larger cables caused by Lorentz load.

The analysis presented in this Chapter showed for the first time how the transverse Lorentz load effect could result a significant inherent degradation to a large size cable. This is a very important piece of information that could help improve the cable design and explain more appropriately the behavior of a full size cable during operation.

CHAPTER 7:
Conclusions

In the ITER design criteria (DDD 1.1-1.3 Appendix C) documented in the late 1990's and issued before starting the series of ITER model coil tests [7.1], it was stated that transverse stress/strain effects due to the electromagnetic loads on the conductor (IxB) had shown no evidence of critical current degradation in the experiments carried out on full size conductors up to that point. No degradation due to transverse loads had been assumed in the document, and axial strains caused by cool down and an operation hoop force were the only strain effects taken into consideration.

The assumption that the Lorentz load effect was not causing degradation came from experimental results performed on single strands and sub-sized cables. Ekin's strand data [7.2] showed no degradation up to about 100 MPa. The transverse load in a large size cable has been always estimated as an averaged "nominal" pressure over the diameter of the cable giving values of around 20 MPa. Considering those values it is clear that the electromagnetic load should not cause any degradation because the nominal pressures expected for ITER CICC cables have been thought to be in the range of the plateau of the single strand data. Additionally, other work on sub-sized cables showed no degradation up to a nominal pressure of 50 MPa so it was concluded that the Lorentz load would not be a problem [7.3-7.4].

The approach of the nominal pressure could be misleading because the local pressure could be much higher since the strand contact area of circular wires is much smaller, as demonstrated in the newly developed model analysis.

In Chapter 5 it was also concluded that the single strand tested in this work did not show degradation up to 100 MPa (Fig. 5.8) if the pressure is appropriately calculated considering the effective area pressed. Nonetheless, the contact pressures in 3-strand cable and 45-strand cable are higher so that those samples show a worse performance under the applied transverse load showing clearly the effect that electromagnetic load can have on a full size cable.

The primary motivation to start the research work of this thesis was that, although the ITER design criteria was not expecting transverse load effects to be important, at the beginning of 2000's the ITER model coil tests of large CICC cables, which had never been tested before at this scale, showed unexpectedly large degradations.

In 2003, Mitchell proposed a "bending" model taking into account of the transverse loads to explain the ITER cable degradations [7.5]. Since then many research activities have been focused on bending effects on strands and cables with regard to the transverse loads [7.6-7.9]. The bending models with theirs modifications have dominated the understanding of CICC cable degradations for the past few years. The bending effect it is one of the sources of degradation but, as it was found in this thesis work, it is necessary to consider also the transverse load and effective contact pressure among strands caused by the Lorentz load.

We have developed a unique experimental setup studying the effect of transverse load on sub-sized cables. The experiment is the first of a kind following those experiments performed 20 years ago.

Our experiments on a 3-strand sample and a 45-strand sample minimized the thermal mismatch by using a titanium alloy and focused on the effect coming only from a mechanically applied transverse load. As mentioned in Chapter 4, no initial degradation was observed in the 3-strand sample where the Lorentz load effect is very small, and the bending effect is also small since the 3-strand cable is well supported since the natural 3-strand configuration has negligible bending. Applying the mechanical load however, we have observed significant degradation. The degradation observed for a single strand and a 3-strand cable have been poorly correlated by the bending model since there is no room for significant bending in these simple and well supported samples.

The newly developed model based on a contact mechanics theory could explain the experimentally observed degradation. The new model evaluates much more accurately the effective contact pressure which is experienced by superconducting strands in a cable than the conventional method using an averaged "nominal" pressure.

In this research work, first a transverse load test device for a circular cable of one turn was developed as described in Chapter 3. This device could be used with an existing magnet of a 195 mm bore 20 T Bitter magnet at NHMFL, Florida State University. At that time the magnet was the only possible choice for the test of a large sample at a high magnetic field (at least 12 T). Four cable samples, fabricated using ITER wires, were tested in the circular samples using the device. However the test results of all samples as described in Chapter 3 showed significant initial degradations without the plateau of the critical current vs. transverse load behavior observed in the experiments by other researchers. Due to this high initial degradation it was difficult to identify transverse load effects in the cable samples.

Fortunately, later on in 2006, a split superconducting magnet of 14 T became available at NHMFL. This magnet allowed us to develop the new transverse load test device for a hairpin sample which was discussed in Chapter 4. The hairpin sample has two straight sections of 125 mm length where transverse load can be applied. The sample test sections are straight; therefore the device becomes very simple and compact. The device has been developed to systematically investigate the transverse load effects on various samples, such as a single strand, 3-strand, 9-strand and 45-strand cables. The samples could be changed in a short period of time at the test site. It was possible to test one sample in less than one week including the time required to change a sample.

Three samples of a single strand, 3-strand, and 45-strand cables made of ITER TF Oxford pre-production wire were tested. Test results were described in Chapter 4. The measured experimental data of the critical currents and the transverse displacements obtained for these samples were investigated using the newly developed contact pressure model. The critical current degradation of the single strand sample was explained very well using the analytical prediction of a line-contact pressure model with Young's modulus of 0.95 GPa which was obtained from the displacement data.

The experimental data of the 3-strand and 45-strand cables were explained using the cross-contact model. The critical currents and the displacements of these samples agreed with the model analysis. The displacement data were accurately predicted by using a Young's modulus between 3 GPa and 4 GPa, however it has been recognized that more experimental work with regard to characterization of mechanical properties of superconducting wires is required to identify Young's modulus values. Knowledge of mechanical properties of superconductors is very important to establish their behavior under loading conditions but those properties are not very well known making the modeling difficult. It has to be observed though, that even if the absolute values of the contact pressures varies with Young's modulus values, the value of this parameter does not change the overall results of the modeling.

The contact mechanics is used to evaluate the contact areas between strands and the effective contact pressures of the strands in a cable by estimating the total number of contacts. The 3-strand experimental data are used to evaluate the transverse load effect on the total critical current of a large cable.

Two different scenarios were considered in the analysis: the first one simulates the response to a known mechanical load representing our experiments and the second one simulated the accumulating effect of the natural electromagnetic force (Lorentz force) in a cable representing a typical full size cable. The second case requires an iteration process to calculate the degradation of a cable for a given nominal current since the critical current in a particular layer in the cable depends on the critical current dominated by the Lorentz load accumulating through other layers.

It was found that the degradation results of the 3-strand cable test could predict the behavior of the 45-strand cable under the applied mechanical load indicating that the model is appropriate in counting the number of contacts in a cable and predicting its behavior by using the 3-strand sample results.

The model was then expanded to evaluate the initial degradation caused by Lorentz load in the 45-strand cable using the 3-strand data. The simulation result partially explains the initial degradation observed in the experiment. Thermal contraction could be responsible of the remaining 15% of the initial degradation. Bending effect due to Lorentz force could also cause an additional degradation.

The degradation of a large full size cable due to Lorentz load effect was also studied evaluating the total number of contacts in a full size cable and using the behavior of the 3-strand sample to calculate the degradation at a certain transport current. The simulation results indicate that the Lorentz force load degradation of an ITER TF cable could be as high as 20% at the operation current of 68 kA. This degradation is the one caused only by the transverse contact pressure Lorentz load. Axial and bending strains caused by thermal contraction and Lorentz load are additional sources of degradation as described in the work done by Mitchell, Zhai and Nijhuis [7.5-7.7]. The overall degradation could then be higher than 20%.

From the preliminary analysis offered in this thesis work the following areas can be suggested to improve a cable operation:

(1) In order to reduce the contact pressure between strands, a shorter twist pitch resulting in a large number of contacts, especially in the first stage, could be very useful. This is in contrast with work done considering the bending effects and which shows a beneficial effect in having longer twist pitch in the first stage [7.6]. A compromise of the two effects should be considered since both effects are inherent to the cable design and they are both important. This thesis work for the first time showed how the transverse Lorentz load effect plays an important role in the degradation and should be taken into consideration together with the bending and axial effects caused by thermal contraction and Lorentz load.

(2) The cabling pattern should be chosen to minimize the effective contact pressure by maximizing the number of contacts between strands. More contacts between strands would reduce the overall contact pressure and the degradation of the strands.

(3) A rectangular shape cable with the shorter side in the same direction as the Lorentz load would reduce the overall accumulation and degradation. However, rectangular cables are not ideal for the cable preparation because it is not easy to obtain a uniform distribution of the strands in the cable cross section.

(4) Sub-bundles of a large cable could be supported mechanically to reduce the accumulation of loads. Each petal would now be considered an entity by itself.

(5) Using smaller size cables would also reduce the Lorentz load effect but it would increase the length of the conductor and the electrical inductance.

(6) Improving the structure design and mechanical properties of a strand, for example increasing the transverse Young's modulus, will reduce the transverse load degradation of a strand.

The importance of this thesis work is that for the first time the Lorentz load effect is quantitatively shown to be a significant fraction of the inherent degradation of a large Nb_3Sn superconducting cable. The model evaluates the number of contacts among strands and the effective pressure among strands caused by the natural electromagnetic load. More experimental work needs to be carried out to verify our model and many different parameters such as twist pitch, cable pattern, and wire diameter could be investigated to improve and optimize a cable design. Experimental tests are rather expensive, therefore a more systematic procedure should be established among the groups working on the same subjects, in order to eliminate redundant tests and to provide effectively the database on the information necessary to make the appropriate cable designs.

For simulations of a large size cable, it has been proposed to use experimental data of a 3-strand cable. This will be an attractive and simple method to provide information regarding transverse load effects of various wires developed.

Improvements in both theoretical and experimental fields are desired to investigate the transverse stress effects and especially its temperature dependence. This information is needed to establish a transverse stress scaling law.

As already noted, more detailed measurements of the mechanical properties of superconducting strands and cables are necessary to implement finite element simulations that could greatly help the understanding of the detailed strain mechanisms under loading conditions. At present, theoretical analysis of transverse load stress and strain effects on the critical currents is very limited even for a single strand. Appropriate finite element simulations could help determining a general behavior of the critical current density as a function of effective contact pressure.

The understanding of a cable-in-conduit-conductor has greatly improved, however the safety margin used for large superconducting magnets is still very large. Superconducting magnets are the most expensive components of a fusion machine. A better understanding of their limitations to predict their behavior, and more efforts in improving their design are of vital importance to the end goal of producing power reliably and cost effectively.

APPENDIX I:
Sample preparation

Chapters 3 and 4 summarize the test results for the sample tested but avoids describing the details of samples preparation. In this appendix, the entire process is described in details. The preparation of a sample includes different stages:

- Cabling
- Sample preparation
- Assembly of the sample for heat treatment,
- Assembly of the sample for the test and mounting on the probe.

Each stage requires special attention since any damage to the sample before the test could jeopardize its performance. The cabling process is the same for all the samples tested (circular samples and hairpin samples). All the other stages depend on which experimental setup was used.

I.1 Cabling

Once the strand is provided by vendors, cables are prepared using the cabling machine located in the basement of MIT building NW22. The cabling process has been described in details somewhere else [I.1] so only the essential information will be reported in this section. A total of eight different samples have been prepared, four single turn circular samples and four hairpin samples. The circular samples (Fig. I.1) are all composed by 36 superconducting strands (3x3x4 cabling pattern) while the hairpin samples are all different: single superconducting strand, triplet (three superconducting strands), nine-strand cable (9 superconducting strands 3x3 cabling pattern) and 45-strand hybrid cable (30 superconducting strands, 15 pure copper strands (2Sc+1Cu)x3x5 cabling pattern) (Fig. I.2).

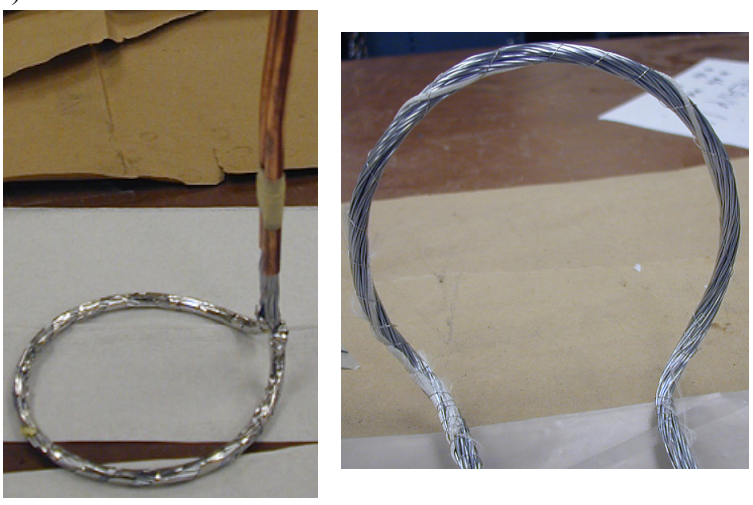

Fig. I.1 Single turn circular sample (about 110 mm diameter). Sample and joints enclosed in copper tubes (left), details of the voltage tap on the sample (right).

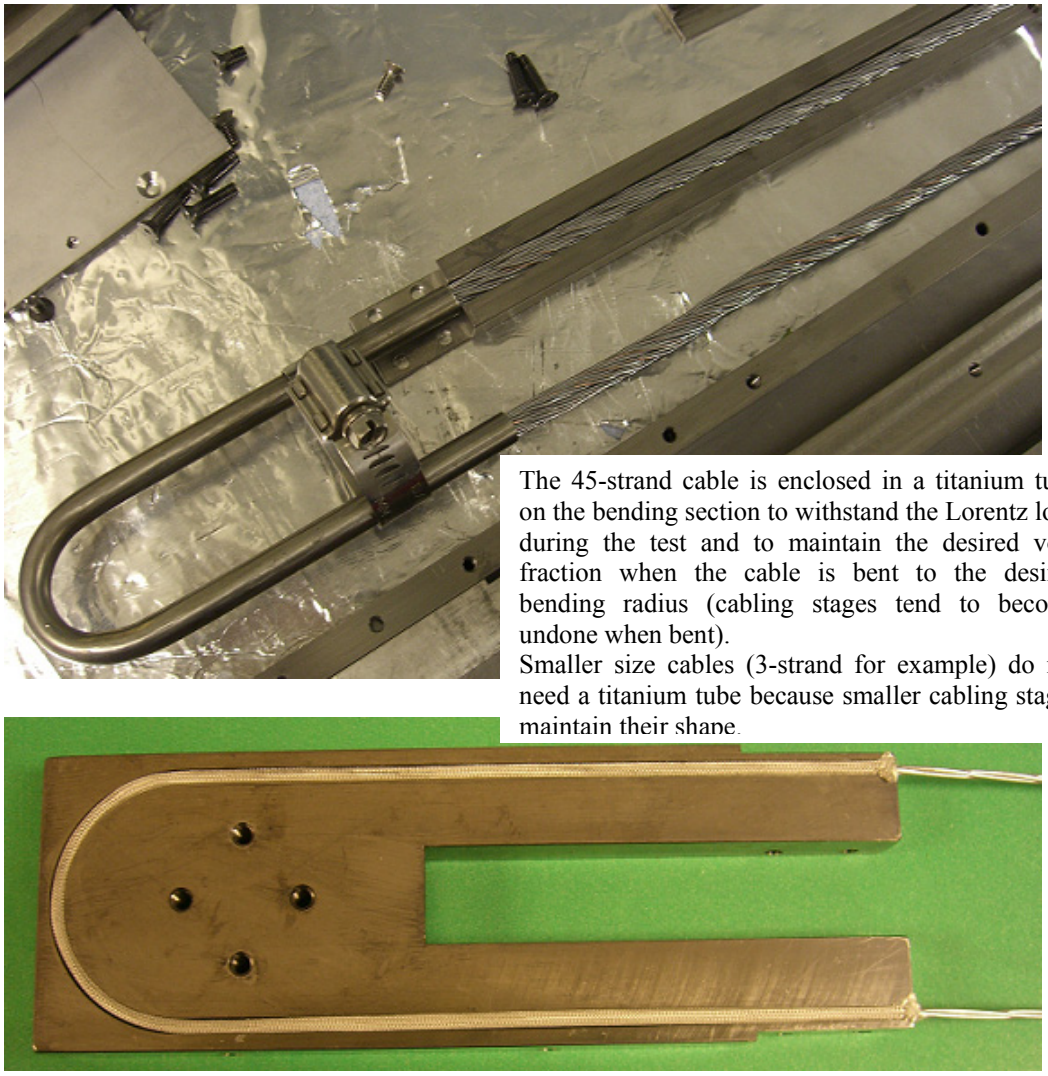

The 45-strand cable is enclosed in a titanium tube on the bending section to withstand the Lorentz load during the test and to maintain the desired void fraction when the cable is bent to the desired bending radius (cabling stages tend to become undone when bent).
Smaller size cables (3-strand for example) do not need a titanium tube because smaller cabling stages maintain their shape.

Fig. I.2 Hairpin samples: 45-strand cable (top), triplet (bottom).

Table I.1 list the type of strands used for the different experiments:

Table I.1 List of strand types used for the experiments. All the strands are Internal Tin type (see Chapter (3-4)).

Sample type	Vendor	MIT Strand ID
36-strand single turn circular cable	IGC	B6771 96-9B
36-strand single turn circular cable	IGC	B6771 96-9B
36-strand single turn circular cable	OKAS	MIT 06-01 (RN2101)
36-strand single turn circular cable	Oxford	MIT 05-05 (CS-OST-A-8405-1)
Single strand hairpin	Oxford	MIT 07-10 (ITER TF B9561-2)
Triplet hairpin	Oxford	MIT 07-10 (ITER TF B9561-2)
9-strand hairpin cable	Oxford	MIT 07-10 (ITER TF B9561-2)
45-strand hybrid hairpin cable	Oxford	MIT 07-10 (ITER TF B9561-2 and ITER TF Oxford Cr-plated Copper)

The dies typically used for cabling are the following:

- Triplet ∅ = 0.07 inches
- 9-strand stage ∅ = 0.118 or 0.127 inches
- 36-strand stage ∅ = 0.246 or 0.265 inches.

Once the cabling process is completed the cables are cut at length: 1.6 m (63 inches) for the single turn circular samples, 1.45 m (57 inches) for the hairpin samples. Those lengths are referring to the total length of the samples (test area and joints). It is necessary to remove the chrome from the two ends of the cable (at least 20" for each end for the circular sample and 11" for the hairpin sample).

Given the fact that the geometries of the two experimental setups were different, the preparation of the samples is also different. Following is a more specific description of the preparation stages for the two sample geometries used in the experiments.

I.2 Single turn circular samples

I.2.a Swaging cable with copper and titanium tubes

Once the cable is ready it is necessary to prepare two pieces of OFHC (oxygen free and high conductivity copper) copper tubes (20" long each) and 1 piece of titanium tube (21" long). All the tubes have a .375" Od, .305" Id, .035" Wall. The copper tubes need to have small holes that will enhance helium cooling during the experiment (hole size ∅ = 1/8"). The holes need to be on one side of the tube.

The copper tubes need to be wiped using lint free cloth with acetone. After this operation they need to be cleaned with hydrochloric acid (37% original) for 10 seconds and with 66% nitric acid for a couple of seconds . It is necessary to rinse them thoroughly with pure water few times and then again with acetone and ethyl alcohol.

It is necessary to remove the chrome from the two ends of the cable (at least 20" for each end) and etch the two copper tubes to assure proper sintering of the current leads length. The cable is inserted in the two pieces of copper and the piece of titanium.

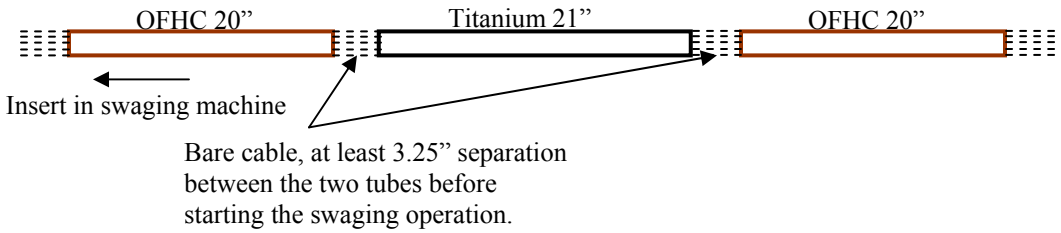

Fig. I.3 Schematic of the cable before being swaged inside copper and titanium tubes.

The swaging process requires the use of 5 different dies for the copper tube (to reach a void fraction of ~23%) and 4 different dies for the titanium one (to reach a void fraction of ~33-35%) (Table I.2).

The tubes should be swaged once at the time starting from one of the copper tube and proceeding in sequence (the cable is stretching at the same time so to avoid bulging of the

cable in the bare cable sections it is necessary to swage the tubes in order). The initial distance between tubes (bare section cables) is ~3.25".

The typical elongation obtained for our cables are: copper tube 20" long becomes ~21.2" long, titanium tube 21" long becomes ~22.75" long. The final distance between the tubes (bare cable sections) is ~2.5".

Attention during the swaging process has to be put in maintaining the holes in the copper tubes to face the same side.

Table I.2. Dies used for the swaging process for the circular samples.

Dies for copper tube	Dies for titanium tube
0.361"	0.361"
0.338"	0.338"
0.325"	0.325"
0.312"	0.312"
0.294"	

I.2 b Bending

Once the swaging of the cable is finished, it is necessary to bend the cable (the section in the titanium tube) to shape the cable to the desired geometry.

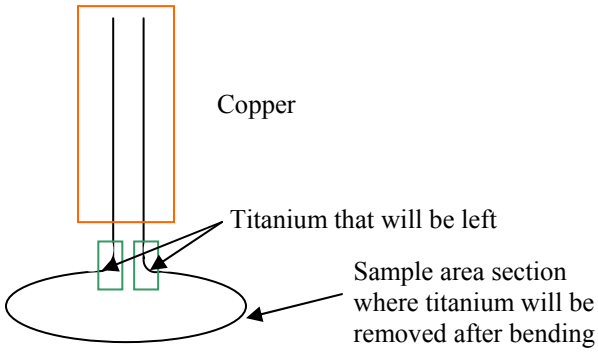

Fig.I.4 Schematic indicating where the titanium will be removed.

Bending the cable is a very delicate operation since the length of the cable needs to be as precise as possible. The titanium will be removed from the circular section and left only on the 90° bending. For this bending process two different bending tools are used:

Fig. I.5 (a) standard bending tool used to perform the 90° bend. (b) Custom designed bending tool for the circular bend.

(a) Standard bending tool for 90° bend (OD 3/8", R 15/16)

Standard bending tool (3/8" OD, 15/16 R)

(b) Specially designed bending tool for circular bend

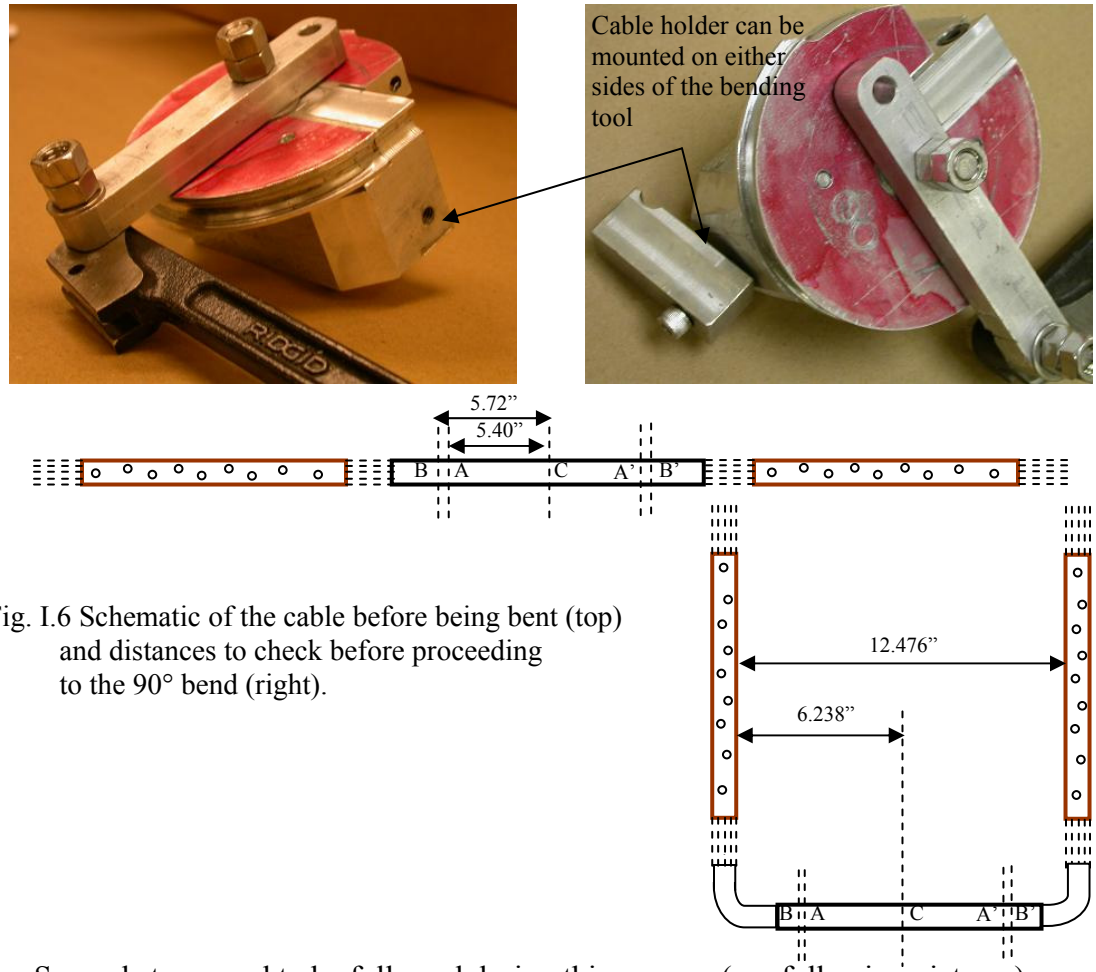

Fig. I.6 Schematic of the cable before being bent (top) and distances to check before proceeding to the 90° bend (right).

Several steps need to be followed during this process (see following pictures):

(i) Mark the center C on the titanium tube

(ii) mark A and A’ (90° sign) at 5.40” from point C. This sign is used to position the bending device at the 0 scale sign and start bending.

(iii) Bend 90° (using the standard bending tool). The holes on the copper tubes should be on the plane.

(iv) Check the 90° arm (6.238”) and if needed adjust the position of A’ for the other arm.

(v) Bend the other arm and check the distance (12.476”).

(vi) Adjust the U-shape cable so that it’s lying on a single plane

(vii) Mark B and B’ at 5.720” from the center. This is the mark that should be used to start removing the titanium tube (so that the bare cable has a total length of 11.44”= 289.56 mm).

(viii) Make the circular bending using the specially designed (for this sample fabrication) bending tool and making sure the holes on copper tubes are on the outer surface (bend the U-shape cable inside the paper in the schematic above). Further bending might be necessary at the final part of the circular bend (at the 90 bend) in order to have a more circular shape. This is usually a difficult step and to apply a stronger force to shape the sample at the corner it is necessary to use a G10 block.

Fig. I.7 Different stages to prepare the circular sample and the 90° bending so that the current leads are perpendicular to the plane where the circular sample lie.

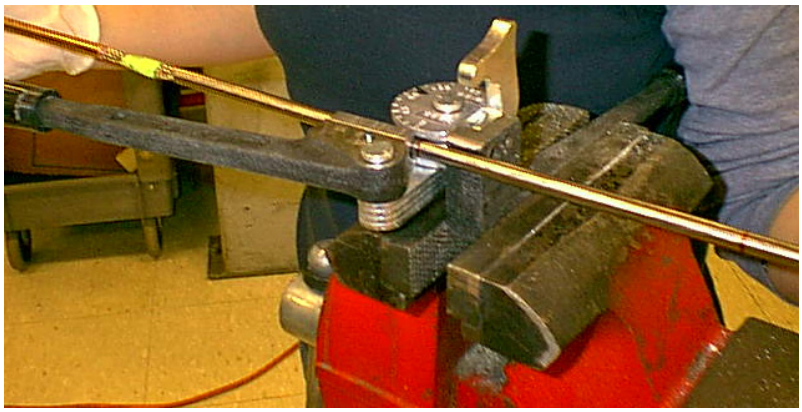

Sample enclosed in copper tubes and titanium tube ready to be bent using the standard bending tool (for 90° bend)

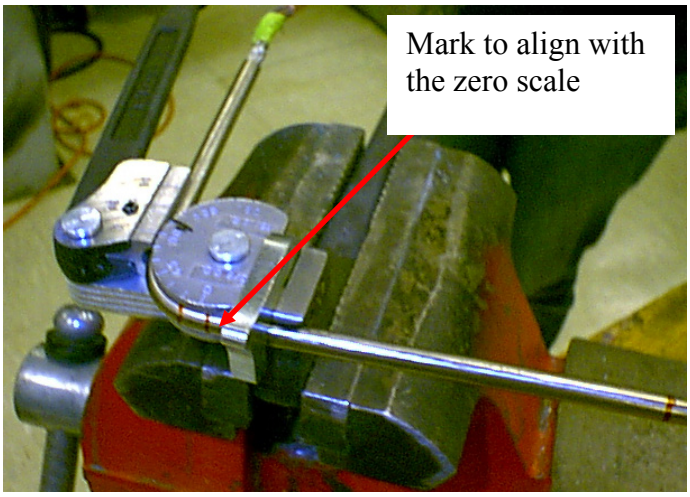

Sample after the first 90° bend. The sample is placed so that the sign indicated is on the zero scale of the bending tool) before starting the bend.

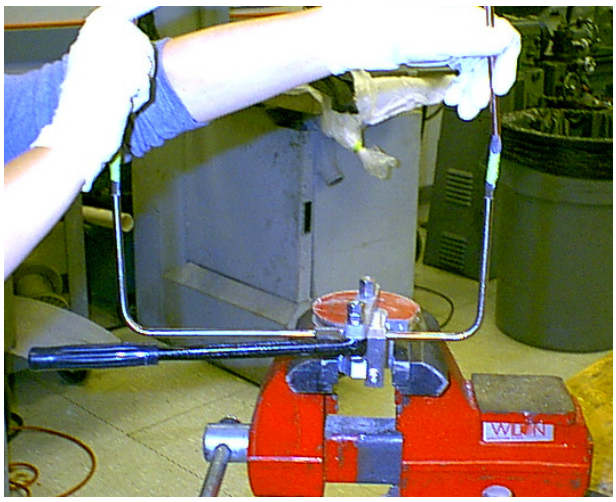

Sample after the two 90° bends. The U-shape sample is on a single plane and the holes on the copper tubes are on the same side of the sample.

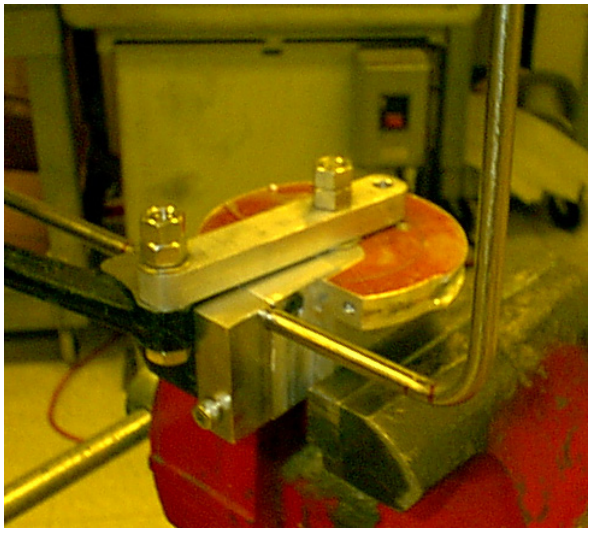

Sample placed in the customized bending tool before starting the circular bend.
The sample is placed so that when it is bent the holes on the copper tubes face the outside.

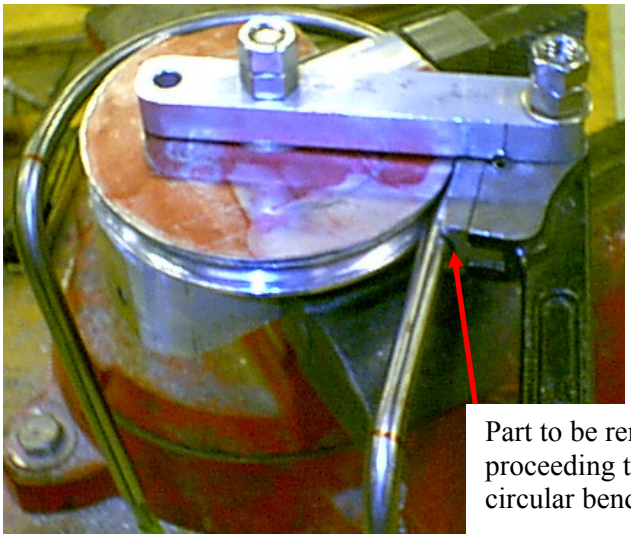

Part to be removed before proceeding to the finalized circular bend.

Partially bent cable. The cable needs to be placed upside down to bend the rest of the circular path.
The part shown in the picture is removed to complete the last section of the bending as shown in the next page.

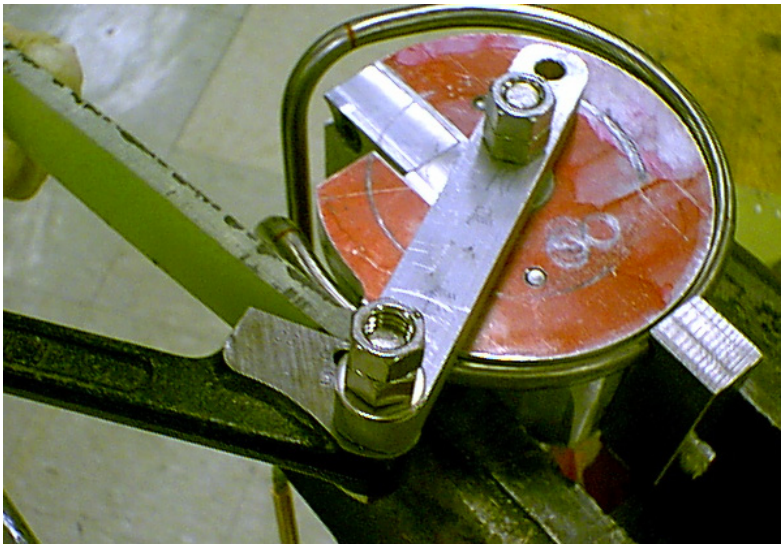

Final operation of the sample bending in circular shape. This operation requires the use of a G10 place to force the cable round in the sections close to the 90° bend (using the cut section of the customized bending tool).

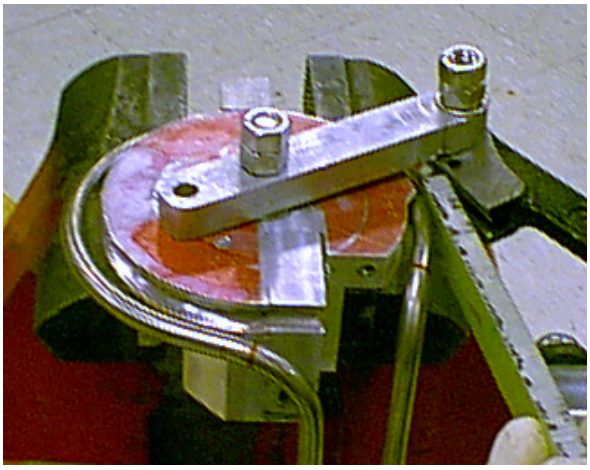

Details of the operation in order to round off completely the cable and make it of the desired shape.

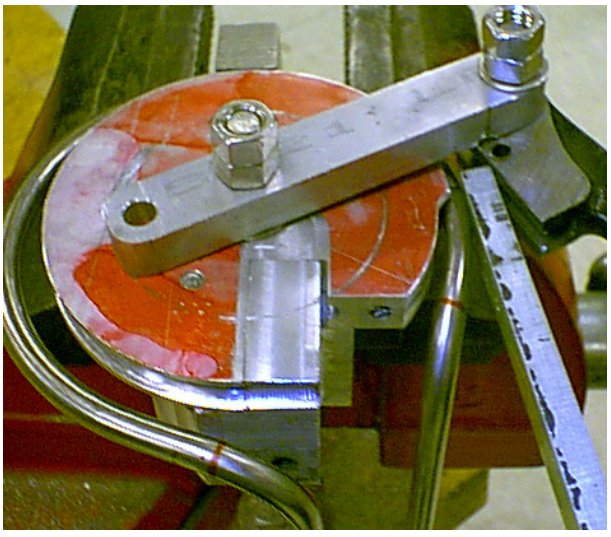

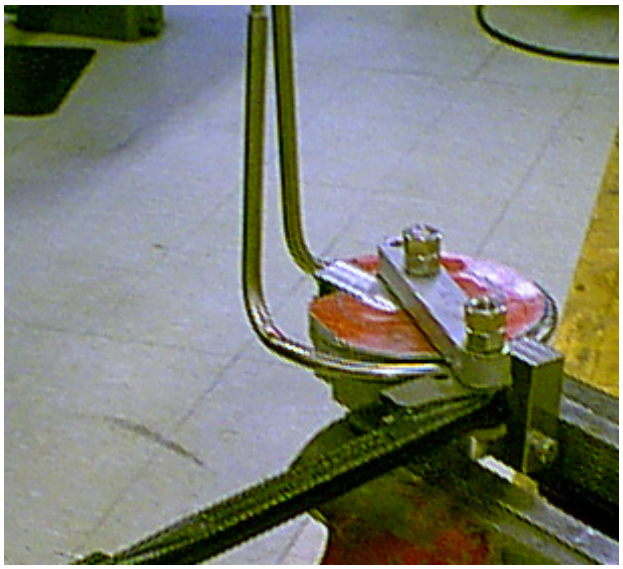

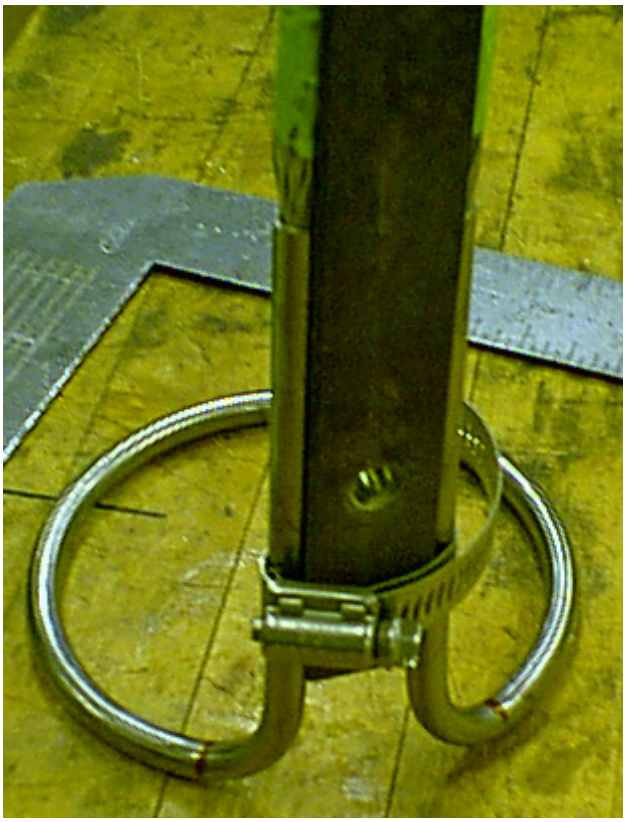

At the end it is necessary to verify that the circular part lies on a single plane and the two leads are perpendicular to this plane and parallel to each other.

I.2.c Remove titanium

Remove the titanium tube cutting at the two sign B. B' being careful not to damage the cable (Fig. I.6).

I.2.d Cleaning parts and anti-sintering powder

Clean all the part and screws of the assembly with alconox and water to remove grease and dirt and then ethyl alcohol. Let dry and put a thin layer of anti-sintering power (Nicrobraz Stop off powder) on each of the parts that could sinter during heat treatment (add ethyl alcohol to the powder till it looks like a white liquid and apply with an acid brush).

I.2.e Voltage taps

Voltage taps need to be mounted on the cable before it is inserted in the structure. The wires used for the voltage taps are composed of a thin stainless steel wire wounded tightly with a thin copper wire (stainless steel wire is strong, the copper has a lower resistance and it is soft so that it can make a good contact to pick up the signal). All the voltage taps wires need to be inserted inside an insulating glass sleeve (size 24). Voltage taps will have a positive and negative side. The positive and negative side will be mounted in opposite sections of the cable. To avoid inductive pick up of the two will be wrapped along the cable and will meet and be twisted together with the other end. If a voltage tap is placed along the cable (together with the voltage taps positioned at the ends), it is necessary to make sure that the voltage tap is positioned so that it is not crashed during the experiment (it is placed in between two fingers). Voltage tap wires are wrapped two or three times at the desired location and part of the copper and the stainless steel wires are used to position as tightly as possible the voltage tap.

I.2.f Mounting sample

It is easier to mount the sample upside down with the leads pointing towards the floor. Stack up the structure pieces and the inner ring (collet). Slide the cable (leads first) inside the support pieces and before it reaches the final position squeeze the legs of the cable so that it is possible to insert the cable inside the outer ring (Haynes 242 ring). Push the cable all the way down to reach the final position in which is sitting nicely between the outer ring and the collet. Add the fingers of the collet so that the cable is enclosed in the two rings. Add the conical wedge and lock it so that the gap between the two rings is as close as possible to 1 mm required distance for the aimed void fraction of ~33-35%).

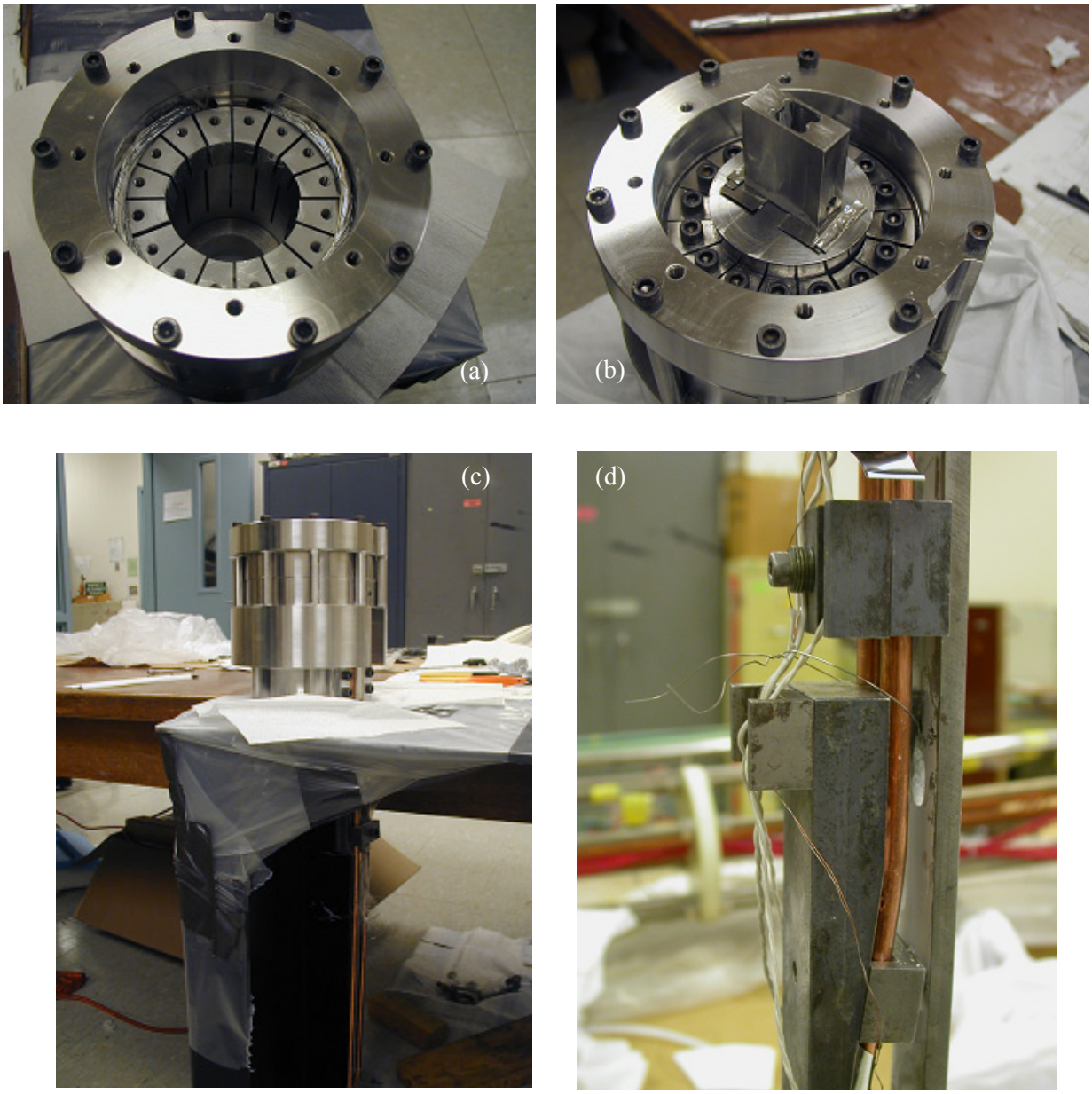

Fig. I.8 (a) Sample sitting in the external ring with the collet positioned but still not closed. (b) The fingers are added on the collet so that the cable is completely enclosed. A stainless steel wedge is inserted to maintain the desired void fraction during heat treatment. (c) Position of the sample during mounting. (d) Location of the bend of the copper joints. The stainless steel parts will be either removed or substitutied with G10 pieces after heat treatment.

I.2.g Bending copper section

Once the sample is settled in the supporting structure it is necessary to bend the copper legs in two different places so that it fits the parts the support the leads during heat treatment and prepare the copper legs to be in the appropriate position when the sample needs to be transfer on the probe and soldered to the current leads.

I.2.h Wrapping in SS foil and insert the sample in the canister for heat treatment

Wrap the structure and the sample (together with the witness sample strand) in SS foil and insert the sample in the canister which will be then welded at the ends and put inside the furnace for heat treatment. One thermal couple will be mounted on the sample holder to monitor the temperature during heat treatment.

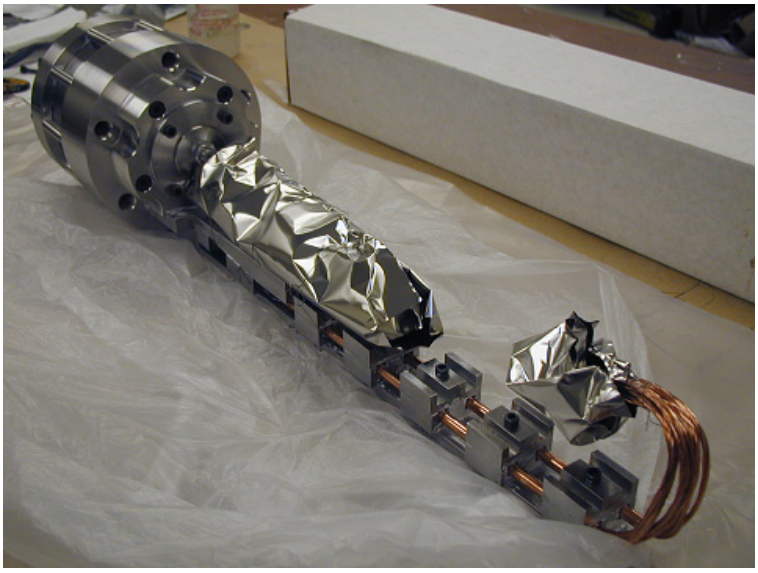

Fig. I.9 Sample ready to be placed in a stainless steel can to be inserted in an horizontal oven.

I.2.i Mounting of the sample on the probe

After heat treatment very few parts are removed in order to avoid moving the sample in a way that it could damage it. The stainless section holding the copper joints is removed and the sample is gently positioned onto the probe so that the copper joints fit in the channel where they will be soldered to the 10 kA current leads.

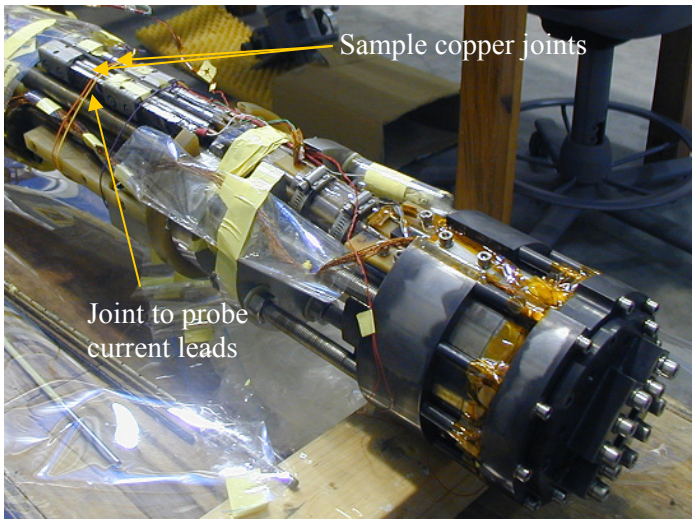

Fig. I.10 Sample mounted on the probe and ready to be inserted in the cryostat.

I.3 Hairpin samples

The advantages of this design has been already largely discussed in Chapter (XXX) so the intent here is to give details on the assembly process for the hairpin cables without repeating what has been said already.

I.3.a Swaging cable with titanium tube and bending

Among the simplification of the hairpin sample design is that a 90° bend is avoided and the cable is lying on the same plane. Nevertheless it is necessary to bend the cable with a U-shape so that the two ends can be connected with the current leads. Bending the cable can cause a de-cabling of the higher stages of sample. It was verified with dummy samples that this effect is significant only for the 45-strand cable so that it was decided to swage a titanium tube only on the bent section of the 45-strand cable (Fig. I.2). A 10.5" titanium tube was used. The single strand, triplet and 9-strand cables were left bare and covered with glass sleeve or anti-sintering powder to avoid sintering during heat treatment. Those small samples were bent in shape by hand while the 45-strand cable with the titanium tube was bent using the same tool of Fig. I.5(a). Once the sample is sitting in the U-bend holder, a plate is positioned on top of it and additional heat treatment parts are connected.

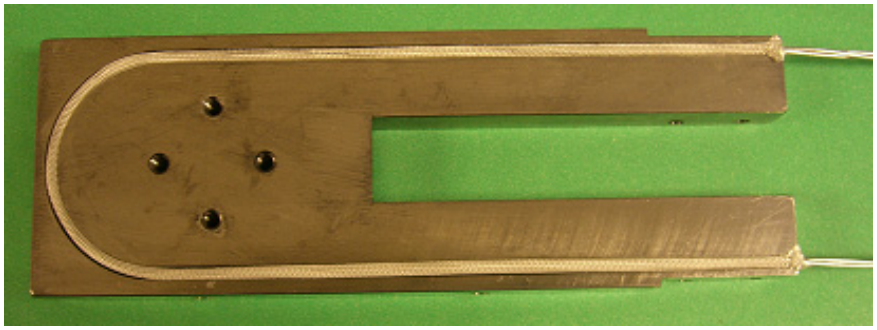

Fig. I.11 Triplet sitting in the sample holder (U-bend section). Glass sleeve was used to avoid sintering. In the straight test area, where the mechanical load is applied, anti-sintering powder was used.

I.3.b Voltage taps and heat treatment preparation

Fig. I.12 shows the sample inside its heat treatment fixture. As described for the circular sample, voltage taps need to be mounted on the cable before it is inserted in the structure. The wires used for the voltage taps are composed of a thin stainless steel wire wounded tightly with a thin copper wire. All the voltage taps wires need to be inserted inside an insulating glass sleeve (size 24). Voltage tap wires are wrapped two or three times at the desired location and part of the copper and the stainless steel wires are used to position as tightly as possible the voltage tap. Voltage taps will have a positive and negative side. There is one pair of wires (one voltage tap) on each straight side of the sample. The third voltage tap is placed along the entire sample with one wire following the entire length of the sample to cancel inductive pick up.

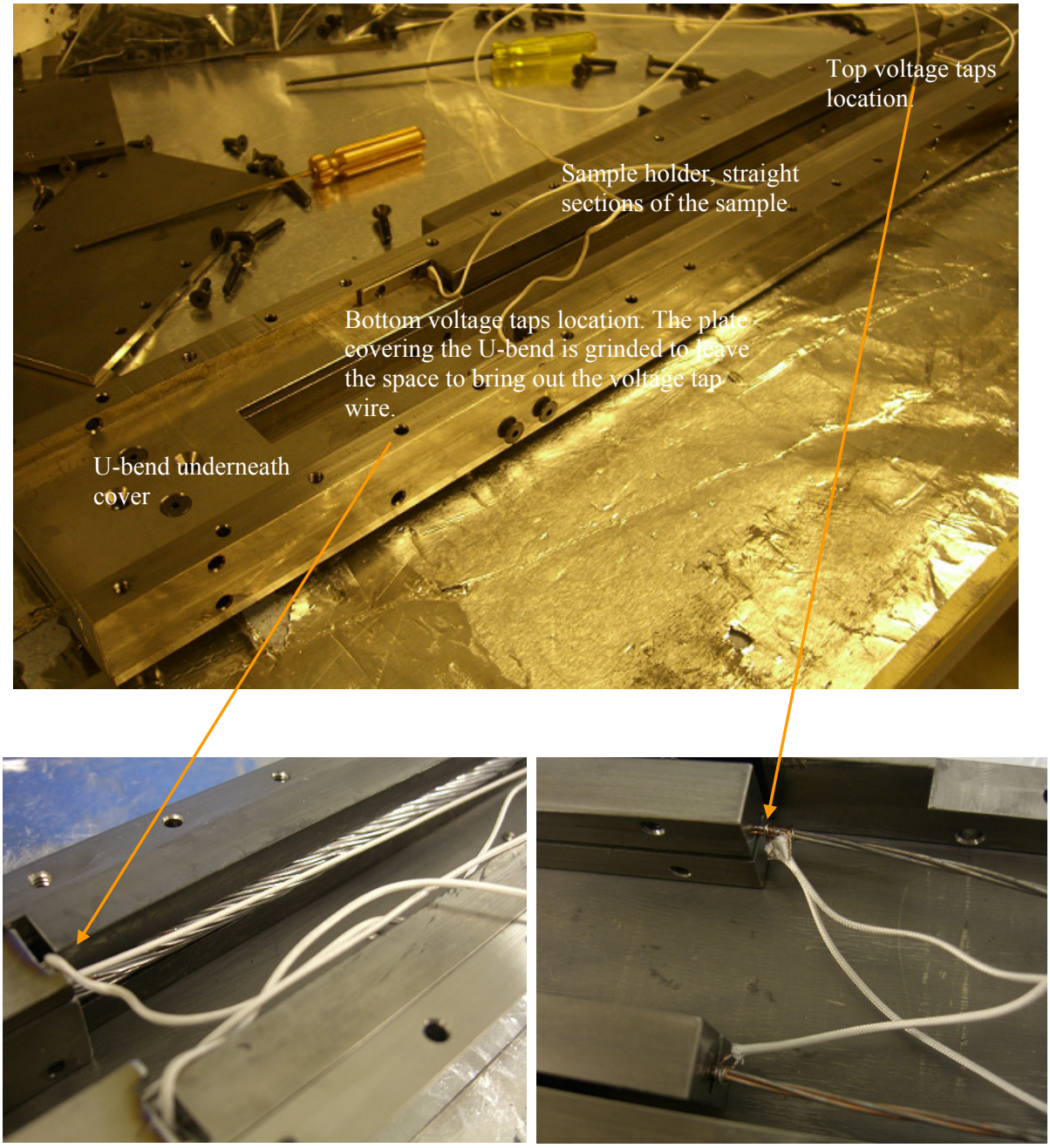

Fig. I.12 The sample is mounted inside the U-shape holder and the two external holders (top). Bottom wires of the voltage taps (voltage taps 1, 2 and total voltage wire running along the sample to cancel inductive pickup) (bottom left). The top cover of the U-bend is grinded to be able to bring out the voltage tap wires without damaging it during the loading process. Voltage taps location at the top of the sample (bottom right).

After adding the voltage tap wires and inserting the sample in the U-bend part and the sample holder straight section parts, the rest of the parts (pressing plate and spacer) needed for heat treatment are positioned in their location (Fig. I.13-I.16). The spacer will be substitute with the moving wedge after heat treatment as described later. The spacer maintains the desired distance between sample holder and pressing plate so that the desired void fraction is maintained during heat treatment but the sample is not pre-stressed during heat treatment (spacer strips are also positioned in location and will be removed after heat treatment). The following figures show the necessary stages performed before heat treatment and how the samples are heat treated.

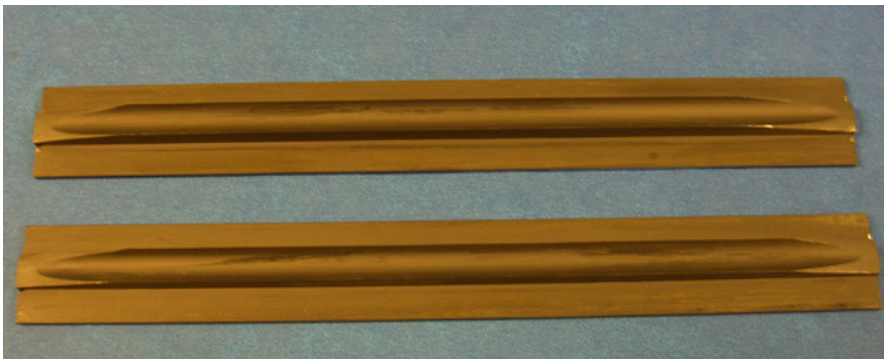

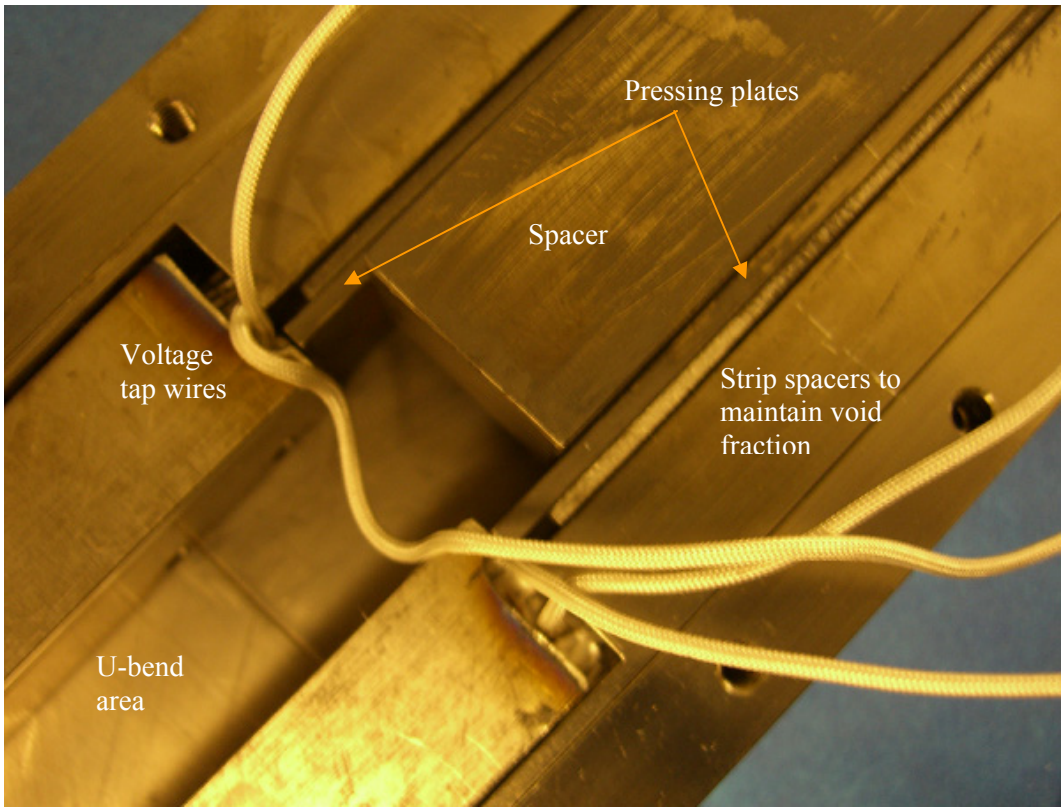

Fig. I.13 Pressing plates (top). The ends are rounded off to avoid sharp contacts between the plates and the cable. Voltage tap wires (bottom). The bottom U-shape holder is rounded to be able to bring out the wires and to avoid damaging them.

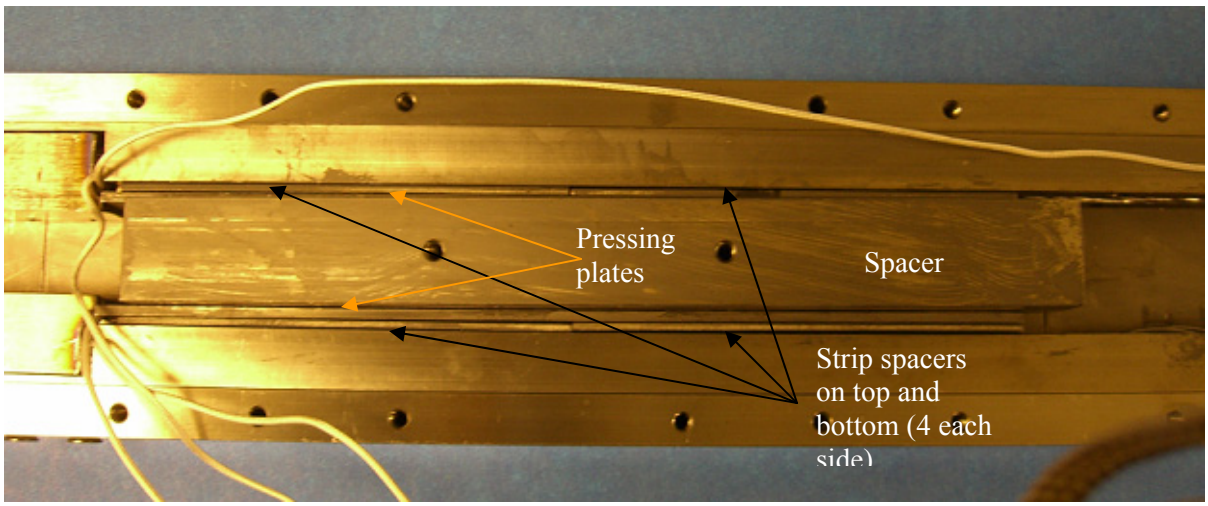

(a)

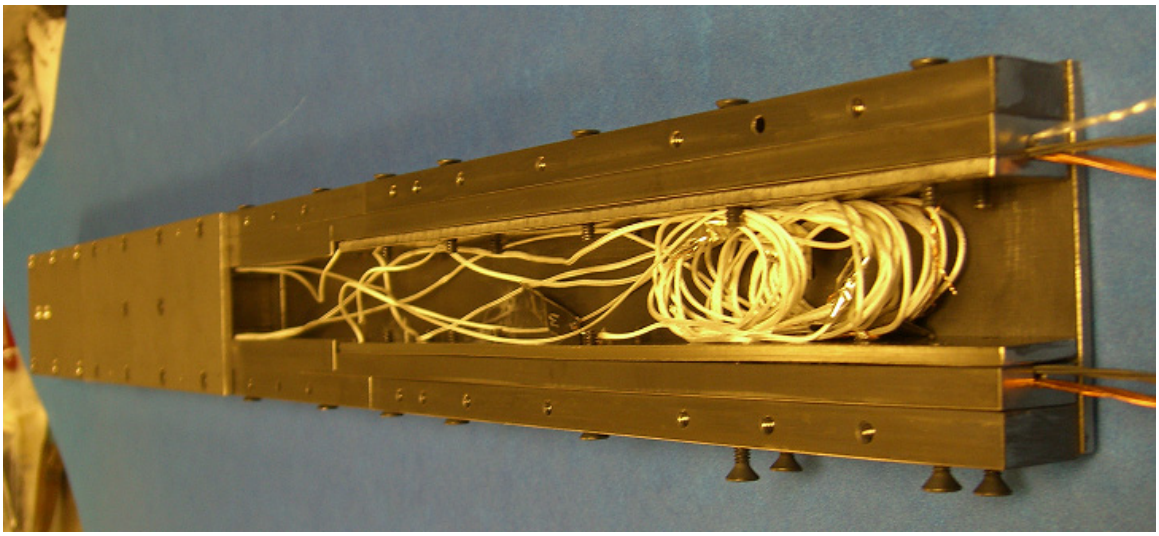

(b)

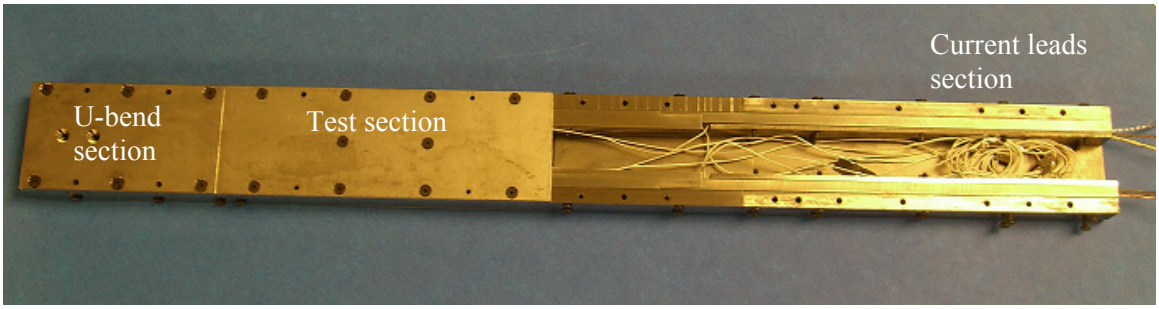

(c)

Fig. I.14 (a) Bottom voltage tap wires and spacer used to maintain the desired void fraction during heat treatment. (b-c) Sample ready for heat treatment.

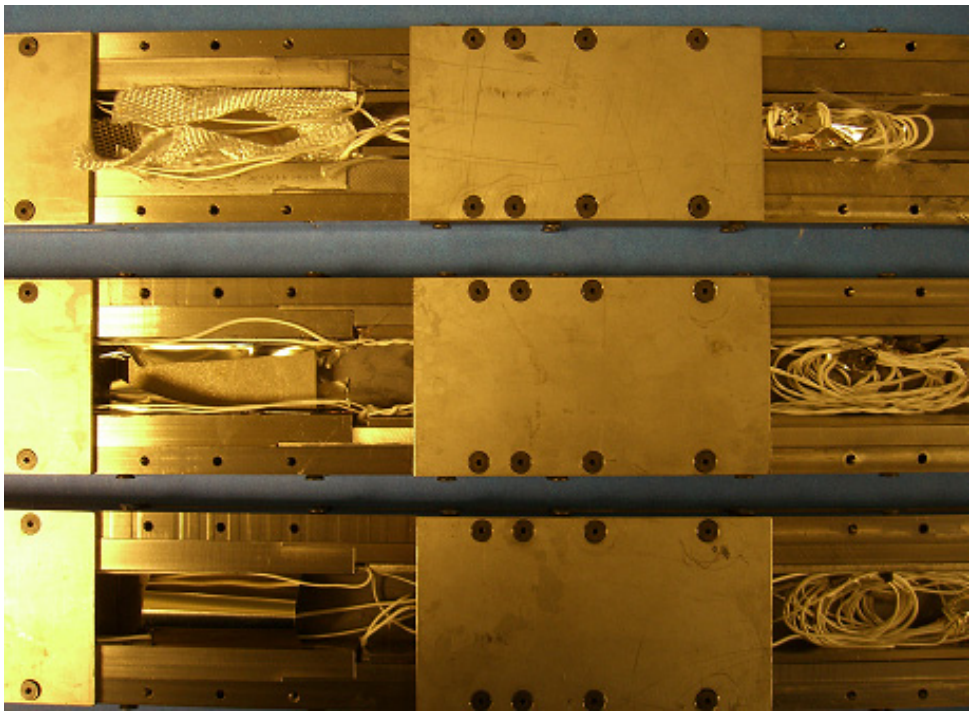

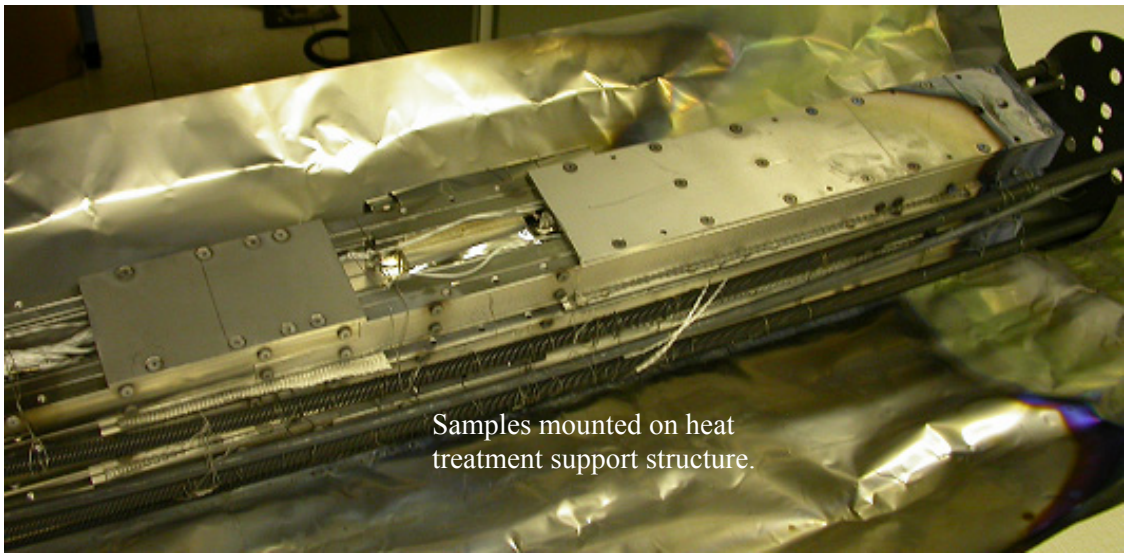

Fig.I.15 Preparation of the samples and installation of the samples on the heat treatment rack. Four samples can be heat treated at the same time.

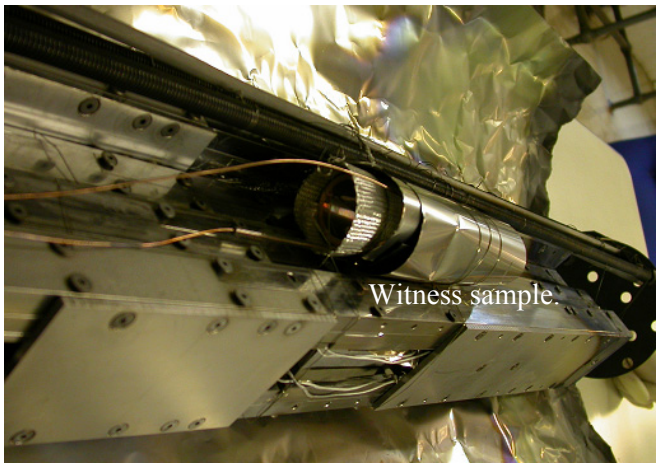

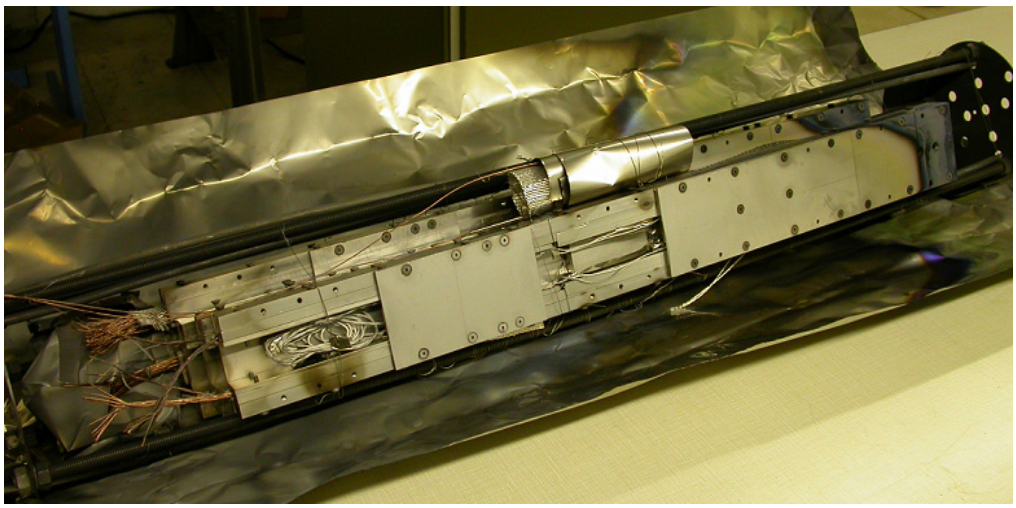

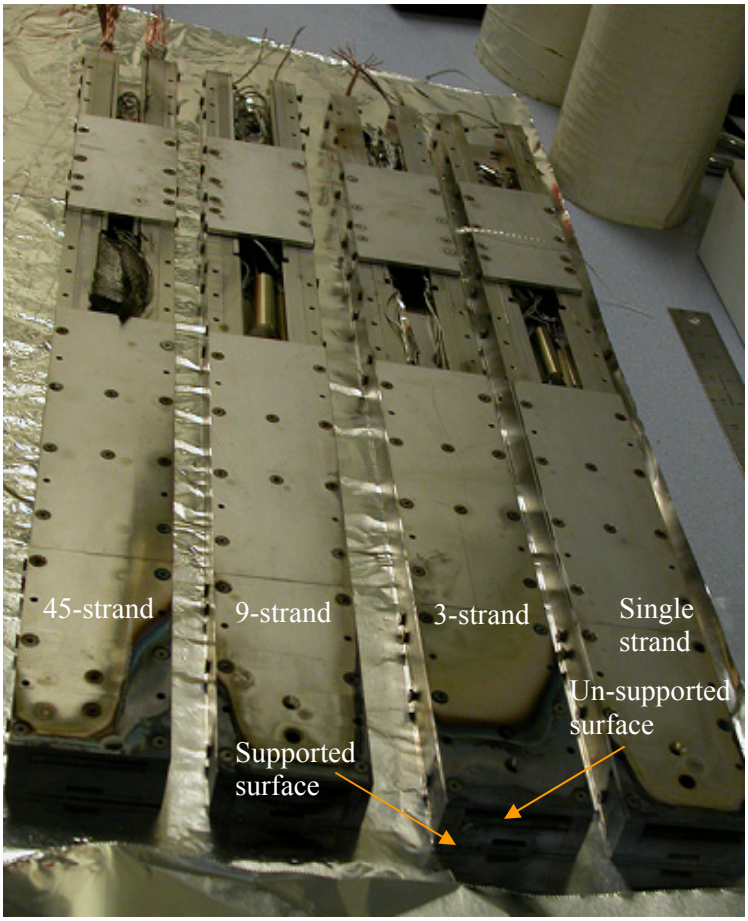

Fig. I.16 Samples taken out of the oven after heat treatment. The bottom sections show a dark color due to residual organic materials formed during heat treatment. Also to notice is that only in this position the cable is supported well in the U-bend section (piece is touching bottom plate). During assembly it is necessary to maintain the sample facing up as in the heat treatment configuration to support the cable at all time.

I.3.c Sample preparation and mounting on the probe

The same probe used for the single turn sample was used for this experiment but the copper leads design had to be changed (the 10 kA vapor cooled leads were not modified). The copper leads are composed of two parts: the top section connecting to the vapor cooled leads and the bottom part where the sample is soldered during the test. The two parts are connected with a screw. Additionally copper+NbTi cables are used to enhance the current transported and improve the flexibility of the two pieces connected (Fig. I.17).

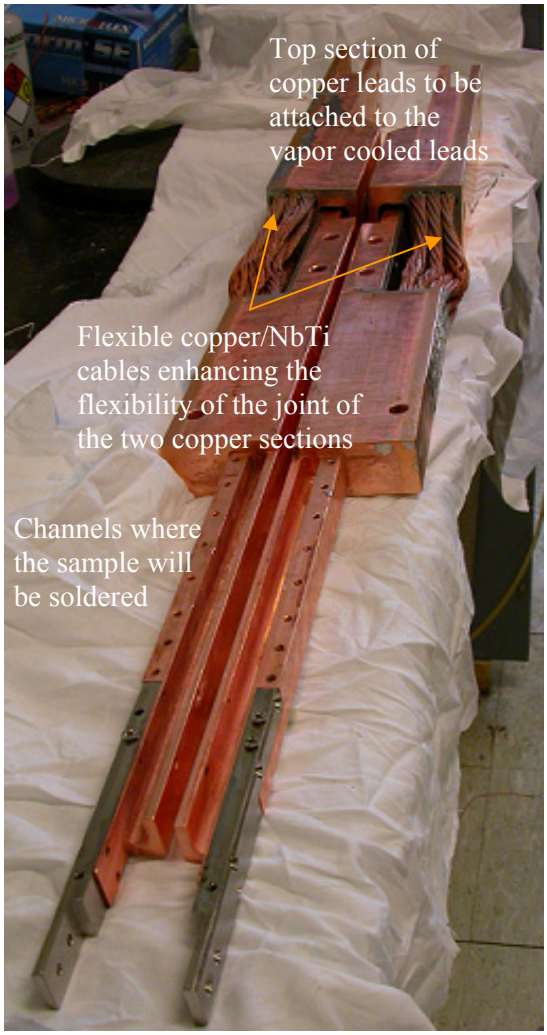

(a)

(b)

Fig. I.17 (a) Copper leads: top section is connected to the vapor cooled leads, the bottom one is where the sample is soldered. (b) Probe set up with 10 kA vapor cooled leads and copper leads.

Once the copper leads are mounted and connected to the 10 kA vapor cooled leads the probe is sat horizontally so that the sample can be mounted more easily.

Following are all the steps required to mount the sample from removing the heat treatment parts not needed during the experiment to the soldering of the sample onto the copper leads. The first step is to remove the spacer piece and the spacer strips used during heat treatment to maintain the void fraction. During the experiment the central spacer is substituted with the movable wedge piece while the spacer strips are removed because we want the press plate to be free to move and apply the load on the cable (Fig. I.18 (a-c)).

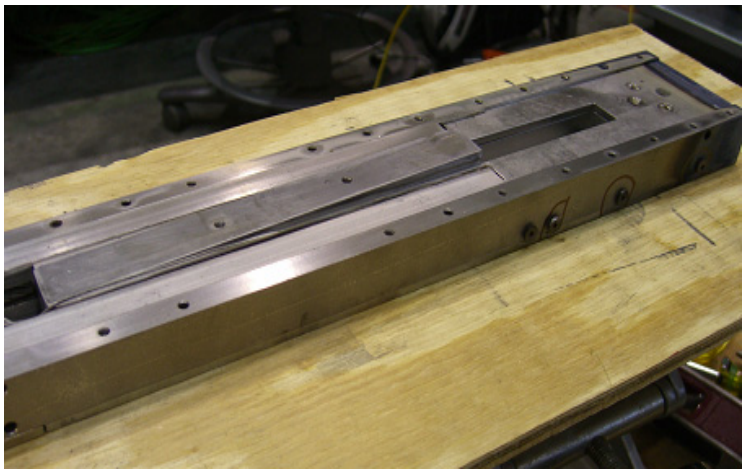

Fig. I.18 (a) After removing the top plate holding the pieces together the central spacer is carefully removed. The probe is sitting on the side where the surface of the U-bend section is in contact with the bottom plate.

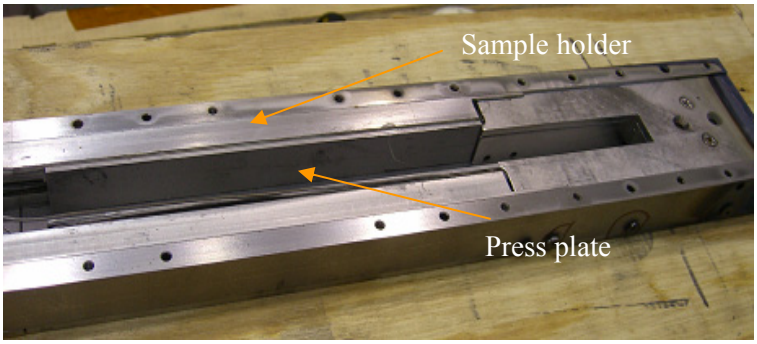

Fig. I.18 (b) Central spacer is removed.

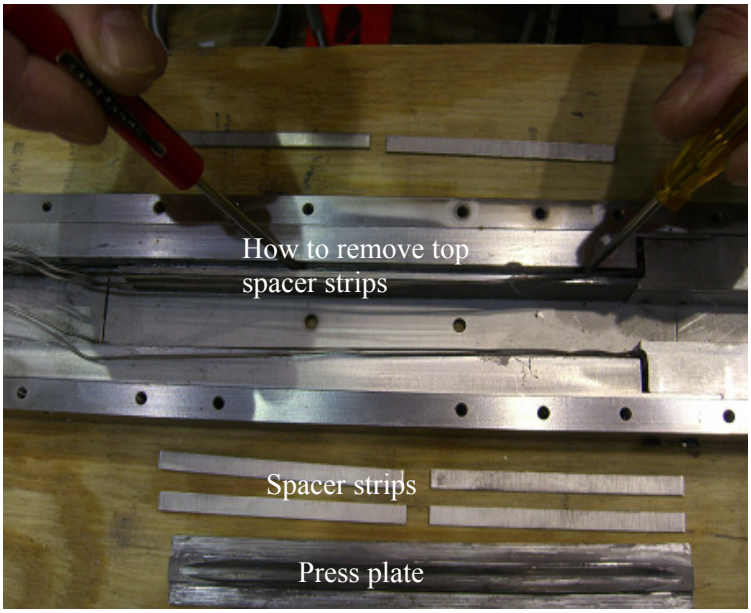

Fig. I.18 (c) Top spacer strips are removed using tweezers and small screwdriver. The bottom spacers are easily removed once the pressing plate is carefully moved from its position.

In Fig. I.19 the procedure of mounting the sample is represented. The pressing plates are put back in place and the wedge and its matching pieces are positioned where the spacer was located during heat treatment. Before being inserted in the slot, those pieces need to be "painted" with powdered Molybdenum Disulfide to reduce friction and avoid sintering between same material pieces during the experimental procedure at liquid helium. The voltage taps wires need to be positioned along the slot between pressing piece and cable holder and are taped at the top to avoid movement and flux trapping during the measurements.

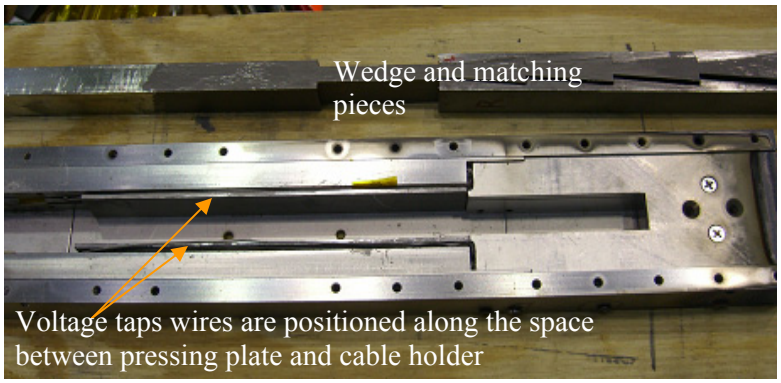

Fig. I.19 Positioning of the wedge, matching wedge pieces, extensometer and voltage tap wires in preparation of the experiment.

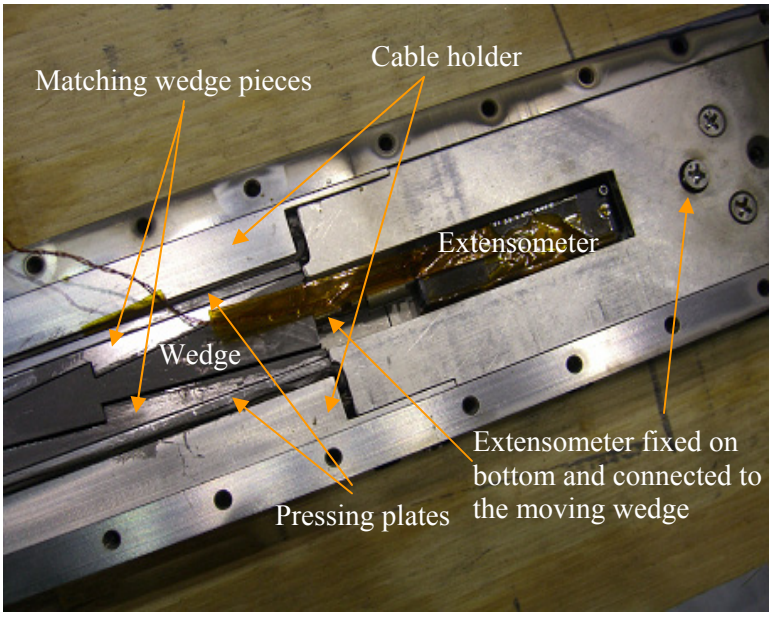

Fig. I.20 shows the working principle of the device which is not visible during operations. The wedge is initially positioned so that it sits on its matching pieces. Once the wedge is pulled vertically upward it goes pushing the matching pieces transversally outward (since they are constrained vertically) and ultimately pushing the cable sitting in the cable holder which is restrained in movement by the outside case (Fig. I.21 and following).

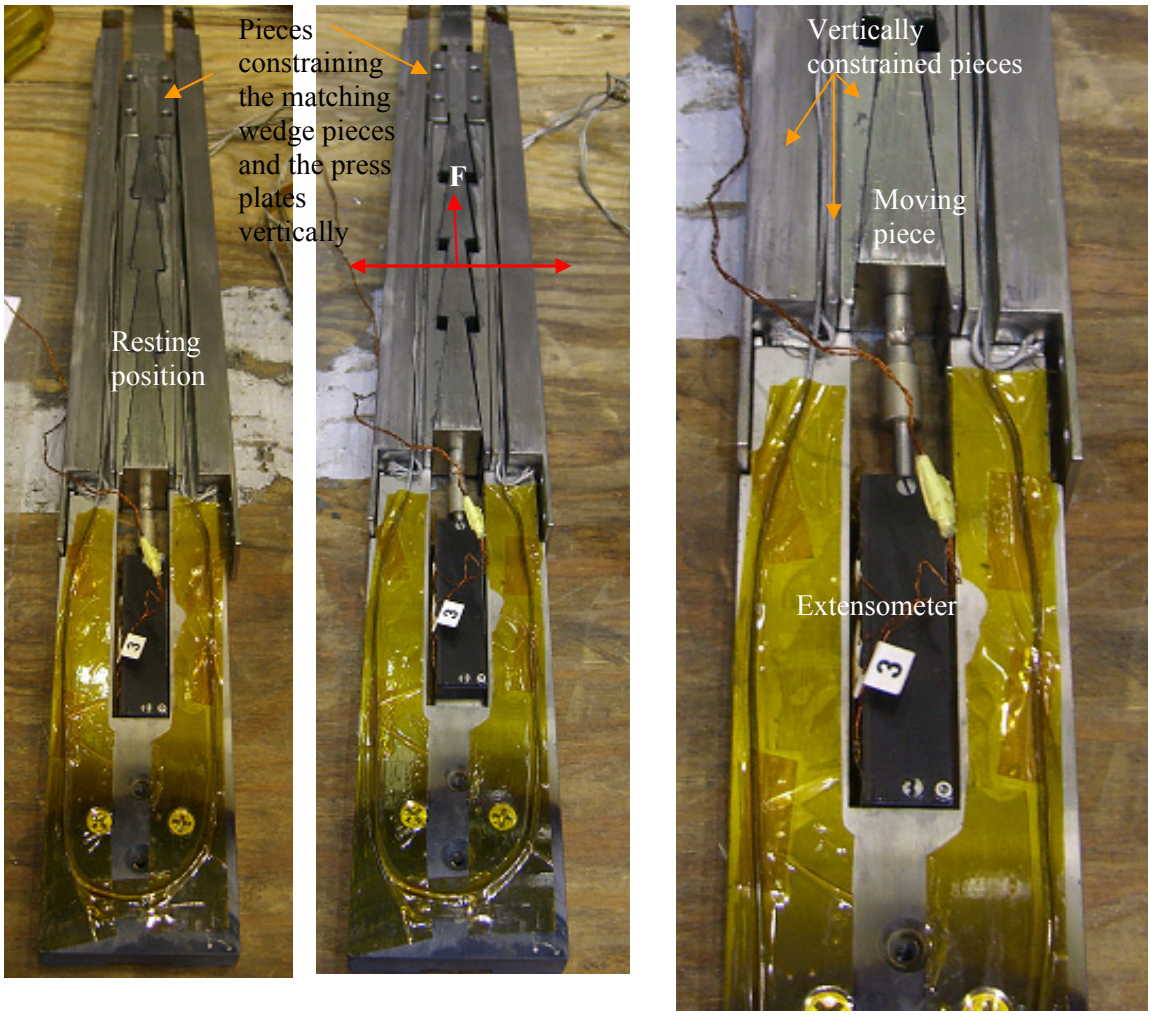

(a) (b) (c)

Fig. I.20 Working principles of the device: (a) resting position of the wedge, (b) vertical displacement of the wedge and movement outward of the matching pieces, (c) displacement measured using the extensometer.

Once the wedge and all the parts are inserted it is necessary to put back a couple of the cover plates and then flip the sample so that the screws holding the bottom plates can be removed. The plates will be left in position and removed one at the time once the structure will be inserted in the single piece case. Some of the plates will be used to hold the top section of the sample while sliding the single piece case so that the sample can not move (Fig. I.21).

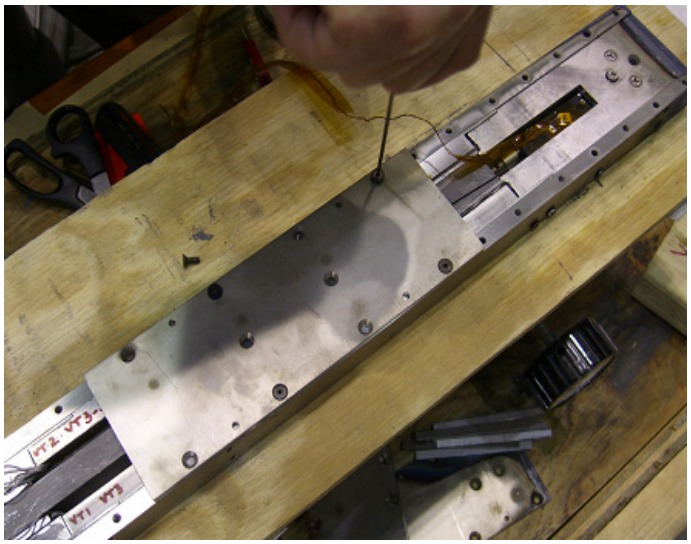

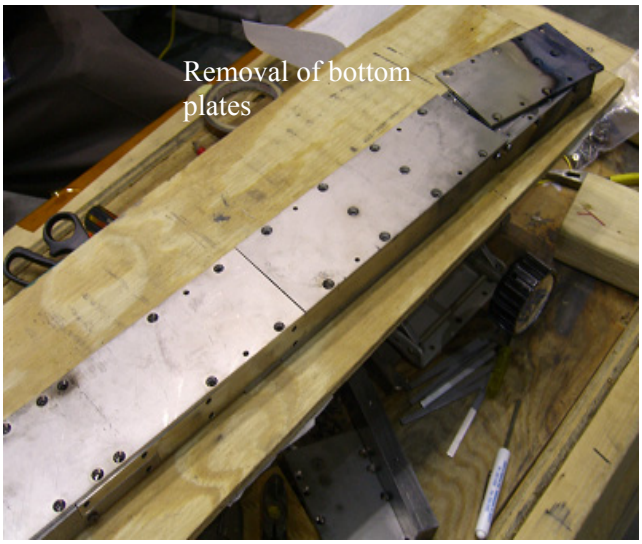

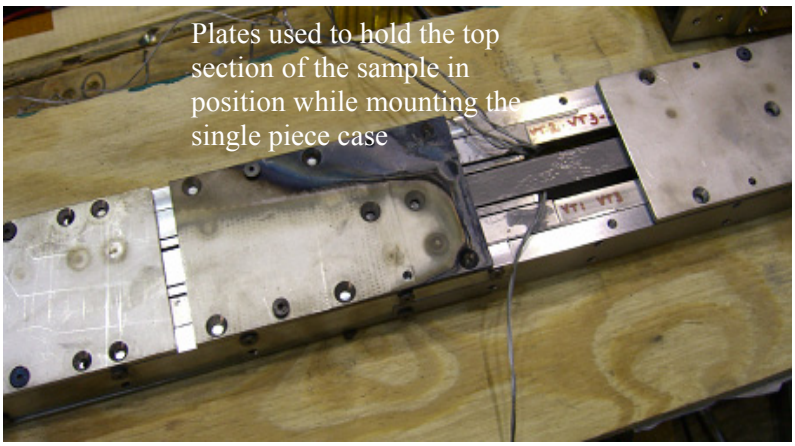

Fig. I.21 Plates from heat treatment are use to hold the sample in position (top and bottom pictures) while the bottom plates are removed (center picture).

Fig. I.22 (a-f) shows the steps necessary to insert the sample inside the single piece case. This is the most delicate procedure of our experiment since the cable is extremely delicate. Most of the heat treatment support pieces have to be removed and substituted with the case so it is necessary to support the cable during the change and avoid any unwanted strain that could cause initial degradation.

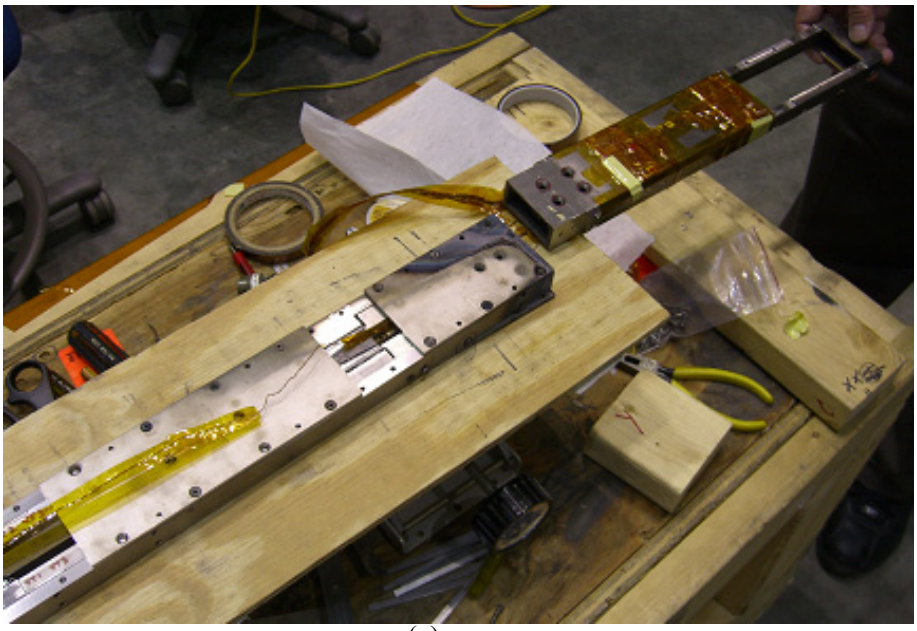

(a)

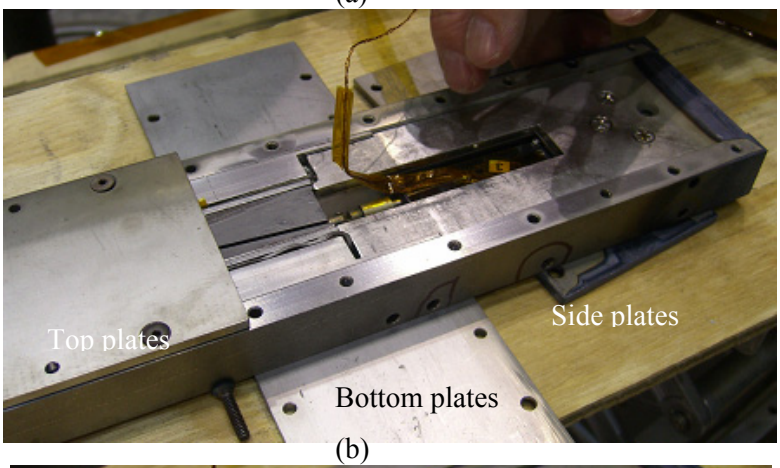

(b)

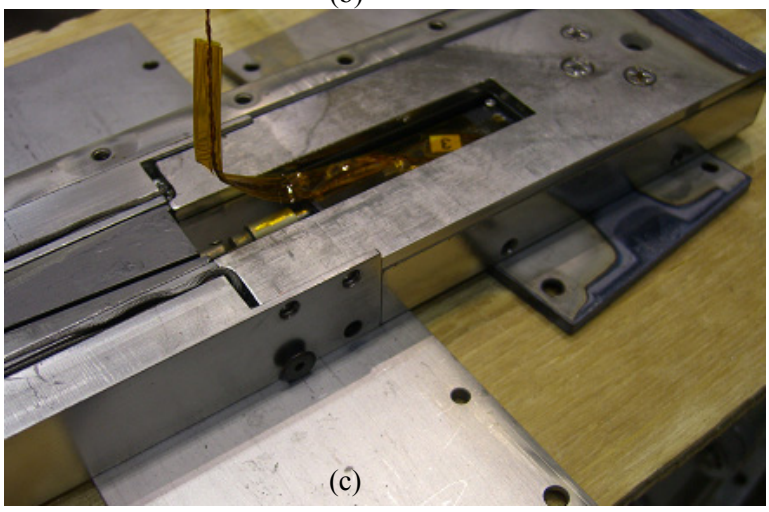

(c)

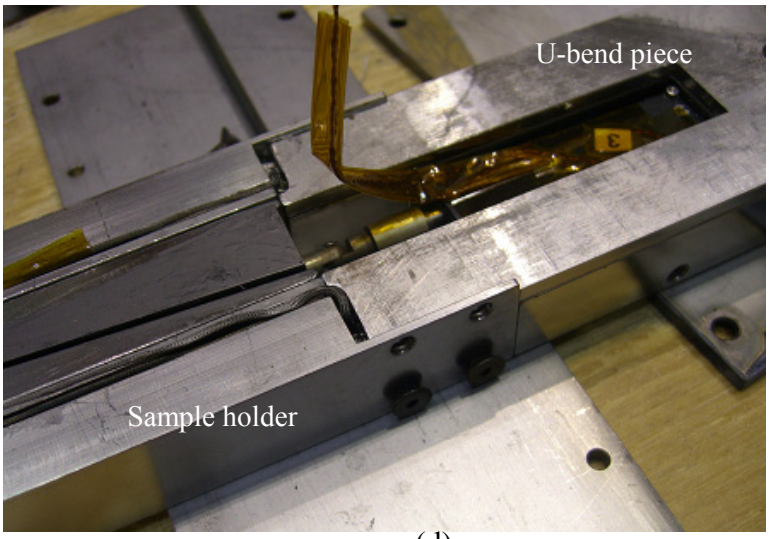

(d)

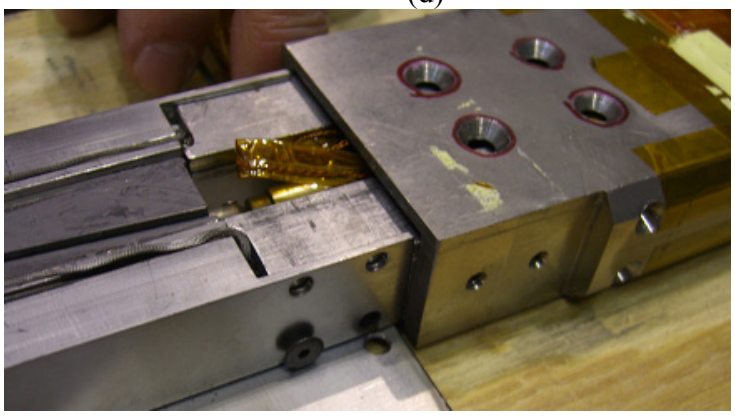

(e)

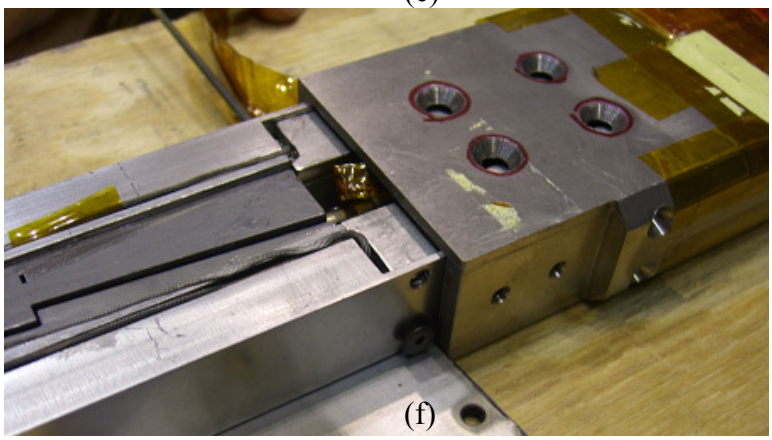

(f)

Fig. I.22 (a) Sample still supported by heat treatment side and top-bottom plates. Those pieces are going to be substituted with a single piece case. (b) Ready to remove side plates. (c-d) After removing the side plates the sample is hold in position momentarily by two side screws joining the sample holder and the U-bend piece. (e-f) The sample slides inside the case (remove the screws holding the sample holder and Y-bend hape). Once the sample is inserted completely into the case screws will be used to firmly position it. These screws will hold case and sample together during the experiment.

Once the sample is firmly mounted inside the case it is possible to flip around the sample so that it matches the design of the copper joints design. The sample is removed from the remaining of the heat treatment support pieces and it is carefully slid towards the copper joints where it is positioned inside grooves where the soldering will be done (Fig. I.23).

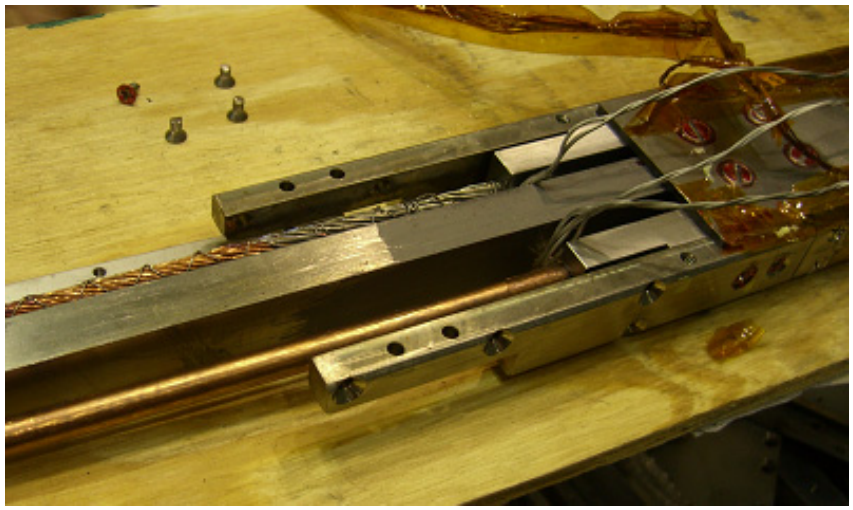

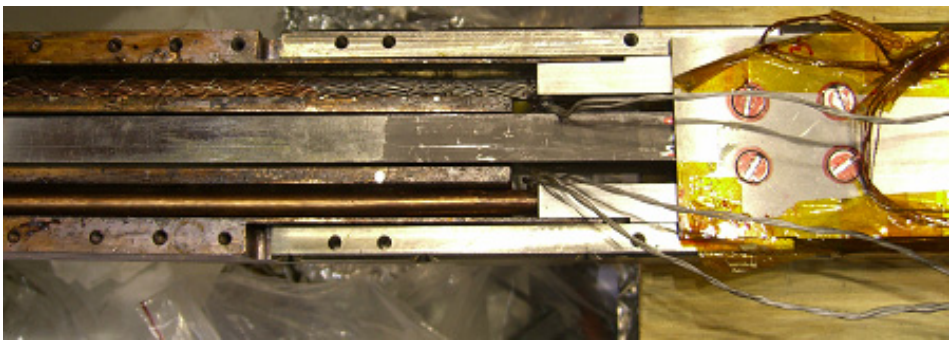

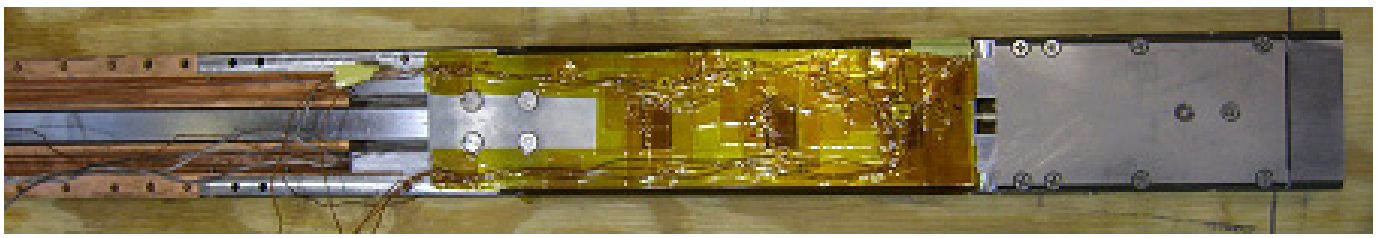

Fig. I.23 The sample is mounted inside the case and the last heat treatment support pieces are removed(top) before the sample is slid inside the grooves on the copper joints area (center and bottom pictures).

Three 1kW cartridge heaters are mounted on the sides of the copper joints and the area is warmed up so that the grooves where the sample is located can be soldered filled (Fig. I.24). Temperature controllers are used to monitor the temperature of the joints and do not overheat the copper joints. The sample is now fully mounted on the probe. The wedge is connected to the shaft connected to the actuator on the top flange, the voltage taps are soldered to the connector and all the instrumentation connectors are mounted. The probe is now ready to be put vertically and to be put inside the dewar (Fig I.25-I.27).

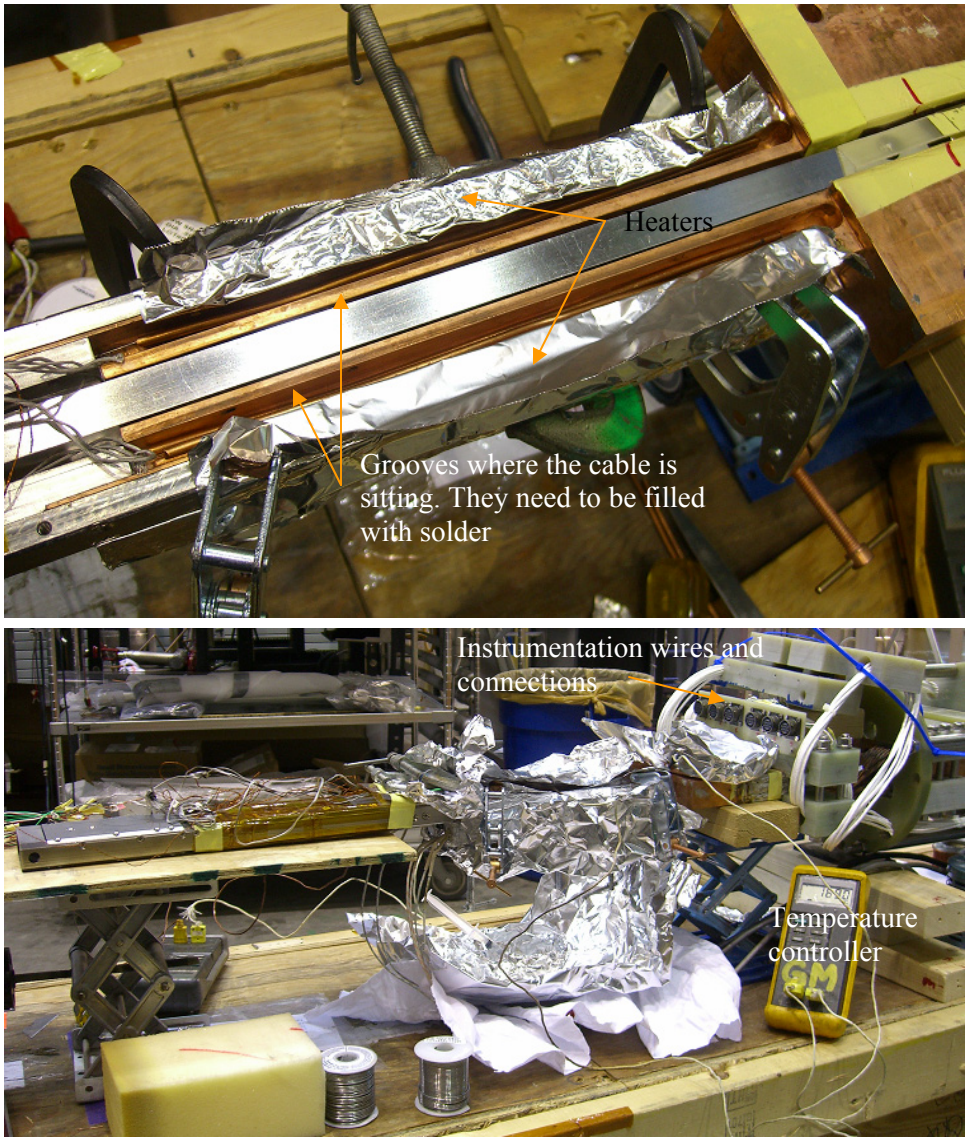

Fig. I.24 Soldering procedure. Cartridge heaters inside aluminum blocks are mounted on the sides and on the bottom of the copper joints area. Temperature controllers are used to monitor the temperature and start filling the grooves with solder.

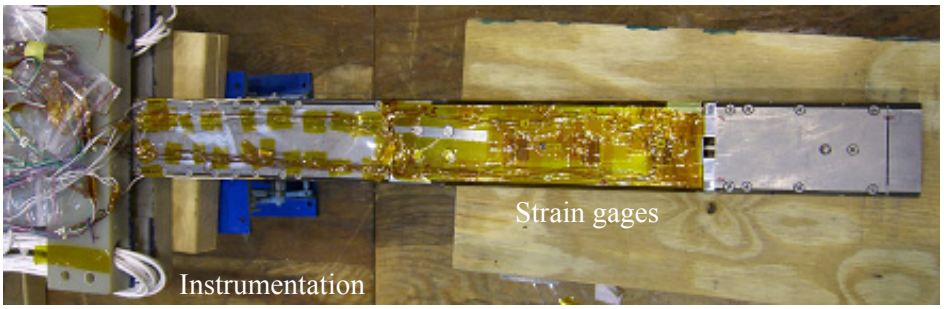

Fig. I.25 Sample soldered. Instrumentation wires are connected to 4 wires Teflon cables that are brought outside the dewar (45 ft long).

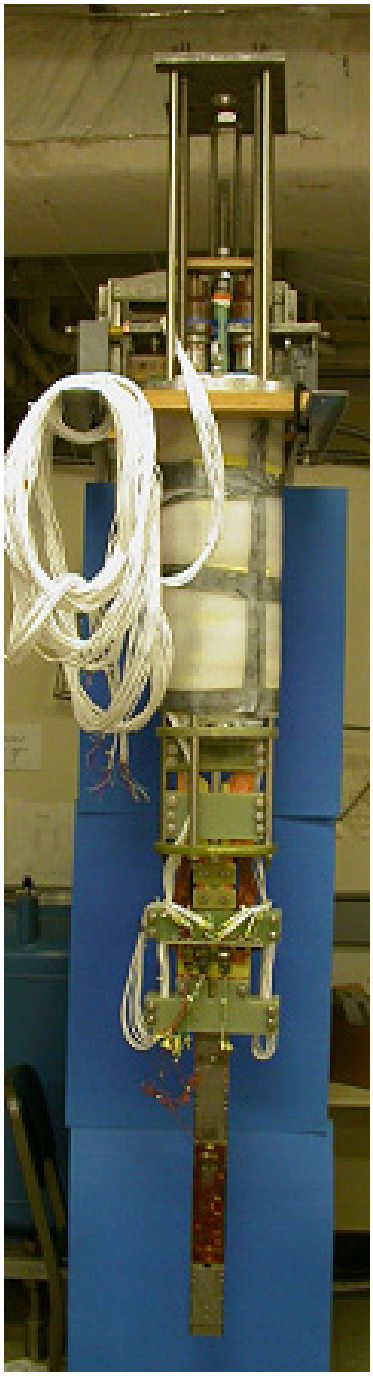

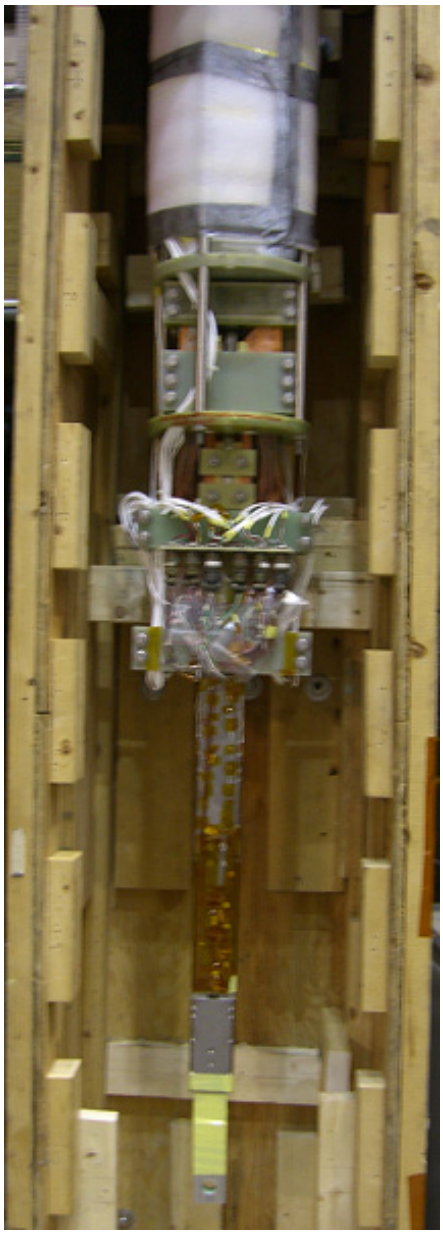

Fig. I.26 Probe ready to me inserted into the dewar.

Fig. I.27 Probe inside the dewar. The picture show the top flange, the bellow used to adjust the height of the probe so that it can be easily connect to the pin sitting on the bottom of the dewar. The linear actuator and the motor used to operate it are sitting on a plate. The linear actuator is connected to the cylinder that contains the load cell and connects the actuator to the shaft connected to the wedge at the sample area.

APPENDIX II:
Advantages of a three-point load configuration

II.1 Introduction

In this appendix, a general approach will be used to justify the choice of applying a three-point load configuration to the single turn experiment setup.

Ideally, it is desired to apply transverse pressure uniformly along the test cable. The test cable in the single turn configuration is not a complete turn, but missing a part of it for the current leads. To improve the load application method after the first and second experiment, it was suggested to modify the expanding collet by using three sections of the collet instead of the continuous circular all-around arrangements, as shown in Fig. II.1.

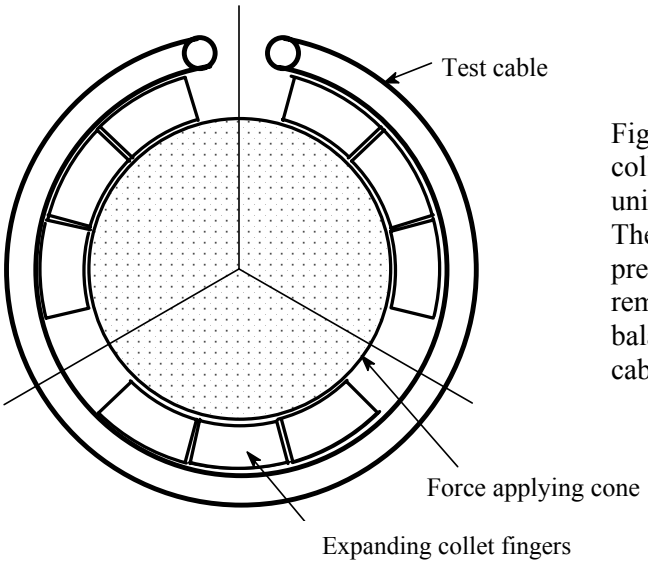

Fig. II.1 Modified expanding collet to apply a more uniform load on the cable. The fingers used to apply pressure on the cable will be removed in two sections to balance the section where the cable is missing.

The missing section of the cable does not have the force cone fingers so additional missing cone finger sections will be created in other two locations (every 120 degrees). In this way the force applying cone faces uniformly to the three groups of the expanding collet fingers so that the applied transverse load could be uniform. The two portions missing the expanding collet fingers (4 and 8 o'clock) will not have the transverse load and will show a normal critical current behavior (no loading condition). It will not be a critical issue to study the effect of transverse loads on a cable as it is explained in the following sections.

The fact that there are sections not loaded does not introduce an error in estimating the critical current as it will be explained. This is true if instead of considering the entire length of the voltage tap, only the length of the pressed section is used to estimate the current.

II.2 Calculation of the critical current and estimation of the error introduced by the non-uniform load

The length of the groove where the cable is sitting is ~ 350 mm. The maximum voltage tap length L is limited to roughly 270 mm.. In the calculations below the critical voltage values V_c of 2.7 μV and 27 μV were used, corresponding to E_c of 10 and 100 μV/m respectively.

We discuss a series of simulations considering single strand values of n = 25 and I_c = 140 A.

From this starting point the critical current measurement error (considering a degraded strand) for the partial load of the sample is evaluated using a corresponding degraded n-value (n_{deg}) estimated by:

$$n_{\deg r} = n * \left(\frac{I_{c-\deg r}}{I_c} \right)$$

Using the critical voltage criteria and the critical current values the V-I curve is given by the following equation:

$$V = V_c * \left(\frac{I}{I_c} \right)^n$$

Let's now call V_1 and V_2 the voltages created by the sample (length L) without and with degradation, respectively. Considering that we are pushing only 2/3 of the cable, the voltage is given by (Fig. II.2):

$$V = \frac{1}{3} * V_1 + \frac{2}{3} * V_2$$

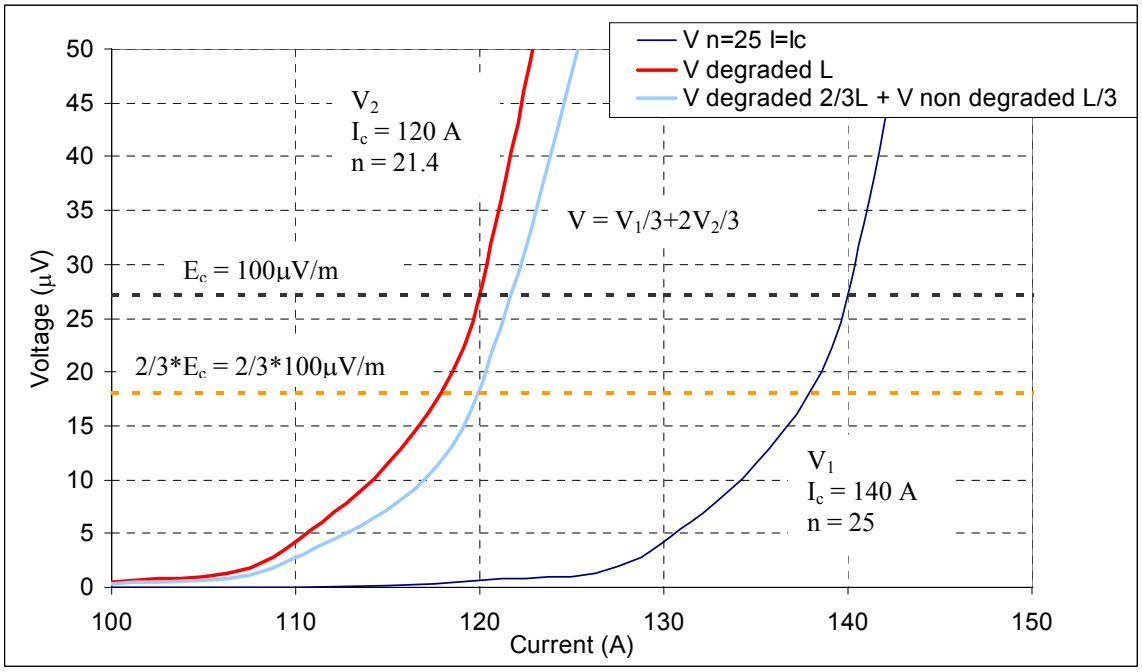

Fig. II.2 V-I curves for various conditions.

This equation (sum of $V_1/3$ of non degraded voltage and $2V_2/3$ of degraded voltage) evaluates the critical current of the partially loaded sample. It is possible to estimate the critical current applying the load on the entire length or only on 2/3 of it (by using the modified collet in Fig. II.1).

The voltage curve V in Fig. II.2 was used to estimate the critical current at E_c = 100 μV/m (corresponding to 27 μV) and 2/3*E_c (corresponding to 18 μV).

It turns out, the critical current estimated using the voltage curve V with the $2E_c/3$ criterion is very close to the critical current obtained by using the voltage V_2 (entire length degraded) at E_c.

The following parameters have been used for these simulations:

$I_{c\text{-}nondegraded}$ = 140 A
$n_{nondegraded}$ = 25

Table II.1 Results of the simulation.

$I_{degraded}$ (A)	$I_{degraded}/I_c$	$n_{degraded}$	I_c at E_c	I_c at $2E_c/3$	Err % for I_c at E_c	Err % for I_c at $2E_c/3$
140	1.00	25	140	138.5	0.00	-1.07
130	0.93	23.2	131.6	129.75	1.23	-0.19
120	0.86	21.4	122.5	120	2.08	0.00
110	0.79	19.6	112.6	110	2.36	0.00
100	0.71	17.9	102.5	100	2.50	0.00
90	0.64	16.1	92.5	90	2.78	0.00
80	0.57	14.3	82.4	80	3.00	0.00
60	0.43	10.7	62.4	60	4.00	0.00
50	0.36	8.9	52.2	50	4.40	0.00
40	0.29	7.1	42.25	40	5.62	0.00
30	0.21	5.4	32.25	30	7.50	0.00

From the table we can clearly see that if the cable is degraded only over 2/3 of the length the critical current estimated by using a criterion of $2E_c/3$ instead of E_c is very close to the critical current obtained with a cable degraded over the entire length (Fig. II.2).

We can conclude that we will be able to measure the correct critical current by a criterion $2E_c/3$ even if the voltage drop is not uniform over the entire length.

If the critical current of the strand (non-loaded) is already degraded (due to fabrication process, for example n = 15 and I_c = 100 A), similar results are obtained (Fig. II.3). The error increases if we use the E_c criterion but it remains the same if we use the $2E_c/3$ criterion.

These results follow from the fact that the voltage of the non-degraded area is negligible.

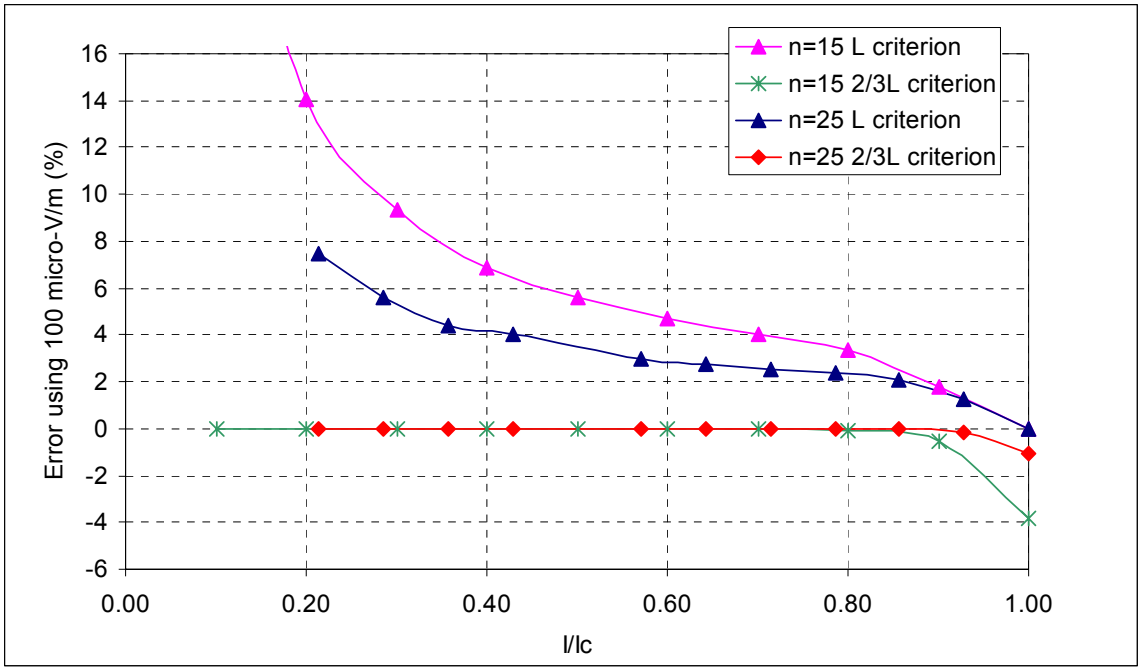

Fig. II.3 Errors on the critical currents using a non-uniform load on the cable for initial currents I_c = 140 A, n = 25 and I_c = 100 A, n = 15. If a $2E_c/3$ criterion is used the error is negligible from the case of uniform load.

These simulations support the feasibility of using an expanding collet that presses only on 2/3 of the cable and not its entire length. The critical current measurement by using this modified collet should not be an issue and it is very close to the critical current of a cable entirely loaded as long as an appropriate criterion is used.

II.3 Transverse Load Measurements

To verify if the three-point load configuration would give a more uniform distribution of load, a 3-D model of ANSYS® was used. Only the outer ring was modeled and a constant pressure was applied where the cable is located. The results of the strain on the outer ring were compared with the measurements taken with the strain gages located on the outer ring (comparison between measurements and strain values obtained with the model taken at the strain gages locations).

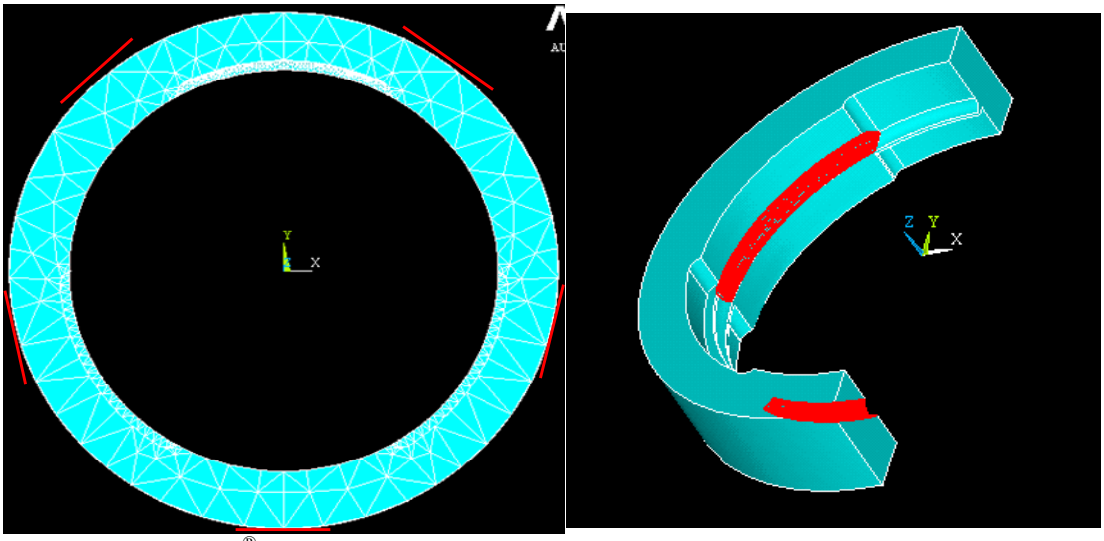

Fig. II.4 3-D ANSYS® model of the outer ring: mesh and position of strain gages on the left, pressure load applied in the model.

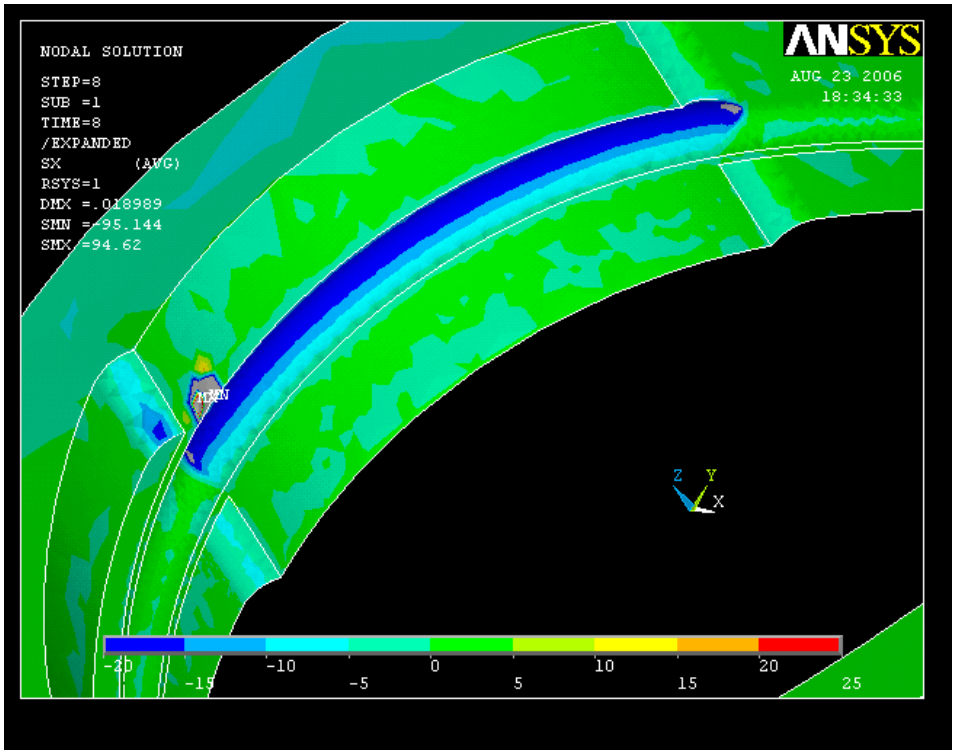

Fig.II.5 Radial stress contour of the ring (the pressure applied is 20 MPa).

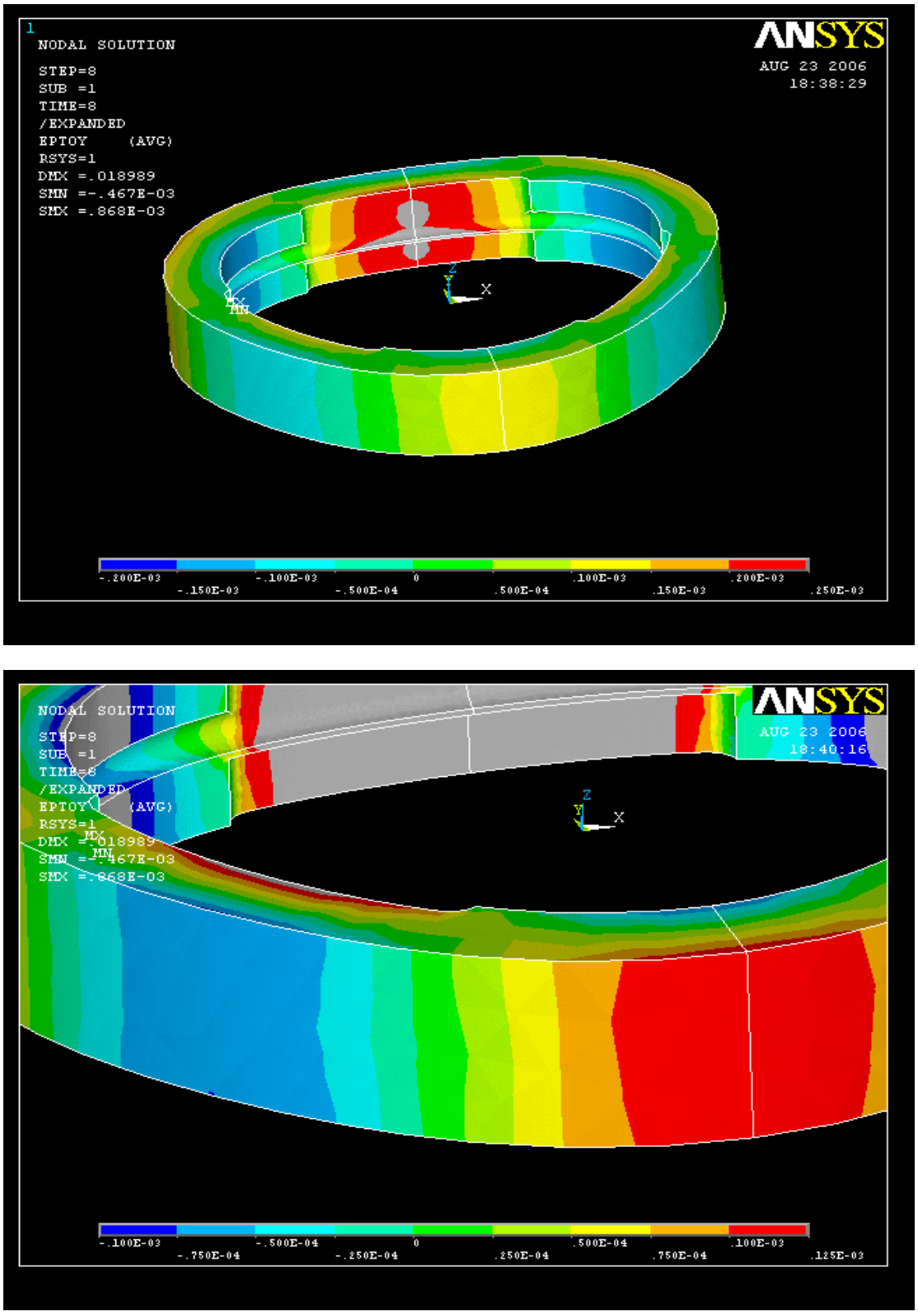

Fig. II.6 Hoop strain along the ring (values to be compared with the strain gages measurements).

Fig. II.7 shows the measurements recorded with the strain gages for the IGC cable as a function of the load applied. The strain gages do not have a monotonic behavior showing asymmetry or non linear effects in the structure. After room temperature experiments performed at MIT it was decided that a 3 points load would have helped in having a more uniform distribution of the strain along the external ring. Using this loading configuration (shown in Fig. II.1) a more uniform behavior was measured with the second experiment as shown in Fig. II.8.

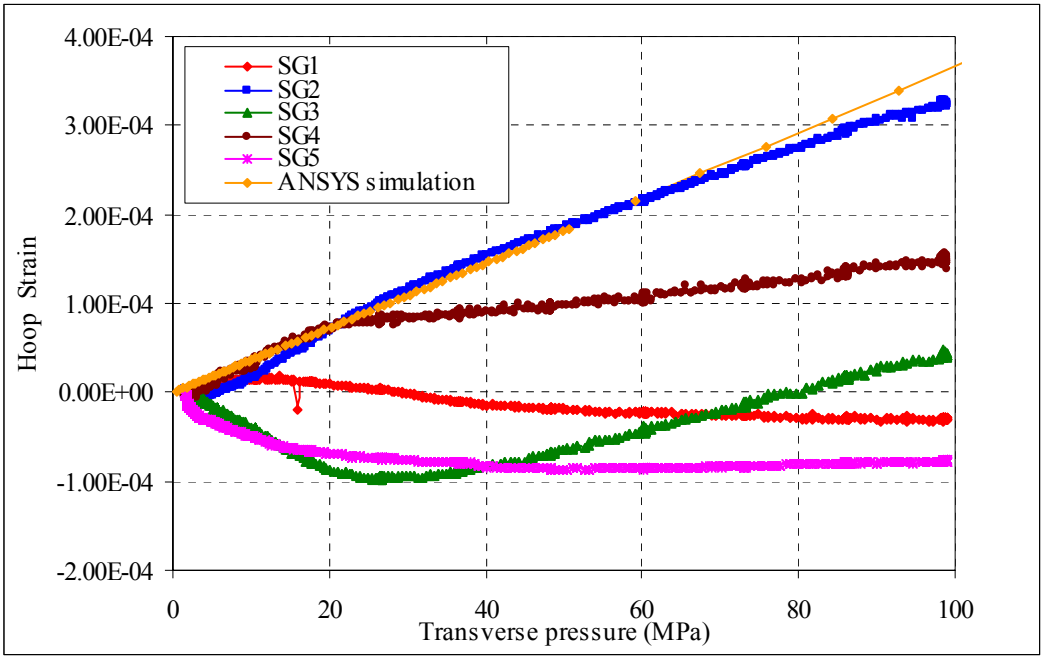

Fig. II.7 Strain gages during the IGC experiment.

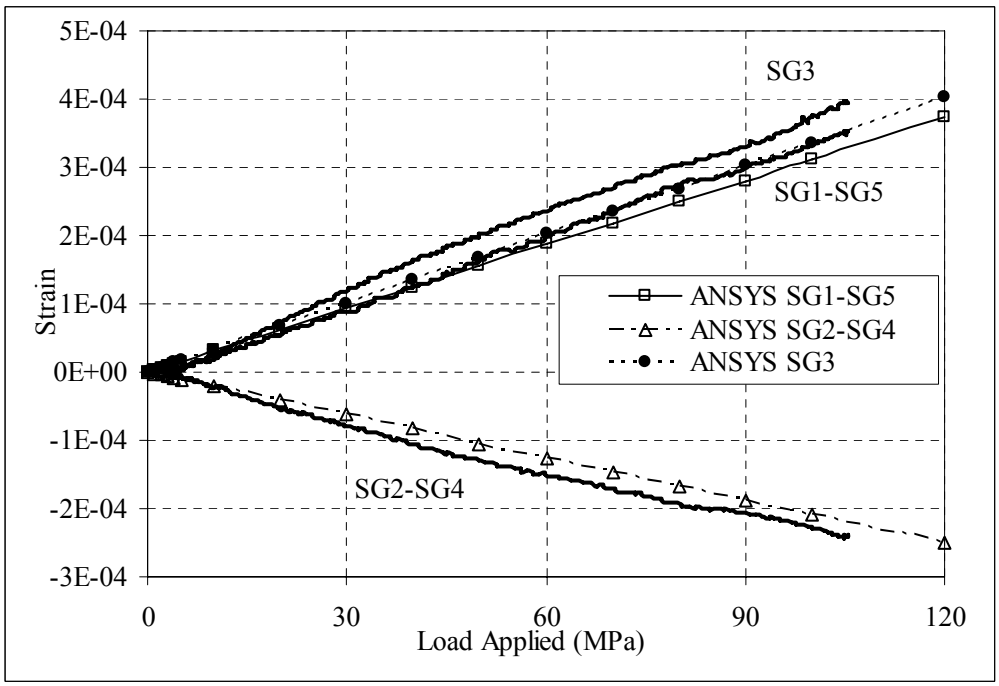

Fig. II.8 Strain gages measurements during the OKAS experiment and their comparison with a 3-D ANSYS® model.

APPENDIX III:
Contact Mechanics Concepts

III.1 Contact mechanics: Hertz theory and line loading of an elastic half space

When two bodies come in contact it is important to study the stresses and the deformation that arise from the contact. Contact mechanics has been studied first by Hertz in 1892 [I.1] while he was studying Newton's optical interference fringes in the gap between to glass lenses and was concerned about the elastic deformation of the surfaces due to their contact pressure. More details have been studied by Timoshenko, Goodier and Lessells [I.2-I.4] who presented derivation of elastic equations for loading of elastic half-spaces (stress, strain and displacement). The case studies most relevant to this thesis will be summarized in this section [I.5].

When two non-conforming solids are brought into contact they touch initially in a single point or along a line and under a certain load they deform in the vicinity of the point of contact. If a coordinate system in which the x-y plane coincides with the tangent plane of the two surfaces is chosen, then the profile of each surface close to the origin can be expressed with the following Eq. III.1:

$$z_1 = A_1 x^2 + B_1 y^2 + C_1 xy + ... \qquad \text{(III.1)}$$

where the higher order terms in x and y are neglected.

The x and y axes can be chosen so that the term in xy vanishes and (III.1) can be written as:

$$z_1 = \frac{1}{2R_1^{'}} x_1^2 + \frac{1}{2R_1^{''}} y_1^2 \qquad \text{(III.1a)}$$

$$z_2 = -\left(\frac{1}{2R_2^{'}} x_2^2 + \frac{1}{2R_2^{''}} y_2^2 \right) \qquad \text{(III.1b)}$$

The separation between the two surfaces is given by (III.2):

$$h = z_1 - z_2 = Ax^2 + By^2 + Cxy = Ax^2 + By^2 = \frac{1}{2R^{'}} x^2 + \frac{1}{2R^{''}} y^2 \qquad \text{(III.2)}$$

where the third equality is obtained by choosing appropriate axes to make the constant C equal to zero, A and B are positive constants and R' and R'' are defined as the principal relative radii of curvature ($1/R^{'} = 1/R_1^{'} + 1/R_2^{'}$; $1/R^{''} = 1/R_1^{''} + 1/R_2^{''}$). If the x_1 and x_2 axis are inclined to each other by an angle ϕ (Fig. III.1) then it can be shown that:

$$(A + B) = \frac{1}{2}\left(\frac{1}{R^{'}} + \frac{1}{R^{''}} \right) = \frac{1}{2}\left(\frac{1}{R_1^{'}} + \frac{1}{R_1^{''}} + \frac{1}{R_2^{'}} + \frac{1}{R_2^{''}} \right) \qquad \text{(III.3)}$$

$$\left|B-A\right| = \frac{1}{2}\left\{\left(\frac{1}{R_1^{'}}-\frac{1}{R_1^{''}}\right)^2+\left(\frac{1}{R_2^{'}}-\frac{1}{R_2^{''}}\right)^2+2\left(\frac{1}{R_1^{'}}-\frac{1}{R_1^{''}}\right)\left(\frac{1}{R_2^{'}}-\frac{1}{R_2^{''}}\right)cos\,2\phi\right\}^{1/2} \quad \text{(III.4)}$$

The equivalent radius R_e is defined as:

$$R_e = (R^{'}R^{''})^{1/2} = \frac{1}{2}(AB)^{-1/2} \quad \text{(III.5)}$$

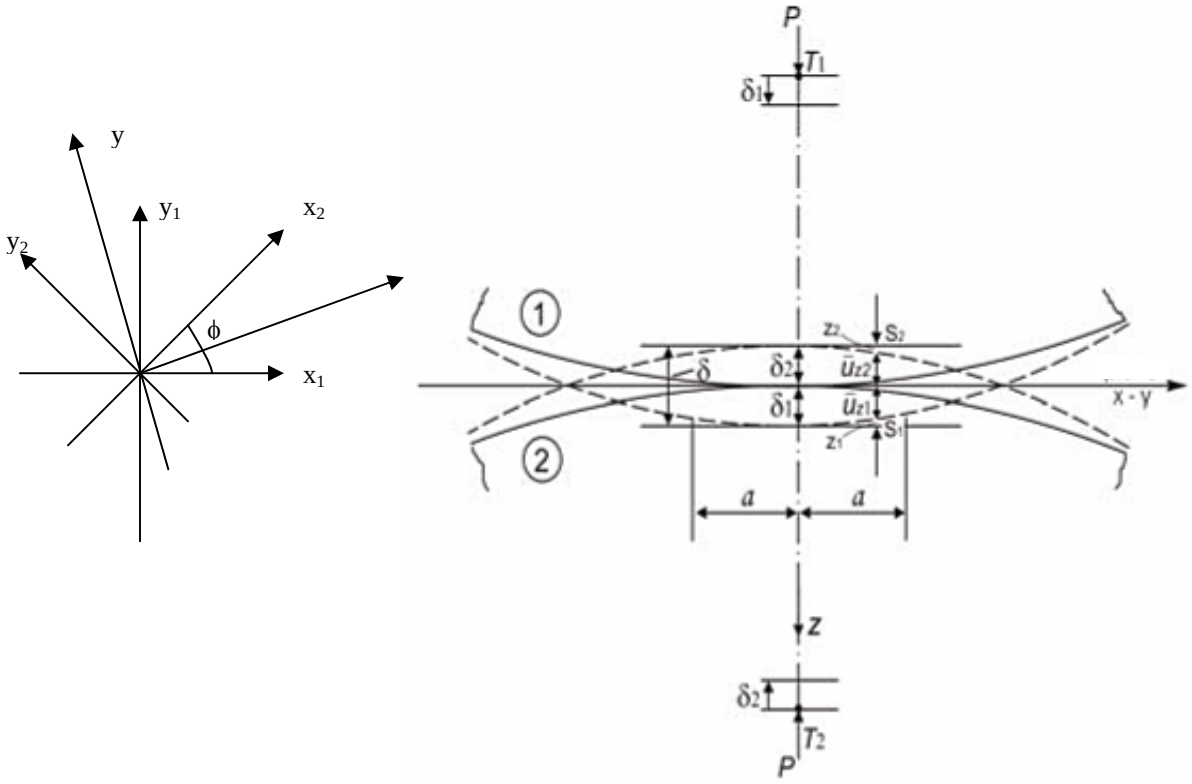

Fig. III.1 Axes used to define h (left). Contact among two solids and their respective deformation once a load P is applied.

Fig. III.1 shows two solids in contact and how they deform once a normal force P is applied. Before deformation the separation between the two corresponding surface points S_1 (x,y,z_1) and S_2 (x,y,z_2) is given by Eq. III.2. During the compression, two distant points T_1 and T_2 move toward the origin by displacements δ_1 and δ_2 respectively. If the two solids did not deform then their profiles would penetrate each other. Due to the contact pressure the surface of each body is displaced by an amount $\bar{u}_{z1}$ and $\bar{u}_{z2}$ relative to the distant points T_1 and T_2. Following the definitions in Fig. III.1 and using Eq. III.2 the total displacement can be written as:

$$\bar{u}_{z1} + \bar{u}_{z2} \geq \delta_1 + \delta_2 - Ax^2 - By^2 \geq \delta - Ax^2 - By^2 \quad \text{(III.6)}$$

where x and y are the common coordinates of S_1 and S_2 projected on the xy plane and δ_1, δ_2 are the displacements of the two bodies. Those two conditions, first introduced by Hertz, must be satisfied by the normal displacements within the contact area (= sign) and outside the contact area (> sign).

By observation, Hertz then assumed that the typical profile of the contact surface is an ellipse. He also introduced the simplification that for the purpose of estimating the local deformations, each body can be considered as an elastic half-space loaded over a small elliptical region. With this assumption the highly concentrated contact stresses are treated separately from the general distribution in the rest of the solid.

In order for this simplification to be justifiable, the contact area must satisfy two conditions:

(i) it must be small compared to the dimensions of each body so that the local stress does not influence the general behavior of the solid

(ii) it must be small compared to the relative radii of curvature of the surfaces so that the strains in the contact region are sufficiently small to lie within the linear theory of elasticity.

Additionally, the two surfaces are assumed to be frictionless. Referring to Fig. III.2, if the significant dimension of the contact area is a and the relative radius of curvature R, the significant radii of each body R_1 and R_2 and their length and depth L, the assumptions made in the Hertz theory can be summarized as:

(i) the surfaces are continuous and non conforming: $2l << R$
(ii) the strains are small: $2l << R$
(iii) each solid can be considered as an elastic half space: $2l << R_{1,2}$, $2l << L$
(iv) the surfaces are frictionless

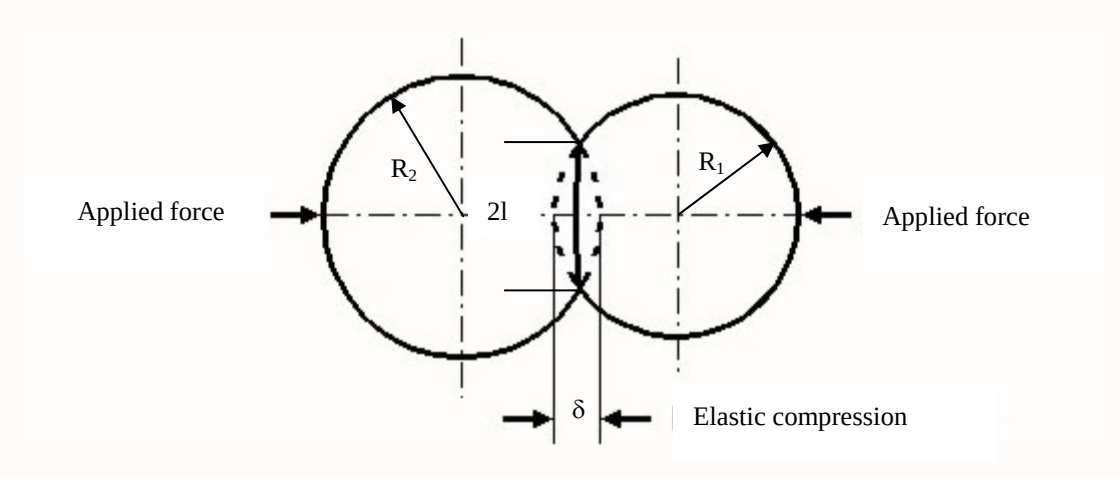

Fig. III.2 Schematic view of two solids in contact.

Two cases are relevant for the analysis of our data: the case of crossing cylinders (resembling the general contacts between strands in a cable) and the case of a cylinder between two plates (resembling the single strand sample). The strategy is to use the general equations to estimate the real contact areas in the cables tested and show that under very reasonable assumption all the samples behaved similarly to respect of the change in critical current as a function of load.

The classical approach to finding the stresses and displacements is due to Boussinesq and Cerruti who made use of the theory of potential. The general profile of a contact between two solids will be described using the theory developed by Hertz and the specific cases discussed later in this section.

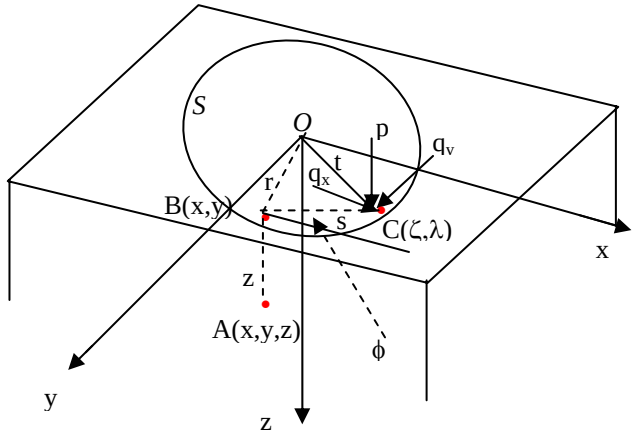

Fig. III.3 Half space used to describe the potential theory [I.5].

If $C(\zeta,\lambda)$ is a general surface point within the loaded surface S and $A(x,y,z)$ a general point in the solid then the distance CA (Fig. III.3) can be expressed as:

$$CA \equiv \chi = \left\{(\zeta - x)^2 + (\lambda - y)^2 + z^2\right\}^{1/2} \tag{III.7}$$

A distribution of pressure $p(\zeta,\lambda)$ and tangential traction $q_x(\zeta,\lambda)$, $q_y(\zeta,\lambda)$ are acting on the surface S. The following potential functions are defined to solve the general problem and find pressure and displacements (III.8):

$$F_1 = \int_S \int q_x(\zeta,\lambda)\cdot\Omega\cdot d\xi d\lambda$$

$$G_1 = \int_S \int q_y(\zeta,\lambda)\cdot\Omega\cdot d\xi d\lambda$$

$$H_1 = \int_S \int p(\zeta,\lambda)\cdot\Omega\cdot d\xi d\lambda$$

$$\Omega = z\cdot ln(\chi + z) - \chi$$

$$F = \frac{\partial F_1}{\partial z} = \int_S \int q_x(\zeta,\lambda)\cdot ln(\chi + z)\cdot d\xi d\lambda$$

$$G = \frac{\partial G_1}{\partial z} = \int_S \int q_y(\zeta,\lambda)\cdot ln(\chi + z)\cdot d\xi d\lambda$$

$$H = \frac{\partial H_1}{\partial z} = \int_S \int p(\zeta,\lambda)\cdot ln(\chi + z)\cdot d\xi d\lambda$$

(III.8)

The function ψ_1 and ψ are also defined:

$$\psi_1 = \frac{\partial F_1}{\partial x} + \frac{\partial G_1}{\partial y} + \frac{\partial H_1}{\partial z}$$
$$\psi = \frac{\partial \psi_1}{\partial z} = \frac{\partial F}{\partial x} + \frac{\partial G}{\partial y} + \frac{\partial H}{\partial z} \qquad \text{(III.9)}$$

Love showed that the components of the elastic displacement at a point *A(x,y,z)* can be expressed as:

$$u_x = \frac{1}{4\pi \cdot G} \cdot \left\{ 2\frac{\partial F}{\partial z} - \frac{\partial H}{\partial x} + 2\nu \frac{\partial \psi_1}{\partial x} - z\frac{\partial \psi}{\partial x} \right\}$$
$$u_y = \frac{1}{4\pi \cdot G} \cdot \left\{ 2\frac{\partial G}{\partial z} - \frac{\partial H}{\partial y} + 2\nu \frac{\partial \psi_1}{\partial y} - z\frac{\partial \psi}{\partial y} \right\} \qquad \text{(III.10)}$$
$$u_z = \frac{1}{4\pi \cdot G} \cdot \left\{ \frac{\partial H}{\partial z} + (1-2\nu)\psi - z\frac{\partial \psi}{\partial x} \right\}$$

Using Hooke's law the corresponding stress can be evaluated:

$$\sigma_x = \frac{2\nu \cdot G}{1-2\nu} \cdot \left(\frac{\partial u_x}{\partial x} + \frac{\partial u_y}{\partial y} + \frac{\partial u_z}{\partial z} \right) + 2G\frac{\partial u_x}{\partial x}$$
$$\sigma_y = \frac{2\nu \cdot G}{1-2\nu} \cdot \left(\frac{\partial u_x}{\partial x} + \frac{\partial u_y}{\partial y} + \frac{\partial u_z}{\partial z} \right) + 2G\frac{\partial u_y}{\partial y} \qquad \text{Normal stress components}$$
$$\sigma_x = \frac{2\nu \cdot G}{1-2\nu} \cdot \left(\frac{\partial u_x}{\partial x} + \frac{\partial u_y}{\partial y} + \frac{\partial u_z}{\partial z} \right) + 2G\frac{\partial u_z}{\partial z} \qquad \text{(III.11)}$$
$$\tau_{xy} = G \cdot \left(\frac{\partial u_x}{\partial y} + \frac{\partial u_y}{\partial x} \right)$$
$$\tau_{yz} = G \cdot \left(\frac{\partial u_y}{\partial z} + \frac{\partial u_z}{\partial y} \right) \qquad \text{Shear stress components}$$
$$\tau_{zx} = G \cdot \left(\frac{\partial u_z}{\partial x} + \frac{\partial u_x}{\partial z} \right)$$

In the analysis performed in this thesis it was assumed the solid is only under the action of a normal pressure $p(\zeta,\lambda)$ (frictionless contact) so that the previous equations can be simplified to:

$$
\begin{aligned}
&F = F_1 = G = G_1 = 0 \\
&\psi_1 = \frac{\partial H_1}{\partial z} = H = \int_S \int p(\zeta,\lambda)\cdot ln(\chi + z)\cdot d\xi d\lambda \\
&\psi = \frac{\partial H}{\partial z} = \frac{\partial \psi_1}{\partial z} = \int_S \int p(\zeta,\lambda)\cdot \frac{1}{\chi}\cdot d\xi d\lambda \\
&u_x = -\frac{1}{4\pi\cdot G}\left\{(1-2\nu)\frac{\partial \psi_1}{\partial x} + z\frac{\partial \psi}{\partial x}\right\} \\
&u_y = -\frac{1}{4\pi\cdot G}\left\{(1-2\nu)\frac{\partial \psi_1}{\partial y} + z\frac{\partial \psi}{\partial y}\right\} \\
&u_z = \frac{1}{4\pi\cdot G}\left\{2(1-\nu)\psi - z\frac{\partial \psi}{\partial z}\right\}
\end{aligned}
\qquad \text{(III.12)}
$$

But ψ and ψ_1 are harmonic functions of x, y, and z so that they satisfy Laplace's equation:

$$
\begin{aligned}
&\nabla^2\psi = \nabla^2\psi_1 = 0 \\
&\Delta \equiv \frac{\partial u_x}{\partial x} + \frac{\partial u_y}{\partial y} + \frac{\partial u_z}{\partial z} = \frac{1-2\nu}{2\pi\cdot G}\frac{\partial \psi}{\partial z}
\end{aligned}
\qquad \text{(III.13)}
$$

Substituting Eq. III.12 into III.12 the components of stress at any point in the solid can be found to be:

$$
\begin{aligned}
&\sigma_x = \frac{1}{2\pi}\left\{2\nu\frac{\partial \psi}{\partial z} - z\frac{\partial^2\psi}{\partial x^2} - (1-2\nu)\frac{\partial^2\psi_1}{\partial x^2}\right\} \qquad \tau_{xy} = -\frac{1}{2\pi}\left\{(1-2\nu)\frac{\partial^2\psi_1}{\partial x\partial y} + 2\frac{\partial^2\psi}{\partial x\partial y}\right\} \\
&\sigma_y = \frac{1}{2\pi}\left\{2\nu\frac{\partial \psi}{\partial z} - z\frac{\partial^2\psi}{\partial y^2} - (1-2\nu)\frac{\partial^2\psi_1}{\partial y^2}\right\} \qquad \tau_{yz} = -\frac{1}{2\pi}z\frac{\partial^2\psi}{\partial y\partial z} \\
&\sigma_x = \frac{1}{2\pi}\left\{\frac{\partial \psi}{\partial z} - z\frac{\partial^2\psi}{\partial x^2}\right\} \qquad \tau_{zx} = -\frac{1}{2\pi}z\frac{\partial^2\psi}{\partial x\partial z}
\end{aligned}
$$

(III.14)

At the surface of the solid the normal stress and the displacements are:

$$\begin{aligned}
\bar{\sigma}_z &= \frac{1}{2\pi}\left(\frac{\partial \psi}{\partial z}\right)_{z=0} = \begin{Bmatrix} -p(\zeta,\lambda) & inside\ S \\ 0 & outside\ S \end{Bmatrix} \\
\bar{u}_x &= -\frac{1-2\nu}{4\pi \cdot G}\left(\frac{\partial \psi_1}{\partial x}\right)_{z=0} \\
\bar{u}_y &= -\frac{1-2\nu}{4\pi \cdot G}\left(\frac{\partial \psi_1}{\partial y}\right)_{z=0} \\
\bar{u}_z &= \frac{1-\nu}{2\pi \cdot G}\left(\frac{\partial \psi_1}{\partial z}\right)_{z=0} = \frac{1-\nu}{2\pi \cdot G}(\psi)_{z=0}
\end{aligned} \qquad \text{(III.15)}$$

(i) Crossing Cylinders(multi-strand cable)

If a general pressure distribution generating an elliptical contact area is assumed (the area of contact is elliptical in shape with semi-axis η and ξ Fig. III.4):

$$p = p_0\left\{1-\left(\frac{x}{\eta}\right)^2-\left(\frac{y}{\xi}\right)^2\right\}^n \qquad \text{(III.16)}$$

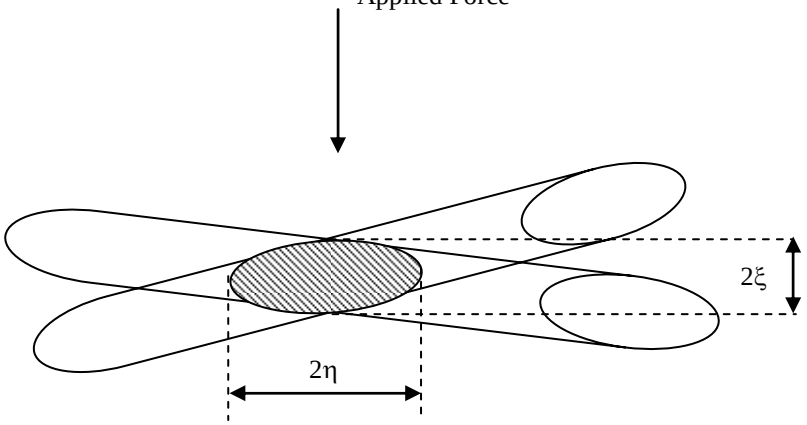

Fig. III.4 Schematic view of the contact area between two strands.

The classical approach, using the potential functions brings to the following results:

$$\psi(x,y,z) = \int_S\int p_0\left\{1-(\zeta/\eta)^2-(\lambda/\xi)^2\right\}^n \rho^{-1} d\zeta d\lambda \qquad \text{(III.17)}$$

where $\rho^2 = (\zeta - x)^2 + (\lambda - y)^2 + z^2$.

The normal displacement is given by:

$$\bar{u}_z = \frac{1-\nu}{2\pi \cdot G}(\psi)_{z=0} \tag{III.18}$$

For a general point in the solid, following the potential theory:

$$\psi(x,y,z) = \frac{\Gamma(n+1)\Gamma(1/2)}{\Gamma(n+3/2)} p_0 \cdot \eta \cdot \xi \cdot \int_{\gamma_1}^{\infty} \left(1 - \frac{x^2}{\eta^2 + w} - \frac{y^2}{\xi^2 + w} - \frac{z^2}{w}\right)^{n+1/2} \times \times \frac{dw}{\left\{(\eta^2 + w)\cdot(\xi^2 + w)\cdot w\right\}^{1/2}} \tag{III.19}$$

where Γ is the gamma function and γ_1 is the positive root of the equation (γ_1 is taken to be zero to evaluate ψ at a surface point within the loaded region):

$$\frac{x^2}{\eta^2 + \gamma} + \frac{y^2}{\xi^2 + \gamma} + \frac{z^2}{\gamma} = 1 \tag{III.20}$$

In the case of Hertzian pressure (most commonly used) *n = 1/2* so that:

$$p = p_0 \left\{1 - \left(\frac{x}{\eta}\right)^2 - \left(\frac{y}{\xi}\right)^2\right\}^{1/2} \tag{III.21}$$

$$\psi(x,y,z) = \frac{1}{2} p_0 \cdot \eta \cdot \xi \cdot \int_{\gamma_1}^{\infty} \left(1 - \frac{x^2}{\eta^2 + w} - \frac{y^2}{\xi^2 + w} - \frac{z^2}{w}\right)^{n+1/2} \times \times \frac{dw}{\left\{(\eta^2 + w)\cdot(\xi^2 + w)\cdot w\right\}^{1/2}}$$

on the surface within the loaded region (III.22)

$$\psi(x,y,0) = \frac{1}{2} p_0 \cdot \eta \cdot \xi \cdot \int_{0}^{\infty} \left(1 - \frac{x^2}{\eta^2 + w} - \frac{y^2}{\xi^2 + w}\right)^{n+1/2} \times \times \frac{dw}{\left\{(\eta^2 + w)\cdot(\xi^2 + w)\cdot w\right\}^{1/2}}$$

This pressure produces displacements within the ellipse given by Eq. III.23:

$$\bar{u}_z = \frac{1-\nu^2}{\pi \cdot E}(L - Mx^2 - Ny^2) \tag{III.23}$$

So that for both bodies (Fig. III.2)

$$\bar{u}_{z1} + \bar{u}_{z2} = (L - Mx^2 - Ny^2)\frac{1}{\pi \cdot E^*} \tag{III.24}$$

with

$$M = \frac{\pi \cdot p_0 \eta \xi}{2}\int_0^\infty \frac{dw}{\left\{(\eta^2 + w)^3(\xi^2 + w)w\right\}^{1/2}} = \frac{\pi \cdot p_0 \xi}{e^2\eta^2}\{K(e) - E(e)\} \tag{III.25}$$

$$N = \frac{\pi \cdot p_0 \eta \xi}{2}\int_0^\infty \frac{dw}{\left\{(\eta^2 + w)(\xi^2 + w)^3 w\right\}^{1/2}} = \frac{\pi \cdot p_0 \xi}{e^2\eta^2}\left\{\frac{\eta^2}{\xi^2}E(e) - K(e)\right\} \tag{III.26}$$

$$L = \frac{\pi \cdot p_0 \eta \xi}{2}\int_0^\infty \frac{dw}{\left\{(\eta^2 + w)(\xi^2 + w)w\right\}^{1/2}} = \pi \cdot p_0 \xi \cdot K(e) \tag{III.27}$$

where e is the eccentricity of the ellipse $e = (1 - \xi^2/\eta^2)^{1/2}$, $K(e)$ and $E(e)$ are complete elliptic integrals of the first and second kind and $1/E^* = (1-\nu_1^2)/E_1 + (1-\nu_2^2)/E_2$. The pressure distribution is semi-ellipsoidal and the total load F is given by $F = (2/3)\cdot p_0 \pi \cdot \eta \cdot \xi$.

The total displacement in Eq. III.24 has to satisfy the condition expressed by Eq. III.6 so that:

$$A = M/\pi \cdot E^* = (p_0/E^*)\cdot(\xi/e^2\eta^2)\cdot\{K(e) - E(e)\} \tag{III.28}$$

$$B = N/\pi \cdot E^* = (p_0/E^*)\cdot(\xi/e^2\eta^2)\cdot\{(\eta^2/\xi^2)E(e) - K(e)\} \tag{III.29}$$

$$\delta_x = y = L/\pi \cdot E^* = (p_0/E^*)\cdot\xi\cdot K(e) \tag{III.30}$$

To find the shape and size of the ellipse of contact the following equations can be used:

$$\frac{B}{A} = \frac{R'}{R''} = \frac{(\eta/\xi)^2 \cdot E(e) - K(e)}{K(e) - E(e)} \tag{III.31}$$

$$(AB)^{1/2} = \frac{1}{2}\left(\frac{1}{R'R''}\right)^{\frac{1}{2}} = \frac{1}{2R_e} = \frac{p_0}{E^*}\frac{b}{a^2e^2}\left[\begin{matrix}\{(a/b)^2E(e) - K(e)\}\times \\ \times\{K(e) - E(e)\}\end{matrix}\right]^{\frac{1}{2}} \tag{III.32}$$

Defining $c = (\eta \cdot \xi)^{1/2}$ and substituting for p_0:

$$c = \left(\frac{3F_c R_e}{4E^*} \right) F_1(e) \tag{III.33}$$

where *F(e)* is also an elliptic integral.

The semi-axes of the ellipse are often evaluated [III.3, III.6-III.8] with the following equations:

$$\eta = \alpha \cdot \left(\frac{F_c \cdot K_D}{E^*} \right)^{1/3} \tag{III.34}$$

$$\xi = \beta \cdot \left(\frac{F_c \cdot K_D}{E^*} \right)^{1/3} \tag{III.35}$$

where F_c is the total force in N, α and β are tabulated values dependent on the crossing angles ϕ between the two solids (Table III.1) and

$$K_D = \frac{3}{2} \cdot \frac{1}{1/R_1^{'} + 1/R_2^{'} + 1/R_1^{''} + 1/R_2^{''}} = \frac{3}{A+B}$$

$$\cos\Omega = \frac{2 \cdot K}{3} \cdot \left\{ \left(\frac{1}{R_1^{'}} - \frac{1}{R_1^{''}} \right)^2 + \left(\frac{1}{R_2^{'}} - \frac{1}{R_2^{''}} \right)^2 + 2\left(\frac{1}{R_1^{'}} - \frac{1}{R_1^{''}} \right)\left(\frac{1}{R_2^{'}} - \frac{1}{R_2^{''}} \right)\cos 2\phi \right\}^{1/2} = \frac{|B-A|}{A+B}$$

Table III.1 Tabulated values of α and β to evaluate the semi-axis of the ellipse of contact [5.7, 5.8].

Ω	α	β	λ
0	-	0	0
1	36.890	0.131	0.047
2	22.260	0.169	0.090
3	16.500	0.196	0.130
4	13.310	0.209	0.165
6	9.790	0.255	0.227
8	7.860	0.285	0.278
10	6.612	0.319	0.320
20	3.778	0.408	0.456
30	2.731	0.493	0.542
35	2.397	0.530	0.579
40	2.136	0.567	0.614
45	1.926	0.604	0.645
50	1.754	0.641	0.672
55	1.611	0.678	0.693
60	1.486	0.717	0.710
65	1.378	0.759	0.724

70	1.284	0.802	0.737
75	1.202	0.846	0.750
80	1.128	0.893	0.764
85	1.061	0.944	0.775
90	1.000	1.000	0.777

The total displacement in this case (deformation of both strands) can be evaluated by using Eq. III.36:

$$\delta_x = \lambda \cdot \sqrt[3]{\frac{F_c^{\,2}}{(E^*)^2 \cdot K_D}} \qquad \text{(III.36)}$$

Using Eq. III.34 and III.35, the contact surface can be evaluated using Eq. III.37.

$$S_c = \pi \cdot \eta \cdot \xi \qquad \text{(III.37)}$$

In the case of 3-strand and 45-strand cables, $R_1^{'} = R_2^{'} = a$; $R_1^{''} = R_2^{''} = \infty$ (a being the radius of a strand) so that:

$$K_D = \frac{3}{2} \cdot \frac{1}{1/R_1^{'} + 1/R_2^{'}} = \frac{3 \cdot a}{4}$$

$$\cos\Omega = \frac{2 \cdot K_D}{3} \cdot \left\{ \left(\frac{1}{a}\right)^2 + \left(\frac{1}{a}\right)^2 + 2\left(\frac{1}{a}\right)\left(\frac{1}{a}\right)\cos 2\phi \right\}^{1/2} = \left\{ \frac{(1+\cos 2\phi)}{2} \right\}^{1/2}$$

(ii) Infinite cylinder (single strand)

The single strand sample (with radius *a*) tested resembles a case in which a long cylinder is pressed in between two flat plates (or two solids with radius much bigger that the single strand diameter) as shown in Fig. III.5.

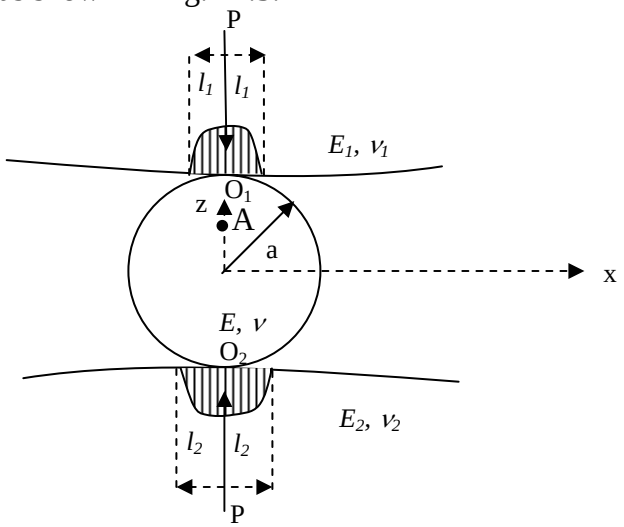

Fig. III.5 Cylinder in contact with two solids. The contact pressure distribution is shown in the figure and is used to estimate the contact width $2l_1$, $2l_2$.

In this case the stresses and deformation are evaluated for an elastic half-space loaded one-dimensionally over a narrow strip (line loading). Considering a more general case, the stress components at any point A of an elastic half space (Fig. III.6) loaded over a strip ($-d<x<g$) by a normal pressure $p(x)$ and tangential traction $q(x)$ can be expressed as[III.2, III.5]:

$$\sigma_x = -\frac{2z}{\pi}\int_{-d}^{g}\frac{p(s)(x-s)^2\,ds}{\left\{(x-s)^2+z^2\right\}^2} - \frac{2}{\pi}\int_{-d}^{g}\frac{q(s)(x-s)^3\,ds}{\left\{(x-s)^2+z^2\right\}^2}$$

$$\sigma_z = -\frac{2z^3}{\pi}\int_{-d}^{g}\frac{p(s)\,ds}{\left\{(x-s)^2+z^2\right\}^2} - \frac{2z^2}{\pi}\int_{-d}^{g}\frac{q(s)(x-s)\,ds}{\left\{(x-s)^2+z^2\right\}^2} \qquad \text{(III.38)}$$

$$\tau_{xz} = -\frac{2z^2}{\pi}\int_{-d}^{g}\frac{p(s)(x-s)\,ds}{\left\{(x-s)^2+z^2\right\}^2} - \frac{2z}{\pi}\int_{-d}^{g}\frac{q(s)(x-s)^2\,ds}{\left\{(x-s)^2+z^2\right\}^2}$$

The elastic displacements on the surface can be found using Hooke's law:

$$\bar{u}_x = -\frac{(1-2\nu)(1+\nu)}{2E}\left\{\int_{-d}^{x}p(s)ds - \int_{x}^{g}p(s)ds\right\} - \frac{2(1-\nu^2)}{\pi\cdot E}\int_{-d}^{g}q(s)\ln\left|x-s\right|ds + C_1$$

$$\bar{u}_z = -\frac{2(1-\nu^2)}{\pi\cdot E}\int_{-d}^{g}p(s)\ln\left|x-s\right|ds + \frac{(1-2\nu)(1+\nu)}{2E}\left\{\int_{-d}^{x}q(s)ds - \int_{x}^{g}q(s)ds\right\} + C_2 \qquad \text{(III.39)}$$

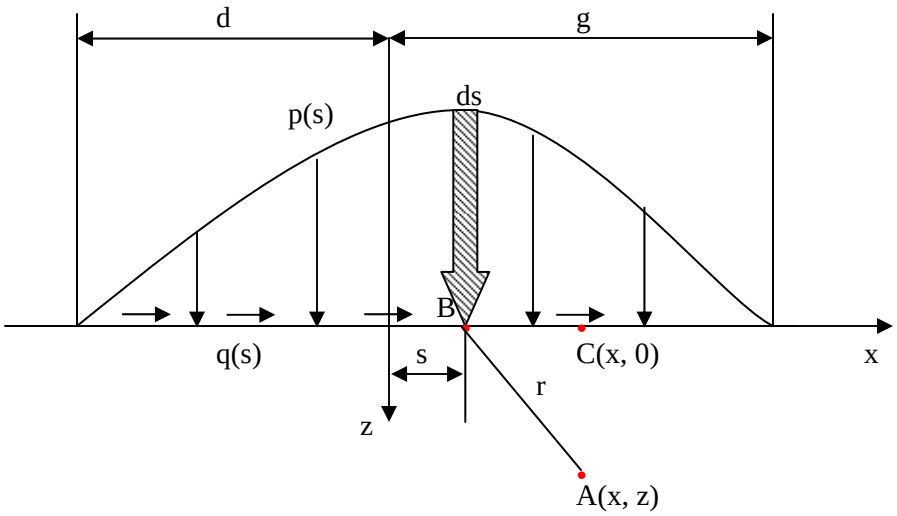

Fig. III.6 Schematic view of an elastic half space loaded with normal pressure p(x) and tangential traction q(x).

Using Eq. III.39 it is possible to estimate the strain in the x direction and the slope of the deformed surface (which will be used later in this section). In particular the case of interest for the single strand is considering a frictionless surface ($q(x)$=0):

$$\begin{aligned} \bar{\varepsilon}_x &= \frac{\partial \bar{u}_x}{\partial x} = -\frac{(1-2\nu)(1+\nu)}{E}\, p(x) \\ \frac{\partial \bar{u}_z}{\partial x} &= -\frac{2(1-\nu^2)}{\pi \cdot E} \int_{-d}^{g} p(s) \frac{1}{x-s} ds \end{aligned} \qquad \text{(III.40)}$$

With the information gathered in the previous equations the case depicted in Fig. III.5 is considered and the approach used by Hertz is followed. Eq. III.41 represents the separation between corresponding points on the unloaded surface (z is the single strand, z_i correspond to the surfaces pressing against it):

$$h = z + z_i = Ax^2 = \frac{1}{2}\left(\frac{1}{a} + \frac{1}{R_i}\right)x^2 = \frac{1}{2}\left(\frac{1}{R_{eq,i}}\right)x^2 \qquad \text{(III.41)}$$

For points lying within the contact area after loading:

$$\bar{u}_z + \bar{u}_{zi} = \delta_z + \delta_{z_i} - Ax^2 = \delta - \frac{1}{2}\left(\frac{1}{R_{eq,i}}\right)x^2 \qquad \text{(III.42)}$$

For points lying outside the contact area after loading:

$$\bar{u}_z + \bar{u}_{zi} > \delta_z + \delta_{z_i} - Ax^2 = \delta - \frac{1}{2}\left(\frac{1}{R_{eq,i}}\right)x^2 \qquad \text{(III.43)}$$

Differentiating Eq. III.43 and using Eq. III.40:

$$\frac{\partial \overline{u}_z}{\partial x} + \frac{\partial \overline{u}_{z_i}}{\partial x} = -\frac{1}{R_{eq,i}} x = -\frac{2}{\pi \cdot E_i^*} \int_{-l_i}^{l_i} \frac{p(s)}{x-s} ds \qquad \text{(III.44)}$$

where $1/E_i^* = (1-\nu^2)/E + (1-\nu^2)/E_i$

Eq. III.44 can be solved to find the pressure distribution $p_l(x)$. $p_l(x)$ has to satisfy the conditions III.32 and III.33 so that if a compressive load per unit axial length F_l (N/m) the pressure distribution is as follow:

$$p_l = \frac{2 \cdot F_l}{\pi \cdot l_i} \left(1 - \frac{x^2}{l_i^2}\right)^{1/2} \qquad \text{(III.45)}$$

where the semi-contact width l_i is given by Eq. III.46:

$$l_i^2 = \frac{4 \cdot F_l \cdot R_{eq,i}}{\pi \cdot E_i^*} \qquad \text{(III.46)}$$

The maximum pressure is:

$$p_0 = \frac{2 \cdot F_l}{\pi \cdot l_i} \qquad \text{(III.47)}$$

The stresses between the two solids can be found substituting the pressure distribution of Eq. III.45 into Eq. III.38. At the contact interface $\sigma_x = \sigma_y = -p(x)$; outside the contact region the stresses vanish to zero and along the z-axis the integration of III.38 gives:

$$\begin{aligned} \sigma_x &= -\frac{p_0}{l_i}\left\{\frac{(l_i^2 + 2z^2)}{(l_i^2 + 2z^2)^{1/2}} - 2z\right\} = -\frac{2F_l}{\pi \cdot l_i^2}\left\{\frac{(l_i^2 + 2z^2)}{(l_i^2 + 2z^2)^{1/2}} - 2z\right\} \\ \sigma_z &= -\frac{p_0}{l_i}\left\{\frac{1}{(l_i^2 + 2z^2)^{1/2}}\right\} = -\frac{2F_l}{\pi \cdot l_i^2}\left\{\frac{1}{(l_i^2 + 2z^2)^{1/2}}\right\} \end{aligned} \qquad \text{(III.48)}$$

In the case of the single strand pressed between two bodies with radius bigger than the radius of the single strand, as shown by Timoshenko and Goodier [III.2], the stress at a point A will be given by Eq. III.41, a uniform biaxial tension ($\sigma_x = \sigma_y = -P/\pi \cdot a$) caused by the diametrically opposed forces cause by the two solid pressing on the cylinder and the stress caused by the pressure at point O_2 (far from A).

Adding all those components the stress components can be written as:

$$\sigma_x = \frac{F_l}{\pi}\left\{\frac{1}{a} - \frac{2(l_i^{\,2} + 2z^2)}{l_i^{\,2}(l_i^{\,2} + 2z^2)^{1/2}} + \frac{4z}{l_i^{\,2}}\right\}$$
$$\sigma_z = \frac{F_l}{\pi}\left\{\frac{1}{a} - \frac{2}{2a - z} - \frac{1}{(l_i^{\,2} + 2z^2)^{1/2}}\right\} \qquad \text{(III.49)}$$

Using plane strain condition ($\varepsilon_y = 0$), those stress components can be used to evaluate the strain component in the z-direction:

$$\varepsilon_z = \{(1-\nu^2)/E\}\left\{\sigma_z - \sigma_x \frac{\nu}{1-\nu}\right\} \qquad \text{(III.50)}$$

Integrating the strain component of z between *z = 0* and *z = a* the compression of the upper and lower half of the cylinder can be found using Eq. III.51 and III.52.

The total displacement is the sum of the displacement from the top and bottom half of the cylinder (Eq. III.53).

$$\delta_1 = \int_0^a \varepsilon_z \cdot dz = F_l \cdot \frac{(1-\nu^2)}{\pi \cdot E}\left\{2 \cdot ln\left(\frac{4a}{l_1}\right) - 1\right\} \qquad \text{(III.51)}$$

$$\delta_2 = \int_0^a \varepsilon_z \cdot dz = F_l \cdot \frac{(1-\nu^2)}{\pi \cdot E}\left\{2 \cdot ln\left(\frac{4a}{l_2}\right) - 1\right\} \qquad \text{(III.52)}$$

$$\delta = 2F_l \cdot \frac{(1-\nu^2)}{\pi \cdot E}\left\{ln\left(\frac{4a}{l_1}\right) + ln\left(\frac{4a}{l_2}\right) - 1\right\} \qquad \text{(III.53)}$$

The results obtained depend on the profile chosen for the pressure distribution. In literature a parabolic profile is often found to describe the pressure distribution [IV.9] but the total displacement is not that different from the one obtained by Eq. III.53 (less than 8% difference).

APPENDIX IV:
Critical Current Evaluation Using Gaussian Method

IV.1 Normalized Critical Current of a Multi-strand Cable

The normalized critical current of a multi-strand cable can be evaluated by knowing the contact pressure and using the critical current data available for a single strand or 3-strand cable as a function of load (Eq. IV.1):

$$I_c = 2 \cdot \int_{-R}^{R} J_{cy-engineering} \cdot \sqrt{(R^2 - y^2)} \cdot (1 - v_f)dy = 2 \cdot \int_{-R}^{R} \frac{I_{c-sin\,glestrand}}{\pi \cdot a^2} \cdot \sqrt{(R^2 - y^2)} \cdot (1 - v_f)dy$$

$$\frac{I_c}{I_{co-45strand}} = 2 \cdot \int_{-R}^{R} \frac{I_{c-sin\,glestrand}}{\pi \cdot a^2 \cdot I_{co-45strand}} \cdot \sqrt{(R^2 - y^2)} \cdot (1 - v_f)dy = 2 \cdot \int_{-R}^{R} \frac{1}{N_s} \frac{I_{c-sin\,glestrand}}{\pi \cdot a^2 \cdot I_{co-sin\,glestrand}} \cdot \sqrt{(R^2 - y^2)} \cdot (1 - v_f)dy \quad \text{(IV.1)}$$

Where $J_{cy\text{-}engineering}$ is the engineering critical current density, R the radius of the multi-strand cable, a the radius of a strand, v_f the void fraction of the cable, N_s the number of strands in the cable.

The integral in Eq. IV.1 is evaluated using the Gaussian method of order 40 [IV.1].

The end result will be a list of force per unit length and normalized critical current as a function of the force per unit length. Additionally, as explained later in this paragraph, the normalized critical current considering also the cycling effect will be obtained (Table IV.1).

Table IV.1 Table obtained as a result of the Gaussian integration.

Total force per unit length (kN/m)	**$I_c/I_{c0\text{-}45\text{-}strand}$**	**$I_c/I_{c0\text{-}45\text{-}strand}$ (considering cycles)**
0	1	1
8	0.99994	0.99637
⋮	⋮	⋮
776	0.16287	0.19138
784	0.16146	0.18863
792	0.16006	0.18592
800	0.15867	0.18325

Each value of the second and third column is calculated using a Gaussian integral as follow (R_{40} is the error on the approximation of the series and it is a small quantity):

$$\int_{b_1}^{b_2} f(y)\cdot dy = \frac{b_2 - b_1}{2}\cdot\sum_{1}^{40} w_i \cdot f(y_i) + R_{40} \qquad \text{(IV.2)}$$

$$f(y_i) = 2\cdot J_{c-engineering}\cdot\sqrt{(R^2 - y_i^2)}\cdot(1-v_f) = 2\cdot\frac{1}{N_s}\frac{1}{\pi\cdot a^2}\frac{I_c}{I_{c0-singlestrand}}\cdot\sqrt{(R^2 - y_i^2)}\cdot(1-v_f) \qquad \text{(IV.3)}$$

where w_i and y_i are weights and abscissas of Gaussian integration for order 40, respectively (Table IV.2, IV.3). N_s is the number of strands in the cable (45), a is the strand radius (0.41 mm), b_1 is $-R_{cable}$ (radius of the cable) and b_2 is R_{cable} and v_f is the void fraction (0.33), y_i varies between $-R_{cable}$ and $+R_{cable}$.
After finding the contact pressure, the single strand data can be used to estimate $\frac{I_{c-singlestrand}}{I_{co-singlestrand}}$ at that particular pressure and evaluate the normalized critical current of a multi-strand cable

Table IV.2 Weight wi used to evaluate the integral of Eq. IV.2

Gauss-Legendre Weights for order 40
+ 0.00452127709853319125847173287818533272783111019970624186918 1
+ 0.01049828453115281361474217106727965237679262131579735646753 4
+ 0.01642105838190788871286348488236392729234229334695864558297 4
+ 0.02224584919416695726150432418420857320703319667935558758455 1
+ 0.02793700698002340109848915750772107730255086205076779113267 2
+ 0.03346019528254784739267818308641084897724178665376591985272 3
+ 0.03878216797447201763997203129044616225345921123202753405059 5
+ 0.04387090818567327199167468604171549581100683717023858885836 1
+ 0.04869580763507223206143416044814638806784302737712140015243 8
+ 0.05322784698393682435499647977226050455532117182200789399171 1
+ 0.05743976909939155136661773091042598560010483585445477402854 6
+ 0.06130624249292893916653799640839859590259376351117506069576 1
+ 0.06480401345660103807455452956675273003269296420848913354420 5
+ 0.06791204581523390382569010823192398598419723837928558951665 3
+ 0.07061164739128677969548363085528683235955910399558509264987 2
+ 0.07288658239580405906051068344251783585755908098579698325534 4
+ 0.07472316905796826420018933626132467319120293442035757884771 4
+ 0.07611036190062624237155807592249482301255955384506836531410 9
+ 0.07703981816424796558830753428381024852443975416393731493599 0
+ 0.07750594797842481126372396295832632696366865278810314766906 3
+ 0.07750594797842481126372396295832632696366865278810314766906 3
+ 0.07703981816424796558830753428381024852443975416393731493599 0
+ 0.07611036190062624237155807592249482301255955384506836531410 9
+ 0.07472316905796826420018933626132467319120293442035757884771 4
+ 0.07288658239580405906051068344251783585755908098579698325534 4
+ 0.07061164739128677969548363085528683235955910399558509264987 2
+ 0.06791204581523390382569010823192398598419723837928558951665 3
+ 0.06480401345660103807455452956675273003269296420848913354420 5
+ 0.06130624249292893916653799640839859590259376351117506069576 1
+ 0.05743976909939155136661773091042598560010483585445477402854 6
+ 0.05322784698393682435499647977226050455532117182200789399171 1
+ 0.04869580763507223206143416044814638806784302737712140015243 8
+ 0.04387090818567327199167468604171549581100683717023858885836 1
+ 0.03878216797447201763997203129044616225345921123202753405059 5
+ 0.03346019528254784739267818308641084897724178665376591985272 3
+ 0.02793700698002340109848915750772107730255086205076779113267 2
+ 0.02224584919416695726150432418420857320703319667935558758455 1
+ 0.01642105838190788871286348488236392729234229334695864558297 4
+ 0.01049828453115281361474217106727965237679262131579735646753 4
+ 0.00452127709853319125847173287818533272783111019970624186918 1

Table IV.3 Abscissas y_i used to evaluate the integral of Eq. IV.2

Gauss-Legendre Abscissas for order 40
- 0.998237709710559200349622702420586492335770381595045808577581
- 0.990726238699457006453054352221372154962220813510860248783 52
- 0.977259949983774262663370283712903806978667932037984851175804
- 0.957916819213791655804540999452759285094883490602744761591148
- 0.932812808278676533360852166845205716434753575282688898929952
- 0.902098806968874296728253330868493103584488081057664431112536
- 0.865959503212259503820781808354619963570546553011094983606217
- 0.824612230833311663196320230666098773907240384242979438623162
- 0.778305651426519387694971545506494848020691316126881762542263
- 0.727318255189927103280996451754930548557378673533316562403522
- 0.671956684614179548379354514961494109970325981383838269965139
- 0.612553889667980237952612450230694877380123781683135778757367
- 0.549467125095128202075931305529517970233975101595637141746493
- 0.483075801686178712908566574244823004599022395533099841136162
- 0.413779204371605001524879745803713682974099624052904661350012
- 0.341994090825758473007492481179194310066953620027313547235050
- 0.268152185007253681141184344808596183424804373236236683321946
- 0.192697580701371099715516852065149894814092021105201079079604
- 0.116084070675255208483451284408024113768728530854211087557655
- 0.038772417506050821933193444024623294679364634383139947198477
+ 0.038772417506050821933193444024623294679364634383139947198477
+ 0.116084070675255208483451284408024113768728530854211087557655
+ 0.192697580701371099715516852065149894814092021105201079079604
+ 0.268152185007253681141184344808596183424804373236236683321946
+ 0.341994090825758473007492481179194310066953620027313547235050
+ 0.413779204371605001524879745803713682974099624052904661350012
+ 0.483075801686178712908566574244823004599022395533099841136162
+ 0.549467125095128202075931305529517970233975101595637141746493
+ 0.612553889667980237952612450230694877380123781683135778757367
+ 0.671956684614179548379354514961494109970325981383838269965139
+ 0.727318255189927103280996451754930548557378673533316562403522
+ 0.778305651426519387694971545506494848020691316126881762542263
+ 0.824612230833311663196320230666098773907240384242979438623162
+ 0.865959503212259503820781808354619963570546553011094983606217
+ 0.902098806968874296728253330868493103584488081057664431112536
+ 0.932812808278676533360852166845205716434753575282688898929952
+ 0.957916819213791655804540999452759285094883490602744761591148
+ 0.977259949983774262663370283712903806978667932037984851175804
+ 0.990726238699457006453054352221372154962220813510860248783 52
+ 0.998237709710559200349622702420586492335770381595045808577581

APPENDIX V:
Calculation of the angle between sub-cables in a multi-strand cable

V.1 Calculation of the angle between sub-cables and its effect on the modeling

In Chapters 5 and 6, the contact area between strands is evaluated using two parameters α and β that depends on the angle ϕ between the two strands. The angle ϕ can be found using a simple 2D model or a more precise 3D model. It turns out there is not much difference between the two model for the tested cables (3-strand cable and 45-strand cable) presented in Chapter 5 but for higher stages cables the more precise model has to be used.

In this appendix, the two approaches will be presented and a comparison between the results will be made for the appropriate cases of interest. Cables composed of three, four and five subcables will be considered in the calculation.

2D model

Referring to Fig. V.1 it can be seen that with a simplified 2D assumption the angle between strands can be estimated with Eq. V.1-2:

$$tan\gamma = \frac{L_p}{2\pi \cdot r_b} \tag{V.1}$$

$$\omega = 2 \cdot (\frac{\pi}{2} - \gamma) \tag{V.2}$$

where L_p is the twist pitch of a particular stage, ω the angle between the strands, b the radius of the subcable, r_b the distance from the center of the cable around which the subcable rotates. This distance depends on the number of subcable inside the cables as shown in Fig. V.1.

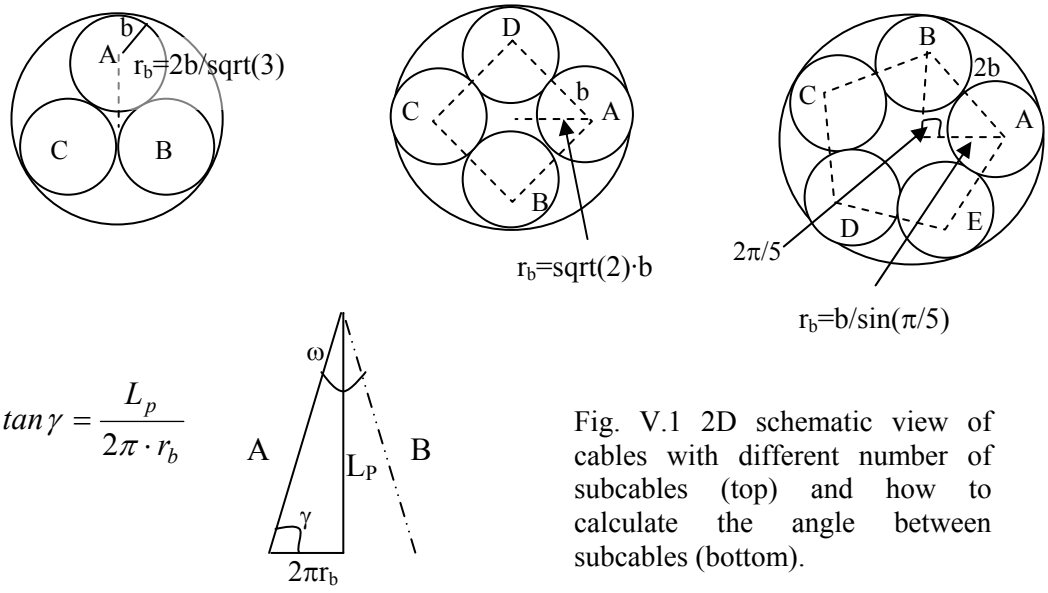

$$tan\gamma = \frac{L_p}{2\pi \cdot r_b}$$

Fig. V.1 2D schematic view of cables with different number of subcables (top) and how to calculate the angle between subcables (bottom).

3D model

Using a 3D approach, three different cases are considered:

(i) Three subcables

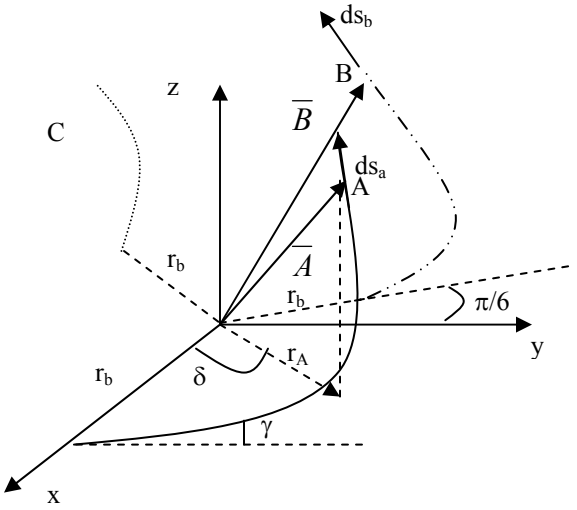

Fig. V.2 3D coordinate system used in the calculation.

The trajectories of the center of sub-cables (or strands) A and B shown in Fig. V.2 can be written with vectors $\overline{A}$ and $\overline{B}$:

$$\overline{A} = r_b \cdot \cos\delta\,\overline{x} + r_b \cdot \sin\delta\,\overline{y} + r_b \cdot \delta \cdot \tan\gamma\,\overline{z} \tag{V.3}$$

$$\overline{B} = r_b \cdot \cos(\delta + \frac{2\pi}{3})\,\overline{x} + r_b \cdot \sin(\delta + \frac{2\pi}{3})\,\overline{y} + r_b \cdot \tan\gamma\,\overline{z} \tag{V.4}$$

with $\tan\gamma = L_p/2\pi r_b$, L_p being twist pitch.

The line vectors on the axis of a sub-cable (or strands) A and B are:

$$\overline{ds_A} = -r_b \cdot \sin\delta \cdot d\delta\,\overline{x} + r_b \cdot \cos\delta \cdot d\delta\,\overline{y} + r_b \cdot \tan\gamma \cdot d\delta\,\overline{z} \tag{V.5}$$

$$\overline{ds_B} = -r_b \cdot \sin(\delta + \frac{2\pi}{3}) \cdot d\delta\,\overline{x} + r_b \cdot \cos(\delta + \frac{2\pi}{3}) \cdot d\delta\,\overline{y} + r_b \cdot \tan\gamma \cdot d\delta\,\overline{z} \tag{V.6}$$

Given the Eq. V.3-V.6 the angle ϕ between the subcables A and B (the angle between $\overline{ds_A}$ and $\overline{ds_B}$), can be found using the well known general vector equation:

$$\cos\phi = \frac{\overline{ds_A} \cdot \overline{ds_B}}{|\overline{ds_A}| \cdot |\overline{ds_B}|} = \frac{2 \cdot \tan^2\gamma - 1}{2 \cdot (1 + \tan^2\gamma)} = \frac{3 \cdot \sin^2\gamma - 1}{2} \tag{V.7}$$

(ii) Four subcables

In case of a cable composed of four subcables (before swaging):

$$\bar{A} = r_b \cdot \cos\delta\bar{x} + r_b \cdot \sin\delta\bar{y} + r_b \cdot \delta \cdot \tan\gamma\bar{z} \quad \text{(V.8)}$$

$$\bar{B} = r_b \cdot \cos(\delta + \frac{\pi}{2})\bar{x} + r_b \cdot \sin(\delta + \frac{\pi}{2})\bar{y} + r_b \cdot \tan\gamma\bar{z} \quad \text{(V.9)}$$

with $\tan\gamma = L_p/2\pi r_b$, L_p being twist pitch.

The line vectors on the axis of a sub-cable (or strands) A and B are:

$$\overline{ds_A} = -r_b \cdot \sin\delta \cdot d\delta\bar{x} + r_b \cdot \cos\delta \cdot d\delta\bar{y} + r_b \cdot \tan\gamma \cdot d\delta\bar{z} \quad \text{(V.10)}$$

$$\overline{ds_B} = -r_b \cdot \sin(\delta + \frac{\pi}{2}) \cdot d\delta\bar{x} + r_b \cdot \cos(\delta + \frac{\pi}{2}) \cdot d\delta\bar{y} + r_b \cdot \tan\gamma \cdot d\delta\bar{z} \quad \text{(V.11)}$$

Given the Eq. V.2-V.5 the angle ϕ between the subcables A and B is:

$$\cos\phi = \frac{\overline{ds_A} \cdot \overline{ds_B}}{|\overline{ds_A}| \cdot |\overline{ds_B}|} = \frac{\tan^2\gamma}{(1+\tan^2\gamma)} = \sin^2\gamma \quad \text{(V.12)}$$

(iii) Five subcables

In case of a cable composed of five subcables (before swaging):

$$\bar{A} = r_b \cdot \cos\delta\bar{x} + r_b \cdot \sin\delta\bar{y} + r_b \cdot \delta \cdot \tan\gamma\bar{z} \quad \text{(V.13)}$$

$$\bar{B} = r_b \cdot \cos(\delta + \frac{2\pi}{5})\bar{x} + r_b \cdot \sin(\delta + \frac{2\pi}{5})\bar{y} + r_b \cdot \tan\gamma\bar{z} \quad \text{(V.14)}$$

with $\tan\gamma = L_p/2\pi r_b$, L_p being twist pitch.

The line vectors on the axis of a sub-cable (or strands) A and B are:

$$\overline{ds_A} = -r_b \cdot \sin\delta \cdot d\delta\bar{x} + r_b \cdot \cos\delta \cdot d\delta\bar{y} + r_b \cdot \tan\gamma \cdot d\delta\bar{z} \quad \text{(V.15)}$$

$$\overline{ds_B} = -r_b \cdot \sin(\delta + \frac{2\pi}{5}) \cdot d\delta\bar{x} + r_b \cdot \cos(\delta + \frac{2\pi}{5}) \cdot d\delta\bar{y} + r_b \cdot \tan\gamma \cdot d\delta\bar{z} \quad \text{(V.16)}$$

Given the Eq. V.2-V.5 the angle ϕ between the subcables A and B is:

$$\cos\phi = \frac{\overline{ds_A} \cdot \overline{ds_B}}{|\overline{ds_A}| \cdot |\overline{ds_B}|} = \frac{\cos(\frac{2\pi}{5}) + \tan^2\gamma}{(1+\tan^2\gamma)} = 1 - (1 - \cos(\frac{2\pi}{5}))\cos^2\gamma \quad \text{(V.17)}$$

Table V.1 gives three examples of different cables and the results obtained using Eq. V.2 and Eq. V.7, V.17. The table clearly shows that the difference between ω and ϕ can be significant for larger cables (45-strand cable). The subcable distance from the center, r_b, is obtained using the information obtained from the previous stage (b for the 9-strand is the radius of the 3-strand, b for the 45-strand is the radius of the 9-strand).

Table V.1 Results using different cables using the 2D and 3D models.

Cable	3-strand	9-strand	45-strand
Stage		3x3	3x3x5
Wire radius a (mm)	0.41	0.41	0.41
Void fraction v_f	0.33	0.33	0.33
Subcable center r_b (mm)	$\frac{2\cdot b}{\sqrt{3}}=\frac{2\cdot a}{\sqrt{3}}=$ =0.473	$\frac{2\cdot b}{\sqrt{3}}=\frac{2\cdot 0.883}{\sqrt{3}}=$ =1.020	$\frac{b}{sin(\pi/5)}=\frac{1.503}{0.5878}=2.557$
Radius after swaging (mm)	0.883	1.503	3.360
Twist Pitch (mm)	45	85	125
tanγ ($L_p/2\pi r_b$)	15.1	13.3	7.8
γ (°)	86.2	85.7	82.7
ω (°)	7.6	8.6	**14.6**
ϕ (°)	6.5	7.5	**8.6**

As presented in Chapter 5 and Appendix III, the angle ϕ is used to estimate the parameters α and β that are used to calculate the semi-axes of the ellipsoidal contact between two strands using the following equations:

$$\cos\Omega=\frac{2\cdot K_D}{3}\cdot\left\{\left(\frac{1}{a}\right)^2+\left(\frac{1}{a}\right)^2+2\left(\frac{1}{a}\right)\left(\frac{1}{a}\right)\cos 2\phi\right\}^{1/2}=\left\{\frac{(1+\cos 2\phi)}{2}\right\}^{1/2}=\cos\phi \quad \text{(V.18)}$$

$$\eta=\alpha\cdot\left(\frac{F\cdot K_D}{E^*}\right)^{1/3} \quad \text{(V.19)}$$

$$\xi=\beta\cdot\left(\frac{F\cdot K_D}{E^*}\right)^{1/3} \quad \text{(V.20)}$$

Table V.2 is reporting α and β as a function of the angle Ω which for the case of our analysis is equal to ϕ.

Fig. V.3 shows the two values as a function of the angle ϕ and it can be seen that in the range of interest between 0 and 30° while β does not vary very rapidly, α is varying sharply especially at small angles. The 3D analysis is used to better estimate the angle ϕ so that the best estimate for the variables α and β can be obtained.

For the cables tested in this work and for a full size cable like the one used in ITER, the angle ϕ varies from 6.5° and 8.6° and the variables α and β do not vary much in this range. Furthermore the majority of crossing points are generated by 3-strand (triplet) bundles so that the 3-strand contact angle $\phi_3=6.5°$ is used in the analysis.

Table V.2 Tabulated values of α and β to evaluate the semi-axis of the ellipse of contact [5.7, 5.8].

Ω=ϕ	α	β
0	-	0
1	36.890	0.131
2	22.260	0.169
3	16.500	0.196
4	13.310	0.209
6	9.790	0.255
8	7.860	0.285
10	6.612	0.319
20	3.778	0.408
30	2.731	0.493
35	2.397	0.530
40	2.136	0.567
45	1.926	0.604
50	1.754	0.641
55	1.611	0.678
60	1.486	0.717
65	1.378	0.759
70	1.284	0.802
75	1.202	0.846
80	1.128	0.893
85	1.061	0.944
90	1.000	1.000

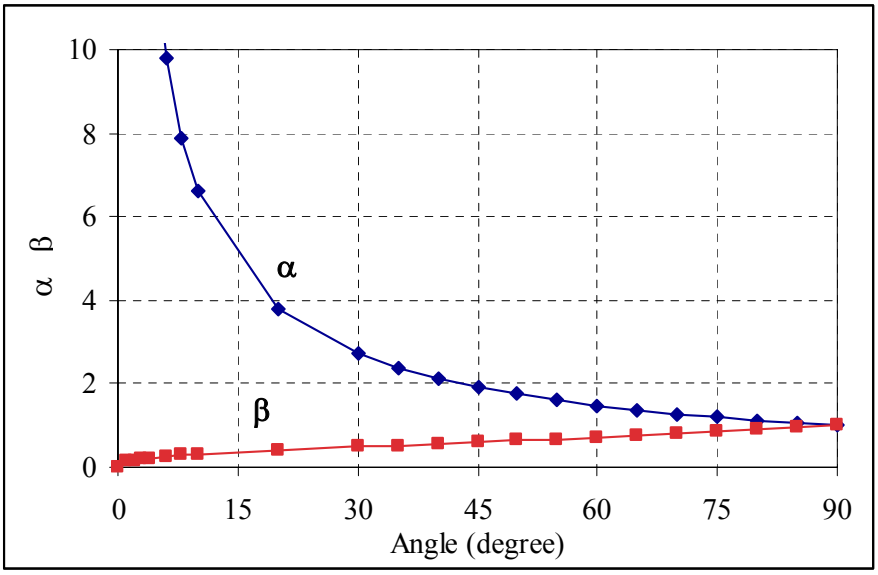

Fig. V.3 Variables α and β, used to evaluate the semi-axes of the contact area between strands, are shown as a function of the angle ϕ.

REFERENCES

Chapter 1

[1.1] Hyperphysics website http://hyperphysics.phy-astr.gsu.edu/hbase/hframe.html

[1.2] A. Godeke, *"Performance boundaries in Nb_3Sn Superconductors",* Ph.D. thesis, University of Twente, Enschede, The Netherlands, 2005.

[1.3] Hyperphysics website http://hyperphysics.phyastr.gsu.edu/hbase/solids/meis.html

[1.4] W. Meissner and R. Ochsenfeld, *"Eh neuer Effekt bei Eintritt der Supraleitfiihigkeit"*, Naturwissenschaften 21, 787 (1933)

[1.5] Y. Iwasa and J.V. Minervini *"Class 22.68j Superconducting Magnets",* Spring 2005

[1.6] J.V. Minervini *"Analysis of Loss Mechanism in Superconducting Windings for Rotating Electric Generators",* PhD Thesis, Massachusetts Institute of Technology, U.S.A. 1981.

[1.7] C.P. Bean and J.D. Livingston, *"Surface Barrier in Type-II Superconductors"*, Phys. Rev. Lett.14 (1964), p. 12.

[1.8] P.W. Anderson and Y.B. Kim, *"Hard superconductivity:Theory of the motion of Abrikosov Flux Lines," Rev. Mod. Phys.*, vol. 36, pp. 39-43, 1964.

[1.9] J.H. Schultz *"The Medium Temperature Superconductor (MTS) Design Phylosophy",* IEEE Trans. On Applied Superconductivity, Vol. 13, No. 2, June 2003, p. 1604-1607.

[1.10] ITER website http://www.iter.org/index.htm, CERN website http://public.web.cern.ch/Public/Welcome.html, Oxford Magnet, http://www.wtec.org/loyola/scpa/02_06.htm, American Superconductors, http://www.hizlitrenbileti.com/maglev.html,.

[1.11] ITER technical basis, *"The plant description document: Chapter 2.1 Magnets"*, ITER website http://www.iter.org/index.htm.

[1.12] G. Bruzzone et al., *"Results of a New Generation of ITER TF Conductor Samples in SULTAN"* IEEE Trans. On Applied Superconductivity, Vol. 18, No. 2, June 2008, p.459-462.

[1.13] A. Nijhuis, *"A solution for transverse load degradation in ITER Nb_3Sn CICCs: verification of cabling effect on Lorentz force response"* Supercond. Sci. Technol. 21 (2008)

[1.14] D. L. Harris, *"Characterization of Nb_3Sn Superconducting Strand Under Pure Bending",* M.S. in Mechanical Engineering, Massachusetts Institute of Technology, U.S.A. 2005.

[1.15] B. Seeber et al., *"Critical current of a Nb3Sn bronze route conductor under uniaxial tensile and transverse compressive stress"* Supercond. Sci. Technol. 20 (2007), S184-S188.

Chapter 2

[2.1] D. R. Dietderich et al. *"Critical Current of Superconducting Rutherford Cable in High Magnetic Fields with Transverse Pressure"* IEEE Trans. On Applied Superconductivity, Vol. 9, No. 2, June 1999, p.122-125.

[2.2] Joel H. Schultz and Peter Titus, *"Transverse Load Degradation of ITER-class Nb_3Sn CICC Performance",* ITER-USMIT-JSchultz-050403-01, May 4, 2003.

[2.3] J.W. Ekin, *"Transverse stress effect on multifilamentary Nb_3Sn superconductor",* Adv in Cryo Eng (Materials), Vol. 34, p. 547, Ed. A.F. Clark and R.P. Reed, Plenum Press, NY, 1988.

[2.4] N. Mitchell, *"Summary, assessment and implications of the ITER model coils test results",* Fusion Engineering and Design, Vol. 66–68, p. 971–993, 2003.

[2.5] D. Boso et al., *"Thermal and Bending Strain on Nb_3Sn Strands"*, IEEE Transactions on Applied Superconductivity, Vol. 16, No. 2, June 2006, p.1823-1827.

[2.6] R. Zanino et al., "Analysis of Bending Effects on Performance Degradation of ITER-Relevant Nb_3Sn Strand Using the THELMA Code", IEEE Transactions on Applied Superconductivity, Vol. 18, No. 2, June 2008, p. 1067-1071.

[2.7] A. Nijhuis, *"A solution for transverse load degradation in ITER Nb_3Sn CICCs: verification of cabling effect on Lorentz force response"*, Supercond. Sci. Technol. 21, 2008.

[2.8] M. Salvetti, *"Strain-Dependence of the Superconducting Critical Temperature Tc in Al, Nb and Nb_3Sn Crystals"*, presented at the IACM/ECCOMAS 2008.

[2.9] W. D. Markiewicz, "Comparison of strain scaling functions for the strain dependence of composite Nb_3Sn superconductors", Supercond. Sci. Technol. 21, 2008.

[2.10] J.W. Ekin *"Strain scaling law for flux pinning in practical superconductors. Part I: Basic relationship and application to Nb_3Sn conductors",* Cryogenics, 20 1980, p. 611-624.

[2.11] L. Bottura, *"$J_C(B,T,\varepsilon)$ Parameterization for ITER Nb_3Sn Production"*, ITER Documentation.

[2.12] Y. Ilyin et al., *"Scaling law for the strain dependence of the critical current in an advanced ITER Nb_3Sn strand"*, Supercond. Sci. Technol. 20, 2007, p. 186–191

[2.13] H.J.N. van Eck et al., *"Critical current versus strain research at the University of Twente"*, Superconductor Science and Technology, v16, n9, Sept. 2003, p.1026-1030.

[2.14] A. Godeke et al., *"A device to investigate the axial strain dependence of the critical current density in superconductors",* Review of Scientific Instruments, v75, n12, Dec. 2004, p 5112-5118.

[2.15] D. Uglietti et al., *"Critical Current vs. Strain Measurements of Long Length Nb3Sn Wires up to 1000A and 17T using a modified Walters Spring"*, IEEE Transactions on Applied Superconductivity, v.13, n2, June 2003, p 3544-3547.

[2.16] J.R. Miller et al. *"The initial filament strain state of cable in conduit superconductors and relation of this strain to large-bore, high-field magnet design",* IEEE Trans. Mag., Vol. MAG-23. March 1987, p. 1547-1551.

[2.17] W. Specking et al. *"The effect of static and cyclic axial strain on I_c of cable in conduit NET subcables",* IEEE Trans. Mag., Vol. MAG-27. March 1991, p. 1825-1828.

[2.18] K. P. Weiss et al., *"Systematic Approach to Examine the Strain Effect on the Critical Current of Nb_3Sn Cable-in-Conduit-Conductors",* IEEE Transactions on Applied Superconductivity, Vol. 17, No. 2, June 2007, p.1469-1472.

[2.19] W.A.J. Wessel et al., "*A novel 'test arrangement for strain influence on strands' (TARSIS): mechanical and electrical testing of ITER Nb3Sn strands"*, AIP Conference Proceedings, n711, pt.2, 2004, p 466-73.

[2.20] A. Nijhuis et al., *"Impact of spatial periodic bending and load cycling on the critical current of a Nb_3Sn strand"*, Supercond. Sci. Technol. 18, 2005, p. S273-S283.

[2.21] P. Michael et al., *"Test of the ITER Central Solenoid Model Coil and CS Insert"*, IEEE Trans. Appl. Superconductivity, Vol. 12, No. 1, March 2002, p. 600-605.

[2.22] B. J. Senkowicz et al., "*Effects of bending on cracking and critical current of Nb3Sn ITER* wires", IEEE Transactions on Applied Superconductivity, v15, n2, pt. III, June, 2005, p 3470-3473.

[2.23] D. L. Harris, *"Characterization of Nb_3Sn Superconducting Strand Under Pure Bending",* M.S. in Mechanical Engineering, Massachusetts Institute of Technology, U.S.A. 2005.

[2.24] A. Allegritti, *"Development and experimental test of a device for the measurements of the critical current of superconducting strands under pure bending conditions",* University of Bologna, Department of Mechanical Engineering, Italy, 2006.

[2.25] Ekin J W 1980 Proc. Topical Conf. on-A15-Supercond. (New York: Plenum) p 187 (IB: 0306-40622-5).

[2.26] A. Nijhuis et al., *"Transverse load optimization in Nb_3Sn CICC design; influence of cabling, void fraction and strand stiffness",* Supercond. Sci. Technol. 19, 2006, p. 945–962.

[2.27] M. Takayasu et al., *"Bending strain results of ITER Nb3Sn wires and preliminary model analysis"*, ITER Task Report, June 2008.

[2.28] M.C. Jewell, P.J. Lee and D.C. Larbalestier, *"The influence of Nb3Sn strand geometry on filament breakage under bend strain as revealed by metallography,"* Supercond Sci Technol, 16, 1005-1011, 2003.

[2.29] J. Ekin, *"Current transfer in multifilamentary superconductors. I. Theory,"* J. Appl. phys. 49, 3406-3409, 1978.

[2.30] J. Ekin and A.F. Clark, *"Current transfer in multifilamentary superconductors. II. Experimental results,"* J. Appl. phys. 49, 3410-3412, 1978.

[2.31] A. Nijhuis, Y. Ilyin, W.A.J. Wessel and W. Abbas, *"Critical current and strand stiffness of three types of Nb3Sn strand subjected to spatial periodic bending,"* Supercon. Sci. Technol. 19, 1136-1145, 2006.

[2.32] J.W. Ekin, *"Effect of transverse compressive stress on the critical current and upper critical field of Nb_3Sn"*, J. Appl. Phys., vol. 62, Dec. 1987, p. 4829.

[2.33] J.W. Ekin, *"Transverse stress effect on multifilamentary Nb_3Sn superconductor"*, Adv. Cryogenics Eng., vol. 34, 1988, p. 547-552.

[2.34] W. Specking et al., *"Effect of transverse compression on I_c of Nb_3Sn multifilamentary wire"*, Adv. Cryogenics Eng., vol. 34, 1988, p. 569.
[2.35] J.W. Ekin et al., *"Effect of transverse stress on the critical current of bronze-process and internal-tin Nb_3Sn"*, J. Appl. Phys., vol. 69, Apr. 1991, p. 4436.
[2.36] J.W. Ekin and S.L. Bray, *"Critical current degradation in Nb_3Sn composite wires due to locally concentrated transverse stress"*, Adv. Cryogenics Eng., vol. 38, 1992.
[2.37] A. Nijhuis et al., *"Spatial periodic contact stress and critical current of a Nb_3Sn strand measured in TARSIS"*, Supercond. Sci. Technol. 19, 2006, p. 1089–1096.
[2.38] B. Seeber et al., *"Critical current of a Nb_3Sn bronze route conductor under uniaxial tensile and transverse compressive stress"*, Supercond. Sci. Technol. 20, 2007, p. S184–S188.
[2.39] A. Nijhuis et al., *"Axial tensile stress–strain characterization of ITER model coil type Nb_3Sn strands in TARSIS"*, Supercond. Sci. Technol. 18, 2005, p. 1523–1532.
[2.40] L.T. Summers and J.R. Miller, *"The effect of transverse stress on the critical current of Nb_3Sn cable in conduit superconductors"*, IEEE Trans. Mag., Vol. 25. March 1989, p. 1835-1838.
[2.41] L.T. Summers and J.R. Miller, *"Further studies of transverse stress effects in cable in conduit conductors"*, internal note LLNL.
[2.42] M. Takayasu, *"Current Sharing Temperature And Critical Current Analyses Based On Single Strand Data,"* CSMC and CSIC Workshop at JAERI, Naka, Japan, November 9 – 11, 2000.
[2.43] L.T. Summers, M.W. Guinan, J.R. Miller, and P.A. Hahn, "*A model for the prediction of Nb_3Sn critical current as a function of field, temperature, strain, and radiation damage"*, IEEE Trans. Mag., 27, 2041, 1991.

Chapter 3

[3.1] Timothy D. Alvey, *"Calorimetric Measurement of Energy Dissipation in Superconducting Cables",* M.S. in Nuclear Engineering, Massachusetts Institute of Technology, U.S.A. 2000.
[3.2] Y. Takahashi, "AC loss Measurements of 46 kA-13 T Nb3Sn Conductor for ITER", IEEE Trans. on Applied Superconductivity, Vol. 1, No. 1, March 2001, p.1546-1549.
[3.3] D. Ciazynski, *"Review of Nb3Sn conductors for ITER"*, Fusion Eng. And Design, 82 (2007) 488–497
[3.4] J. W. Ekin, *"Strain Effects in Superconducting Compounds"*, Adv. Cryo. Eng. 30, 823-836 (1984).
[3.5] A. Nijhuis et al.,*"Performance of an ITER CS1 Model Coil Conductor under Transverse Cyclic Loading up to 40000 cycles"* , IEEE Trans. on Applied Superconductivity, Vol. 14, No. 2, June 2004, p.1489-1494.

Chapter 4

[4.1] A. Nijhuis et al.,*"Performance of an ITER CS1 Model Coil Conductor under Transverse Cyclic Loading up to 40000 cycles"* , IEEE Trans. on Applied Superconductivity, Vol. 14, No. 2, June 2004, p.1489-1494.

Chapter 5

[5.1] H. Hertz, *"Miscellaneous papers"*, Macmillan and Co., New York 1896.
[5.2] S.P. Timoshenko and J.N. Goodier, *"Theory of Elasticity"*, 3rd edition, McGraw-Hill Book, 1970.
[5.3] S.P. Timoshenko and J.M. Lessells, *"Applied Elasticity"*, Westinghouse Techical Night School Press, East Pittsburgh, PA 1925.
[5.4] S.P. Timoshenko, *"Strength of Materials"*, Van Nostrand Reinhold Company.
[5.5] K.L. Johnson, *"Contact Mechanics"*, Cambridge University Press,1985.
[5.6] R. J. Roark, W.C. Young, *"Formulas for Stress and Strain"*, 5th edition, McGraw-Hill Book.
[5.7] H.L. Whittemore and S.N. Petrenko, *"Friction and Carrying Capacity of Ball and Roller Bearings"*, Technical Paper of the Bureau of Standards #201, 1921.
[5.8] M. Kornhauser, *"A note on elastic surface deformation"*, Journal of Applied Mechanics, vol. 18, 1951, p. 251-252.
[5.9] A. Foppl, *"Technische Mechanik"*, 4th edition, vol. 5, 1907, p. 350.
[5.10] C. Bond, *"A New Integration Method Providing the Accuracy of Gauss-Legendre with Error Estimation Capability"*, http://www.crbond.com/papers/gbint.pdf

Chapter 6

[6.1] A. Nijhuis, *"A solution for transverse load degradation in ITER Nb_3Sn CICCs: verification of cabling effect on Lorentz force response"*, Supercond. Sci. Technol. 21, 2008.
[6.2] N. Mitchell, *"Mechanical and magnetic load effects in Nb_3Sn cable-in-conduit conductors"*, Cryogenics, Vol. 43/3-5, p. 255–70, 2003
[6.3] Y. Zhai and M. Bird, "Florida electro-mechanical cable model of Nb_3Sn CICCs for high-field magnet design", Supercond. Sci. Technol. 21, 2008.
[6.4] L. Bottura, *"$J_C(B,T,\varepsilon)$ Parameterization for ITER Nb_3Sn Production"*, ITER Documentation.

Chapter 7

[7.1] ITER Naka Joint Work Site, Superconducting Coils and Structures Division, "1a. DDD 1.1-1.3 Appendix C Design Criteria," December 8, 1997.
[7.2] J.W. Ekin and S.L. Bray, *"Critical current degradation in Nb_3Sn composite wires due to locally concentrated transverse stress"*, Adv. Cryogenics Eng., vol. 38, 1992.
[7.3] L.T. Summers and J.R. Miller, *"The effect of transverse stress on the critical*

current of Nb_3Sn cable in conduit superconductors", IEEE Trans. Mag., Vol. 25. March 1989, p. 1835-1838.

[7.4] L.T. Summers and J.R. Miller, *"Further studies of transverse stress effects in cable in conduit conductors"*, internal note LLNL.

[7.5] N. Mitchell, *"Mechanical and magnetic load effects in Nb_3Sn cable-in-conduit conductors"*, Cryogenics, Vol. 43/3-5, p. 255–70, 2003

[7.6] A. Nijhuis, *"A solution for transverse load degradation in ITER Nb_3Sn CICCs: verification of cabling effect on Lorentz force response"*, Supercond. Sci. Technol. 21, 2008.

[7.7] Y. Zhai and M. Bird, "Florida electro-mechanical cable model of Nb_3Sn CICCs for high-field magnet design", Supercond. Sci. Technol. 21, 2008.

[7.8] N. Martovetsky et al, *"Effect of conduit material on CICC performance under high cyclic load"*, IEEE Transactions on Applied Superconductivity, v.15, n2, June 2005, p 1367-1370.

[7.9] P. Bruzzone et al, *"Tets results of a Nb_3Sn cable-in-conduit conductor with variable pitch sequence"*, to be published, presented at ASC 2008.

Appendix I

[AI.1] L. Chiesa, *"Development of an Experiment to study the effects of transverse stress on the critical current of a Niobium-tin superconducting cable",* M.S. in Nuclear Engineering, Massachusetts Institute of Technology, U.S.A. 2006.

Appendix III

[III.1] H. Hertz, *"Miscellaneous papers"*, Macmillan and Co., New York 1896.

[III.2] S.P. Timoshenko and J.N. Goodier, *"Theory of Elasticity"*, 3rd edition, McGraw-Hill Book, 1970.

[III.3] S.P. Timoshenko and J.M. Lessells, *"Applied Elasticity"*, Westinghouse Techical Night School Press, East Pittsburgh, PA 1925.

[III.4] S.P. Timoshenko, *"Strength of Materials"*, Van Nostrand Reinhold Company.

[III.5] K.L. Johnson, *"Contact Mechanics"*, Cambridge University Press,1985.

[III.6] R. J. Roark, W.C. Young, *"Formulas for Stress and Strain"*, 5th edition, McGraw-Hill Book.

[III.7] H.L. Whittemore and S.N. Petrenko, *"Friction and Carrying Capacity of Ball and Roller Bearings"*, Technical Paper of the Bureau of Standards #201, 1921.

[III.8] M. Kornhauser, *"A note on elastic surface defromation"*, Journal of Applied Mechanics, vol. 18, 1951, p. 251-252.

[III.9] A. Foppl, *"Technische Mechanik"*, 4th edition, vol. 5, 1907, p. 350.

Appendix IV

[IV.1] C. Bond, *"A New Integration Method Providing the Accuracy of Gauss-Legendre with Error Estimation Capability"*, http://www.crbond.com/papers/gbint.pdf